ARO 21656.10-EL

②

AD-A222 989

TRANSIENT SIGNAL DISTORTION AND COUPLING
IN MULTILAYER MULTICONDUCTOR MIC MICROSTRIPS

by

Constantine A. Balanis and James P.Gilb

Final Report

May 22, 1990

Prepared by

Department of Electrical Engineering
Telecommunication Research Center
Arizona State University
Tempe, AZ 85287-7206

DISTRI...

Ap...

REPORT DOCUMENTATION PAGE	Form Approved OMB No. 0704-0188

1a. REPORT SECURITY CLASSIFICATION	1b. RESTRICTIVE MARKINGS
Unclassified	

2a. SECURITY CLASSIFICATION AUTHORITY	3. DISTRIBUTION / AVAILABILITY OF REPORT
2b. DECLASSIFICATION / DOWNGRADING SCHEDULE	

4. PERFORMING ORGANIZATION REPORT NUMBER(S)	5. MONITORING ORGANIZATION REPORT NUMBER(S)
DWA 1682	Dr. James W. Mink Electronics Division, ARO

6a. NAME OF PERFORMING ORGANIZATION	6b. OFFICE SYMBOL (If applicable)	7a. NAME OF MONITORING ORGANIZATION
Dept. of Electrical Engineering Telecommunications Research Ctr		Office of Naval Research Resident Representative

6c. ADDRESS (City, State, and ZIP Code)	7b. ADDRESS (City, State, and ZIP Code)
Arizona State University Tempe, AZ 85287-7206	University of New Mexico Bandelier Hall West Albuquerque, NM 87131

8a. NAME OF FUNDING / SPONSORING ORGANIZATION	8b. OFFICE SYMBOL (If applicable)	9. PROCUREMENT INSTRUMENT IDENTIFICATION NUMBER
U.S. Army Research Office		Contract No. DAAG29-85-K-0078

8c. ADDRESS (City, State, and ZIP Code)	10. SOURCE OF FUNDING NUMBERS			
Electronics Division P.O. Box 12211 Research Triangle Park, NC 27709-2211	PROGRAM ELEMENT NO.	PROJECT NO.	TASK NO.	WORK UNIT ACCESSION NO.

11. TITLE (Include Security Classification)
Transient Signal Distortion and Coupling in Multilayer Multiconductor MIC Microstrips (unclassified)

12. PERSONAL AUTHOR(S)
Balanis, Constantine A., and Gilb, James P.

13a. TYPE OF REPORT	13b. TIME COVERED	14. DATE OF REPORT (Year, Month, Day)	15. PAGE COUNT
Final	FROM 4/1/85 TO 3/31/90	May 22, 1990	197

16. SUPPLEMENTARY NOTATION

17. COSATI CODES			18. SUBJECT TERMS (Continue on reverse if necessary and identify by block number)
FIELD	GROUP	SUB-GROUP	Transient signals, distortion, dispersion, microstrip lines, multiconductor, multilayer, effective dielectric constant

19. ABSTRACT (Continue on reverse if necessary and identify by block number)

The frequency dependent characteristics of symmetric coupled microstrips in multilayer structures are considered in order to study transient signal distortion and coupling on these structures. Using the spectral domain approach with TE^y (LSE) and TM^y (LSM) modes, a simple recurrence relation is derived for the generalized Green's function of arbitrary multilayer structures. The frequency domain approach is used in conjunction with the even/odd mode analysis to formulate the time domain response for both of the coupled lines. Numerical results are presented for single layer structures, showing the effects of substrate materials, center conductor spacing, and line length. Results for multilayer structures are also given, showing the effects of additional substrates and superstrates on the line parameters. A new method for equalizing the even and odd phase velocities, and thus controlling the signal distortion and coupling, over a wide band of frequencies by properly selecting the dimensions and electrical properties of the substrate materials is presented.

20. DISTRIBUTION / AVAILABILITY OF ABSTRACT	21. ABSTRACT SECURITY CLASSIFICATION
[X] UNCLASSIFIED/UNLIMITED [ ] SAME AS RPT [ ] DTIC USERS	Unclassified

22a. NAME OF RESPONSIBLE INDIVIDUAL	22b. TELEPHONE (Include Area Code)	22c. OFFICE SYMBOL

DD Form 1473, JUN 86 Previous editions are obsolete.

TABLE OF CONTENTS

LIST OF FIGURES

CHAPTER 1
INTRODUCTION

The printed circuit transmission line has become an integral part of many high frequency circuit applications, creating an ever increasing demand for accurate theoretical predictions of circuit performance. While approximate formulations were acceptable in the past, rising performance expectations as well as the desire for circuits that don't require post-production tuning have made the use of more exact formulations necessary. This report uses exact formulations to address four major areas of concern in high frequency printed circuit design; complex microstrip structures (multiple lines and/or dielectric layers), coupling between lines, distortion of non-periodic signals on complex structures, and a new method to control coupling on multilayer structures, as well as presenting numerical results for each of these areas. This chapter discusses the uses of microstrips, discusses the various types of approaches used to solve the above mentioned problems, and outlines the solution methods and numerical results presented in this report.

1.1 History and Applications of Microstrips

While the use of printed circuit transmission lines is a relatively recent development, today its technology is considered to be mature. The first printed circuit transmission line, the strip line,

was developed in World War II while the microstrip was first proposed and investigated in the early fifties. Yet, by 1955, the *IRE Transactions on Microwave Theory and Techniques* [1] devoted an entire issue to the research and design of this new form of microwave circuitry. Early research in this field was concerned with calculating the low frequency parameters of the microstrip using a quasi-static TEM approach. Demands for higher operating frequencies, shorter pulse widths, and smaller circuit dimensions required that researchers address the frequency dependent nature of the microstrip parameters. Today, the research field is concerned with obtaining more rigorous solutions of complex microstrip structures that include:

1. Multiple dielectric layers.

2. Multiple conductors on different layers.

3. Anisotropic dielectrics.

4. Operating frequencies that approach the optical range.

5. Discontinuities in the line.

6. Losses in the conductors and the dielectrics.

7. Losses due to radiation.

The design of microwave integrated circuits has become very advanced, so that there are several commercial computer aided design packages on the market [2]. Thus microstrip circuit design has become sufficiently advanced to be considered a mature technology.

In spite of the microwave integrated circuit's (MIC's) low power handling capabilities, it enjoys increasing popularity due to its many advantages over waveguide and coaxial lines. MIC's are relatively inexpensive to make and the fabrication process is simple. Because of

its planar structure, modern surface mounted components, such as GaAs
FET's, are easily included in the circuit structure, giving the MIC
circuit a low profile and reduced weight. MIC's are very versatile so
that most of the common passive devices, such as inductors, capacitors,
and resistors, can be realized using microstrips, eliminating the need
to add these passive devices as discrete components. In addition,
MIC's can be used to make phase shifters, mixers, amplifiers, filters,
power dividers, power combiners, and directional couplers. As an
antenna, the MIC is often used on the exterior skin of aircraft and
missiles because its low profile does not affect the aerodynamics of
the vehicle.

MIC's are currently being used in a wide range of high frequency
applications that affect all fields of electrical engineering. MIC
components have been designed to operate in the UHF, microwave, and
millimeter wave regions, and its use is being extended into the low
optical frequencies. Current practical applications include high speed
digital transmission and optoelectronic switches. Microstrips have
even been applied to pulse shaping for a laser used to start a fusion
reaction [3].

1.2 The Effective Dielectric Constant of a Single Microstrip

One of the most common figures of merit used when describing a
microstrip line is the frequency dependent effective dielectric
constant, $\varepsilon_{reff}(f)$. The frequency dependence of ε_{reff} is due to the
discontinuity of the dielectric at the conductor interface, prohibiting
the propagation of a pure TEM mode. This frequency dependence is

responsible for the microstrip's dispersive behavior at higher frequencies, which, in general, is an undesirable property. Although the early efforts in research emphasized the use of a TEM mode or quasi-static approximation, later work in the field approaches the problem from an exact modal or so called full wave solution.

The first attempts at solving for ε_{reff} were approximations that attempted to model the microstrip as a variation of a simpler electromagnetic problem. Conformal mapping of the microstrip structure was used [4], which transforms the geometry of the microstrip into a simpler coordinate system and then solves the quasi-static boundary value problem. The microstrip was also modeled as a ridged waveguide and the solution obtained in terms of longitudinal side electric (LSE) modes [5]. More recently a coupled mode approach has been used, where a TEM is coupled to either at TM_0 mode [6], [7] or a TE_0 mode [8]-[10] to solve the boundary conditions.

As computers became more inexpensive and prevalent, methods were introduced that solved, numerically, the microstrip boundary value problem in spatial variables. These methods, known as spatial domain techniques, achieve answers in the form of a set of simultaneous linear equations that must be solved with a matrix inversion. The formulations are exact in the limit as the number of equations are increased, but large amounts of computer time are required to achieve high accuracy. One spatial domain approach is to formulate a singular integral equation for the microstrip [11], [12] which results in the system of linear equations. Another approach is to use the finite difference method [13], [14] which uses Maxwell's equations in its

first order differential form to specify the fields at a set of discrete points. The first order derivatives are calculated using a difference approximation to create the set of linear equations. Dekelva [15] used a moment method approach, enforcing the boundary conditions at a discrete number of points to achieve results for ε_{reff}. Mode matching [16], [17] splits the microstrip into different regions where the boundary conditions are uniform. The fields in each region are expanded into an infinite set of modes that satisfy the boundary conditions of the particular region. Then the continuity of the fields between regions is enforced by equating the modal sets at the boundaries of each region.

In an effort to reduce the amount of computer time used by the spatial domain techniques while retaining the accuracy of an exact formulation, the Spectral Domain Approach (SDA) was introduced [18]. The SDA begins the solution of the boundary value problem by Fourier transforming the spatial domain fields into the spectral domain. This transformation greatly simplifies the formulation of the boundary value problem and allows accurate results with minimal computer time. Early work with the SDA approached the problem assuming TE^z and TM^z modal configurations for the fields [19]-[21]. While this approach yields the correct answers, as guaranteed by the uniqueness theorem, its derivation is lengthy and complex. To simplify this derivation, TE^y (LSE) and TM^y (LSM) modal configurations were also used, [22], [23], since the microstrip structure closely resembles the partially filled dielectric waveguide. Using this modal configuration, the derivation is simplified and there is less chance for error. The SDA has become

perhaps the most popular technique for solving microstrip problems and in 1985, *IEEE Transactions on Microwave Theory and Techniques* published an invited paper [24] which contains a relatively complete history and description of the SDA as well as an extensive bibliography.

1.3 Coupled Microstrips

While research of single isolated microstrips is important, the effects of neighboring conductors must also be considered in practical circuit design. The simplest structure that can be used to study these effects is the symmetric coupled microstrip, where the presence of the second conductor adds another degree of complexity to the solution of the boundary value problem. However, it is possible to split this problem into two simpler ones that can easily be solved by utilizing the concept of even and odd modes, proposed by Wheeler in 1956 [25]. This method is described in detail in Chapter 2. When the structure is not symmetric, the problem can be split into a similar pair of modes, usually referred to as c and π modes [26].

As with the single microstrip, early research centered on obtaining easily computed approximate equations to describe the frequency dependence of ε_{reff}. Many of the approaches used for single microstrips have also been used for the computation of coupled microstrips, such as conformal mapping [27], an LSE capacitance model [28], and a parallel plate waveguide model [29]. In addition, some curve fitted formulas have also been presented, using both experimental data [30] and results computed with the spectral domain approach [31]. Although these approximate formulas are useful, their application is

limited to a few specific cases. To be able to consider more general structures with high accuracy, full wave methods are used, as in the case of the single microstrip.

Like the approximate modelings, exact formulations for coupled microstrips closely parallel the derivations for single microstrips. Also like the single microstrip formulations, the boundary value problem can be solved in either the spatial or spectral domain. Solutions for the spatial domain are given by Krage and Haddad [32] by expanding the fields into an infinite set of modes in each medium and enforcing, numerically, the vanishing of the electric field on the center conductors. The spectral domain, however, is the easiest of all methods to extend the solution from a single conductor to multiple conductors because it uses a Green's function approach. This approach formulates the boundary value problem assuming only a point source at first. The solution for the actual structure is obtained by using superposition of the point sources to represent the actual current densities. Thus the Green's function derived for the single microstrip can be used without modification for the coupled microstrip problem. The spectral domain has been applied to single [33] and multiple substrate [34] coupled microstrip structures.

1.4 Pulse Dispersion

For single frequency (CW) operation on a microstrip, it is sufficient to know only a single value of ε_{reff}, which can then be used to compute most of the other parameters of interest. However, if either non-periodic or wide band signals are to be used on the

microstrip, then it is important to study the effects of the frequency dependence of ε_{reff} on the signal. Since the microstrip, as a transmission line, is dispersive (the phase velocity is a function of frequency), its response must be analyzed in the frequency domain, whereas a component whose response in time is non-linear, such as transistors or diodes, must be analyzed in the time domain. There are three different methods for determining the time domain response of a dispersive transmission line;

1) Represent the transmission line as a set of matrix parameters, such as ABCD or S parameters.

2) Compute the inverse Fourier transform of the product of the frequency domain transfer function of the line and the Fourier transform of the signal.

3) Model the structure using the time domain finite difference method.

The transmission line parameter approach has been used in conjunction with the microstrip [35], [36], where the matrix parameters were determined using approximate formulas. Although this approach is useful for cases where the transmission line has unmatched loads, accurate computation of the matrix parameters requires additional effort that is not necessary with the Fourier transform method. The time domain finite difference method [14] is similar to the finite difference approach used to find the effective dielectric constant, except that the time derivatives approximated as well as the spatial derivatives. This additional degree of freedom greatly increases the complexity of the derivation, as well as the numerical expense.

The Fourier transform method, using both approximate formulas and full wave solutions to determine $\varepsilon_{reff}(f)$, has been widely used for determining the time domain response of microstrip and coplanar waveguide (CPW) structures to non-periodic signal inputs. Using approximate formulas for $\varepsilon_{reff}(f)$ sacrifices the accuracy of the full wave solution, but drastically reduces the required computer time. Graphs of distorted pulses using approximate formulas for the single microstrip have been presented [3], [37]-[41], with experimental results shown in [38], [42]. CPW's have also been examined with approximate formulas [43]. Numerical predictions of pulse distortion using full wave solutions have been investigated for both the single microstrip [44]-[46] and for CPW's [47], [48]. However pulse distortion on coupled microstrips has not been examined from a full wave perspective, or for very general structures.

1.5 Scope of Research

Decreasing computational costs coupled with increasing computational speed have made the rigorous analysis of microstrip boundary value problems a practical choice for calculating highly accurate solutions. This report formulates full wave solutions of the boundary value problem to achieve expressions that can be solved for the frequency dependent parameters of very general microstrip structures. The versatility of the derivations is emphasized, allowing many different microstrip circuit problems to be solved. Since the accuracy of the solutions was the prime concern, extensive optimization of the computer programs in order to reduce run time was not attempted.

While there are many single frequency applications for microstrips, the propagation of non-periodic signals on printed circuit lines is also an important concern, and so the degradation of pulsed signals is considered in this report. The use of the time domain Fourier transform for the calculation of transient response is discussed, with the emphasis on application to non-periodic signals. The Fourier transform method is then applied in conjunction with results from other sections to predict pulse distortion on complex microstrip structures. The types of complex microstrip structures dealt with include;

1) Multiple dielectric substrates and superstrates.

2) Symmetric coupled conductors.

3) Shielded and open configurations.

The derivations for pulse distortion and other parameters are done in a efficient and general manner, so that the computations are both flexible and expedient.

The coupling between adjacent center conductors on the microstrip structure is analyzed, since such results are vital for any realistic microstrip circuit design. The concept of even and odd modes is introduced and is then extended so that any number of symmetrically center conductors can be analyzed. This approach emphasizes the versatility of the spectral domain approach, because no modification of the Green's function is necessary for computation. Results for pulse dispersion on multiple conductors are presented, showing not only the signal degradation due to coupling, but also the effect of crosstalk on adjacent lines.

Since modern microwave circuit design involves structures that are much more complicated than the simple single conductor, single layer, open microstrip, the Green's function is formulated in a very general manner so that it is applicable to any planar geometry. First, the spectral domain approach is discussed for a simple structure to illustrate how the Green's function is used to calculate the microstrip parameters. Next, The Green's function for an arbitrary planar microstrip structure is derived using a rigorous full wave solution, giving a simple recurrence formula for its calculation. Using this Green's function, calculations of the effective dielectric constant for multiple dielectric structures are given, showing the effect of cover layers and substrate layers on the frequency dependence of both multiple and single lines. These results will lead to the design of multi-conductor structures that have small or no coupling between lines. Finally, pulse dispersion on these lines is presented, showing the decrease in both signal distortion and crosstalk.

Using exact formulations whenever possible, highly accurate results for microstrip parameters and pulse distortion are computed. The time domain Fourier transform is used to calculate pulse distortion on complex microstrip structures. The coupling between adjacent center conductors is considered using an even/odd mode formulation. Using a rigorous boundary value method, a generalized Green's function is derived for arbitrary planar structures. Numerical results for pulse distortion on complex microstrip structures are presented including shielded and open configurations, multiple dielectric layers, and coupling with adjacent center conductors.

CHAPTER 2
FULL WAVE ANALYSIS OF MICROSTRIP

This chapter considers the microstrip structure in an exact formulation. First the various types of lines that can be treated using this approach are described, and the geometry used for the derivation is presented. Next, the Fourier transform used in the derivation is introduced and the various terms and conventions used throughout the report are defined. Then the spectral domain approach is applied to a simple structure, the shielded microstrip, to illustrate the use of this method. This derivation is then modified to better handle slot line type structures. Finally, a simple recursive formulation for the Green's function of a generalized planar structure is presented.

2.1 The Microstrip Structure

There are many different types of printed circuit transmission lines, each appropriate for different applications, all of which can be solved using the Spectral-Domain Approach (SDA). Four types of these transmission lines are shown in Fig. 2.1; microstrip, coupled stripline, coplanar waveguide (CPW), and slot line. Of the four, microstrips have the lowest dispersion, high Q, and highest power handling capabilities, and while series mounting of devices is easy, shunt mounting is very difficult. On the other hand the CPW can mount
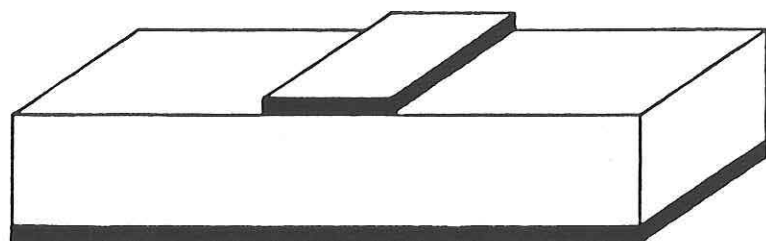
(a) Microstrip
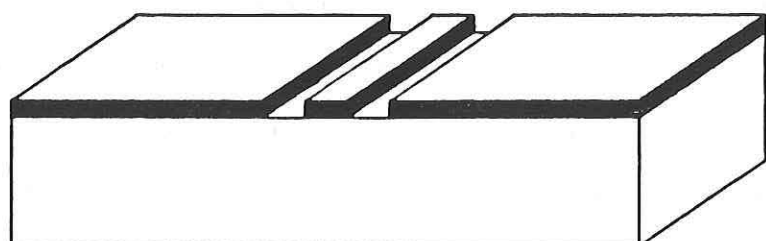
(b) Coplanar Waveguide
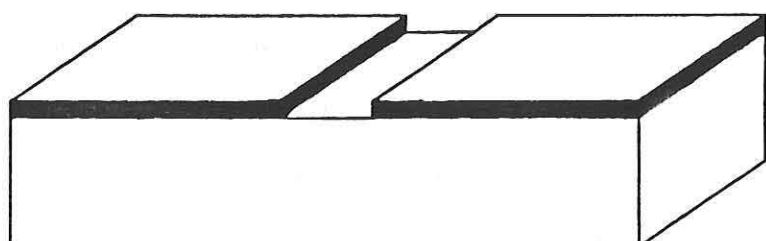
(c) Slot line
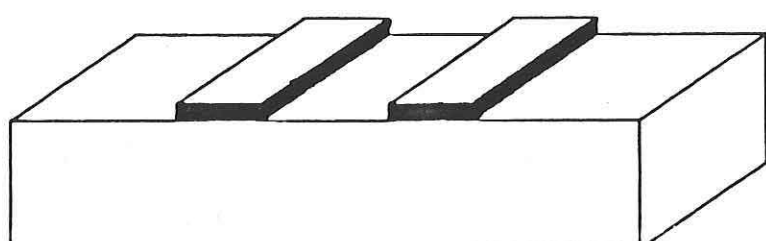
(d) Coupled Striplines

Fig. 2.1. Common planar waveguide structures.

both series and shunt elements easily and can have a high Q [49],
however it has average power handling, and dispersion characteristics.
The slot line allows easy mounting of shunt elements, but has
difficulty with series components. In addition, it suffers from high
radiation losses, low Q, low power capabilities, and is highly
dispersive. Finally, the coupled strip line offers a wide range of
characteristic impedances, but has a low Q, average power handling, and
average dispersion characteristics.

The microstrip geometry used for the derivation of the SDA's
Green's function, as well as for the computation of the current density
expansion functions, is shown in Fig 2.2. A standard right-handed
cartesian coordinate system is used (the z axis is out of the paper),
and the structure is considered to be uniform in the z direction,
reducing it to a two-dimensional problem. There are N planar
dielectric layers below the center conductor interface and M layers
above it, where the height of the ith layer, upper or lower, is denoted
by h_{Ui} or h_{Li} respectively. The electrical parameters of each ith
layer are denoted by ε_i and μ_i, representing the permitivity and
permeability, respectively. The dielectric materials are assumed to be
isotropic, so both μ_i and ε_i are scalars, although μ_i is not
necessarily equal to the free space value. The dielectric constant,
ε_i, is considered initially to be pure real (lossless case), but it
could be generalized to be complex (lossy case). The microstrip is
surrounded on all four sides by perfect electric conductors (PEC's), as
in a shielded configuration. If the particular microstrip structure is
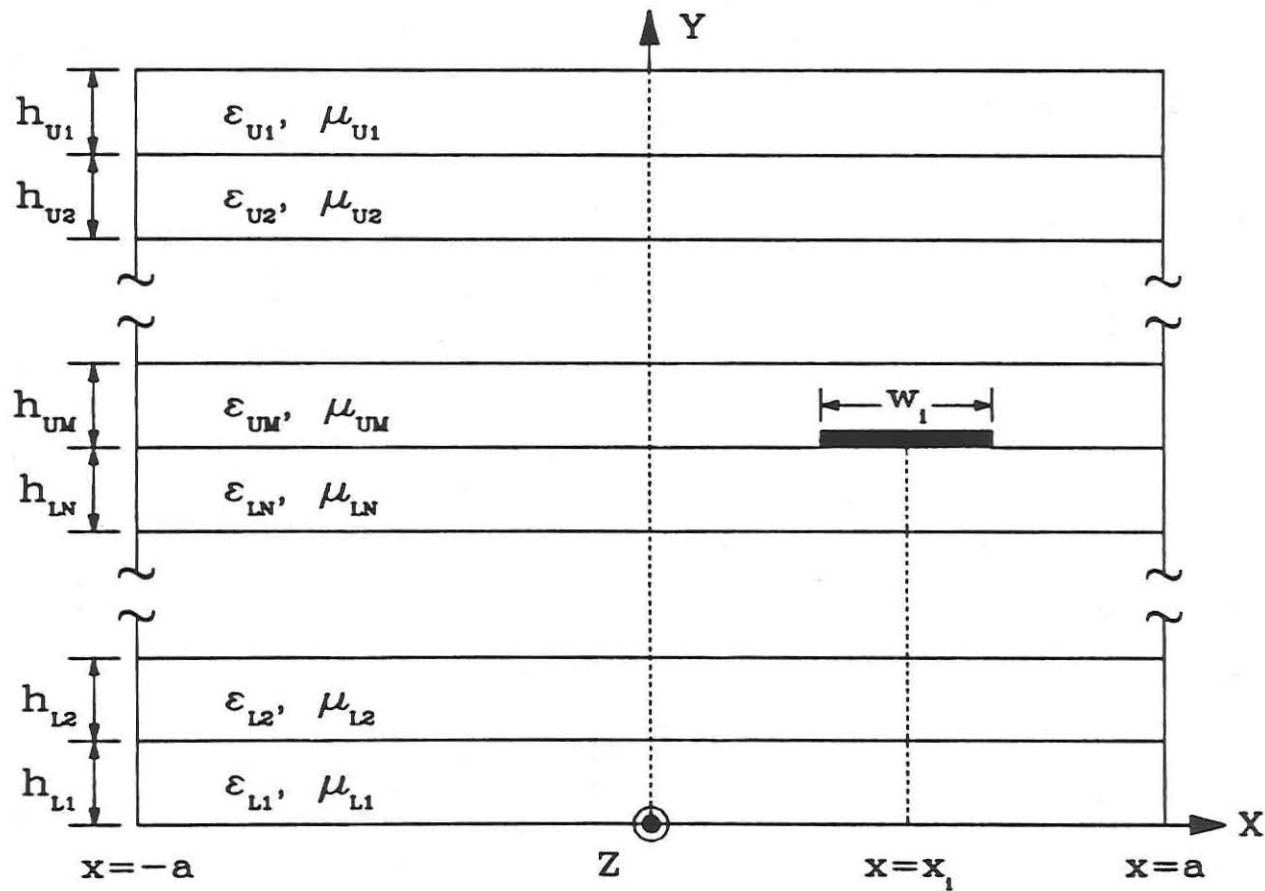
Fig. 2.2. Geometry for general multilayer, multiconductor microstrip structure.

to have no side walls, then a $\longrightarrow \infty$, while if it has no cover sheet or no ground plane, then h_{U1} or $h_{L1} \longrightarrow \infty$, respectively.

Because the SDA is formulated for a unit impulse current source at an arbitrary x location, any arrangement of conductors that are uniform in the z direction may be considered through superposition. In this report, the position of the ith signal conductor is determined, as in Figure 2.2, by the position of the center, x_i, and the width, w_i. In addition, each of the center conductors is assumed to be of zero thickness so that the formulation of the problem doesn't become excessively complex. Although there may be any finite number of these center conductors on the interface, for clarity, only one is shown.

2.2 The Fourier Transform

Throughout the paper an $e^{+j\omega t}$ time convention is used, and the complex wave number in the ith medium and/or direction is designated by γ_i, with a real part α_i and an imaginary part β_i. The two-dimensional Fourier transform pair used with the SDA is defined as:

$$\mathcal{F}\left\{g(x,y,z)\right\} = \tilde{G}(\beta_x, y, \beta_z)$$

$$= \int_{-\infty}^{\infty} \int_{-\infty}^{\infty} g(x,y,z) \, e^{j(\beta_x x + \beta_z z)} \, dx \, dz \qquad (2.1)$$

$$\mathcal{F}^{-1}\left\{\tilde{G}(\beta_x, y, \beta_z)\right\} = g(x,y,z)$$

$$= \frac{1}{(2\pi)^2} \int_{-\infty}^{\infty} \int_{-\infty}^{\infty} \tilde{G}(\beta_x, y, \beta_z) \, e^{-j(\beta_x x + \beta_z z)} \, d\beta_x \, d\beta_z \qquad (2.2)$$

where β_x and β_z are the wave numbers in the x and z directions. If the structure under consideration is finite in the x direction, i.e. $a \neq \infty$,

then the wave numbers in the x direction are discrete instead of
continuous, and a slightly different transform pair is used;

$$\mathcal{F}\left\{g(x,y,z)\right\} = \tilde{G}(\beta_{xn},y,\beta_z)$$

$$= \int_{-\infty}^{\infty} \int_{-a}^{a} g(x,y,z)\ e^{j(\beta_{xn}x+\beta_z z)}\ dx\ dz \qquad (2.3)$$

$$\mathcal{F}^{-1}\left\{\tilde{G}(\beta_{xn},y,\beta_z)\right\} = g(x,y,z)$$

$$= \frac{1}{(2\pi)^2} \sum_{n=-\infty}^{\infty} \left\{\int_{-\infty}^{\infty} \tilde{G}(\beta_{xn},y,\beta_z)e^{-j\beta_z z}\ d\beta_z\right\} e^{-j\beta_{xn}x}\ \Delta\beta_x$$

$$(2.4)$$

where

$$\beta_{xn} = \frac{(2n-1)\pi}{2a} \qquad (2.5)$$

$$\Delta\beta_{xn} = \pi/a \qquad (2.6)$$

This transform is equivalent to using a Fourier series expansion in the
x direction instead of a Fourier transform. All Fourier transform
quantities are denoted with a $\sim$ superscript while vectors are
underlined.

This definition of the Fourier transform is not the same as the
one that is normally found in the literature since the exponent of the
exponential in (2.1) is positive instead of negative. It is, however,
equally valid and allows the transform of the partial derivative with
respect to z to be equivalent to assuming an $e^{-j\beta_z z}$ variation, as is
conventionally used; i.e.,

$$\mathcal{F}\left\{\frac{\partial f(z)}{\partial z}\right\} = -j\beta_z\ \tilde{F}(\beta_z) \longleftrightarrow \frac{\partial}{\partial z}\left\{e^{-j\beta_z z}\right\} = -j\beta_z\ e^{-j\beta_z z} \qquad (2.7)$$

While this new definition changes some of properties of the Fourier
transform, as well as some of the transform pairs, there is a simple
relation between the two definitions. If the transform of f(z) using

the more common definition is given by $\widetilde{F}(\beta_z)$, then the transform using (2.1) is given by $\widetilde{F}(-\beta_z)$.

2.3 The Spectral-Domain Approach

The Spectral-Domain Approach (SDA) is preferred over other full wave solutions for planar circuits, especially spatial domain methods, because of its simple formulation, high versatility, low memory requirements, short computation time, and accurate results. The derivation of the SDA is simpler in many ways than spatial techniques. For example, for the geometry of Figure 2.2, the partial derivatives with respect to x and z in spatial coordinates become multiplications in the spectral domain. The Green's function approach used in the SDA makes it applicable to many different types of planar circuits including the following:

    a. An unlimited number of signal conductors confined to one plane.

    b. An unlimited number of dielectric layers above and below the interface containing the conductors.

    c. Top (cover) and/or bottom (ground plane) conductor (either present or absent).

    d. Conductor side walls (either present or absent).

Unlike spatial domain formulations, large matrices are not required to obtain accurate results with the SDA. In addition, large structures, such as open microstrips, are handled as easily as smaller ones, without the huge increase in memory requirements as there is with spatial methods. Because the matrices used by the SDA are much smaller and fewer numerical integrations are needed, computer run time is much

less than that of other formulations. Since the SDA is a full wave
formulation, the results are very accurate, and it has even been used
to produce a reference standard [50].

2.3.1 *The Wave Equations in the Spectral Domain*

The SDA begins by transforming the fields and boundary conditions
from the spatial domain to the spectral domain in order to simplify the
derivation process. Using a transform to solve the second order
differential equation is equivalent to using an eigenfunction
expansion, but the formulation is more straight forward. As indicated
previously in Section 2.2, the Fourier transform changes both the z and
x partial derivatives into multiplications, simplifying the electric
and magnetic wave equations as well as the vector potential approach.
Transforming, as in (2.1), the time-harmonic electric and magnetic wave
equations for lossless media with only a current source present gives;

$$\nabla^2\underline{E} + \beta^2\underline{E} = -j\omega\mu\underline{J} \longleftrightarrow \left[\frac{\partial^2}{\partial y^2} + \beta_y^2\right]\underline{\tilde{E}} = -j\omega\mu\underline{\tilde{J}} \tag{2.8}$$

$$\nabla^2\underline{H} + \beta^2\underline{H} = -\nabla\times\underline{J} \longleftrightarrow \left[\frac{\partial^2}{\partial y^2} + \beta_y^2\right]\underline{\tilde{H}} = -\hat{a}_x\left[j\beta_z\tilde{J}_y + \frac{\partial}{\partial y}\tilde{J}_z\right]$$

$$+ \hat{a}_y j\left[\beta_z\tilde{J}_x - \beta_z\tilde{J}_z\right] + \hat{a}_z\left[j\beta_x\tilde{J}_y + \frac{\partial}{\partial y}\tilde{J}_x\right] \tag{2.9}$$

Since the microstrip conductor is assumed to be infinitely thin, there
is no current density in the y direction and the partial derivatives
with respect to y of the x and z current densities are zero. Using
this, the transform of the magnetic wave equation can be written more
concisely as:

$$\left[\frac{\partial^2}{\partial y^2} + \beta_y^2\right]\widetilde{\mathsf{H}} = j\ \hat{a}_y\left[\beta_z\widetilde{\mathfrak{J}}_x - \beta_z\widetilde{\mathfrak{J}}_z\right] \tag{2.10}$$

The transformed wave equations are second order partial differential equations of only a single variable, y, and so they give no information or constraint on the x or z variations. The x and z dependence of the problem is now contained implicitly in the transforms of either the current densities or the electric fields through the functional dependence on β_x and β_z. To illustrate the use of the SDA, a simple structure, the shielded microstrip is considered. First, the derivation for TM^y mode is done, and the TE^y follows.

2.3.2 TM^y Modes for the Shielded Microstrip

The geometry of the shielded microstrip, shown in Figure 2.3, is the equivalent to the geometry found in Figure 2.2 with $N = M = 1$, $h_{U1} = h_2$, $h_{L1} = h_1$, $x_i = 0$, and $w_i = w$. Since the structure has walls at a finite distance, the second Fourier transform is used as stated in (2.3) through (2.6). This derivation can also be generalized to the open microstrip structure by letting $a \longrightarrow \infty$ and $h_2 \longrightarrow \infty$ and using the first Fourier transform pair of (2.1) and (2.2). Transforming the fields and the vector potential, $\underline{A}$, into the spectral domain gives:

$$\underline{A} = \hat{a}_y A_y(x,y,z) \qquad \longleftrightarrow \qquad \widetilde{\underline{A}} = \hat{a}_y \widetilde{A}_y(\beta_x,y,\beta_z) \tag{2.11}$$

$$E_x^{TM} = -j\frac{1}{\omega\mu\varepsilon}\frac{\partial^2}{\partial x\partial y}A_y \qquad \longleftrightarrow \qquad \widetilde{E}_x^{TM} = -\frac{\beta_x}{\omega\mu\varepsilon}\frac{\partial}{\partial y}\widetilde{A}_y \tag{2.12a}$$

$$E_y^{TM} = -j\frac{1}{\omega\mu\varepsilon}\left[\frac{\partial^2}{\partial y^2}+\beta^2\right]A_y \qquad \longleftrightarrow \qquad \widetilde{E}_y^{TM} = -j\frac{1}{\omega\mu\varepsilon}\left[\frac{\partial^2}{\partial y^2}+\beta^2\right]\widetilde{A}_y \tag{2.12b}$$

$$E_z^{TM} = -j\frac{1}{\omega\mu\varepsilon}\frac{\partial^2}{\partial z\partial y}A_y \qquad \longleftrightarrow \qquad \widetilde{E}_z^{TM} = -\frac{\beta_z}{\omega\mu\varepsilon}\frac{\partial}{\partial y}\widetilde{A}_y \tag{2.12c}$$
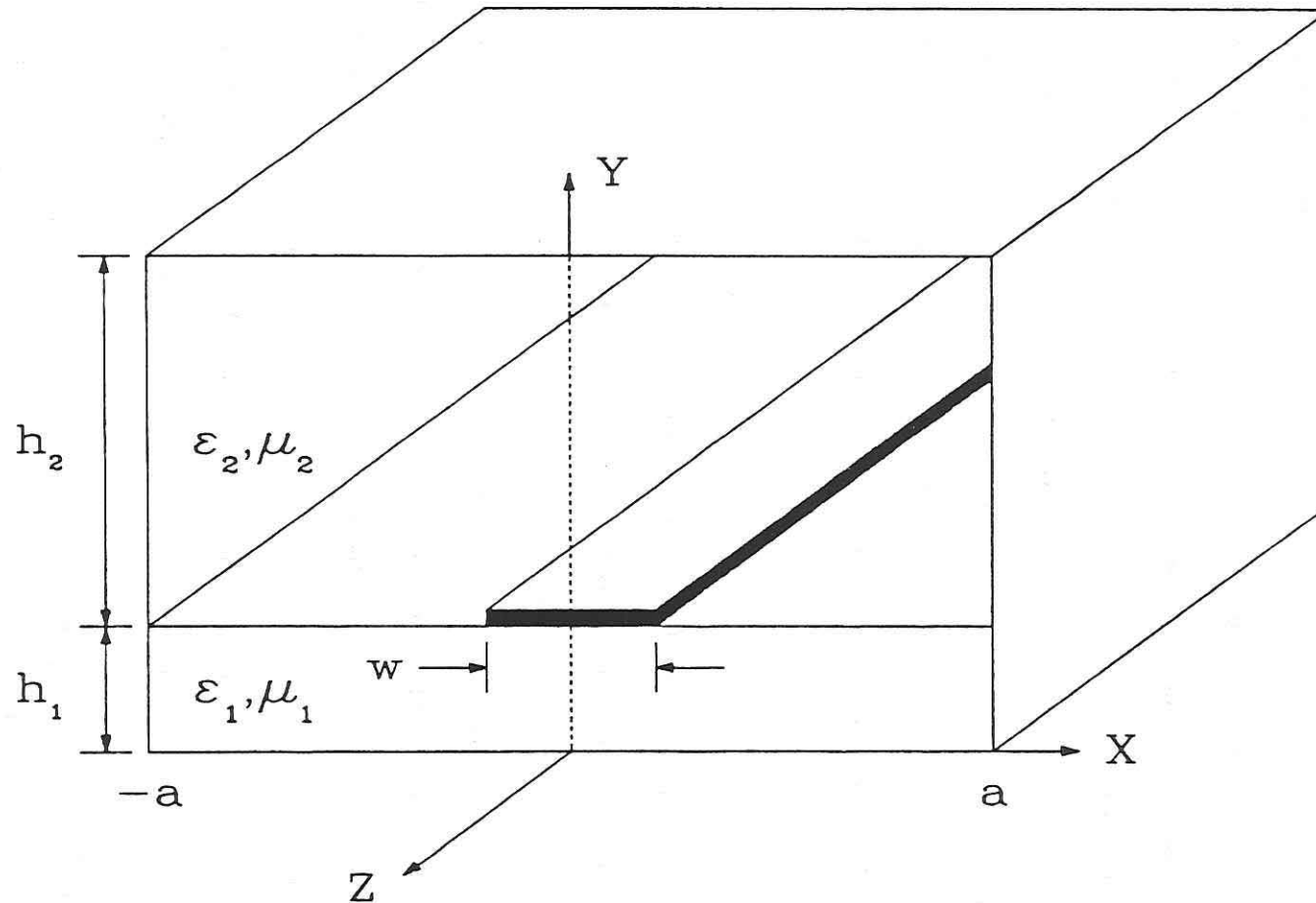
Fig. 2.3. Geometry for two layer, shielded microstrip structure.

$$H^{TM}_x = - \frac{1}{\mu} \frac{\partial}{\partial z} A_y \qquad \longleftrightarrow \qquad \tilde{H}^{TM}_x = j \frac{\beta_z}{\mu} \tilde{A}_y \qquad (2.12d)$$

$$H^{TM}_y = 0 \qquad \longleftrightarrow \qquad \tilde{H}^{TM}_y = 0 \qquad (2.12e)$$

$$H^{TM}_z = \frac{1}{\mu} \frac{\partial}{\partial x} A_y \qquad \longleftrightarrow \qquad \tilde{H}^{TM}_z = - j \frac{\beta_x}{\mu} \tilde{A}_y \qquad (2.12f)$$

The scalar potential $\tilde{A}_{yi}(\beta_x, y, \beta_z)$ for the ith layer, $i = 1$ or 2, is chosen as follows:

REGION 1: $(0 \leq y \leq h_1)$

$$\tilde{A}_{y1} = \tilde{B}_1(\beta_x, \beta_z) \cosh(\alpha_{y1} y) \qquad (2.13)$$

REGION 2: $(h_1 \leq y \leq h_2)$

$$\tilde{A}_{y2} = \tilde{B}_2(\beta_x, \beta_z) \cosh[\alpha_{y2}(h_2 + h_1 - y)] \qquad (2.14)$$

$\tilde{B}_1(\beta_x, \beta_z)$ and $\tilde{B}_2(\beta_x, \beta_z)$ are unknown functions of the transform variables, which are to be determined from the boundary conditions. They are abbreviated as $\tilde{B}_1$ and $\tilde{B}_2$ throughout. $\tilde{A}_{y1}$ and $\tilde{A}_{y2}$ are chosen based on; 1) the tangential $\underline{E}$ fields vanishing at $y = 0$ (at the ground plane) and 2) the tangential $\underline{E}$ fields vanishing at $y = h_1 + h_2$. The hyperbolic cosine is chosen since the structure should have standing waves in the y direction.

If the TM^y mode is an independent solution of the boundary value problem, then either the x or the z directed fields can be used to enforce the boundary conditions. On the other hand, if using the x and z directed fields gives different answers, then the TM^y mode is not a solution and the problem must be solved as a superposition of two orthogonal modes. Using the scalar potentials in (2.13) and (2.14) with the equations for the fields in (2.12a-f), the electric and magnetic fields in each region are calculated.

REGION 1:

$$\tilde{E}_{x1} = -\tilde{B}_1 \frac{\beta_x \alpha_{y1}}{\omega\mu_1\varepsilon_1} \sinh(\alpha_{y1}y)$$ (2.15a)

$$\tilde{E}_{z1} = -\tilde{B}_1 \frac{\beta_z \alpha_{y1}}{\omega\mu_1\varepsilon_1} \sinh(\alpha_{y1}y)$$ (2.15b)

$$\tilde{H}_{x1} = j\,\tilde{B}_1 \frac{\beta_z}{\mu_1} \cosh(\alpha_{y1}y)$$ (2.15c)

$$\tilde{H}_{z1} = -j\,\tilde{B}_1 \frac{\beta_x}{\mu_1} \cosh(\alpha_{y1}y)$$ (2.15d)

where

$$\beta_1^2 = \beta_x^2 + \beta_z^2 - \alpha_{y1}^2 = \omega^2\mu_1\varepsilon_1$$ (2.16)

REGION 2:

$$\tilde{E}_{x2} = \tilde{B}_2 \frac{\beta_x \alpha_{y2}}{\omega\mu_2\varepsilon_2} \sinh[\alpha_{y2}(h_1+h_2-y)]$$ (2.17a)

$$\tilde{E}_{z2} = \tilde{B}_2 \frac{\beta_z \alpha_{y2}}{\omega\mu_2\varepsilon_2} \sinh[\alpha_{y2}(h_1+h_2-y)]$$ (2.17b)

$$\tilde{H}_{x2} = j\,\tilde{B}_2 \frac{\beta_z}{\mu_2} \cosh[\alpha_{y2}(h_1+h_2-y)]$$ (2.17c)

$$\tilde{H}_{z2} = -j\,\tilde{B}_2 \frac{\beta_x}{\mu_2} \cosh[\alpha_{y2}(h_1+h_2-y)]$$ (2.17d)

where

$$\beta_2^2 = \beta_x^2 + \beta_z^2 - \alpha_{y2}^2 = \omega^2\mu_2\varepsilon_2$$ (2.18)

Now that the expression for the fields have been specified, the boundary conditions can be applied to eliminate $\tilde{B}_1$ and $\tilde{B}_2$.

1) $\tilde{E}_{x1}\Big|_{y=h_1} = \tilde{E}_{x2}\Big|_{y=h_1}$

$$-\tilde{B}_1 \frac{\beta_x \alpha_{y1}}{\omega\mu_1\varepsilon_1} \sinh(\alpha_{y1}h_1) = \tilde{B}_2 \frac{\beta_x \alpha_{y2}}{\omega\mu_2\varepsilon_2} \sinh(\alpha_{y2}h_2)$$ (2.19)

$$\tilde{B}_1 = -\tilde{B}_2 \frac{\alpha_{y2}\varepsilon_{r1}\mu_{r1}}{\alpha_{y1}\varepsilon_{r2}\mu_{r2}} \frac{\sinh(\alpha_{y2}h_2)}{\sinh(\alpha_{y1}h_1)}$$ (2.20)

The z directed electric fields are now considered.

2) $\tilde{E}_{z1}\Big|_{y=h_1} = \tilde{E}_{z2}\Big|_{y=h_1}$

$$-\tilde{B}_1 \frac{\beta_z \alpha_{y1}}{\omega\mu_1\varepsilon_1} \sinh(\alpha_{y1}h_1) = \tilde{B}_2 \frac{\beta_z \alpha_{y2}}{\omega\mu_2\varepsilon_2} \sinh(\alpha_{y2}h_2) \qquad (2.21)$$

$$\tilde{B}_1 = -\tilde{B}_2 \frac{\alpha_{y2}\varepsilon_{r1}\mu_{r1}}{\alpha_{y1}\varepsilon_{r2}\mu_{r2}} \frac{\sinh(\alpha_{y2}h_2)}{\sinh(\alpha_{y1}h_1)} \qquad (2.22)$$

This gives the same result as the x fields, as desired.

Next, the discontinuity of the <u>H</u> fields at the center conductor interface due to the presence of a current source is enforced.

3) $\tilde{H}_{x1}\Big|_{y=h_1} - \tilde{H}_{x2}\Big|_{y=h_1} = \tilde{J}_z^{TM}$

$$j\,\tilde{B}_1 \frac{\beta_z}{\mu_1} \cosh(\alpha_{y1}h_1) - j\,\tilde{B}_2 \frac{\beta_z}{\mu_2} \cosh(\alpha_{y2}h_2) = \tilde{J}_z^{TM} \qquad (2.23)$$

Substituting in for $\tilde{B}_1$ using (2.20)

$$-j\,\tilde{B}_2 \frac{\beta_z \alpha_{y2}\varepsilon_{r1}}{\mu_2 \alpha_{y1}\varepsilon_{r2}} \coth(\alpha_{y1}h_1)\sinh(\alpha_{y2}h_2) - j\,\tilde{B}_2 \frac{\beta_z}{\mu_2} \cosh(\alpha_{y2}h_2) = \tilde{J}_z^{TM}$$

$$(2.24)$$

$$\tilde{B}_2 \left[\frac{\varepsilon_{r1}\coth(\alpha_{y1}h_1)}{\alpha_{y1}} + \frac{\varepsilon_{r2}\coth(\alpha_{y2}h_2)}{\alpha_{y2}} \right] = j\, \frac{\varepsilon_{r2}\mu_2}{\alpha_{y2}\beta_z} \tilde{J}_z^{TM}\,\mathrm{csch}(\alpha_{y2}h_2) \qquad (2.25)$$

Let

$$\tilde{Y}_{s1}^{TM} = \frac{\varepsilon_{r1}\coth(\alpha_{y1}h_1)}{\alpha_{y1}} \qquad (2.26a)$$

$$\tilde{Y}_{s2}^{TM} = \frac{\varepsilon_{r2}\coth(\alpha_{y2}h_2)}{\alpha_{y2}} \qquad (2.26b)$$

This simplifies (2.25) to

$$\tilde{B}_2 = j\, \frac{\varepsilon_{r2}\mu_2}{\alpha_{y2}\beta_z} \tilde{J}_z^{TM}\,\mathrm{csch}(\alpha_{y2}h_2) \left[\tilde{Y}_{s1}^{TM} + \tilde{Y}_{s2}^{TM} \right]^{-1} \qquad (2.27)$$

Next, the z directed magnetic fields are checked to see if they give the same answer.

4) $\tilde{H}_{z1}\Big|_{y=h_1} - \tilde{H}_{z2}\Big|_{y=h_1} = -\tilde{J}_x^{TM}$

$$-j\,\tilde{B}_1 \frac{\beta_x}{\mu_1} \cosh(\alpha_{y1}h_1) + j\,\tilde{B}_2 \frac{\beta_x}{\mu_2} \cosh(\alpha_{y2}h_2) = -\tilde{J}_x^{TM} \qquad (2.28)$$

Using (2.20) for $\tilde{B}_1$ as before,

$$-j\,\tilde{B}_2\,\frac{\beta_x\alpha_{y2}\varepsilon_{r1}}{\mu_2\alpha_{y1}\varepsilon_{r2}}\coth(\alpha_{y1}h_1)\sinh(\alpha_{y2}h_2)\;-j\,\tilde{B}_2\,\frac{\beta_x}{\mu_2}\cosh(\alpha_{y2}h_2)\;=\;-\tilde{\mathfrak{J}}_x^{TM}$$

$$(2.29)$$

Simplifying this equation using (2.26a) and (2.26b) leads to

$$\tilde{B}_2\;=\;j\,\frac{\varepsilon_{r2}\mu_2}{\alpha_{y2}\beta_x}\,\tilde{\mathfrak{J}}_x^{TM}\,\mathrm{csch}(\alpha_{y2}h_2)\,\left[\tilde{Y}_{s1}^{TM}+\tilde{Y}_{s2}^{TM}\right]^{-1} \qquad (2.30)$$

In order for the TM^y mode to be an independent solution in the spectral domain, (2.27) should be equivalent to (2.30). This occurs if the x and z directed modal currents are related as follows;

$$\beta_z\tilde{\mathfrak{J}}_x^{TM}\;=\;\beta_x\tilde{\mathfrak{J}}_z^{TM} \qquad (2.31)$$

To show that this relation is indeed true, the magnetic wave equation with only an electric current source present, as in (2.10) is used:

$$\left[\frac{\partial^2}{\partial y^2}+\beta_y^2\right]\tilde{H}_y\;=\;j\,\left[\beta_z\tilde{\mathfrak{J}}_x-\beta_z\tilde{\mathfrak{J}}_z\right] \qquad (2.32)$$

Since the TM^y mode has no H_y, the left side of (2.32) is zero and so

$$\boxed{\beta_z\tilde{\mathfrak{J}}_x^{TM}\;=\;\beta_x\tilde{\mathfrak{J}}_z^{TM}} \qquad (2.33)$$

Therefore the TM^y mode satisfies all the boundary conditions in the spectral domain. To complete the solution, the tangential fields at the center conductor interface are required. Replacing $\tilde{B}_2$ in (2.17a) and (2.17b) with (2.27), and evaluating them at $y = h_1$ leads to

$$\tilde{E}_{x2}^{TM}\;=\;j\,\frac{1}{\omega\varepsilon_0}\,\frac{\beta_x}{\beta_z}\,\tilde{Z}^{TM}\,\tilde{\mathfrak{J}}_z^{TM} \qquad (2.34)$$

$$\tilde{E}_{z2}^{TM}\;=\;j\,\frac{1}{\omega\varepsilon_0}\,\tilde{Z}^{TM}\,\tilde{\mathfrak{J}}_z^{TM} \qquad (2.35)$$

where $\widetilde{Z}^{TM}$ is the modal input impedance, defined as

$$\widetilde{Z}^{TM} = \left[\widetilde{Y}^{TM}_{s1} + \widetilde{Y}^{TM}_{s2}\right]^{-1} \tag{2.36}$$

2.3.3 TE^y Modes for the Shielded Microstrip

Having solved the TM^y mode, the TE^y mode is considered.

$$F = \hat{a}_y F_y(x,y,z) \qquad \longleftrightarrow \qquad \widetilde{F} = \hat{a}_y \widetilde{F}_y(\beta_x, y, \beta_z) \tag{2.37}$$

$$E^{TE}_x = \frac{1}{\varepsilon} \frac{\partial}{\partial z} F_y \qquad \longleftrightarrow \qquad \widetilde{E}^{TE}_x = -j \frac{\beta_z}{\varepsilon} \widetilde{F}_y \tag{2.38a}$$

$$E^{TE}_y = 0 \qquad \longleftrightarrow \qquad \widetilde{E}^{TE}_y = 0 \tag{2.38b}$$

$$E^{TE}_z = -\frac{1}{\varepsilon} \frac{\partial}{\partial x} F_y \qquad \longleftrightarrow \qquad \widetilde{E}^{TE}_z = j \frac{\beta_x}{\varepsilon} \widetilde{F}_y \tag{2.38c}$$

$$H^{TE}_x = -j\frac{1}{\omega\mu\varepsilon} \frac{\partial^2}{\partial x \partial y} F_y \qquad \longleftrightarrow \qquad \widetilde{H}^{TE}_x = -\frac{\beta_x}{\omega\mu\varepsilon} \frac{\partial}{\partial y} \widetilde{F}_y \tag{2.38d}$$

$$H^{TE}_y = -j\frac{1}{\omega\mu\varepsilon}\left[\frac{\partial^2}{\partial y^2}+\beta^2\right]F_y \qquad \longleftrightarrow \qquad \widetilde{H}^{TE}_y = -j\frac{1}{\omega\mu\varepsilon}\left[\frac{\partial^2}{\partial y^2}+\beta^2\right]\widetilde{F}_y \tag{2.38e}$$

$$H^{TE}_z = -j\frac{1}{\omega\mu\varepsilon} \frac{\partial^2}{\partial z \partial y} F_y \qquad \longleftrightarrow \qquad \widetilde{H}^{TE}_z = -\frac{\beta_z}{\omega\mu\varepsilon} \frac{\partial}{\partial y} \widetilde{F}_y \tag{2.38f}$$

The scalar potential $\widetilde{F}_{yi}(\beta_x, y, \beta_z)$ for the ith layer, $i = 1$ or 2, is chosen as follows:

REGION 1: $(0 \leq y \leq h_1)$

$$\widetilde{F}_{y1} = \widetilde{A}_1(\beta_x, \beta_z) \sinh(\alpha_{y1}y) \tag{2.39}$$

REGION 2: $(h_1 \leq y \leq h_2)$

$$\widetilde{F}_{y2} = \widetilde{A}_2(\beta_x, \beta_z) \sinh[\alpha_{y2}(h_2+h_1-y)] \tag{2.40}$$

$\widetilde{A}_1(\beta_x, \beta_z)$ and $\widetilde{A}_2(\beta_x, \beta_z)$ are unknown functions of the transform variables, which are to be determined from the boundary conditions. They are abbreviated as $\widetilde{A}_1$ and $\widetilde{A}_2$ throughout. $\widetilde{F}_{y1}$ and $\widetilde{F}_{y2}$ are chosen based on; 1) the tangential $\underline{E}$ fields vanishing at $y = 0$ (at the ground

plane) and 2) the tangential $\underline{E}$ fields vanishing at $y = h_1 + h_2$. The hyperbolic sine is chosen since the structure should have standing waves in the y direction.

As with the TM^y mode, if the TE^y mode is an independent solution of the boundary value problem, then either the x or the z directed fields can be used to enforce the boundary conditions. Likewise, if they are not equivalent then the TE^y mode isn't an independent solution and the problem needs to be solved with a superposition of two orthogonal modes. Using the scalar potentials in (2.39) and (2.40) with the equations for the fields in (2.38a-f), the electric and magnetic fields in each region are calculated.

REGION 1:

$$\tilde{E}_{x1} = -j \, \tilde{A}_1 \, \frac{\beta_z}{\varepsilon_1} \, \sinh(\alpha_{y1} y) \tag{2.41a}$$

$$\tilde{E}_{z1} = j \, \tilde{A}_1 \, \frac{\beta_x}{\varepsilon_1} \, \sinh(\alpha_{y1} y) \tag{2.41b}$$

$$\tilde{H}_{x1} = -\tilde{A}_1 \, \frac{\beta_x \alpha_{y1}}{\omega \mu_1 \varepsilon_1} \, \cosh(\alpha_{y1} y) \tag{2.41c}$$

$$\tilde{H}_{z1} = -\tilde{A}_1 \, \frac{\beta_z \alpha_{y1}}{\omega \mu_1 \varepsilon_1} \, \cosh(\alpha_{y1} y) \tag{2.41d}$$

where

$$\beta_1^2 = \beta_x^2 + \beta_z^2 - \alpha_{y1}^2 = \omega^2 \mu_1 \varepsilon_1 \tag{2.41}$$

REGION 2:

$$\tilde{E}_{x2} = -j \, \tilde{A}_2 \, \frac{\beta_z}{\varepsilon_2} \, \sinh[\alpha_{y2}(h_1 + h_2 - y)] \tag{2.42a}$$

$$\tilde{E}_{z2} = j \, \tilde{A}_2 \, \frac{\beta_x}{\varepsilon_2} \, \sinh[\alpha_{y2}(h_1 + h_2 - y)] \tag{2.42b}$$

$$\tilde{H}_{x2} = \tilde{A}_2 \, \frac{\beta_x \alpha_{y2}}{\omega \mu_2 \varepsilon_2} \, \cosh[\alpha_{y2}(h_1 + h_2 - y)] \tag{2.42c}$$

$$\tilde{H}_{z2} = \tilde{A}_2 \frac{\beta_z \alpha_{y2}}{\omega \mu_2 \varepsilon_2} \cosh[\alpha_{y2}(h_1 + h_2 - y)] \tag{2.42d}$$

where

$$\beta_2^2 = \beta_x^2 + \beta_z^2 - \alpha_{y2}^2 = \omega^2 \mu_2 \varepsilon_2 \tag{2.42}$$

Now that the fields have been determined, the boundary conditions can be applied to eliminate $\tilde{A}_1$ and $\tilde{A}_2$.

1) $\tilde{E}_{x1}\big|_{y=h_1} = \tilde{E}_{x2}\big|_{y=h_1}$

$$-j\,\tilde{A}_1 \frac{\beta_z}{\varepsilon_1} \sinh(\alpha_{y1} h_1) = -j\,\tilde{A}_2 \frac{\beta_z}{\varepsilon_2} \sinh(\alpha_{y2} h_2) \tag{2.43}$$

$$\tilde{A}_1 = \tilde{A}_2 \frac{\varepsilon_{r1}}{\varepsilon_{r2}} \frac{\sinh(\alpha_{y2} h_2)}{\sinh(\alpha_{y1} h_1)} \tag{2.44}$$

The z directed electric fields are now considered.

2) $\tilde{E}_{z1}\big|_{y=h_1} = \tilde{E}_{z2}\big|_{y=h_1}$

$$-j\,\tilde{A}_1 \frac{\beta_x}{\varepsilon_1} \sinh(\alpha_{y1} h_1) = -j\,\tilde{A}_2 \frac{\beta_x}{\varepsilon_2} \sinh(\alpha_{y2} h_2) \tag{2.45}$$

$$\tilde{A}_1 = \tilde{A}_2 \frac{\varepsilon_{r1}}{\varepsilon_{r2}} \frac{\sinh(\alpha_{y2} h_2)}{\sinh(\alpha_{y1} h_1)} \tag{2.46}$$

which is the same result as using the x fields, as required.

Next, the discontinuity of the H fields at the center conductor interface due to the presence of a current source is enforced.

3) $\tilde{H}_{x1}\big|_{y=h_1} - \tilde{H}_{x2}\big|_{y=h_1} = \tilde{J}_z^{TE}$

$$-\tilde{A}_1 \frac{\beta_x \alpha_{y1}}{\omega \mu_1 \varepsilon_1} \cosh(\alpha_{y1} h_1) - \tilde{A}_2 \frac{\beta_x \alpha_{y2}}{\omega \mu_2 \varepsilon_2} \cosh(\alpha_{y2} h_2) = \tilde{J}_z^{TE} \tag{2.47}$$

Substituting in for $\tilde{A}_1$ using (2.44) leads to

$$-\tilde{A}_2 \frac{\beta_x \alpha_{y1}}{\omega \mu_1 \varepsilon_2} \coth(\alpha_{y1} h_1)\sinh(\alpha_{y2} h_2) - \tilde{A}_2 \frac{\beta_x \alpha_{y2}}{\omega \mu_2 \varepsilon_2} \cosh(\alpha_{y2} h_2) = \tilde{J}_z^{TE} \tag{2.48}$$

$$\tilde{A}_2 \left[\frac{\alpha_{y1} \coth(\alpha_{y1} h_1)}{\mu_{r1}} + \frac{\alpha_{y2} \coth(\alpha_{y2} h_2)}{\mu_{r2}} \right] = -\frac{\omega \mu_0 \varepsilon_2}{\beta_x} \tilde{J}_z^{TE} \operatorname{csch}(\alpha_{y2} h_2) \tag{2.49}$$

Let

$$\tilde{Y}^{TE}_{s1} = \frac{\alpha_{y1}\coth(\alpha_{y1}h_1)}{\mu_{r1}} \tag{2.50a}$$

$$\tilde{Y}^{TE}_{s2} = \frac{\alpha_{y2}\coth(\alpha_{y2}h_2)}{\mu_{r2}} \tag{2.50b}$$

This simplifies (2.49) to

$$\tilde{A}_2 = -\frac{\omega\mu_0\varepsilon_2}{\beta_x}\tilde{J}^{TE}_z \, \text{csch}(\alpha_{y2}h_2)\left[\tilde{Y}^{TE}_{s1} + \tilde{Y}^{TE}_{s2}\right]^{-1} \tag{2.51}$$

Next, the z directed magnetic fields are checked to see if they give the same answer.

4) $\left.\tilde{H}_{z1}\right|_{y=h_1} - \left.\tilde{H}_{z2}\right|_{y=h_1} = -\tilde{J}^{TE}_x$

$$-\tilde{A}_1\frac{\beta_x\alpha_{y1}}{\omega\mu_1\varepsilon_1}\cosh(\alpha_{y1}h_1) - \tilde{A}_2\frac{\beta_x\alpha_{y2}}{\omega\mu_2\varepsilon_2}\cosh(\alpha_{y2}h_2) = -\tilde{J}^{TE}_x \tag{2.52}$$

Using (2.44) for $\tilde{A}_1$ as before,

$$-\tilde{A}_2\frac{\beta_x\alpha_{y1}}{\omega\mu_1\varepsilon_2}\coth(\alpha_{y1}h_1)\sinh(\alpha_{y2}h_2) - \tilde{A}_2\frac{\beta_x\alpha_{y2}}{\omega\mu_2\varepsilon_2}\cosh(\alpha_{y2}h_2) = -\tilde{J}^{TE}_x \tag{2.53}$$

Simplifying this equation using (2.50a) and (2.50b) leads to

$$\tilde{A}_2 = \frac{\omega\mu_0\varepsilon_2}{\beta_z}\tilde{J}^{TE}_x \, \text{csch}(\alpha_{y2}h_2)\left[\tilde{Y}^{TE}_{s1} + \tilde{Y}^{TE}_{s2}\right]^{-1} \tag{2.54}$$

In order for the TE^y mode to be an independent solution in the spectral domain, (2.51) should be equivalent to (2.54). This occurs if the x and z directed modal currents are related as follows;

$$\beta_z\tilde{J}^{TE}_z = -\beta_x\tilde{J}^{TE}_x \tag{2.55}$$

To show that this relation is indeed true, the continuity equation is used with a time varying volume charge density, q(x,z;t), equal to $\rho_v(x,z)e^{j\omega t}$, giving

$$\nabla\cdot\underline{J} = -\frac{\partial}{\partial t}\left[\rho_v(x,z)e^{j\omega t}\right] \tag{2.56}$$

Computing the time derivative and suppressing the time dependence

reduces (2.56) to

$$\frac{\partial}{\partial x} J_x + \frac{\partial}{\partial y} J_y + \frac{\partial}{\partial z} J_z = -j\omega \rho_v(x,z) \tag{2.57}$$

Fourier transforming the (2.57) twice, with respect to x and z as in

(2.1) and letting $\tilde{J}_y = 0$ (due to zero strip thickness) leads to

$$-j\beta_x \tilde{J}_x^{TE} - j\beta_z \tilde{J}_z^{TE} = -j\omega \tilde{\rho}_v \tag{2.58}$$

For a TE^y field, the normal $\underline{E}$ field (E_y) is zero everywhere. The

boundary condition of $\hat{n} \circ \varepsilon\underline{E} = \rho_v$ then implies that $\rho_v(x,z) = 0$

everywhere, and so $\tilde{\rho}_v(\beta_x,\beta_z) = 0$ also. Therefore (2.58) reduces to

$$\boxed{\beta_z \tilde{J}_z^{TE} = -\beta_x \tilde{J}_x^{TE}} \tag{2.59}$$

Thus the TE^y mode independently satisfies all the boundary

conditions in the spectral domain. To complete the solution, the

tangential fields at the center conductor interface are required.

Replacing $\tilde{A}_2$ in (2.42a) and (2.42b) with (2.51), and evaluating them at

$y = h_1$ leads to

$$\tilde{E}_{x2}^{TE} = j\,\omega\mu_0 \frac{\beta_z}{\beta_x} \tilde{Z}^{TE}\,\tilde{J}_z^{TE} \tag{2.60}$$

$$\tilde{E}_{z2}^{TE} = -j\,\omega\mu_0\,\tilde{Z}^{TE}\,\tilde{J}_z^{TE} \tag{2.61}$$

where $\tilde{Z}^{TE}$ is the TE^y modal input impedance, defined as:

$$\tilde{Z}^{TE} = \left[\tilde{Y}_{s1}^{TE} + \tilde{Y}_{s2}^{TE}\right]^{-1} \tag{2.62}$$

The tangential electric fields at the center conductor interface

have been determined for each mode in terms of the modal current

densities. However, since solution of the microstrip problem requires

the total fields at the interface, the modal fields of (2.34), (2.35),

(2.60) and (2.61) are added together to form the x and z directed

fields giving

$$\tilde{E}_{x2} = \tilde{E}_{x2}^{TM} + \tilde{E}_{x2}^{TE} = j \left\{ \left[\frac{1}{\omega\varepsilon_0} \frac{\beta_x}{\beta_z} \tilde{Z}^{TM} \right] \tilde{J}_z^{TM} + \left[\omega\mu_0 \frac{\beta_z}{\beta_x} \tilde{Z}^{TE} \right] \tilde{J}_z^{TE} \right\} \qquad (2.63a)$$

$$\tilde{E}_{z2} = \tilde{E}_{z2}^{TM} + \tilde{E}_{z2}^{TE} = j \left\{ \left[\frac{1}{\omega\varepsilon_0} \tilde{Z}^{TM} \right] \tilde{J}_z^{TM} - \left[\omega\mu_0 \tilde{Z}^{TE} \right] \tilde{J}_z^{TE} \right\} \qquad (2.63b)$$

2.3.3 Current Density Relations

To combine the TE^y and TM^y modal solutions there needs to be an

equation relating the modal current densities $\tilde{J}_z^{TE}$, $\tilde{J}_x^{TE}$, $\tilde{J}_z^{TM}$, and $\tilde{J}_x^{TM}$,

to the total current densities $\tilde{J}_x$ and $\tilde{J}_z$. Each modal solution, TE^y or

TM^y, contains only one independent current component, the other is

related to it by either (2.33) or (2.59). Therefore the combined modal

solution for the microstrip must contain two independent current

distributions. Since the total fields are a combination of the modal

fields, the total current densities can be written as the sum of the

modal current densities; that is

$$\tilde{J}_z^{TM} + \tilde{J}_z^{TE} = \tilde{J}_z \qquad (2.64)$$

$$\tilde{J}_x^{TM} + \tilde{J}_x^{TE} = \tilde{J}_x \qquad (2.65)$$

Substituting (2.33) and (2.59) into (2.65) leads to

$$\tilde{J}_x = \tilde{J}_z^{TM} \frac{\beta_x}{\beta_z} - \tilde{J}_z^{TE} \frac{\beta_z}{\beta_x} \qquad (2.66)$$

Multiplying (2.64) by β_z/β_x reduces to

$$\tilde{J}_z \frac{\beta_z}{\beta_x} = \tilde{J}_z^{TM} \frac{\beta_z}{\beta_x} + \tilde{J}_z^{TE} \frac{\beta_z}{\beta_x} \qquad (2.67)$$

Adding (2.67) to (2.66) leads to

$$\tilde{J}_z^{TM} \left[\frac{\beta_z}{\beta_x} + \frac{\beta_x}{\beta_z} \right] = \tilde{J}_z \frac{\beta_z}{\beta_x} + \tilde{J}_x \qquad (2.68)$$

Multiplying both sides of (2.68) by $\beta_x\beta_z/(\beta_x^2 + \beta_z^2)$, the current density $\widetilde{J}_z^{TM}$ can be written as

$$\widetilde{J}_z^{TM} = \frac{\beta_z(\widetilde{J}_z\beta_z + \widetilde{J}_x\beta_x)}{(\beta_x^2 + \beta_z^2)} \qquad (2.69)$$

To get the relationship for the TE^y current density, multiply (2.66) by $-\beta_z/\beta_x$ reduces to

$$-\widetilde{J}_x\frac{\beta_z}{\beta_x} = -\widetilde{J}_z^{TM} + \widetilde{J}_z^{TE}\left[\frac{\beta_z}{\beta_x}\right]^2 \qquad (2.70)$$

Adding (2.70) to (2.64) leads to

$$\widetilde{J}_z^{TE}\left[1 + \frac{\beta_z^2}{\beta_x^2}\right] = \widetilde{J}_z - \widetilde{J}_x\frac{\beta_z}{\beta_x} \qquad (2.71)$$

Multiplying both sides of (2.71) by $\beta_x^2/(\beta_x^2 + \beta_z^2)$, the current density $\widetilde{J}_z^{TE}$ can be written as

$$\widetilde{J}_z^{TE} = \frac{\beta_x(\widetilde{J}_z\beta_x - \widetilde{J}_x\beta_z)}{(\beta_x^2 + \beta_z^2)} \qquad (2.72)$$

2.3.5 Green's Functions

Having obtained relationships between the modal and total current densities, the total electric fields at the interface can be expressed in terms of the total current densities. Using (2.72) and (2.69) to express the modal currents in terms of the total currents in (2.63a) and (2.63b), the total fields at the center conductor interface can be written as

$$E_{x2} = \frac{j}{\beta_x^2+\beta_z^2} \left\{ J_z\left[\frac{\beta_x\beta_z}{\omega\varepsilon_0}Z^{TM} + \omega\mu_0\beta_z\beta_x Z^{TE}\right] + J_x\left[\frac{\beta_x^2}{\omega\varepsilon_0}Z^{TM} - \omega\mu_0\beta_z^2 Z^{TE}\right]\right\} \qquad (2.73a)$$

$$E_{z2} = \frac{j}{\beta_x^2+\beta_z^2} \left\{ J_z\left[\frac{\beta_z^2}{\omega\varepsilon_0}Z^{TM} - \omega\mu_0\beta_x^2 Z^{TE}\right] + J_x\left[\frac{\beta_x\beta_z}{\omega\varepsilon_0}Z^{TM} + \omega\mu_0\beta_z\beta_x Z^{TE}\right]\right\} \qquad (2.73b)$$

$$E_{z2} = \frac{j}{\omega\varepsilon_0} \left[J_z G_{zz} + J_x G_{xz}\right] \qquad (2.74a)$$

$$E_{x2} = \frac{j}{\omega\varepsilon_0} \left[J_z G_{zx} + J_x G_{xx}\right] \qquad (2.74b)$$

where

$$G_{zz} = \frac{\beta_z^2 Z^{TM} - \beta_x^2\beta_0^2 Z^{TE}}{\beta_x^2+\beta_z^2} \qquad (2.75a)$$

$$G_{xx} = \frac{\beta_x^2 Z^{TM} - \beta_z^2\beta_0^2 Z^{TE}}{\beta_x^2+\beta_z^2} \qquad (2.75b)$$

$$G_{xz} = G_{zx} = \beta_x\beta_z\frac{Z^{TM} + \beta_0^2 Z^{TE}}{\beta_x^2+\beta_z^2} \qquad (2.75c)$$

Equations (2.74a) and (2.74b), for a given frequency and structural parameters, have two unknown variables; β_x and β_z, and four unknown functions; $J_z(\beta_x)$, $J_x(\beta_x)$, $E_{z2}(\beta_x,\beta_z)$, and $E_{x2}(\beta_x,\beta_z)$. Furthermore, the magnetic and electric wave equations, after being transformed twice, give no information or constraints on the form of the four functions, as it does in the spatial domain. It is advantageous, then to use a method which can eliminate the four functions and one variable.

2.3.6 Galerkin's Method

Galerkin's method is a method of moments technique that uses the same expansion and testing functions to solve an integral equation. To

apply this method, the current densities are expanded into complete

sets of basis functions

$$\tilde{\mathfrak{J}}_z = \sum_{n=1}^{\infty} a_n \tilde{\mathfrak{J}}_{zn} \tag{2.76a}$$

$$\tilde{\mathfrak{J}}_x = \sum_{m=1}^{\infty} b_m \tilde{\mathfrak{J}}_{xm} \tag{2.76b}$$

where a_n and b_m are unknown constants that specify the amplitudes of

each current expansion function.

The x and z current densities in the electric fields of (2.74a)

and (2.74b) are now replaced by the series expansions for the currents

of (2.76a) and (2.76b). This replaces the unknown x and z current

densities with known basis functions of unknown amplitude, resulting

in,

$$\tilde{E}_{z2} = \sum_{n=1}^{\infty} a_n \tilde{\mathfrak{J}}_{zn} \tilde{G}_{zz} + \sum_{m=1}^{\infty} b_m \tilde{\mathfrak{J}}_{xm} \tilde{G}_{zx} \tag{2.77a}$$

$$\tilde{E}_{x2} = \sum_{n=1}^{\infty} a_n \tilde{\mathfrak{J}}_{zn} \tilde{G}_{zx} + \sum_{m=1}^{\infty} b_m \tilde{\mathfrak{J}}_{xm} \tilde{G}_{xx} \tag{2.77b}$$

Now (2.77a) is multiplied by the complex conjugate of (2.76a) and

(2.77b) is multiplied by the complex conjugate of (2.76b) which gives

$$\sum_{n=1}^{\infty} a_n \tilde{\mathfrak{J}}_{zn}^{\star} \tilde{E}_{z2} = \sum_{n=1}^{\infty} a_n \tilde{\mathfrak{J}}_{zn}^{\star} \left[\sum_{n=1}^{\infty} a_n \tilde{\mathfrak{J}}_{zn} \tilde{G}_{zz} + \sum_{m=1}^{\infty} b_m \tilde{\mathfrak{J}}_{xm} \tilde{G}_{zx} \right] \tag{2.78a}$$

$$\sum_{m=1}^{\infty} b_m \tilde{\mathfrak{J}}_{xm}^{\star} \tilde{E}_{x2} = \sum_{m=1}^{\infty} b_m \tilde{\mathfrak{J}}_{xm}^{\star} \left[\sum_{n=1}^{\infty} a_n \tilde{\mathfrak{J}}_{zn} \tilde{G}_{zx} + \sum_{m=1}^{\infty} b_m \tilde{\mathfrak{J}}_{xm} \tilde{G}_{xx} \right] \tag{2.78b}$$

Integrating both sides of (2.78a) and (2.78b) from minus infinity to

plus infinity with respect to β_x gives

$$\sum_{n=1}^{\infty} a_n \left[\int_{-\infty}^{\infty} \tilde{\mathfrak{J}}_{zn}^{\star} \tilde{E}_{z2} \, d\beta_x \right] = \sum_{n=1}^{\infty} a_n \left[\sum_{n=1}^{\infty} a_n \tilde{K}_{nn} + \sum_{m=1}^{\infty} b_m \tilde{K}_{mn} \right] \tag{2.79a}$$

$$\sum_{m=1}^{\infty} b_m \left[\int_{-\infty}^{\infty} \tilde{\mathfrak{J}}_{xm}^{\star} \tilde{E}_{x2} \, d\beta_x \right] = \sum_{m=1}^{\infty} b_m \left[\sum_{n=1}^{\infty} a_n \tilde{K}_{nm} + \sum_{m=1}^{\infty} b_m \tilde{K}_{mm} \right] \tag{2.79b}$$

where for open configuration (a = ∞)

$$K_{nn} = \int_{-\infty}^{\infty} \tilde{\mathfrak{J}}_{zn}^{*}(\beta_x) \tilde{\mathfrak{J}}_{zn}(\beta_x) \tilde{G}_{zz}(\beta_x, \beta_z) \, d\beta_x \qquad (2.80a)$$

$$K_{mn} = \int_{-\infty}^{\infty} \tilde{\mathfrak{J}}_{zn}^{*}(\beta_x) \tilde{\mathfrak{J}}_{xm}(\beta_x) \tilde{G}_{zx}(\beta_x, \beta_z) \, d\beta_x \qquad (2.80b)$$

$$K_{nm} = \int_{-\infty}^{\infty} \tilde{\mathfrak{J}}_{xm}^{*}(\beta_x) \tilde{\mathfrak{J}}_{zn}(\beta_x) \tilde{G}_{zx}(\beta_x, \beta_z) \, d\beta_x \qquad (2.80c)$$

$$K_{mm} = \int_{-\infty}^{\infty} \tilde{\mathfrak{J}}_{xm}^{*}(\beta_x) \tilde{\mathfrak{J}}_{xm}(\beta_x) \tilde{G}_{xx}(\beta_x, \beta_z) \, d\beta_x \qquad (2.80d)$$

For shielded configurations (a ≠ ∞) the integrations are replaced by summations since β_x is a discrete instead of a continuous variable and $d\beta_x$ is replaced by $\Delta\beta_x$ as in (2.5) and (2.6). Using these changes in the above four equations gives

$$K_{nn} = \sum_{i=-\infty}^{\infty} \tilde{\mathfrak{J}}_{zn}^{*}(\beta_{xi}) \tilde{\mathfrak{J}}_{zn}(\beta_{xi}) \tilde{G}_{zz}(\beta_{xi}, \beta_z) \, \Delta\beta_x \qquad (2.81a)$$

$$K_{mn} = \sum_{i=-\infty}^{\infty} \tilde{\mathfrak{J}}_{zn}^{*}(\beta_{xi}) \tilde{\mathfrak{J}}_{xm}(\beta_{xi}) \tilde{G}_{zx}(\beta_{xi}, \beta_z) \, \Delta\beta_x \qquad (2.81b)$$

$$K_{nm} = \sum_{i=-\infty}^{\infty} \tilde{\mathfrak{J}}_{xm}^{*}(\beta_{xi}) \tilde{\mathfrak{J}}_{zn}(\beta_{xi}) \tilde{G}_{zx}(\beta_{xi}, \beta_z) \, \Delta\beta_x \qquad (2.81c)$$

$$K_{mm} = \sum_{i=-\infty}^{\infty} \tilde{\mathfrak{J}}_{xm}^{*}(\beta_{xi}) \tilde{\mathfrak{J}}_{xm}(\beta_{xi}) \tilde{G}_{xx}(\beta_{xi}, \beta_z) \, \Delta\beta_x \qquad (2.81d)$$

In practice, the integrations in (2.80) will be done numerically, so (2.81) with finite limits for the summations, are more representative of the actual equations that need to be computed.

The left hand sides of (2.79a) and (2.79b) can be shown to be zero through the application of Parseval's theorem, which states [51]:

Given two functions f(t) and g(t) that are Fourier transformable with transforms represented by

$$g(t) \longleftrightarrow \tilde{G}(\omega) \quad \text{and} \quad f(t) \longleftrightarrow \tilde{F}(\omega) \qquad (2.82a)$$

then

$$\int_{-\infty}^{\infty} g(t)f(t) \ dt = \frac{1}{2\pi} \int_{-\infty}^{\infty} \tilde{G}(\omega)\tilde{F}^*(\omega) \ d\omega \qquad (2.82b)$$

where * denotes the complex conjugate. Thus the integration of the left hand side of (2.79a) is

$$\int_{-\infty}^{\infty} \tilde{J}_{zn}^*(\beta_x)\tilde{E}_{z2}(\beta_x,\beta_z) \ d\beta_x = 2\pi \int_{-\infty}^{\infty} J_{zn}(x)E_{z2}(x,\beta_z) \ dx \qquad (2.83)$$

Note that the current density exists only on the strip and the tangential electric fields are zero there because it is a perfect electric conductor. The tangential electric fields, on the other hand, are non-zero only where there is not a conductor, and therefore where there is no current density. Thus the product of the current density and electric field is always zero since neither is non-zero where the other exists. Therefore, the integrand is zero for all x and so the integration in the spatial domain is also zero. Since the integration in the spatial domain is zero, through Parseval's theorem, the integration in the spectral domain is also zero. In a similar fashion, the left side of (2.79b) can also be shown to be zero. Replacing the infinite limits of the summations with finite ones, (2.79a) and (2.79b) become

$$\sum_{n=1}^{N} a_n \left[\sum_{n=1}^{N} a_n K_{nn} + \sum_{m=1}^{M} b_m K_{mn} \right] = 0 \qquad (2.84a)$$

$$\sum_{m=1}^{M} b_m \left[\sum_{n=1}^{N} a_n K_{nm} + \sum_{m=1}^{M} b_m K_{mm} \right] = 0 \qquad (2.84b)$$

where N and M are the total number of current densities used in the expansion.

These equations can be solved numerically for β_z as a function of frequency and/or structural parameters by using a nonlinear equation solver to find the zero of the determinant of the resulting matrix. To obtain an exact solution, the number of basis functions used must be infinite. However, if the basis functions are chosen properly, so that they closely model the actual current distributions, then few terms are necessary to obtain very good results. For frequencies well into the dispersive region of the structure, only a two by two matrix (i.e. M=1, N=1) is necessary to get very good results.

2.3.7 Slot Lines and Coplanar Waveguides

For slot line and CPW type structures, the electric fields exist over a smaller portion of the center conductor interface than the current densities. Therefore it is usually more convenient to specify the electric fields in the spaces as opposed to the currents on the conductors. To solve these types of problems, it is advantageous to reformulate (2.74a) and (2.74b) so that the currents are expressed in terms of the electric fields.

The analysis begins by simplifying (2.74a-b) for the fields on the conductor interface. Both sides of these equations are multiplied by $\frac{-j}{\omega\mu_0}(\beta_x^2+\beta_z^2)$ and they can then be written as

$$\frac{-j}{\omega\mu_0}\tilde{E}_{z2}(\beta_x^2+\beta_z^2) = \tilde{J}_z\left[\beta_z^2\beta_0^{-2}\tilde{Z}^{TM}-\beta_x^2\tilde{Z}^{TE}\right]+\tilde{J}_x\left[\beta_x\beta_z\left\{\beta_0^{-2}\tilde{Z}^{TM}+\tilde{Z}^{TE}\right\}\right] \qquad (2.85a)$$

$$\frac{-j}{\omega\mu_0}\tilde{E}_{x2}(\beta_x^2+\beta_z^2) = \tilde{J}_z\left[\beta_x\beta_z\left\{\beta_0^{-2}\tilde{Z}^{TM}+\tilde{Z}^{TE}\right\}\right]+\tilde{J}_x\left[\beta_x^2\beta_0^{-2}\tilde{Z}^{TM}-\beta_z^2\tilde{Z}^{TE}\right] \qquad (2.85b)$$

These equations are now in the form of a matrix equation, i.e.

$$\frac{-j}{\omega\mu_0}(\beta_x^2+\beta_z^2)\begin{bmatrix} E_{z2} \\ E_{x2} \end{bmatrix} = \begin{bmatrix} a & b \\ b & c \end{bmatrix}\begin{bmatrix} J_x \\ J_z \end{bmatrix} \tag{2.86}$$

where

$$a = \beta_z^2\beta_0^{-2}z^{TM}-\beta_x^2z^{TE} \tag{2.87a}$$

$$b = \beta_x\beta_z\left\{\beta_0^{-2}z^{TM}+z^{TE}\right\} \tag{2.87b}$$

$$c = \beta_x^2\beta_0^{-2}z^{TM}-\beta_z^2z^{TE} \tag{2.87c}$$

The matrix equation in (2.86) can be solved for J_x and J_z by

multiplying both sides by the inverse of the square matrix; i.e.,

$$\begin{bmatrix} J_x \\ J_z \end{bmatrix} = \frac{-j}{\omega\mu_0}(\beta_x^2+\beta_z^2)\begin{bmatrix} a & b \\ b & c \end{bmatrix}^{-1}\begin{bmatrix} E_{z3} \\ E_{x3} \end{bmatrix} = \frac{-j}{\omega\mu_0}(\beta_x^2+\beta_z^2)\begin{bmatrix} e & f \\ f & g \end{bmatrix}\begin{bmatrix} E_{z3} \\ E_{x3} \end{bmatrix} \tag{2.88}$$

where

$$e = c/(ca-b^2) \tag{2.89a}$$

$$f = -b/(ca-b^2) \tag{2.89b}$$

$$g = a/(ca-b^2) \tag{2.89c}$$

Begin by finding the denominator of the matrix elements

$$(ca-b^2) = \left[\beta_z^2\beta_0^{-2}z^{TM} - \beta_x^2z^{TE}\right]\left[\beta_x^2\beta_0^{-2}z^{TM} - \beta_z^2z^{TE}\right]$$

$$-\left[\beta_x^2\beta_z^2\left\{\beta_0^{-2}z^{TM} + z^{TE}\right\}\right]^2 \tag{2.90}$$

$$(ca-b^2) = \beta_x^2\beta_z^2\beta_0^{-4}z^{TM^2}-\beta_z^4\beta_0^{-2}z^{TM}z^{TE}-\beta_x^4\beta_0^{-2}z^{TM}z^{TM}$$

$$+\beta_x^2\beta_z^2z^{TE^2}-\beta_x^2\beta_z^2\beta_0^{-4}z^{TM^2}-2\beta_x^2\beta_z^2\beta_0^{-2}z^{TM}z^{TE}-\beta_x^2\beta_z^2z^{TE^2} \tag{2.91}$$

$$(ca-b^2) = -z^{TM}z^{TE}\beta_0^{-2}\left[\beta_z^4+2\beta_x^2\beta_z^2+\beta_x^4\right] \tag{2.94}$$

$$(ca-b^2) = -z^{TM}z^{TE}\beta_0^{-2}\left[\beta_x^2+\beta_z^2\right]^2 \tag{2.95}$$

Let

$$Y^{TM} = 1/Z^{TM} \qquad (2.96a)$$

$$Y^{TE} = 1/Z^{TE} \qquad (2.96b)$$

Using these substitutions with the equation for the denominator in (2.95), the elements of the inverted matrix are;

$$e = c/(ca-b^2) = \left[\beta_z^2\beta_0^2 Y^{TM} - \beta_x^2 Y^{TE}\right]\left[\beta_x^2+\beta_z^2\right]^{-2} \qquad (2.97a)$$

$$f = -b/(ca-b^2) = \beta_x\beta_z\left[Y^{TM} + \beta_0^2 Y^{TE}\right]\left[\beta_x^2+\beta_z^2\right]^{-2} \qquad (2.97b)$$

$$g = a/(ca-b^2) = \left[\beta_x^2\beta_0^2 Y^{TM} - \beta_z^2 Y^{TE}\right]\left[\beta_x^2+\beta_z^2\right]^{-2} \qquad (2.97c)$$

Substituting back into the matrix and writing out the equations

$$J_z = \frac{-j}{\omega\mu_0}\left[E_{z2}H_{zz}+E_{x2}H_{xz}\right] \qquad (2.98a)$$

$$J_x = \frac{-j}{\omega\varepsilon_0}\left[E_{z2}H_{zx}+E_{x2}H_{xx}\right] \qquad (2.98b)$$

where

$$H_{zz} = \frac{\beta_x^2\beta_0^2 Y^{TM}-\beta_z^2 Y^{TE}}{\beta_x^2+\beta_z^2} \qquad (2.99a)$$

$$H_{xx} = \frac{\beta_z^2\beta_0^2 Y^{TM}-\beta_x^2 Y^{TE}}{\beta_x^2+\beta_z^2} \qquad (2.99b)$$

$$H_{xz} = H_{zx} = \beta_x\beta_z\frac{\beta_0^2 Y^{TM}+Y^{TE}}{\beta_x^2+\beta_z^2} \qquad (2.99c)$$

Equations (2.98a) and (2.98b) can then be solved in the same manner as (2.76a) and (2.76b) for β_z by expanding the electric fields instead of the currents. The expansion functions for the electric field are chosen to be the same as the current expansion functions, except that the J_{zn} functions are used for E_{xm} expansions and the J_{xm} functions are used for the E_{zn} expansions.

2.3.8 Green's Function for Multilayer Structures

With the increasing emphasis on MMIC technology, the need to compute microstrip parameters for multilayer structures has become more important. The introduction of additional substrate layers, even relatively thin ones, has a strong effect on the effective dielectric constant of the structure [52]. In general, the addition of superstrates does not significantly affect the parameters of planar circuits. However, in certain cases, especially when the circuit is shielded, these layers also can have a large impact on the propagation characteristics of the structure. Although the effect of multiple layers is very important, almost all of the approximate formulations have been done for a single dielectric substrate, and they cannot be modified to handle more general cases. However, because of their exact formulation, most full wave solutions can treat the multilayer problem.

One drawback with using full wave solutions, such as the SDA, to solve multilayer problems is that they normally require a different computer program for each structure that would potentially be studied. In the case of the SDA, a new Green's function must be derived for each possible configuration by solving the appropriate boundary value problem. As the number of layers increases, the number of unknown constants and equations in the boundary value problem quadruples. Thus to obtain the Green's function of a structure with six dielectric layers using a combination of TE^x, TM^x, TE^z, or TM^z modes would require simultaneously solving twenty four equations for twenty four unknowns. If TE^y and TM^y modes are used, the problem simplifies slightly to two

separate sets of twelve equations and twelve unknowns. Thus the development of an easily computed, generalized Green's function for planar printed circuit lines will greatly simplify both the theoretical development as well as the computational process.

In this section, a general Green's function is presented that is easily computed through a recursive formulation. This Green's function is applicable to structures with any number of layers above or below the center conductor interface. Since the information about the y variations in the structure are contained in the modal input impedances, they are the only part of the Green's function that must be recalculated for multi-layer structures. The input impedance for either the TE^y or TM^y mode can be thought of as a parallel combination of the admittances seen above and below the center conductor interface, i.e.

$$\tilde{Z}^{(i)} = \frac{1}{\tilde{Y}^{(i)}_{LN} + \tilde{Y}^{(i)}_{UM}} \tag{2.100}$$

where i is either TE or TM, L and U indicate the lower and upper layers respectively, and N and M are the total number of planar layers below and above the interface, as in Fig. 2.2. The admittances $\tilde{Y}^{(i)}_{(j)}$ are determined using a recursive formulation for either the upper or lower layers, beginning with j = L1 or U1 through j = LN or UM, using

$$\tilde{Y}^{TM}_{(j)} = \frac{\tilde{Y}^{TM}_{s(j)} \tilde{Y}^{TM}_{(j-1)} + \alpha^2_{y(j)}/\mu^2_{r(j)}}{\tilde{Y}^{TM}_{s(j)} + \tilde{Y}^{TM}_{(j-1)}} \tag{2.101}$$

$$\tilde{Y}^{TE}_{(j)} = \frac{\tilde{Y}^{TE}_{s(j)} \tilde{Y}^{TE}_{(j-1)} + \epsilon^2_{r(j)}/\alpha^2_{y(j)}}{\tilde{Y}^{TE}_{s(j)} + \tilde{Y}^{TE}_{(j-1)}} \tag{2.102}$$

$$\tilde{Y}^{TE}_{s(j)} = \frac{\alpha_{y(j)} \coth\left[\alpha_{y(j)} h_{(j)}\right]}{\mu_{r(j)}} \tag{2.103}$$

$$\tilde{Y}^{TM}_{s(j)} = \frac{\varepsilon_{r(j)} \coth\left[\alpha_{y(j)} h_{(j)}\right]}{\alpha_{y(j)}} \tag{2.104}$$

$\tilde{Y}^{(i)}_{(j)}$ can be thought of as the input admittance seen looking outward through the jth layer (away from the conductor interface) and $\tilde{Y}^{(i)}_{s(j)}$ is the self admittance of the layer for the particular mode configuration.

For $j = U1$ or $L1$, then the $(j-1)$ layer, $U0$ or $L0$, is a perfect electric conductor (i.e., a ground plane or cover sheet), and $\tilde{Y}^{(i)}_{(k)0} \longrightarrow \infty$, for $k = U$ or L, since a perfect conductor has zero resistance. Taking the limit of either (2.101) or (2.102b) as $\tilde{Y}^{(i)}_{(k)0}$ goes to infinity, then $\tilde{Y}^{(i)}_{(k)1} = \tilde{Y}^{(i)}_{s(k)1}$.

If the $(k)1^{th}$ layer is dielectric of infinite height (i.e., a structure with no ground plane or cover sheet), then $h_{(k)1} \longrightarrow \infty$ and therefore $\coth(\alpha_{y(k)1} h_{(k)1}) \longrightarrow 1$, respectively. The conditions for $\tilde{Y}^{(i)}_{(k)0}$ and $\tilde{Y}^{(i)}_{(k)1}$ are the same as above, as though there is a conductor at an infinite distance. This is a valid assumption since the outward radiation condition specifies that $\underline{E} \longrightarrow 0$ as $y \longrightarrow \pm\infty$. This particular configuration, no ground plane and/or cover sheet, results in

$$\tilde{Y}^{TE}_{(k)1} = \tilde{Y}^{TE}_{s(k)1} = \alpha_{y(k)1}/\mu_{r(k)1} \tag{2.105}$$

$$\tilde{Y}^{TM}_{(k)1} = \tilde{Y}^{TM}_{s(k)1} = \varepsilon_{r(k)1}/\alpha_{y(k)1} \tag{2.106}$$

Note that these equations are the same for layers both above and below the conductor interface because the uniqueness theorem states that solution of the boundary value problem is invariant to the method of solution (if done correctly). Certainly it is not possible for the structure to 'know' which layers are 'above' or 'below'. This symmetry

in the equations is valid only for strips of vanishingly small thickness and becomes invalid when the strip thickness approaches the height of the dielectric layer that contains it.

Thus the Spectral Domain Approach is a simple, fast and efficient method for determining the propagation constants of planar transmission lines. Starting by Fourier transforming of all the field quantities, the derivation of the Green's function is simplified. TE^y and TM^y modes are then used because they can independently satisfy the boundary condition in the spectral domain. The total electric fields at the interface can then be obtained by relating the modal currents to the total current densities. After the total electric fields are found, the total currents are expanded into a complete set of basis functions so that the problem can be solved using Galerkin's method. Finally the equations are solved numerically to obtain the propagation constants of the structure under consideration.

CHAPTER 3
TRANSIENT SIGNAL ANALYSIS

While many applications of printed circuit transmission lines require only single frequency operation, there also is a demand for circuits that use finite time domain signals. This chapter presents the formulations necessary to analyze the distortion of transient signals on isolated, as well as coupled transmission lines. Since planar printed circuits are inherently dispersive, i.e. the phase velocity is a function of frequency, the analysis of transient signal distortion on these lines begins with a frequency domain approach. In order to consider the coupling between adjacent lines in a rigorous manner, the even/odd mode formulation is then presented. Finally, this formulation is used to derive the appropriate equations for the propagation of finite time domain signals on dispersive and lossy symmetric coupled transmission lines.

3.1 The Frequency Domain Approach

The analysis of the time dependent response of a transient signal may be formulated in either the time domain or the frequency domain. For a non-dispersive transmission line, it is easiest to analyze signal propagation in the time domain. On the other hand, if the transmission line is dispersive, then the analysis in the time domain, while possible [14], is much more difficult and time consuming. The

simplest and most efficient method for examining pulse propagation on these types of structures is to consider the pulse in the frequency domain.

The analysis of the system response begins by defining a Fourier transform pair that relates the time domain response to the frequency domain spectrum. Using a time variable t and the corresponding transform variable ω, the Fourier transform pair is defined as

$$\tilde{V}(\omega,z) = \mathcal{F}\left\{v(t,z)\right\} = \int_{-\tau/2}^{\tau/2} v(t,z)\ e^{-j\omega t}\ dt \tag{3.1}$$

$$v(t,z) = \mathcal{F}^{-1}\left\{\tilde{V}(\omega,z)\right\} = \frac{1}{2\pi} \int_{-\infty}^{\infty} \tilde{V}(\omega,z)\ e^{j\omega t}\ d\omega \tag{3.2}$$

where τ is the total time over which the pulse exists. Since the signal exists only over a finite time period, its spectrum $\tilde{V}(\omega,z)$ is continuous and exists from $-\infty < \omega < \infty$.

The time domain response of a linear system to an input signal is equal to the convolution integral of the impulse response of the system and the input signal. If the input signal is $v(t,z)$ and the impulse response of the system is $h(t,z)$, then the system response, in time, is given by

$$y(t,z) = \int_{-\infty}^{\infty} h(\tau,z)\ v(t-\tau,z)\ d\tau \tag{3.3}$$

Since the convolution integral of two functions in the time domain is equivalent to multiplication of their Fourier transforms in the frequency domain, (3.3) can also be written as

$$\tilde{Y}(\omega,z) = \tilde{H}(\omega)\ \tilde{V}(\omega,z) \tag{3.4}$$

where $\tilde{Y}(\omega,z)$, $\tilde{H}(\omega,z)$, and $\tilde{V}(\omega,z)$ are the Fourier transforms of $y(t,z)$, $h(t,z)$, and $v(t,z)$, respectively. To find the system response in time,

the inverse transform of (3.2) is applied to both sides of (3.4) giving

$$y(t,z) = \frac{1}{2\pi} \int_{-\infty}^{\infty} \tilde{V}(\omega,z) \tilde{H}(\omega) \, e^{j\omega t} \, d\omega \qquad (3.5)$$

The impulse response of a matched transmission line is simply a phase advance equal to the product of the complex propagation constant and the distance traveled, i.e.

$$H(\omega,z) = e^{-\gamma_z(\omega)z} = e^{-[\alpha_z(\omega)+j\beta_z(\omega)]z} \qquad (3.6)$$

where $\gamma_z(\omega)$ is the complex propagation constant, $\alpha_z(\omega)$ is the attenuation constant, and $\beta_z(\omega)$ is the phase constant. Using (3.6) for $\tilde{H}(\omega,z)$ in (3.5), the response on a transmission line at a time t and a position z_0 to a signal $v(t,z)$ can be written as

$$y(t,z_0) = \frac{1}{2\pi} \int_{-\infty}^{\infty} \tilde{V}(\omega,z) \, e^{-[\alpha_z(\omega)+j\beta_z(\omega)]z_0} e^{j\omega t} \, d\omega \qquad (3.7)$$

or

$$y(t,z_0) = \frac{1}{2\pi} \int_{-\infty}^{\infty} \tilde{V}(\omega,z) \, e^{-\alpha_z(\omega)z_0} e^{j[\omega t-\beta_z(\omega)z_0]} \, d\omega \qquad (3.8)$$

The exponential containing α_z in the integrand causes the degradation of the signal due to attenuation whereas the exponential with β_z is responsible for the phase advance.

Dispersion distortion happens when $\beta_z(\omega)$ is a nonlinear function of frequency, i.e. the phase velocity is not constant with varying frequencies. The effect of dispersion distortion can be visualized by considering the pulse as a summation of many single frequency signals with different amplitudes, i.e. a Fourier series representation. At the beginning of the transmission line, all the signals line up properly and add together to recreate the input signal. However, as the pulse travels down the line, each frequency component travels at a

slightly different speed, since the phase velocity is not the same for each frequency. Thus, each frequency component of the pulse arrives slightly shifted in time with respect to the other components. Since the frequency components do not add together as they did originally, the pulse shape is distorted. Although dispersion distortion does not change the amplitudes of the the individual frequency components, the amplitude of the distorted pulse will normally be less than the amplitude of the original pulse. In addition, the pulse spreads out in time since some frequency components arrive earlier and some later than if they had all traveled the same speed.

If $\alpha_z(\omega)$ is a constant with respect to frequency, then attenuation will only reduce the amplitude of the signal and not distort it. On the other hand, when $\alpha_z(\omega)$ varies with frequency, then each frequency component is reduced by a different amount and it changes the reconstruction of the signal. However, unlike dispersion distortion, attenuation in general will not cause widening of the pulse, only a reduction in amplitude.

3.2 Even/Odd Mode Formulation

In 1956, J. Reed and H. Wheeler introduced a method for obtaining the response of a symmetric four-port network called the even/odd mode approach [25]. The even/odd mode approach, also known as the symmetry approach, simplifies the analysis of a symmetric four-port network by splitting it up into two simpler, two-port networks. Although this method of analysis applies only to symmetric networks, asymmetric networks can be analyzed in a similar fashion [26].

The even/odd mode analysis begins by assuming that a signal of unit amplitude is applied to port one as in Fig. 3.1, and the outputs are measured at ports two and three. It is also assumed that ports two and three are perfectly matched, so that there are no reflections. The input signal is split up into two different signals, an even mode and an odd mode as in Fig. 3.1. The even and odd mode signals are chosen such that they add together to produce a unit amplitude signal at port one and no signal at port four, recreating the original signal. The even mode consists of two signals of one-half amplitude that are in phase and so they create a voltage maximum at every point along the line of symmetry. This is equivalent to an open circuit or a perfect magnetic conductor separating the two lines. The odd mode, on the other hand, has two signals of one-half amplitude that are 180 degrees out of phase, and it produces a voltage minimum at every point along the line of symmetry. This is equivalent to a short circuit or having the lines separated by a perfect electric conductor. In general, the even and the odd modes will have different phase velocities, attenuation constants, and characteristic impedances.

Coupling distortion can best be understood by considering the response on both lines to be a linear combination of four pulses, two on each line, as in Fig. 3.2. In general, the in phase pair (even) and the out of phase pair (odd), will travel down the line at two different speeds, due to the differences in the phase velocities of the even and odd modes. The even and odd modes pairs of pulses add constructively on the signal line and destructively on the sense line. To isolate the effects of even/odd mode distortion, a hypothetical lossless and
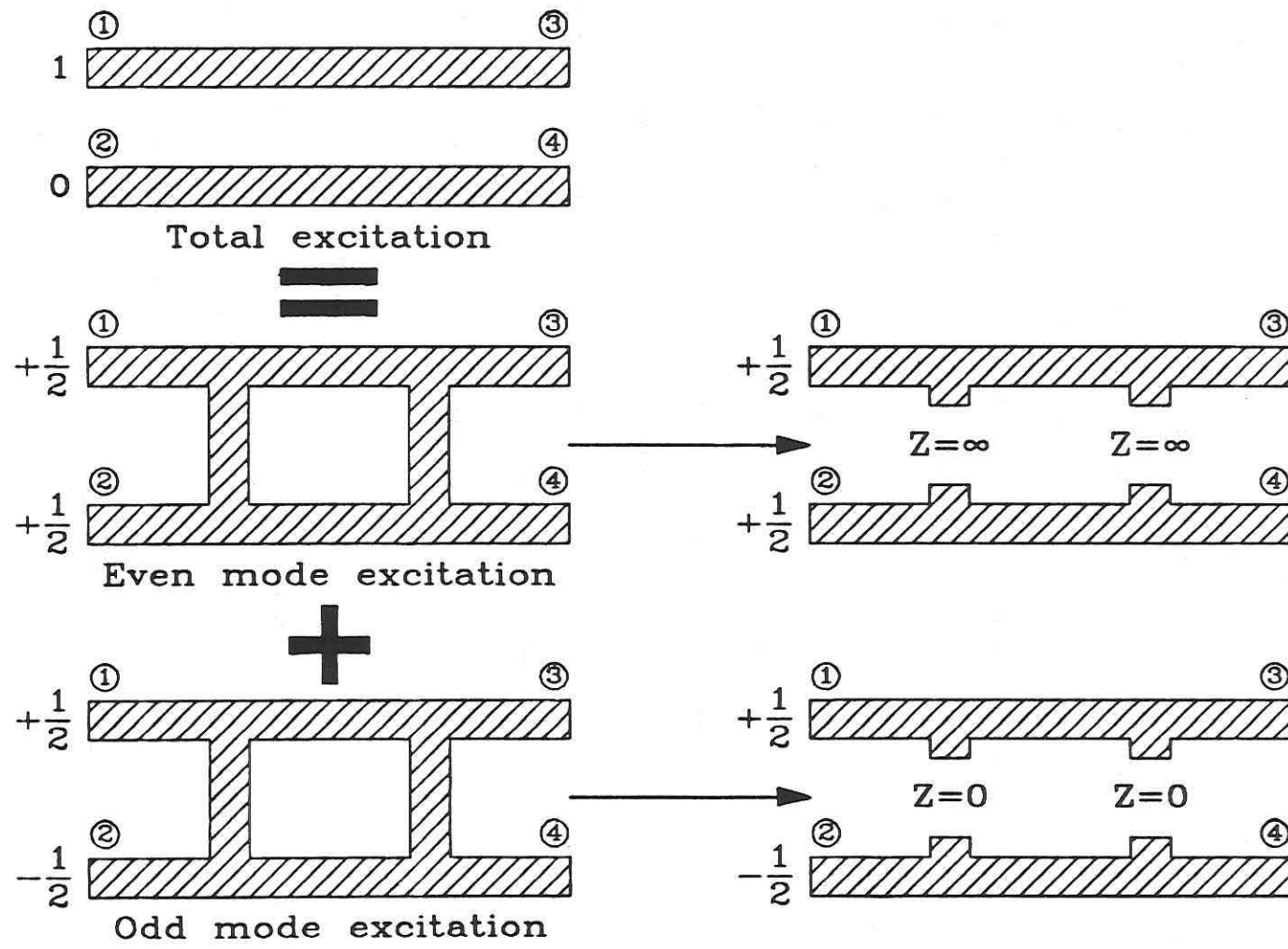
Fig 3.1. Even/odd mode approach for symmetric two port networks
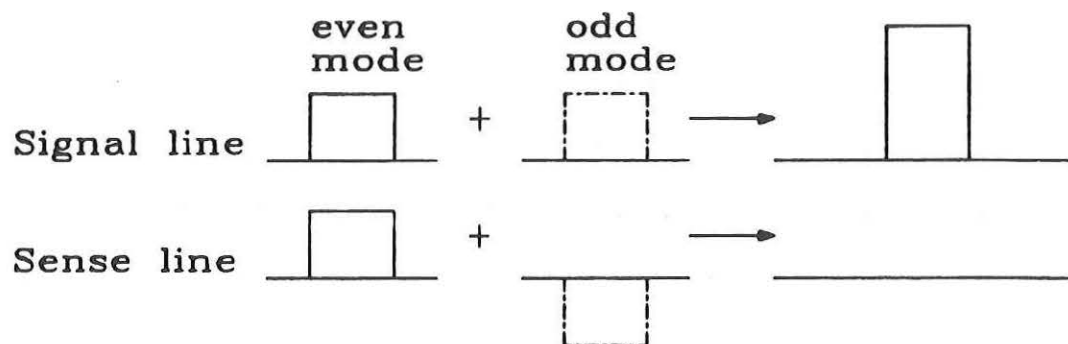
(a) Breaking into even and odd modes
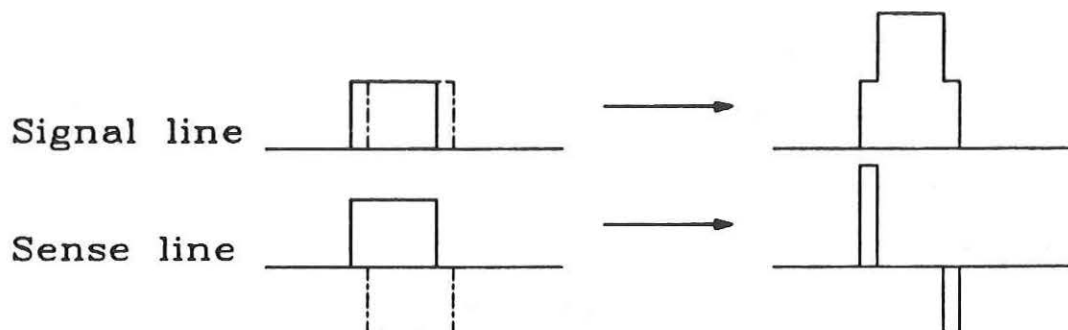
(b) Distortion after a short distance
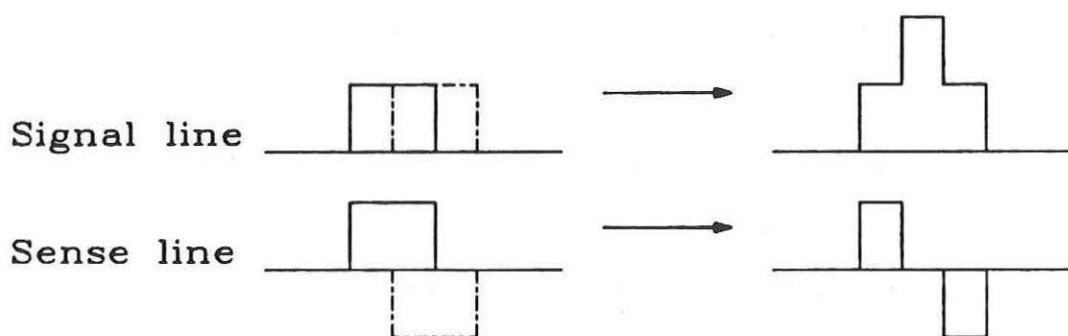
(c) Increasing distortion with distance
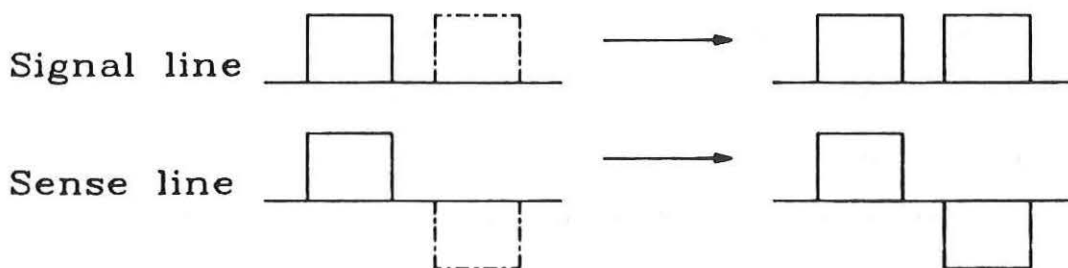
(d) Even and odd separate completely

Fig. 3.2. Coupling distortion on lossless and dispersionless transmission lines.

dispersionless symmetric two conductor transmission line is considered. A rectangular pulse is used for simplicity, and it is assumed that the odd mode phase velocity is higher than that of the even mode.

When the signal first starts out, the even and odd pairs have not separated very much, and almost completely cancel each other on the sense line and reproduce the signal fairly accurately on the signal line, as shown in Fig. 3.2(b). As the signal travels farther, Fig. 3.2(c), the even and odd pairs begin to separate. Now they do not cancel completely on the sense line or reproduce the signal very well on the signal line; the result being distortion and crosstalk. The signal line response has also been widened and the leading and trailing edges have dropped off in amplitude. After the signal has traveled a very long distance, Fig. 3.2(d), the even and odd mode pairs separate completely, so that there are two pulses of one-half amplitude that are in phase on the signal line and two pulses of one-half amplitude that are 180 degrees out of phase on the sense line.

In Fig. 3.2(b)-(d), the leading response of the sense line is negative, because it was assumed that the odd mode had a higher phase velocity than the even mode. If this is not the case, then the leading response on the sense line is positive, because the even mode will arrive before the odd mode. In addition, as the distance increases, the amplitude of the response on both lines will tend to approach one-half of the value of the response on a single, isolated line. Since pulse spreading is due to the difference in the phase velocities,

the total pulse spread, in time, due to only even/odd distortion at a distance z, can be written as

$$t_s = \left| \frac{z}{v_e} - \frac{z}{v_o} \right| \tag{3.9}$$

where v_e and v_o are the even and odd mode phase velocities, respectively. Since the phase velocities are related to the effective dielectric constants, (3.9) can also be written as

$$t_s = \frac{z}{c} \left| \sqrt{\varepsilon_{re}} - \sqrt{\varepsilon_{ro}} \right| \tag{3.10}$$

where ε_{re} and ε_{ro} are the effective dielectric constants for the even and odd modes, respectively, and c is the speed of light in free space. Note that distortion due to coupling may be present even if the lines are dispersive and lossy as well, since each of the three distortion mechanisms, dispersion, losses, and coupling, are independent of each other. If the transmission line is lossy and dispersive, then the analysis is the same, except that the even and odd mode pairs suffer distortion due to dispersion and losses as they travel down the line, increasing the pulse spread and reducing further the amplitude of the signal.

3.3 Symmetric Coupled Transmission Lines

In this section, the even/odd mode formulation is applied with the frequency domain approach to determine the response on symmetric coupled lines. To compute the response on both lines due to an input signal on only one line, the input signal is split into the even and odd mode components. The response on both lines due to each mode is then obtained as a function of time or distance for a specific distance

or time respectively. These responses are then added together to obtain the total response on both lines at a particular time or distance.

Using this approach, the response on both lines due to a signal on the first line, the signal line, with no excitation on the second line, the sense line, can be written using the superposition of the even and odd mode responses as

$$v_1(t,z) = \frac{1}{2}\left[v_e(t,z) + v_o(t,z)\right] \qquad (3.11a)$$

$$v_2(t,z) = \frac{1}{2}\left[v_e(t,z) - v_o(t,z)\right] \qquad (3.11b)$$

where $v_e(t,z)$ and $v_o(t,z)$ are the responses of the even and odd modes, respectively, to the input signal and $v_1(t,z)$ and $v_2(t,z)$ are the voltages on lines one and two at a time t and position z. Using (3.8), the even and odd mode responses can be written as

$$v_e(t,z) = \frac{1}{2\pi}\int_{-\infty}^{\infty} \tilde{V}(\omega,z)\, e^{-\gamma_{ze}(\omega)z}\, e^{j\omega t}\, d\omega \qquad (3.12a)$$

$$v_o(t,z) = \frac{1}{2\pi}\int_{-\infty}^{\infty} \tilde{V}(\omega,z)\, e^{-\gamma_{zo}(\omega)z}\, e^{j\omega t}\, d\omega \qquad (3.12a)$$

where $\gamma_{ze}(\omega)$ and $\gamma_{zo}(\omega)$ are the frequency dependent complex propagation constants for the even and odd modes respectively. Substituting these two equations into (3.11a) and (3.11b) yields

$$v_1(t,z) = \frac{1}{4\pi}\int_{-\infty}^{\infty} \tilde{V}(\omega,z)\left[e^{-\gamma_{ze}z}\, e^{j\omega t} + e^{-\gamma_{zo}z}\, e^{j\omega t}\right]d\omega \qquad (3.13a)$$

$$v_2(t,z) = \frac{1}{4\pi}\int_{-\infty}^{\infty} \tilde{V}(\omega,z)\left[e^{-\gamma_{ze}z}\, e^{j\omega t} - e^{-\gamma_{zo}z}\, e^{j\omega t}\right]d\omega \qquad (3.13a)$$

Factoring out $e^{j\omega t}\, e^{-z[\gamma_{ze}+\gamma_{zo}]/2}$ in (3.13a) and (3.13b) leads to

$$v_1(t,z) = \frac{1}{2\pi}\int_{-\infty}^{\infty}\tilde{V}(\omega,z)\, e^{j\omega t}\, e^{-z[\gamma_{ze}+\gamma_{zo}]/2} \times$$

$$\frac{1}{2}\left[e^{z[\gamma_{zo}-\gamma_{ze}]/2} + e^{-z[\gamma_{zo}-\gamma_{ze}]/2}\right]d\omega \qquad (3.14a)$$

$$v_2(t,z) = \frac{1}{2\pi}\int_{-\infty}^{\infty}\tilde{V}(\omega,z)\, e^{j\omega t}\, e^{-z[\gamma_{ze}+\gamma_{zo}]/2} \times$$

$$\frac{1}{2}\left[e^{z[\gamma_{zo}-\gamma_{ze}]/2} - e^{-z[\gamma_{zo}-\gamma_{ze}]/2}\right]d\omega \qquad (3.14b)$$

These equations can be simplified further by recognizing that the terms in the parenthesis in (3.14a) and (3.14b) are the hyperbolic cosine and sine functions, respectively. Using this identity, (3.14a) and (3.14b) can be expressed as

$$v_1(t,z) = \frac{1}{2\pi}\int_{-\infty}^{\infty}\tilde{V}(\omega,z)\, e^{j\omega t-z[\gamma_{ze}+\gamma_{zo}]/2}\cosh\left[z\frac{\gamma_{zo}-\gamma_{ze}}{2}\right]d\omega \qquad (3.15a)$$

$$v_2(t,z) = \frac{1}{2\pi}\int_{-\infty}^{\infty}\tilde{V}(\omega,z)\, e^{j\omega t-z[\gamma_{ze}+\gamma_{zo}]/2}\sinh\left[z\frac{\gamma_{zo}-\gamma_{ze}}{2}\right]d\omega \qquad (3.15a)$$

Equations (3.15a) and (3.15b) may be used to compute the pulse distortion on coupled, lossy, and dispersive transmission lines by evaluating the integrals either in closed form or numerically. However, in their present form these formulas do not give much insight into the mechanisms of distortion due to coupling, losses, or dispersion. In order to gain an understanding of these coupling mechanisms, equations (3.15a-b) need to be simplified to separate out each of the three mechanisms.

The first step is to expand each term in the integrands into real and imaginary parts. While many signals of interest are symmetric

about some specific time and thus have a completely real Fourier
transform, many useful signals are asymmetric with respect to time, and
therefore their Fourier transforms are complex. The real part $\tilde{V}(\omega,z)$
is designated as $\tilde{V}_r$ and the imaginary part as $\tilde{V}_i$. In addition, to
simplify the notation, the following substitutions are made

$$\Delta\alpha = \text{Re}\left[\frac{\gamma_{zo}-\gamma_{ze}}{2}\right] = \frac{\alpha_{zo}-\alpha_{ze}}{2} \tag{3.16a}$$

$$\Delta\beta = \text{Im}\left[\frac{\gamma_{zo}-\gamma_{ze}}{2}\right] = \frac{\beta_{zo}-\beta_{ze}}{2} \tag{3.16b}$$

$$\alpha_{av} = \text{Re}\left[\frac{\gamma_{zo}+\gamma_{ze}}{2}\right] = \frac{\alpha_{zo}+\alpha_{ze}}{2} \tag{3.16c}$$

$$\beta_{av} = \text{Im}\left[\frac{\gamma_{zo}+\gamma_{ze}}{2}\right] = \frac{\beta_{zo}+\beta_{ze}}{2} \tag{3.16d}$$

Using these replacements, the integrands of (3.15a) and (3.15b) can be
rewritten as

$$I_1 = \tilde{V}(\omega,z)\ e^{j\omega t - z[\gamma_{ze}+\gamma_{zo}]/2}\ \cosh\left[z\frac{\gamma_{zo}-\gamma_{ze}}{2}\right]$$

$$= \left[\tilde{V}_r + j\,\tilde{V}_i\right]e^{-\alpha_{av}z}\ e^{j[\omega t-\beta_{av}z]}\ \cosh\left[z(\Delta\alpha + j\Delta\beta)\right] \tag{3.17a}$$

$$I_2 = \tilde{V}(\omega,z)\,e^{j\omega t - z[\gamma_{ze}+\gamma_{zo}]/2}\ \sinh\left[z\frac{\gamma_{zo}-\gamma_{ze}}{2}\right]$$

$$= \left[\tilde{V}_r + j\,\tilde{V}_i\right]e^{-\alpha_{av}z}\ e^{j[\omega t-\beta_{av}z]}\ \sinh\left[z(\Delta\alpha + j\Delta\beta)\right] \tag{3.17b}$$

Next the complex exponential in (3.17a-b) is expanded into cosine and
sine terms giving

$$I_1 = e^{-\alpha_{av}z}\left[\tilde{V}_r + j\,\tilde{V}_i\right]\left[\cos(\omega t-\beta_{av}z) + j\,\sin(\omega t-\beta_{av}z)\right] \times$$

$$\cosh\left[z(\Delta\alpha + j\Delta\beta)\right] \tag{3.18a}$$

$$I_2 = e^{-\alpha_{av}z_0} \left[\tilde{V}_r + j\, \tilde{V}_i \right] \left[\cos(\omega t - \beta_{av} z) + j\, \sin(\omega t - \beta_{av} z) \right] \times$$

$$\sinh\left[z(\Delta\alpha + j\Delta\beta) \right] \qquad (3.18b)$$

The hyperbolic sine and cosine can also be expanded into real and imaginary parts with the following formulas

$$\sinh(\theta + j\phi) = \sinh(\theta)\cos(\phi) + j\, \cosh(\theta)\sin(\phi) \qquad (3.19a)$$

$$\cosh(\theta + j\phi) = \cosh(\theta)\cos(\phi) + j\, \sinh(\theta)\sin(\phi) \qquad (3.19b)$$

Using these formulas in (3.18a-b) leads to

$$I_1 = e^{-\alpha_{av}z} \left[\tilde{V}_r + j\, \tilde{V}_i \right] \left[\cos(\omega t - \beta_{av} z) + j\, \sin(\omega t - \beta_{av} z) \right] \times$$

$$\left[\cosh(\Delta\alpha z)\, \cos(\Delta\beta z) + j\, \sinh(\Delta\alpha z)\, \sin(\Delta\beta z) \right] \qquad (3.20a)$$

$$I_2 = e^{-\alpha_{av}z} \left[\tilde{V}_r + j\, \tilde{V}_i \right] \left[\cos(\omega t - \beta_{av} z) + j\, \sin(\omega t - \beta_{av} z) \right] \times$$

$$\left[\sinh(\Delta\alpha z)\, \cos(\Delta\beta z) + j\, \cosh(\Delta\alpha z)\, \sin(\Delta\beta z) \right] \qquad (3.20b)$$

Finally, the multiplications in (3.20a) and (3.20b) are carried out and the results are separated into real and imaginary parts. The real part of the first integrand is

$$Re(I_1) = e^{-\alpha_{av}z} \left\{ \tilde{V}_r \left[\cos(\omega t - \beta_{av} z)\, \cos(\Delta\beta z)\, \cosh(\Delta\alpha z) \right. \right.$$

$$- \sin(\omega t - \beta_{av} z)\, \sin(\Delta\beta z)\, \sinh(\Delta\alpha z) \Big]$$

$$- \tilde{V}_i \left[\sin(\omega t - \beta_{av} z)\, \cos(\Delta\beta z)\, \cosh(\Delta\alpha z) \right.$$

$$\left. \left. + \cos(\omega t - \beta_{av} z)\, \sin(\Delta\beta z)\, \sinh(\Delta\alpha z) \right] \right\} \qquad (3.21a)$$

and its imaginary part is

$$
\begin{aligned}
\mathrm{Im}(I_1) = e^{-\alpha_{av}z} \Big\{ &\tilde{V}_r\Big[\sin(\omega t-\beta_{av}z)\ \cos(\Delta\beta z)\ \cosh(\Delta\alpha z) \\
&+ \cos(\omega t-\beta_{av}z)\ \sin(\Delta\beta z)\ \sinh(\Delta\alpha z)\Big] \\
+ &\tilde{V}_i\Big[\cos(\omega t-\beta_{av}z)\ \cos(\Delta\beta z)\ \cosh(\Delta\alpha z) \\
&- \sin(\omega t-\beta_{av}z)\ \sin(\Delta\beta z)\ \sinh(\Delta\alpha z)\Big]\Big\}
\end{aligned}
$$

(3.21b)

Similarly, the real part of the second integrand is found to be

$$
\begin{aligned}
\mathrm{Re}(I_2) = e^{-\alpha_{av}z} \Big\{ &\tilde{V}_r\Big[\cos(\omega t-\beta_{av}z)\ \cos(\Delta\beta z)\ \sinh(\Delta\alpha z) \\
&- \sin(\omega t-\beta_{av}z)\ \sin(\Delta\beta z)\ \cosh(\Delta\alpha z)\Big] \\
- &\tilde{V}_i\Big[\sin(\omega t-\beta_{av}z)\ \cos(\Delta\beta z)\ \sinh(\Delta\alpha z) \\
&+ \cos(\omega t-\beta_{av}z)\ \sin(\Delta\beta z)\ \cosh(\Delta\alpha z)\Big]\Big\}
\end{aligned}
$$

(3.21c)

and its imaginary part is

$$
\begin{aligned}
\mathrm{Im}(I_2) = e^{-\alpha_{av}z} \Big\{ &\tilde{V}_r\Big[\sin(\omega t-\beta_{av}z)\ \cos(\Delta\beta z)\ \sinh(\Delta\alpha z) \\
&+ \cos(\omega t-\beta_{av}z)\ \sin(\Delta\beta z)\ \cosh(\Delta\alpha z)\Big] \\
+ &\tilde{V}_i\Big[\cos(\omega t-\beta_{av}z)\ \cos(\Delta\beta z)\ \sinh(\Delta\alpha z) \\
&- \sin(\omega t-\beta_{av}z)\ \sin(\Delta\beta z)\ \cosh(\Delta\alpha z)\Big]\Big\}
\end{aligned}
$$

(3.21d)

For real time signals, the real part of the Fourier transform, $\tilde{V}_r$, is an even function of ω, and the imaginary part, $\tilde{V}_i$, is an odd function of ω [51]. In addition, while $\beta_z(\omega)$ is an odd function of ω, $\alpha_z(\omega)$ is an even function of ω. This can be shown by considering the phase propagation equation for both positive and negative frequencies.

For positive frequencies, the phase accumulation of a propagating wave is

$$\phi(\omega) = e^{j\omega t - \gamma_z(\omega)z} = e^{-\alpha_z(\omega)z}\, e^{j[\omega t - \beta_z(\omega)z]} \tag{3.22}$$

and for negative frequencies,

$$\phi(-\omega) = e^{-j\omega t - \gamma_z(-\omega)z} = e^{-\alpha_z(-\omega)z}\, e^{-j[\omega t + \beta_z(-\omega)z]} \tag{3.23}$$

In order to satisfy the outward radiation condition, the magnitude of the signal cannot increase with increasing distance, and so $\alpha_z(-\omega)$ must be equal to $\alpha_z(\omega)$. Similarly, in order for phase to advance as distance or time increases then $\beta_z(-\omega)$ must be equal to $-\beta_z(\omega)$. Thus $\alpha_z(\omega)$ is an even function of frequency and $\beta_z(\omega)$ is an odd function.

Note that the imaginary part of the integrands in (3.21b) and (3.21d) are odd functions of ω and that the integrals in (3.15a) and (3.15b) are over symmetric interval, from minus infinity to plus infinity. Since the integral of an odd function over a symmetric interval is zero, the imaginary components of the integrand do not contribute to the voltage responses and can be ignored. On the other hand, the real part of the integrands, (3.21a) and (3.21c), are even functions of ω, and so the integration from minus infinity to plus infinity will be simply twice the integration from zero to either plus or minus infinity. This is the anticipated result, since if real time signal is input to a real system, then the output should be a real function as well. Eliminating the imaginary parts, the two integrands become

$$I_1 = e^{-\alpha_{av}z} \left\{ \tilde{V}_r \left[\cos(\omega t - \beta_{av}z) \ \cos(\Delta\beta z) \ \cosh(\Delta\alpha z) \right.\right.$$

$$\left. - \sin(\omega t - \beta_{av}z) \ \sin(\Delta\beta z) \ \sinh(\Delta\alpha z) \right]$$

$$- \tilde{V}_i \left[\sin(\omega t - \beta_{av}z) \ \cos(\Delta\beta z) \ \cosh(\Delta\alpha z) \right.$$

$$\left.\left. + \cos(\omega t - \beta_{av}z) \ \sin(\Delta\beta z) \ \sinh(\Delta\alpha z) \right] \right\} \qquad (3.24a)$$

$$I_2 = e^{-\alpha_{av}z} \left\{ \tilde{V}_r \left[\cos(\omega t - \beta_{av}z) \ \cos(\Delta\beta z) \ \sinh(\Delta\alpha z) \right.\right.$$

$$\left. - \sin(\omega t - \beta_{av}z) \ \sin(\Delta\beta z) \ \cosh(\Delta\alpha z) \right]$$

$$- \tilde{V}_i \left[\sin(\omega t - \beta_{av}z) \ \cos(\Delta\beta z) \ \sinh(\Delta\alpha z) \right.$$

$$\left.\left. + \cos(\omega t - \beta_{av}z) \ \sin(\Delta\beta z) \ \cosh(\Delta\alpha z) \right] \right\} \qquad (3.24b)$$

Equations (3.24a) and (3.24b) are the most general forms of the integrands in (3.15a) and (3.15b). The sine and cosine terms with β_{av} represent the propagation of the signals at an average phase velocity, while the $\Delta\beta$ sine and cosine terms account for the distortion of the signal due to even/odd mode coupling. Similarly, the signals can be thought of as having and average attenuation value of α_{av}, due to the real exponential, while attenuation coupling between the lines is due to the hyperbolic sine and cosine terms with $\Delta\alpha$ arguments.

Having obtained these formulas, some special cases may be considered. If the attenuation constants are the same for each mode, then $\Delta\alpha = 0$ and $\alpha_{av} = \alpha_z$. This reduces (3.21a-b) to

$$I_1 = e^{-\alpha_z z} \cos(\Delta\beta z) \left\{ \tilde{V}_r \cos(\omega t - \beta_{av}z) - \tilde{V}_i \sin(\omega t - \beta_{av}z) \right\} \qquad (3.22a)$$

$$I_2 = - e^{-\alpha_z z} \sin(\Delta\beta z) \left\{ \tilde{V}_r \sin(\omega t - \beta_{av}z) + \tilde{V}_i \cos(\omega t - \beta_{av}z) \right\} \qquad (3.22b)$$

In this case, the signals on both lines are attenuated equally, but there is coupling due to $\Delta\beta$ and dispersion if β_{ze} and β_{zo} are functions of frequency.

If, in addition, the propagation constants for the even and odd modes are equal, i.e. $\Delta\beta = 0$ and $\beta_{av} = \beta_z$, then there is no response on the sense line, and the signal line response is given as

$$I_1 = e^{-\alpha_z z} \left\{ \tilde{V}_r \cos(\omega t - \beta_z z) - \tilde{V}_i \sin(\omega t - \beta_z z) \right\} \qquad (3.23)$$

This is the familiar result for pulse propagation on a single, isolated, lossy transmission line [40], [41], [44], [46].

However, if the attenuation constants for the even and odd modes are different but the propagation constants are the same, then the voltages on the two lines can be expressed as

$$I_1 = e^{-\alpha_{av} z} \cosh(\Delta\alpha z) \left\{ \tilde{V}_r \cos(\omega t - \beta_{av} z) - \tilde{V}_i \sin(\omega t - \beta_{av} z) \right\} \qquad (3.22a)$$

$$I_2 = e^{-\alpha_{av} z} \sinh(\Delta\alpha z) \left\{ \tilde{V}_r \cos(\omega t - \beta_{av} z) - \tilde{V}_i \sin(\omega t - \beta_{av} z) \right\} \qquad (3.22b)$$

Expanding the hyperbolic sine and cosine into exponentials and multiplying the result with the exponential in front of (3.22a) and (3.22b) results in

$$I_1 = \frac{1}{2} \left[e^{-\alpha_{ze} z} + e^{-\alpha_{zo} z} \right] \left[\tilde{V}_r \cos(\omega t - \beta_{av} z) - \tilde{V}_i \sin(\omega t - \beta_{av} z) \right] \qquad (3.22a)$$

$$I_2 = \frac{1}{2} \left[e^{-\alpha_{ze} z} - e^{-\alpha_{zo} z} \right] \left[\tilde{V}_r \cos(\omega t - \beta_{av} z) - \tilde{V}_i \sin(\omega t - \beta_{av} z) \right] \qquad (3.22b)$$

Since the exponentials in (3.22b) are not equal, then I_2 is non-zero and therefore there will be a response on the sense line. Thus even if the phase velocities of the even and the odd mode are the same, there still may be coupling due to differences in the attenuation

constants for the two modes. The response on the sense line has zero

magnitude at $z_0 = 0$ and is zero again as $z_0 \rightarrow \infty$. The maximum response

on the sense line occurs when the derivative with respect to z of the

exponentials in the front of (3.22b) vanishes, i.e.

$$\frac{d}{dz} \left[e^{-\alpha_{zo} z} - e^{-\alpha_{ze} z} \right] = 0 \tag{3.23}$$

Performing the indicated derivative,

$$-\alpha_{ze} \, e^{-\alpha_{ze} z} + \alpha_{zo} \, e^{-\alpha_{zo} z} = 0 \tag{3.24}$$

$$\alpha_{ze} \, e^{-\alpha_{ze} z} = \alpha_{zo} \, e^{-\alpha_{zo} z} \tag{3.25}$$

Both sides are multiplied by $\exp(\alpha_{zo} z)/\alpha_{ze}$, giving

$$e^{-\alpha_{ze} z + \alpha_{zo} z} = \frac{\alpha_{zo}}{\alpha_{ze}} \tag{3.26}$$

To remove the exponential, the natural logarithm is taken of both

sides.

$$-\alpha_{ze} z + \alpha_{zo} z = \ln(\alpha_{zo}/\alpha_{ze}) \tag{3.27}$$

This equation can now be easily solved for z.

$$z = \frac{\ln(\alpha_{zo}/\alpha_{ze})}{\alpha_{zo} - \alpha_{ze}} \tag{3.28}$$

This is the position of the maximum response on the sense line due to

attenuation coupling. Note that if the attenuation constants are a

function of frequency, which is usually the case, then location of the

maximum sense line response is different for each frequency component

of the pulse. Thus it may not be possible to accurately predict, using

(3.28) the actual location of the maximum sense line response due to

attenuation coupling.

Using Fourier transform theory and the even/odd mode approach, the

equations for signal propagation on symmetric coupled, lossy, and

dispersive transmission lines were derived. The Fourier transform provides a simple and straightforward way to represent the frequency dependent characteristics of both the transmission line and the signal, allowing quick computation of the time domain response of the system. The even/odd mode approach reduces the symmetric four-port system by representing it as two simple two-port networks. Together, these two methods were used to derive equations that relate the distortion mechanisms of dispersion, even/odd mode coupling, and attenuation coupling.

CHAPTER 4
RESULTS

This chapter uses the formulations from chapters two and three to compute the frequency dependent parameters of complex microstrip structures and to analyze pulse distortion due to dispersion and coupling on these lines. Initially, a very simple structure is considered, the single layer open symmetric coupled microstrip. The effective dielectric constant is computed versus frequency for different substrate materials and strip spacings. Using this data, pulse distortion on these structures is considered for different lengths and spacings. Next, the generalized Green's function is used to compute the effective dielectric constant of structures with multiple dielectric layers. Again results are presented for different spacings, materials, and heights of the layers. Finally multilayer symmetric coupled microstrips are considered, particularly with respect to structures that exhibit low coupling due to the control of the electrical properties of the substrates and superstrates.

4.1 Symmetric Coupled Microstrips

Coupling between adjacent transmission lines is a very important consideration in circuit design, since it is a limiting factor in the overall size and operation speed of the circuit. However, due to the wideband nature of finite time domain signals, no single parameter or

rule of thumb can accurately take into account the effects of coupling on pulse propagation, especially for multilayer structures. For accurate results, the analysis needs to be carried out in a more rigorous manner, considering the distance the signal travels and the entire spectrum of both the signal and the impulse response of the network.

This section considers open symmetric coupled microstrip structures with a single dielectric substrate. While this is not a very complex structure, it is very useful in demonstrating many of the principles of coupling and dispersion distortion. Four different dielectric substrates are used throughout this chapter as typical examples of some of the different types of materials that are used in production: 1) RT/duroid 5880, ε_r = 2.2, 2) beryllium oxide, ε_r = 6.8, 3) alumina, ε_r = 9.7, and 4) gallium arsenide, ε_r = 12.2. To demonstrate distortion, a Gaussian pulse is used which has time and frequency responses given by

$$v(t) = Ae^{-\ln(2)(t/\tau)^2} \longleftrightarrow \tilde{V}(\omega) = A\tau \sqrt{\frac{\pi}{\ln(2)}} e^{-(\omega\tau/2)^2/\ln(2)} \qquad (4.1)$$

where A is the amplitude of the pulse, τ is the voltage half width-half amplitude maximum, and the pulse is centered about t = 0.

The effective dielectric constant of the even mode, ε_{re}, and the odd mode, ε_{ro}, are plotted as a function of frequency in Figs. 4.1 through 4.8 for the four different substrate materials with six different spacings. The even mode is shown in Figs. 4.1, 4.3, 4.5, and 4.7, while the odd mode is graphed in Figs. 4.2, 4.4, 4.6, and 4.8. The smallest spacing, s = 0.6 mm is very close and would normally be
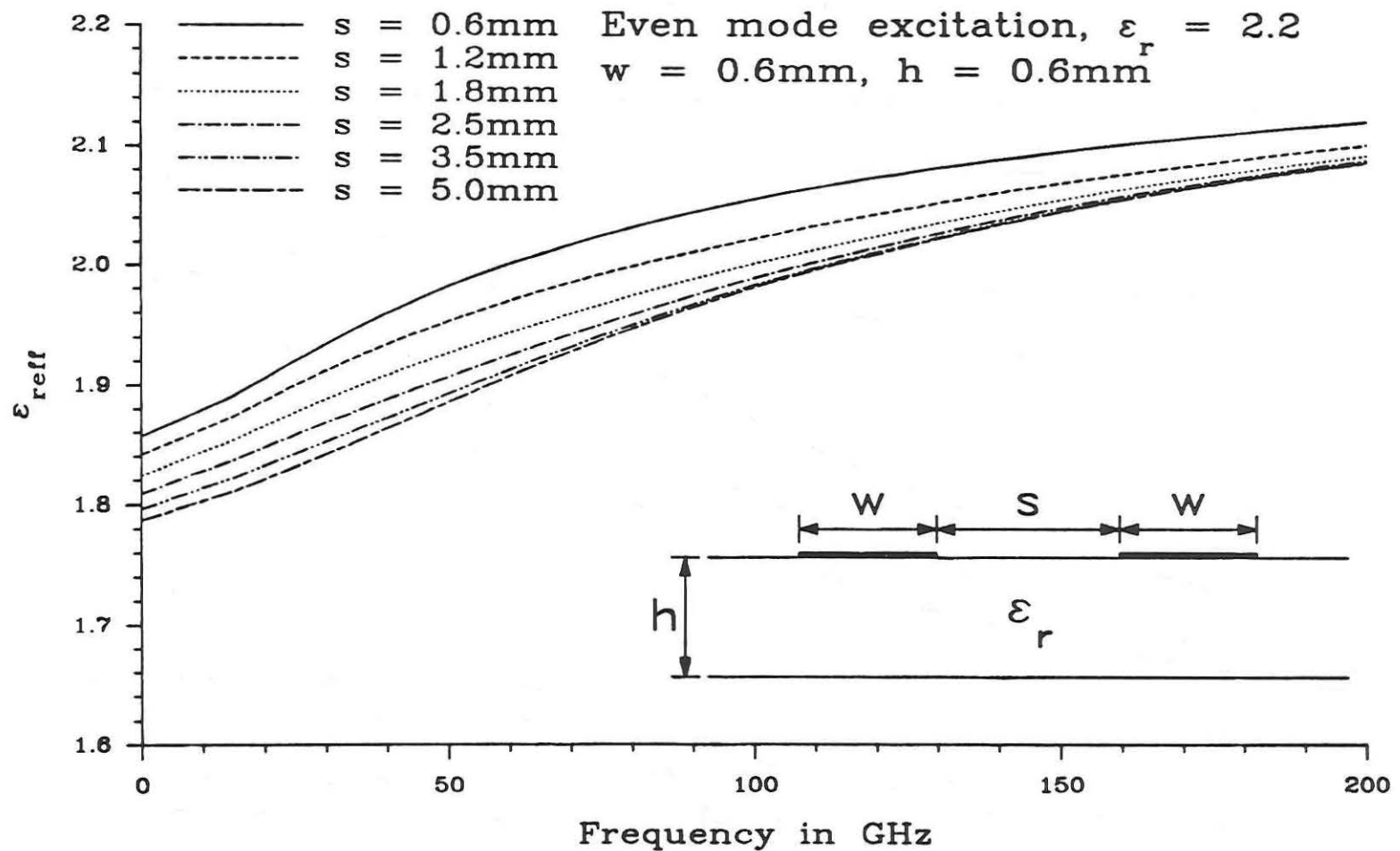
Fig. 4.1. ε_{reff} vs. frequency for open symmetric coupled microstrips on RT/duroid 5880 substrate, even mode.
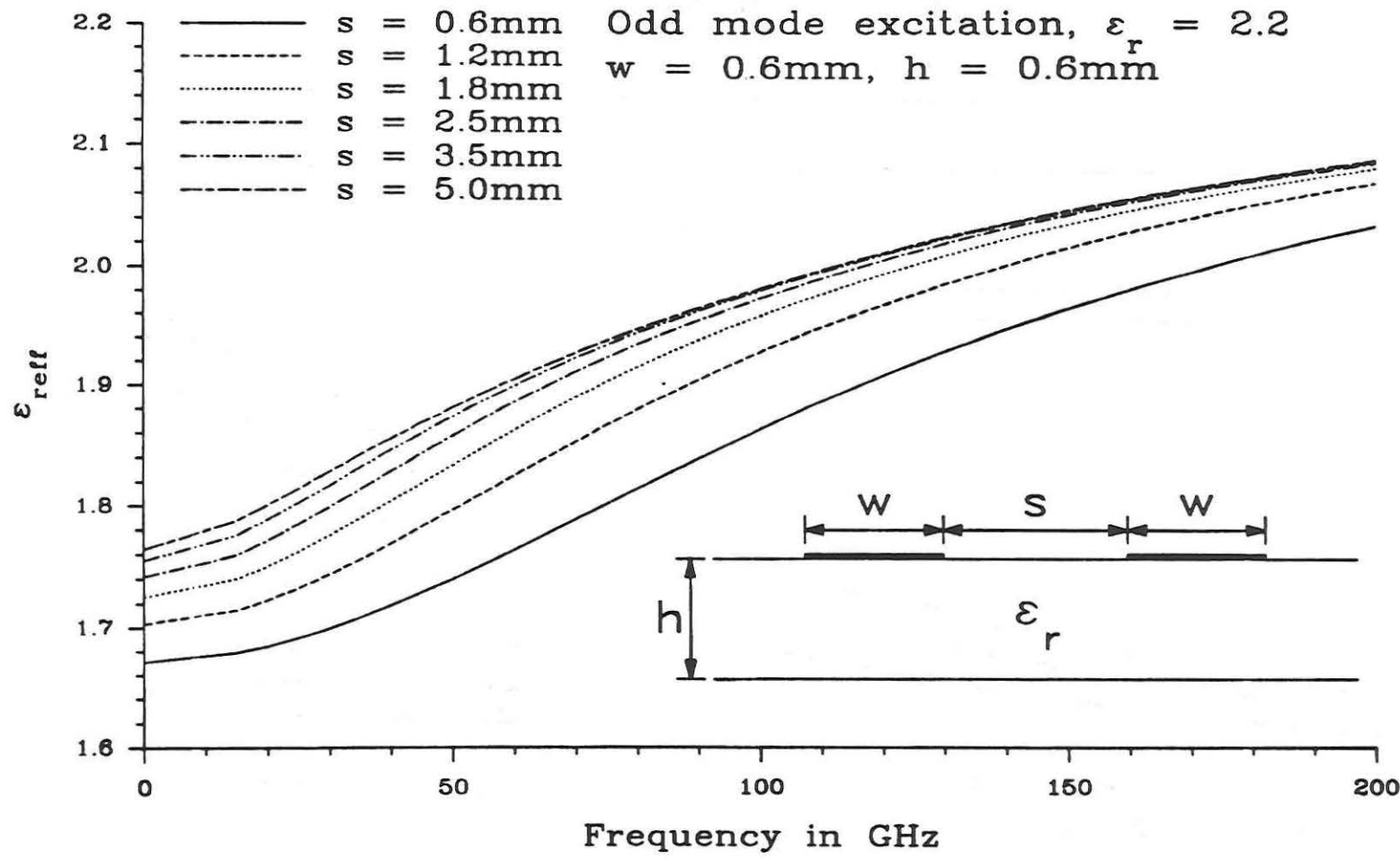
Fig. 4.2. ε_{reff} vs. frequency for open symmetric coupled microstrips on RT/duroid 5880 substrate, odd mode.
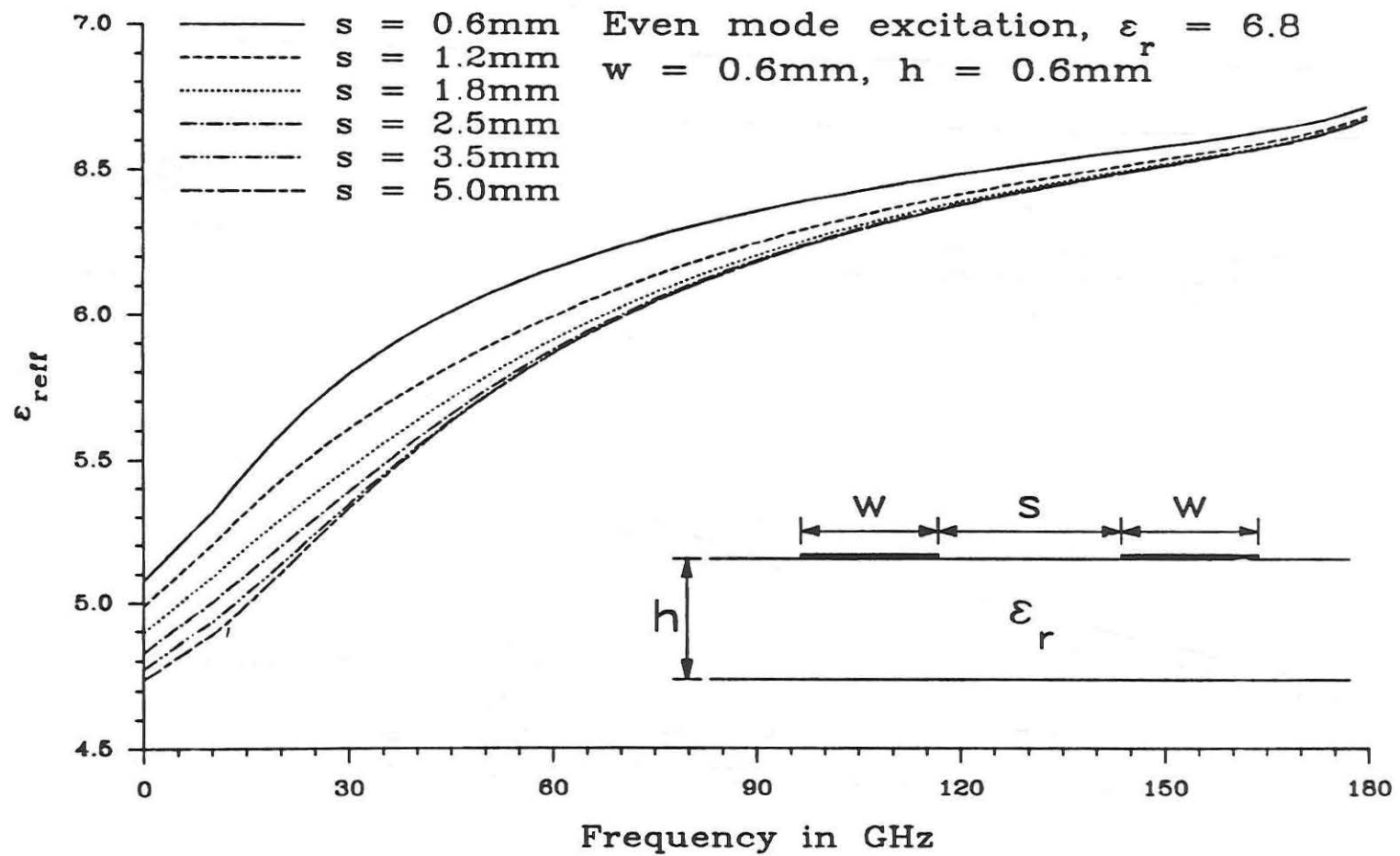
Fig. 4.3. ε_{reff} vs. frequency for open symmetric coupled microstrips on beryllium oxide substrate, even mode.
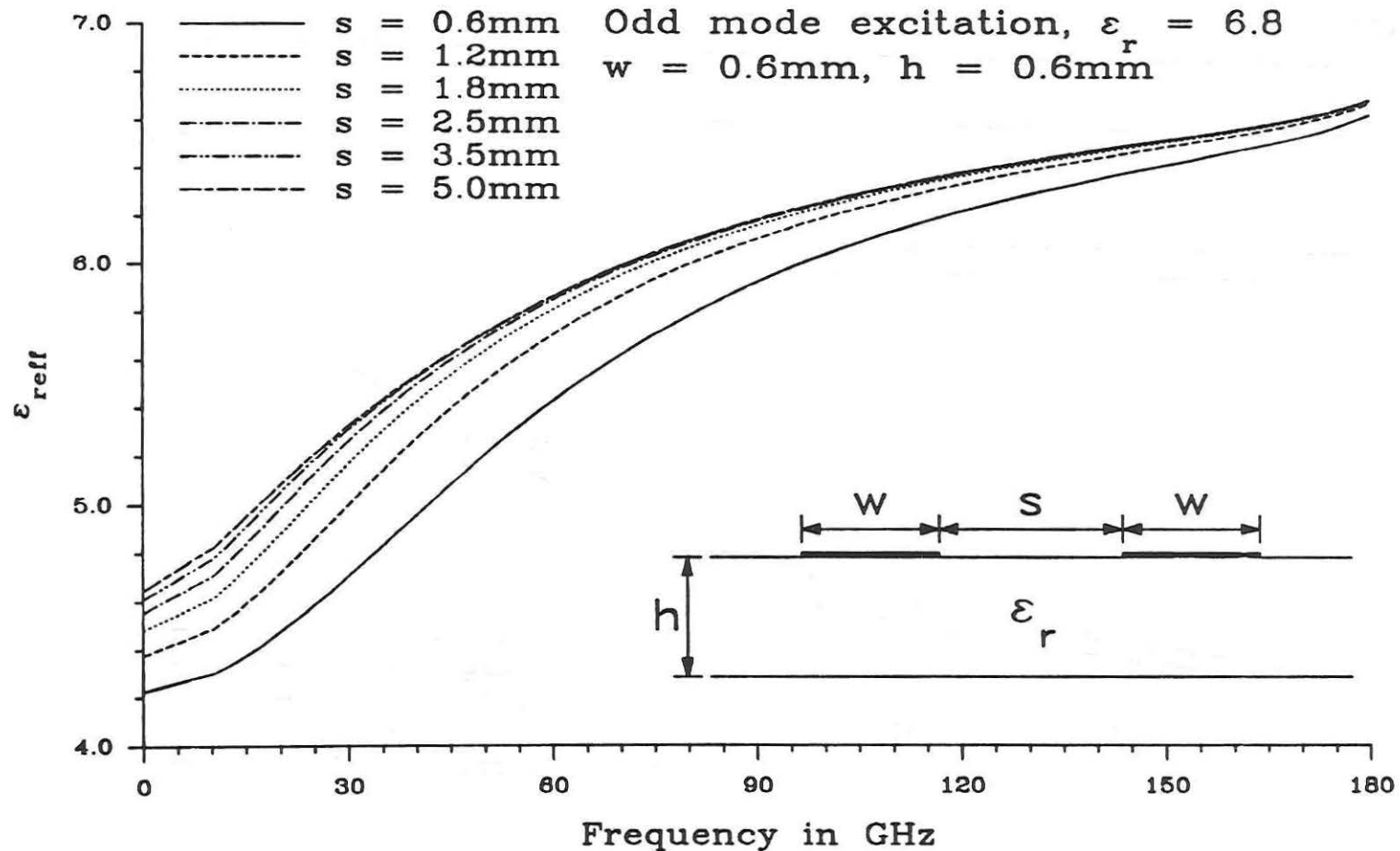
Fig. 4.4. ε_{reff} vs. frequency for open symmetric coupled microstrips on beryllium oxide substrate, odd mode.
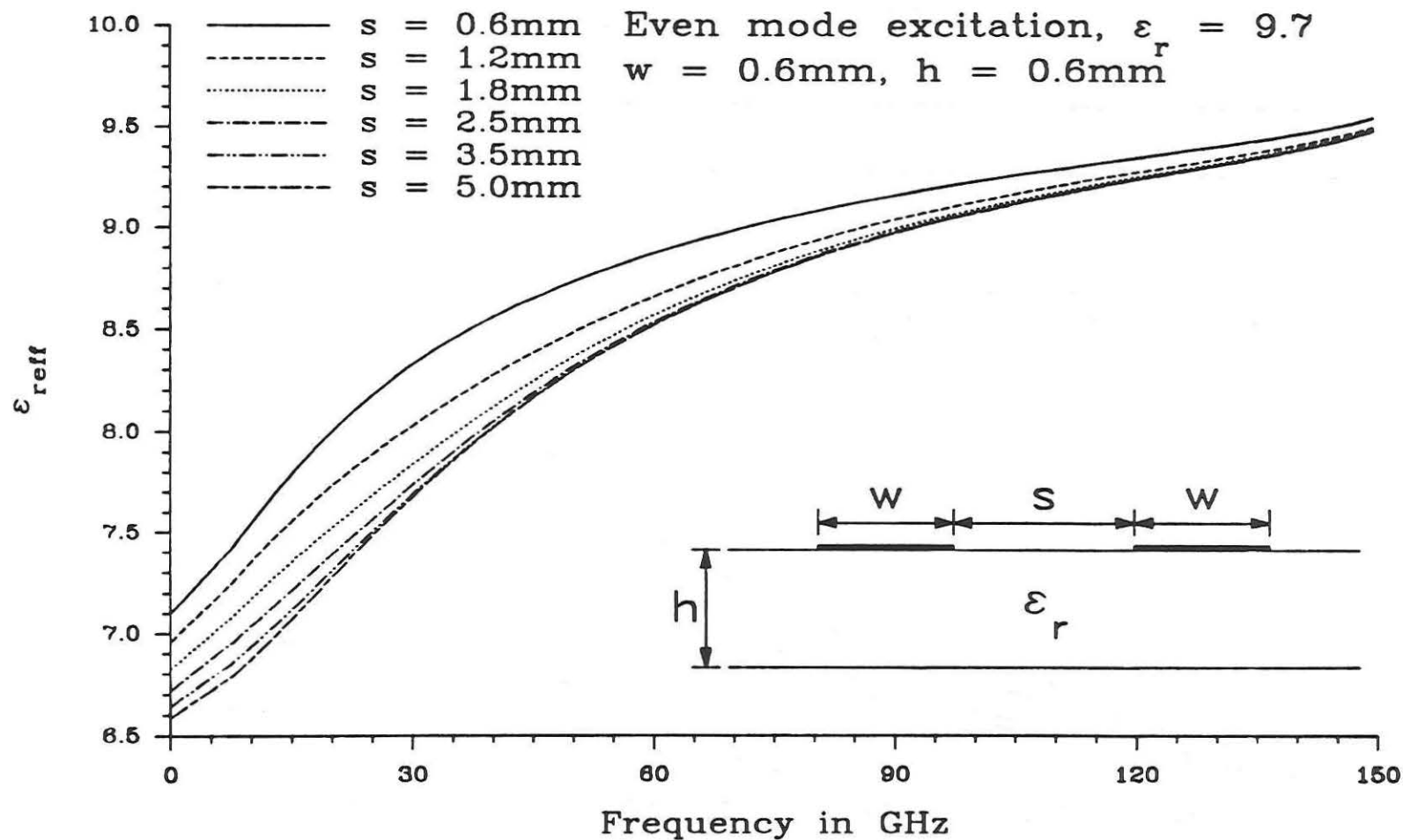
Fig. 4.5. $\varepsilon_{\text{reff}}$ vs. frequency for open symmetric coupled microstrips on alumina substrate, even mode.
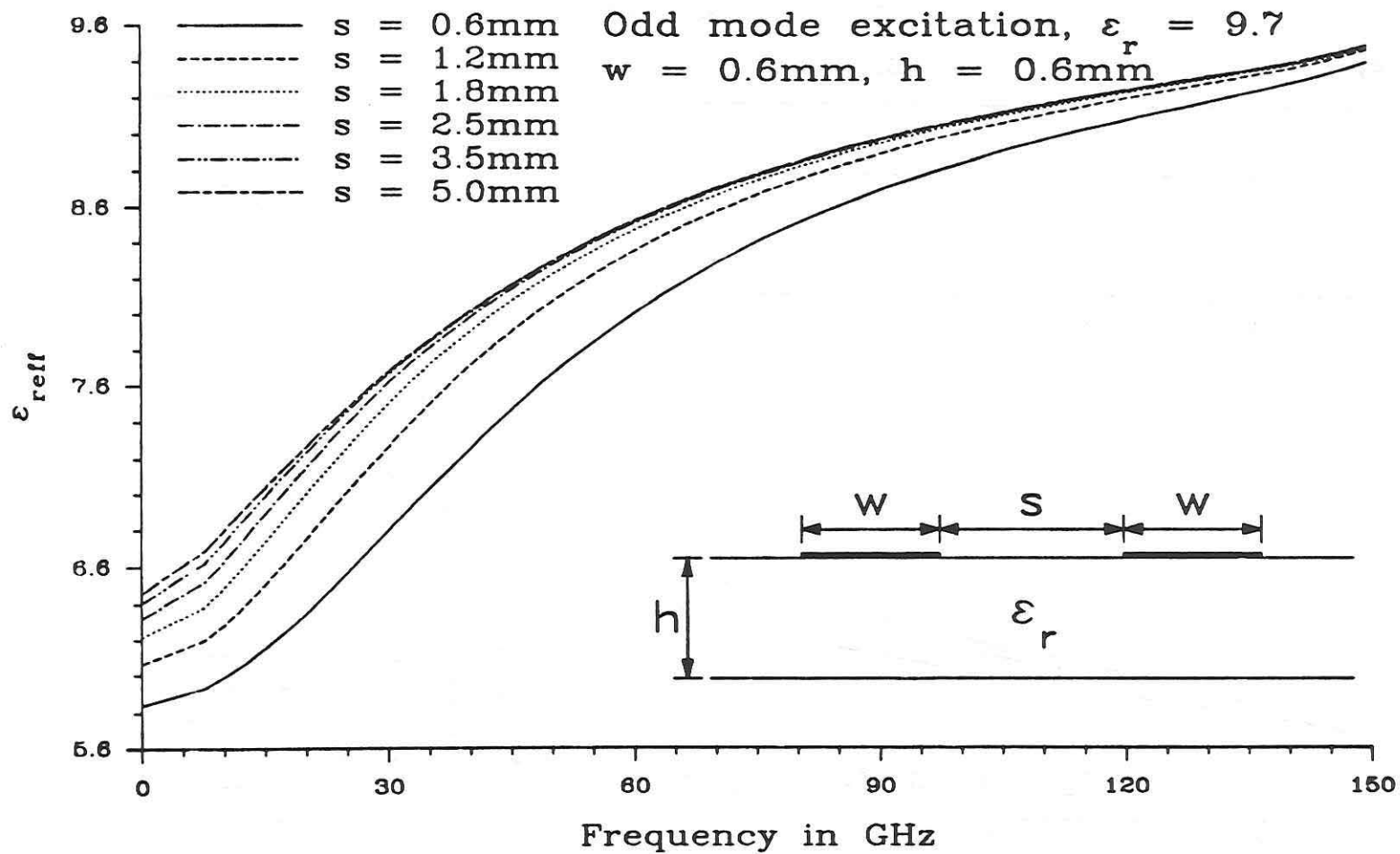
Fig. 4.6. ε_{reff} vs. frequency for open symmetric coupled microstrips on alumina substrate, odd mode.
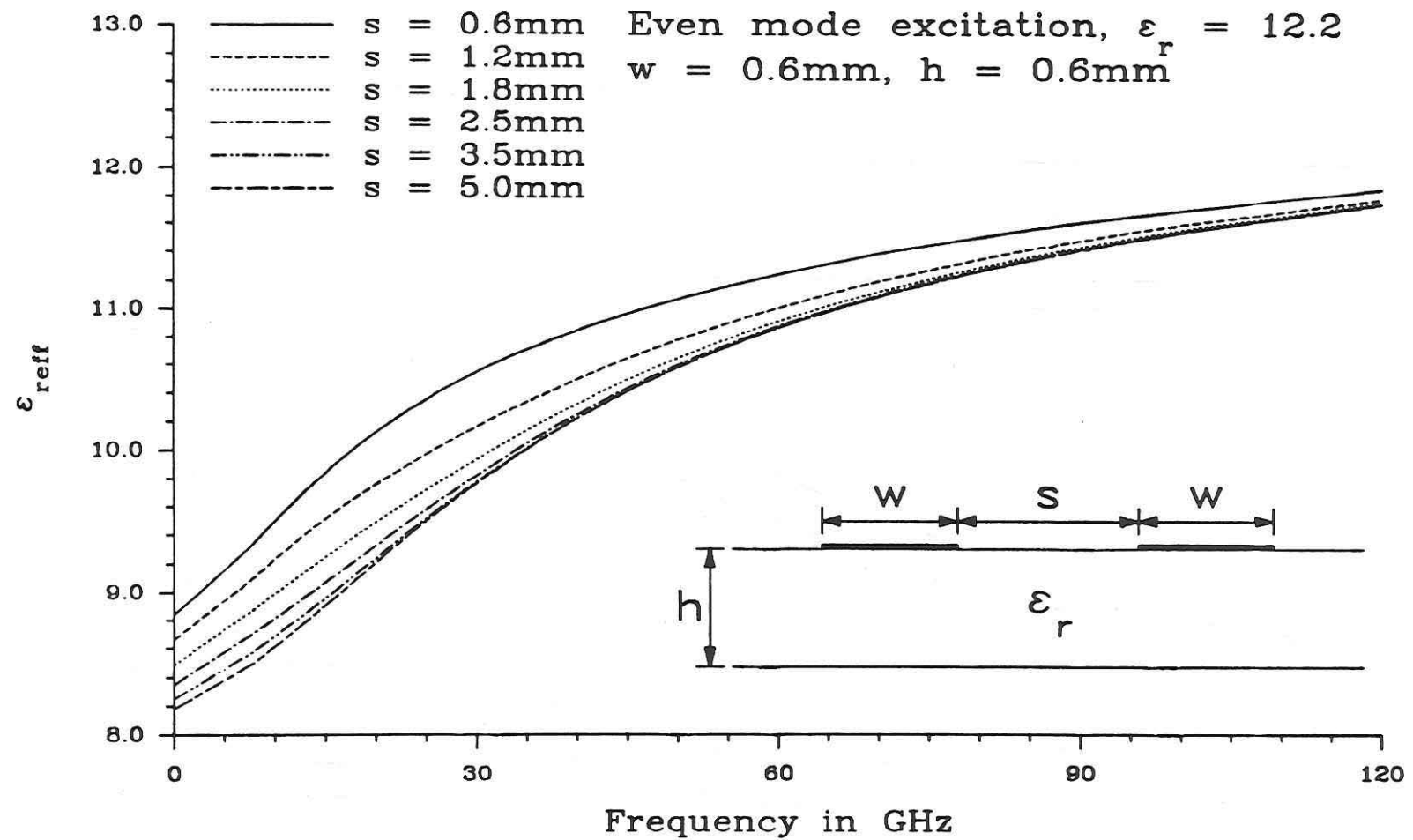
Fig. 4.7. ε_{reff} vs. frequency for open symmetric coupled microstrips on gallium arsenide substrate, even mode.
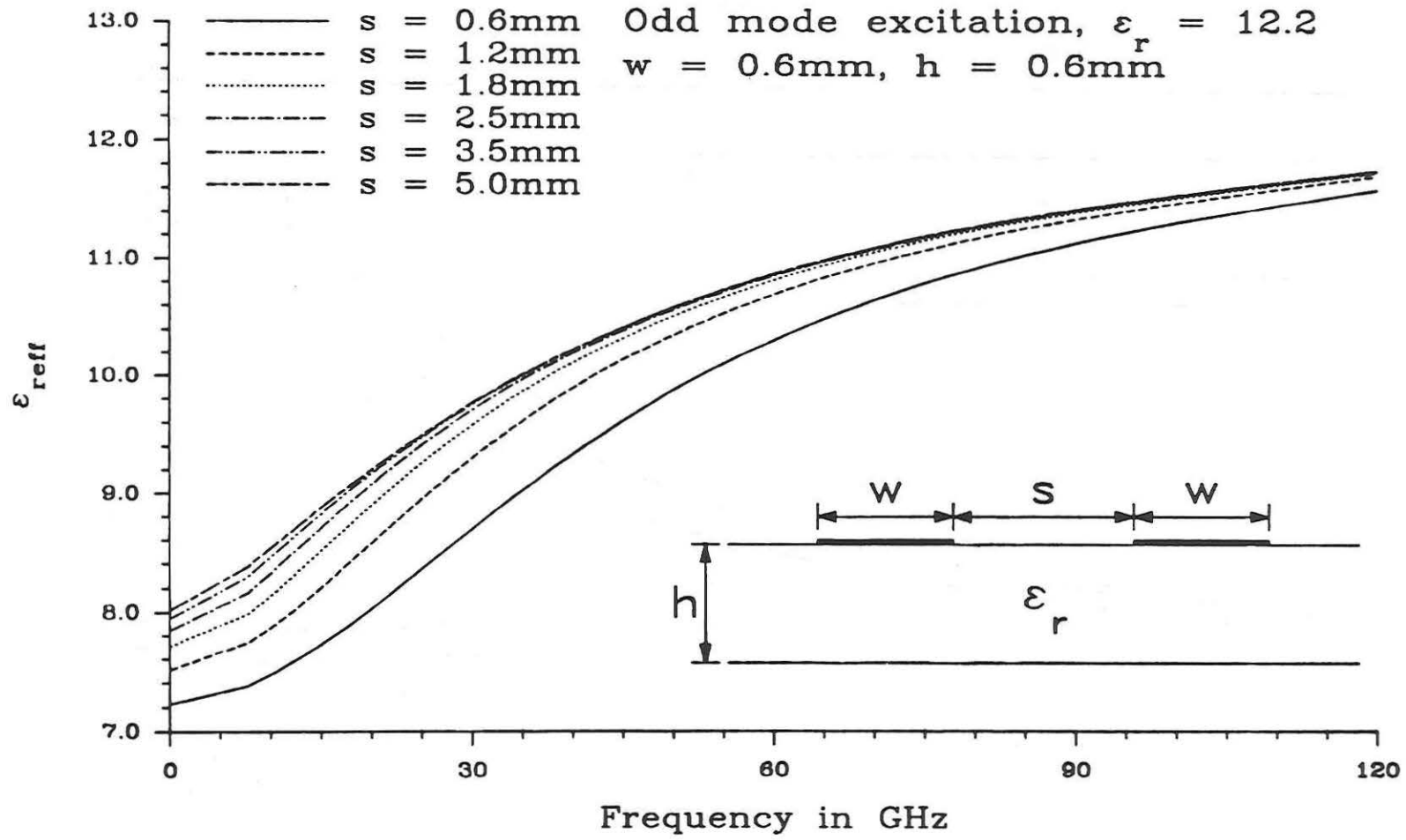
Fig. 4.8. ε_{reff} vs. frequency for open symmetric coupled microstrips on gallium arsenide substrate, odd mode.

used only when strong coupling between the lines is desired. The values for s = 5.0 mm, both even and odd mode, are very close to the values for s $\rightarrow \infty$, i.e. a single isolated microstrip, and so $\varepsilon_{re} \simeq \varepsilon_{ro}$ for this spacing. In microwave circuit design, the most common rule of thumb for designing uncoupled lines is to place them at least three center conductor widths or three substrate heights apart. For the substrate height and center conductor width of Figs. 4.1-4.8, this spacing is represented by the s = 1.8 mm graphs. The greatest difference in ε_{re} and ε_{ro} for the single layer configuration occurs when the spacing is the smallest. As the spacing increases, ε_{re} decreases in value, ε_{ro} increases, and both asymptotically approach the value of ε_{reff} for a single isolated microstrip.

As can be seen from the derivation in Chapter 3, dispersion distortion is due to the change in the phase velocity with frequency. In particular, dispersion distortion of finite time domain signals is related to the differences in the inverse of the phase velocities over the band of frequencies of interest. Since the inverse of the phase velocity is proportional to the square root of the effective dielectric constant, the amount of distortion due to dispersion is related to

$$\ell \left| \sqrt{\varepsilon_{reff}(f_1)} - \sqrt{\varepsilon_{reff}(f_2)} \right| \tag{4.2}$$

where ℓ is the distance traveled down the line, and f_1 and f_2 are the lower and upper frequencies that define the band of interest. Thus, the amount of dispersion that is acceptable depends on three factors; 1) how ε_{reff} varies as a function of frequency, 2) the bandwidth of the system and signal, and 3) the distance the pulse must travel. The least dispersive structure of the four is the RT/duroid 5880 substrate,

whose results are shown in Figs. 4.1 and 4.2, since its effective
dielectric constant changes very little, only about 0.23 from 0 to 125
GHz. The beryllium oxide, Fig. 4.3 and 4.4, and alumina substrates,
Fig. 4.5 and 4.6, are a little more dispersive than the duroid and the
gallium arsenide is the most dispersive, showing a change in ε_{reff} of
about 3.8 from 0 to 125 GHz.

While dispersion is an important consideration in the design of
MMIC's, the effects of coupling distortion and crosstalk also are a
major concern. Since both coupling distortion and crosstalk are due to
the difference in the even and odd mode phase velocities, the amount of
pulse spread due to even/odd coupling is characteristic of the amount
of pulse distortion due to coupling. From (3.24a-b) the amount of
pulse spread due to differences in ε_{re} and ε_{ro} can be written as

$$t_s(\omega) = \frac{\ell}{c}\left[\sqrt{\varepsilon_{re}(\omega)} - \sqrt{\varepsilon_{ro}(\omega)}\right] \tag{4.3}$$

where $t_s(\omega)$ is the amount of pulse spread in time for a given
frequency, ℓ is the distance traveled, and c is the speed of light.
Figs. 4.9 and 4.10 show ε_{re} and ε_{ro} as a function of frequency for the
four different substrates. As the substrate dielectric constant
increases, the separation between ε_{re} and ε_{ro} at a given frequency
increases as well. Thus the gallium arsenide substrate has a much
tighter coupling between the lines than the duroid for structures with
identical dimensions. For the single layer microstrip, the largest
difference in ε_{re} and ε_{ro} occurs at low frequencies, in the quasi-TEM
region, although this is not the case for all structures, as will be
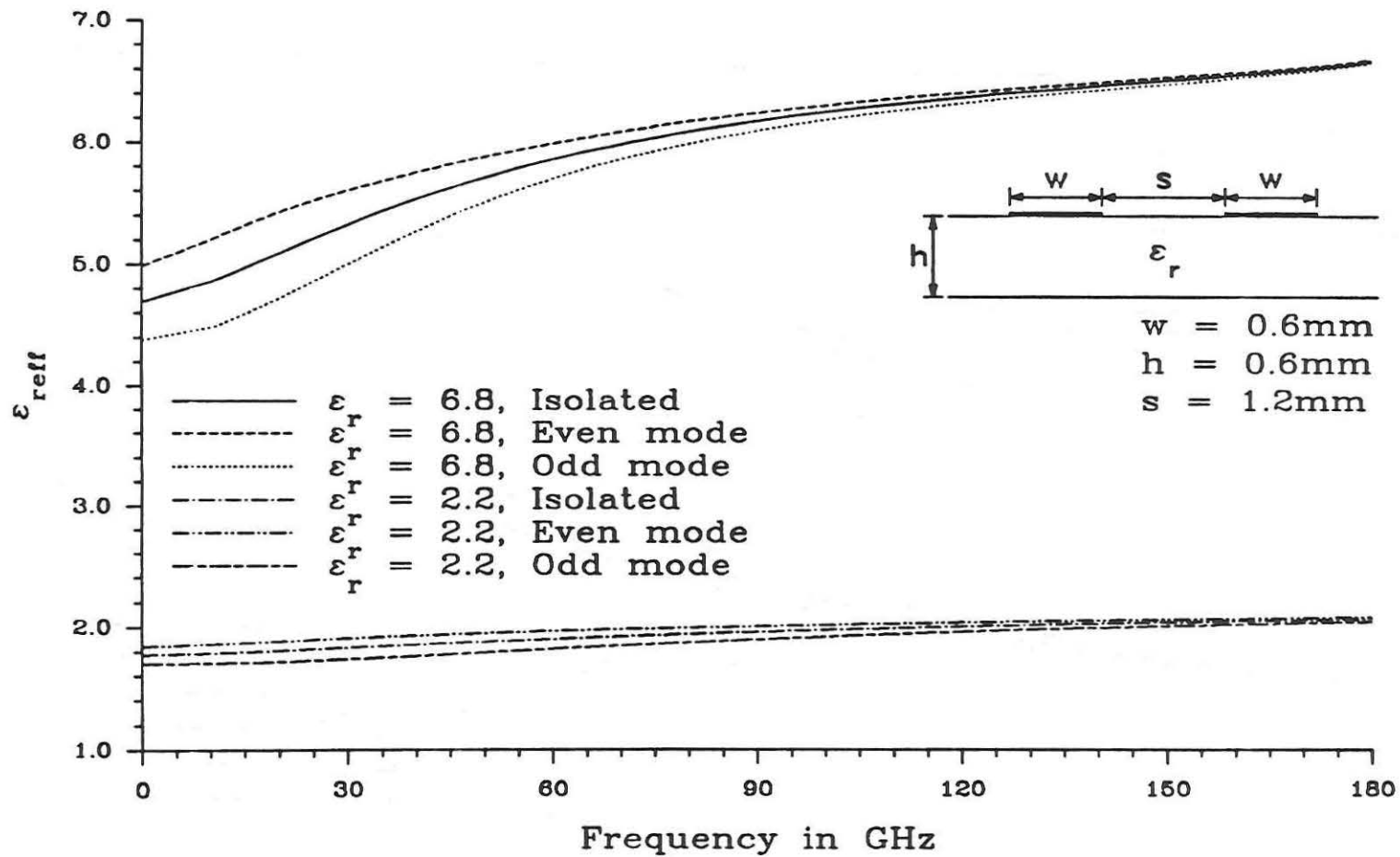
Fig. 4.9. ε_{reff} vs. frequency for open symmetric coupled microstrips on RT/duroid 5880 and beryllium oxide substrates.
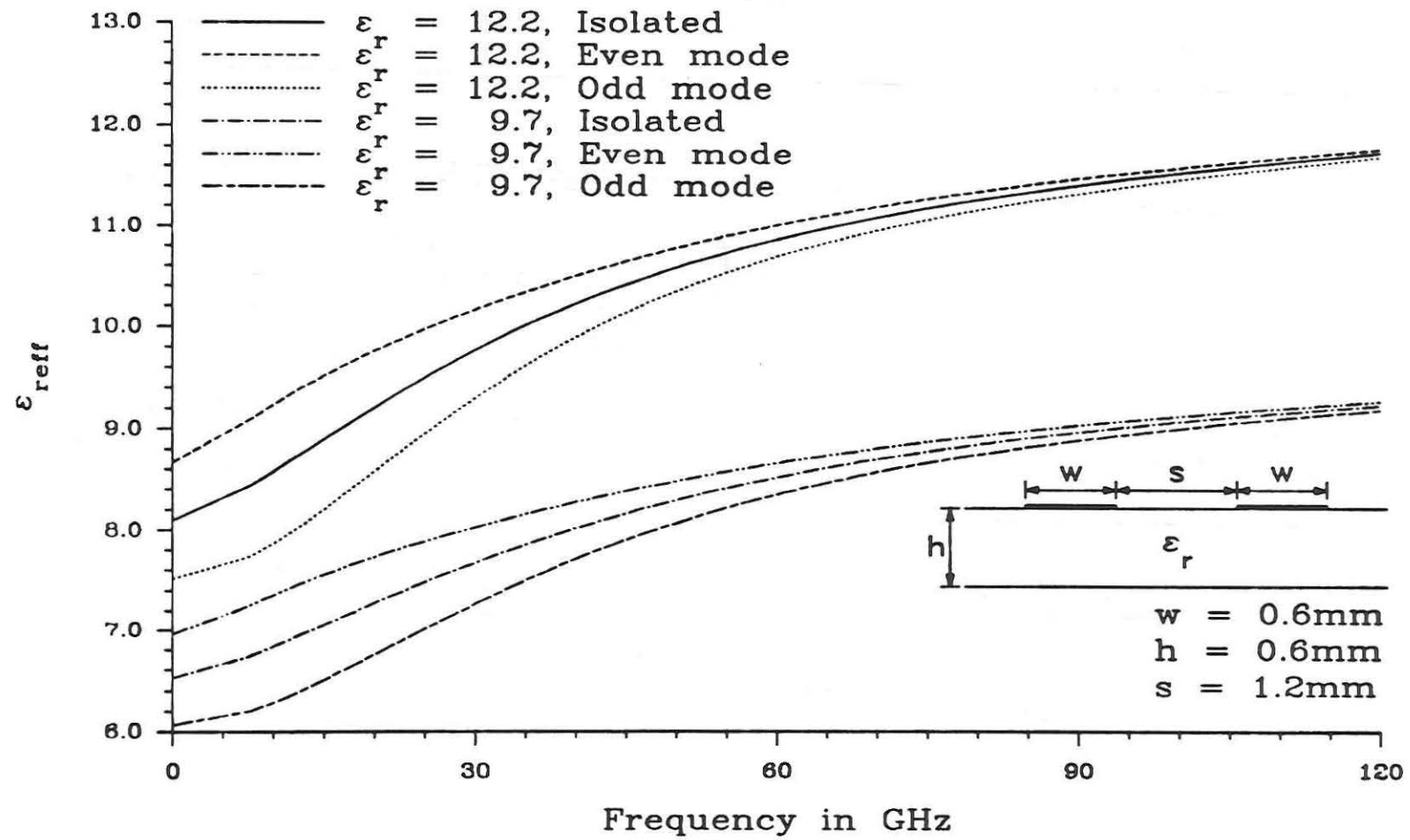
Fig. 4.10. ε_{reff} vs. frequency for open symmetric coupled microstrips on alumina and gallium arsenide substrates.

shown in section 4.3. As frequency increases, ε_{re} and ε_{ro} approach the value of ε_{reff} for the isolated microstrip.

This behavior is characteristic of all coupled microstrip structures, even multilayer ones, because as frequency increases, the electrical distance separating the coupled lines increases, decreasing the coupling and enhancing the isolation of the lines. So while dispersion is a high frequency concern, since it increases as the bandwidth of the signal increases, even/odd mode coupling is normally a low frequency phenomenon, decreasing as frequency increases. Therefore, even if the signal is narrowband and therefore would not experience significant dispersion distortion, even/odd mode distortion, however, may be an important factor in the design.

Now that the frequency dependent effective dielectric constant has been computed for the structures, pulse distortion can be considered using the Fourier transform approach. Throughout this chapter four different designations are used to refer to the time domain responses of the transmission lines; signal line, sense line, undistorted, and isolated. The undistorted designation refers to pulses that are propagated on a TEM, lossless, uncoupled transmission line whose effective dielectric constant is invariant with respect to frequency and it is equal to the zero frequency value of the structure being considered, i.e. $\varepsilon_{reff}(\omega) = \varepsilon_{reff}(0)$ for all ω. The isolated response indicates that the pulse is sent down a dispersive, lossless, and uncoupled transmission line. The effective dielectric constant for this pulse is computed using the SDA with just a single center

conductor whose width is the same as the width of either center conductor of the symmetric coupled lines.

When the signal is impressed on a coupled line, there are two time domain responses of interest, the response on the line where the signal is impressed, called the signal line, and the response on the line coupled to it, referred to as the sense line. The amount of distortion due to dispersion is shown by the difference between the undistorted and the isolated response. Distortion due to even/odd mode coupling is represented by the difference between the isolated line and the signal line waveforms, and the sense line response gives an indication of the amount of crosstalk present in the structure.

The effects of dispersion distortion and even/odd mode coupling distortion on pulse propagation are shown in Figs. 4.11 through 4.18 for different distances and substrate materials. A Gaussian pulse with an amplitude of 5 and a τ equal to 30 picoseconds is used along with a spacing, center conductor width, and substrate height of 0.6 mm. Since the pulse travels at different speeds on each substrate, the distances were scaled appropriately to have all the responses arrive at similar times and to more clearly illustrate the distortion mechanisms. Also, two distances were chosen for each pulse, in order to show how increasing distance affects both coupling and dispersion distortion.

The first structure considered, shown in Figs. 4.11 and 4.12, uses RT/duroid as the substrate material. In spite of the large distance that the input signal has traveled, it shows very little distortion due to dispersion. Even at 250 mm, the isolated and undistorted responses agree very well. Even/odd mode distortion, on the other hand, has
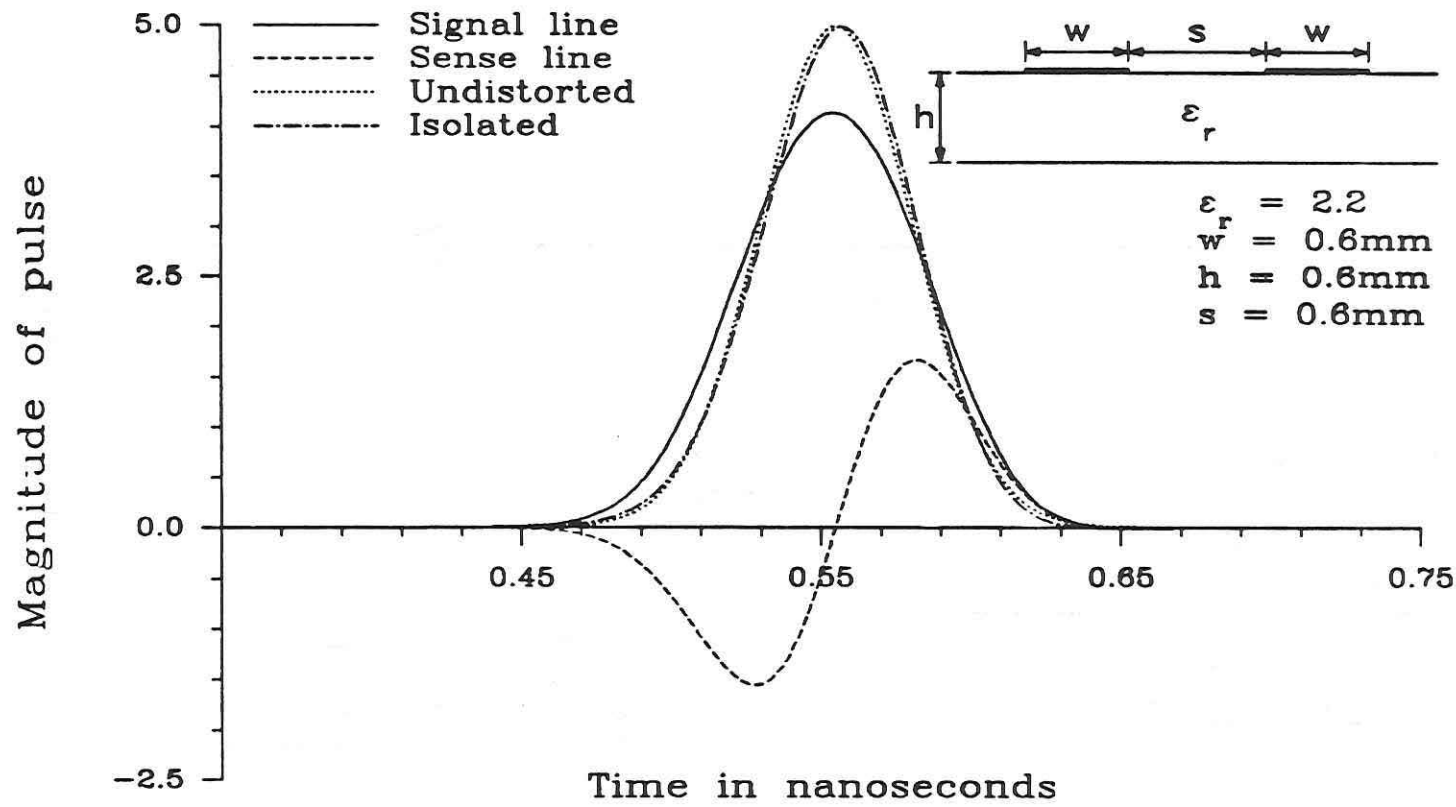
Fig. 4.11. Pulse distortion on coupled lines, s = 0.6mm, l = 125mm,
τ = 30ps, RT/duroid 5880 substrate.
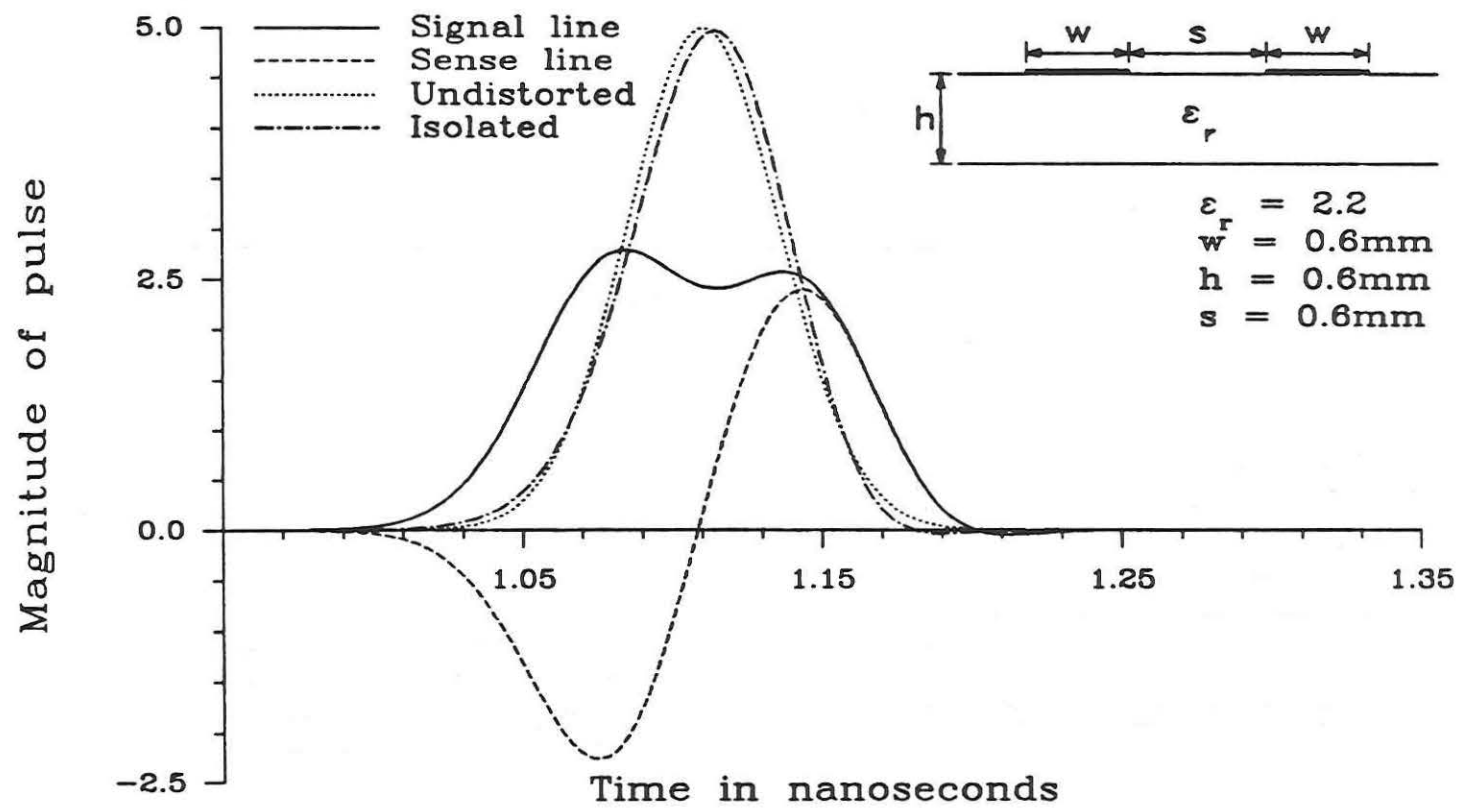
Fig. 4.12. Pulse distortion on coupled lines, s = 0.6mm, l = 250mm,
τ = 30ps, RT/duroid 5880 substrate.
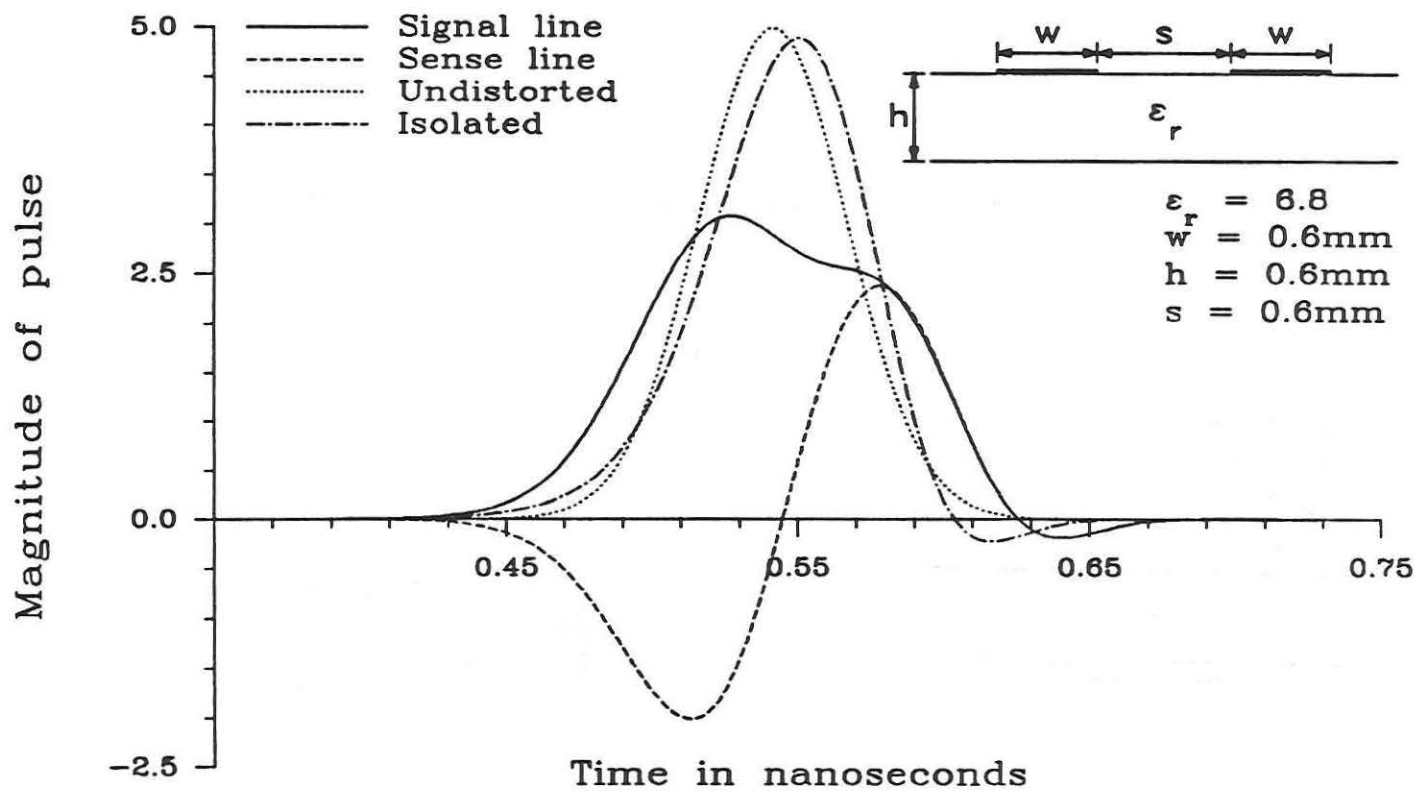
Fig. 4.13. Pulse distortion on coupled lines, s = 0.6mm, l = 75mm,
τ = 30ps, beryllium oxide substrate.
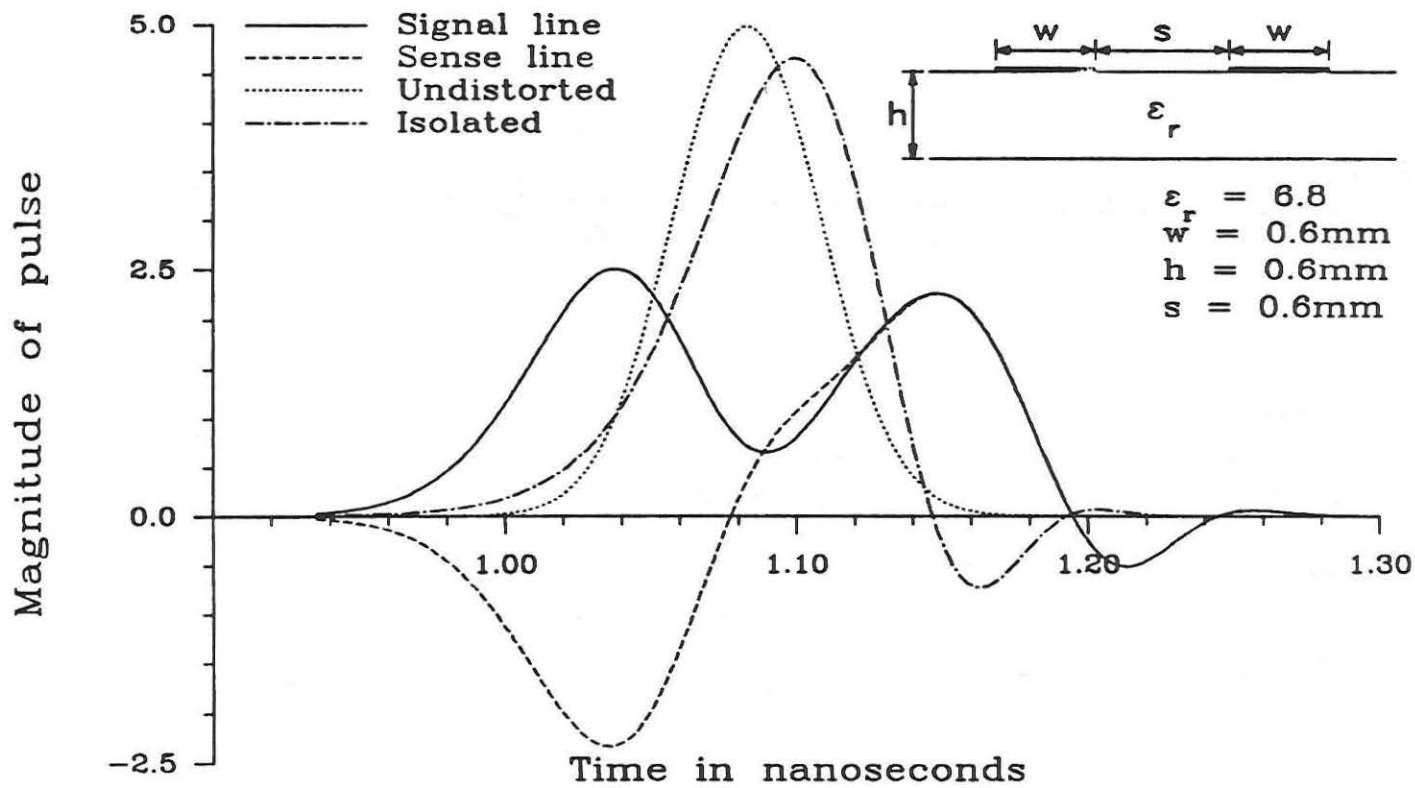
Fig. 4.14. Pulse distortion on coupled lines, s = 0.6mm, l = 150mm, τ = 30ps, beryllium oxide substrate.
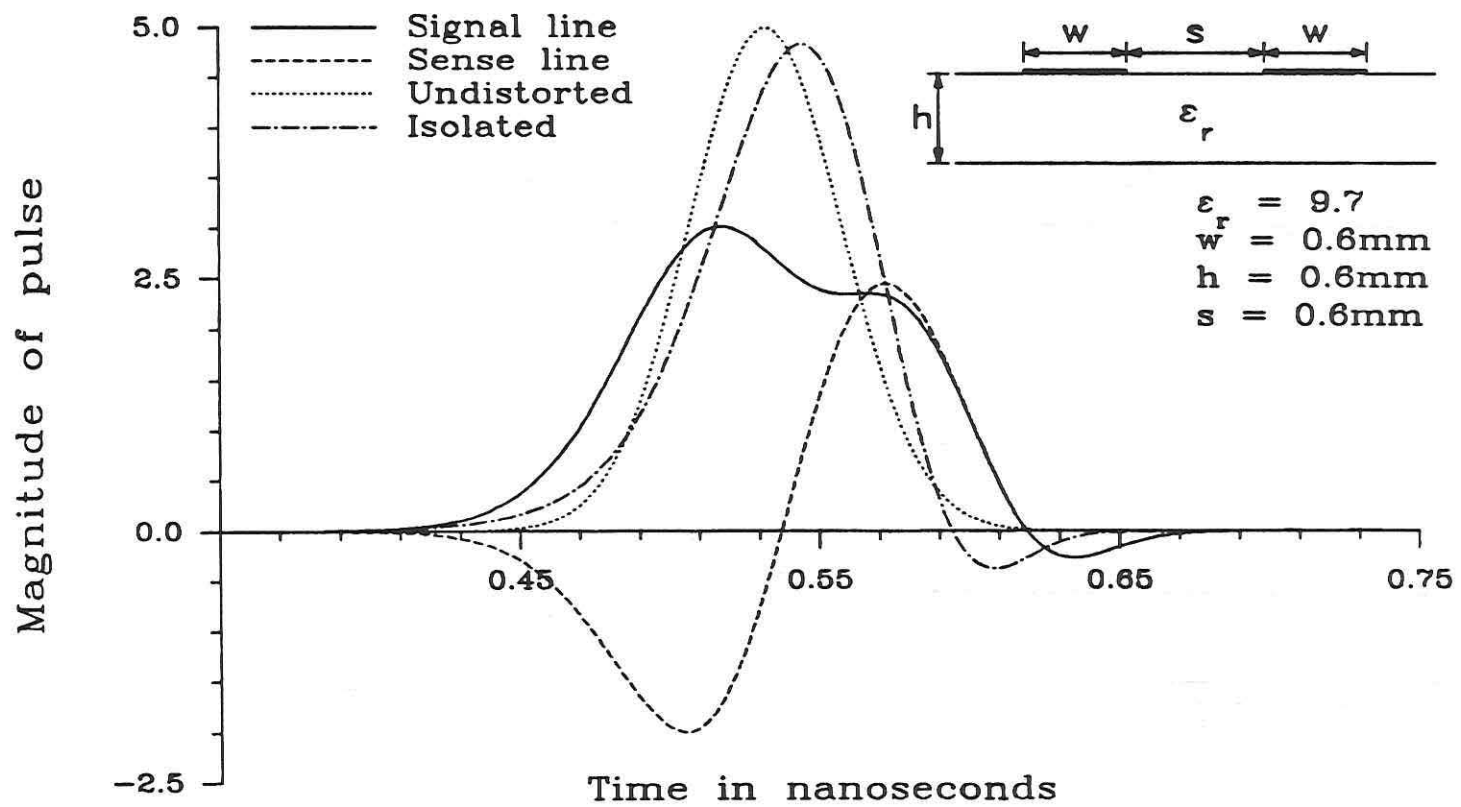
Fig. 4.15. Pulse distortion on coupled lines, s = 0.6mm, l = 62.5mm, τ = 30ps, alumina substrate.
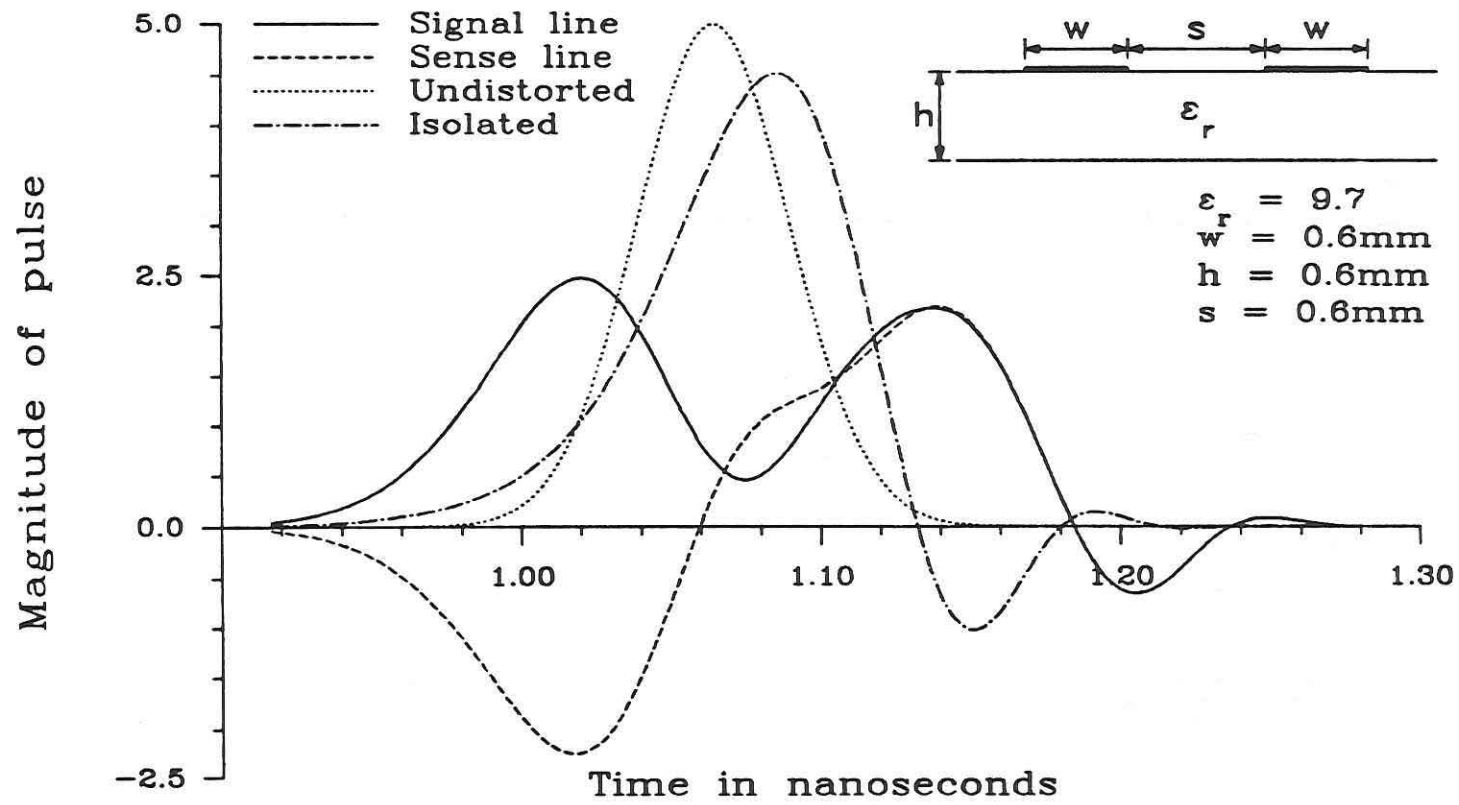
Fig. 4.16. Pulse distortion on coupled lines, s = 0.6mm, l = 125mm, τ = 30ps, alumina substrate.
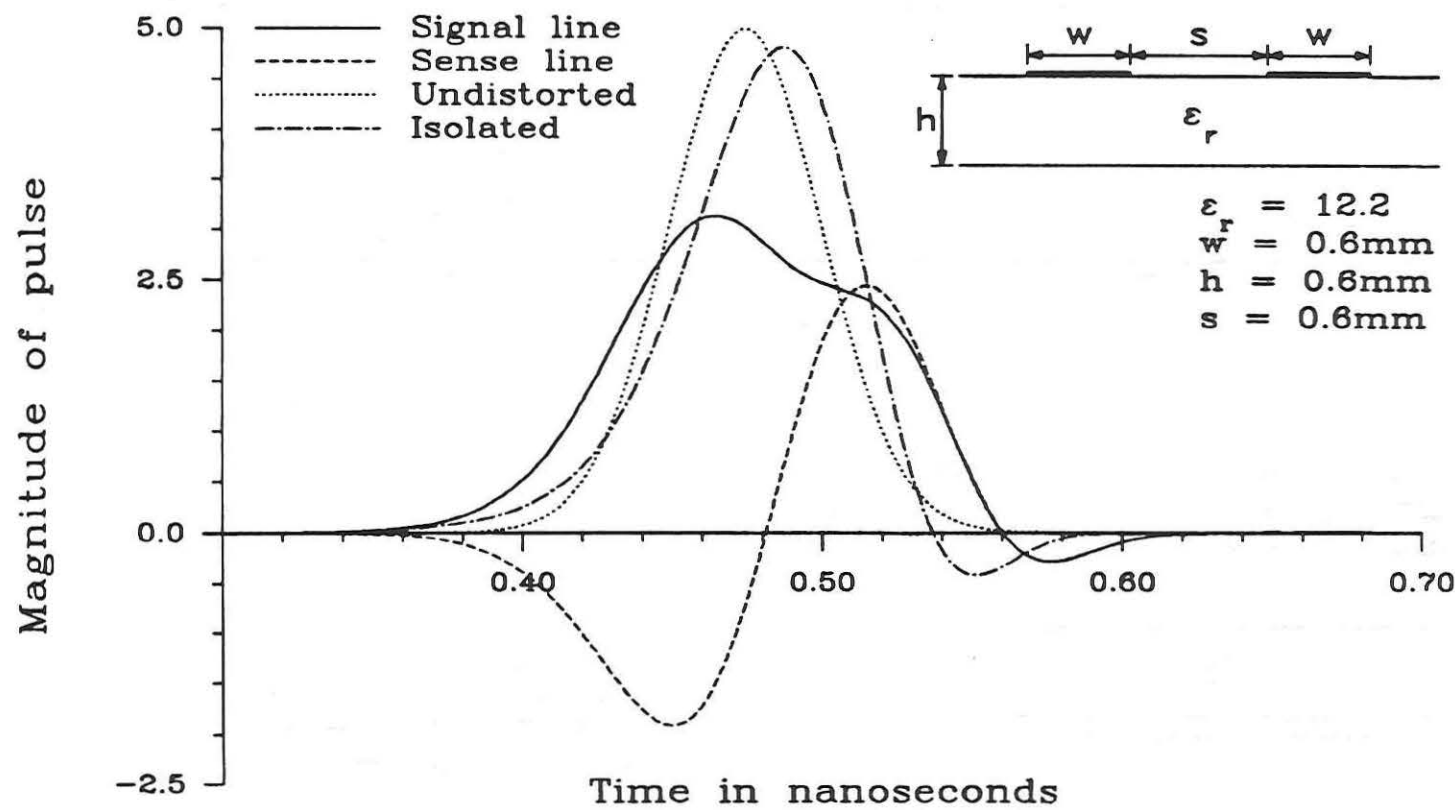
Fig. 4.17. Pulse distortion on coupled lines, s = 0.6mm, l = 50mm,
τ = 30ps, gallium arsenide substrate.
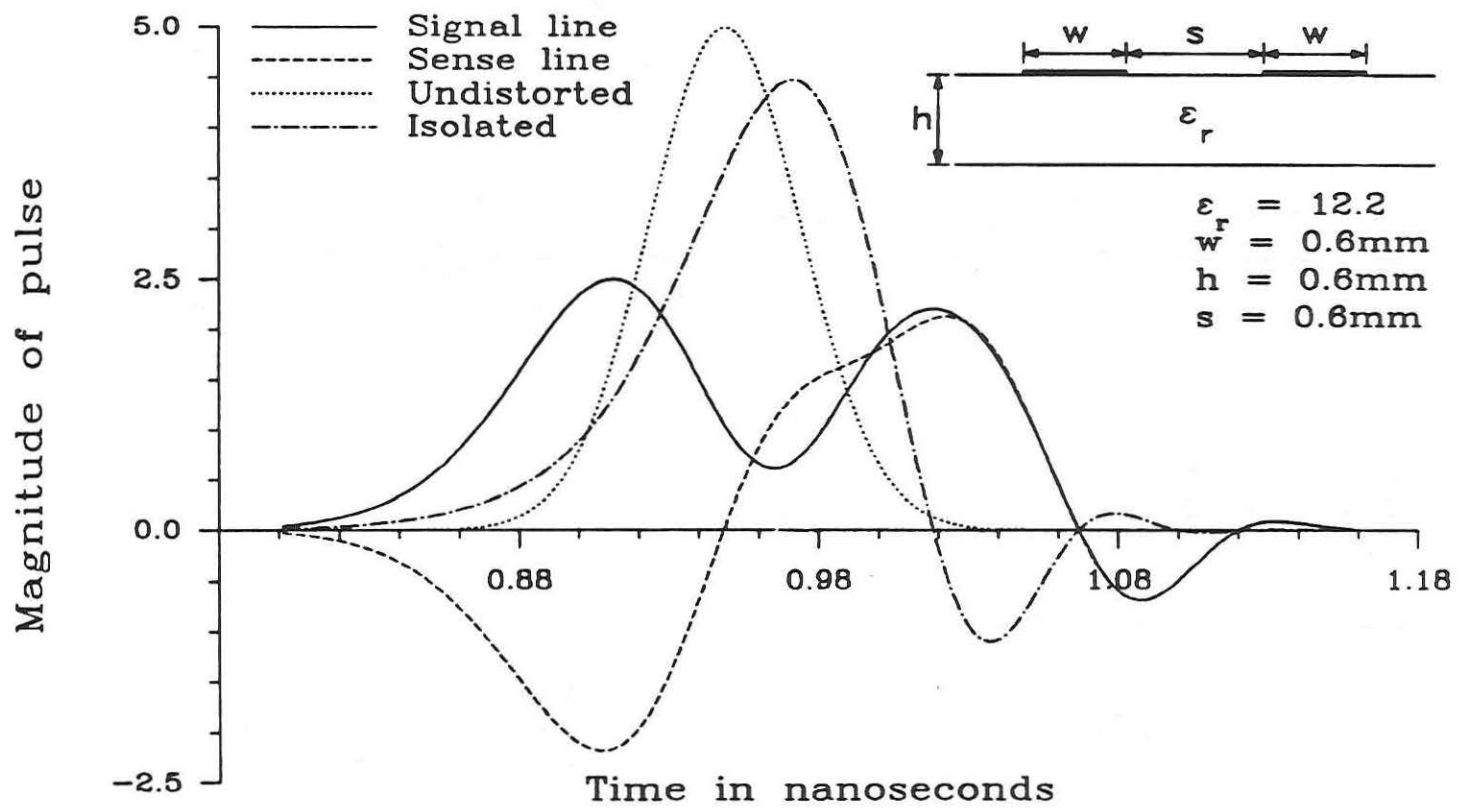
Fig. 4.18. Pulse distortion on coupled lines, s = 0.6mm, l = 100mm, τ = 30ps, gallium arsenide substrate.

significantly degraded the signal line response at just 125 mm, and shows a large response on the sense line as well. At 250 mm the signal has become almost unrecognizable and the sense line response has risen to almost the same amplitude as the signal line.

As the relative dielectric constant of the substrate increases, changing from 2.2 to 6.8 and 9.7, the effects of dispersion become more pronounced due to the greater change in the phase velocity with frequency for these structures. The beryllium oxide substrate, Figs. 4.13 and 4.14, has slightly more distortion due to dispersion, particularly at $l = 150$ mm, and even/odd mode distortion affects the pulse even more than the duroid structure did. At 150 mm, the signal line response begins to look like two separate in phase pulses and the sense line like two pulses, 180 degrees out of phase. Also, like all the pulse response graphs in this section, the leading response on the sense line is negative, indicating that the odd mode leads the even mode. In other words, the odd mode phase velocity is greater than the even mode and hence $\varepsilon_{re} > \varepsilon_{ro}$. This is characteristic of all single layer microstrip structures, but as will be shown in section 4.2, it is not necessarily true for multilayer structures. The structure with alumina substrate, Figs. 4.15 and 4.16, has results very similar to the beryllium oxide, except that the distances have decreased from 75 and 150 mm to 62.5 and 125 mm and the distortion of the pulses has increased slightly.

The gallium arsenide structure, as anticipated, has the greatest dispersion and coupling distortion of the four substrate materials. In spite of having scaled the distances down to 50 and 100 mm, there is

still significant distortion, both from coupling and dispersion. At 50mm, dispersion has shifted the pulse in time, slowing it down slightly, as well as widening it. Coupling had reduced the signal line to 70 percent of the original amplitude and has a sense line response that is almost 50 percent of the undistorted pulse. By 100 mm, both the signal and sense line responses have separated almost completely into the even and odd mode pulses. Unlike the other substrates, dispersion adds significant distortion to the pulse, reducing the amplitude by ten percent and significantly increasing the pulse width.

The effect of center conductor spacing on the transient response of the coupled transmission lines is as important as the distance considerations. Figures 4.19 through 4.26 show the effects of different line spacings on pulse distortion for the four different substrates. The signal line responses are given in Figs. 4.19, 4.21, 4.23, and 4.25 with the corresponding sense line values in Figs. 4.20, 4.22, 4.24, and 4.26. The isolated response, i.e. $s = \infty$, is not included, but is closely approximated by the $s = 5$ mm response on the signal line and by a zero response on the sense line.

As before, the structure with RT/duroid substrate, with results shown in Figs. 4.19 and 4.20, is not significantly affected by the dispersive effects of the line, but is highly susceptible to coupling distortion. At the smallest spacing, $s = 0.6$ mm, the signal line amplitude has decreased by one-half and the sense line has risen to the same magnitude as the signal line. As the spacing increases, the amplitude on the signal line increases and the sense line decreases. When $s = 1.8$ mm, the signal line response has been degraded by only 10
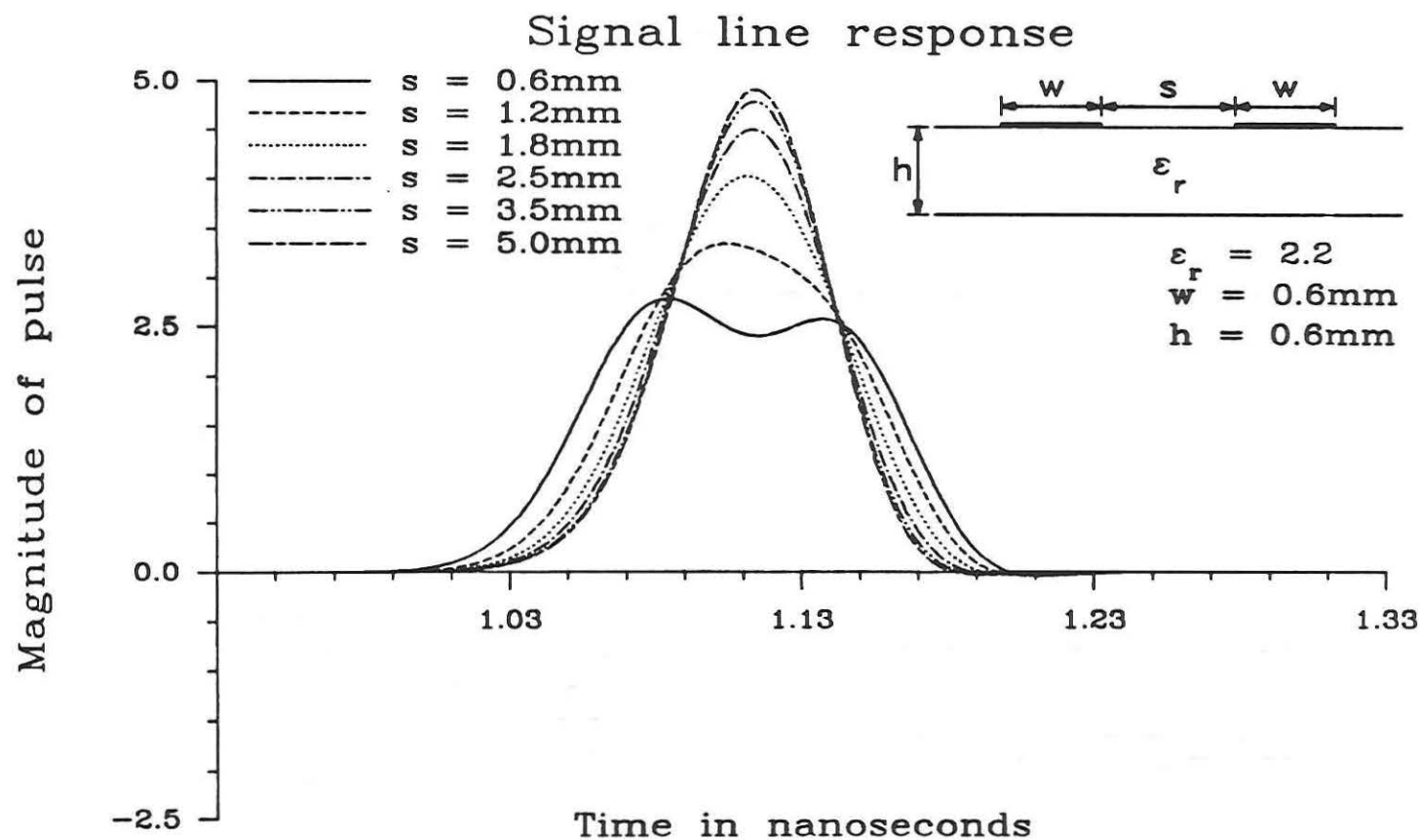
Fig. 4.19. Pulse distortion on coupled lines vs. spacing, signal line response
$l = 250$mm, $\tau = 30$ps, RT/duroid 5880 substrate.
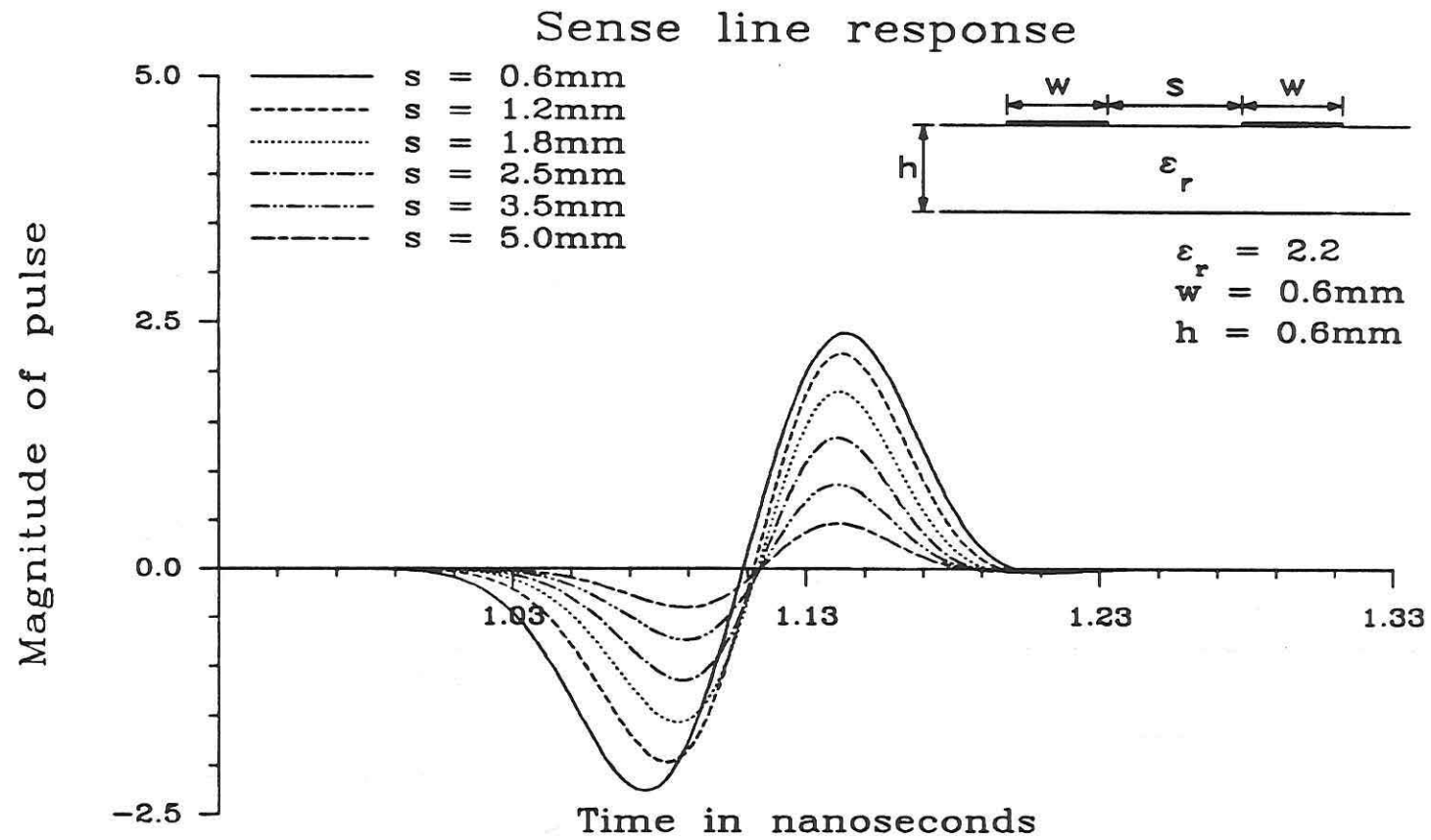
Fig. 4.20. Pulse distortion on coupled lines vs. spacing, sense line response
l = 250mm, τ = 30ps, RT/duroid 5880 substrate.

Signal line response
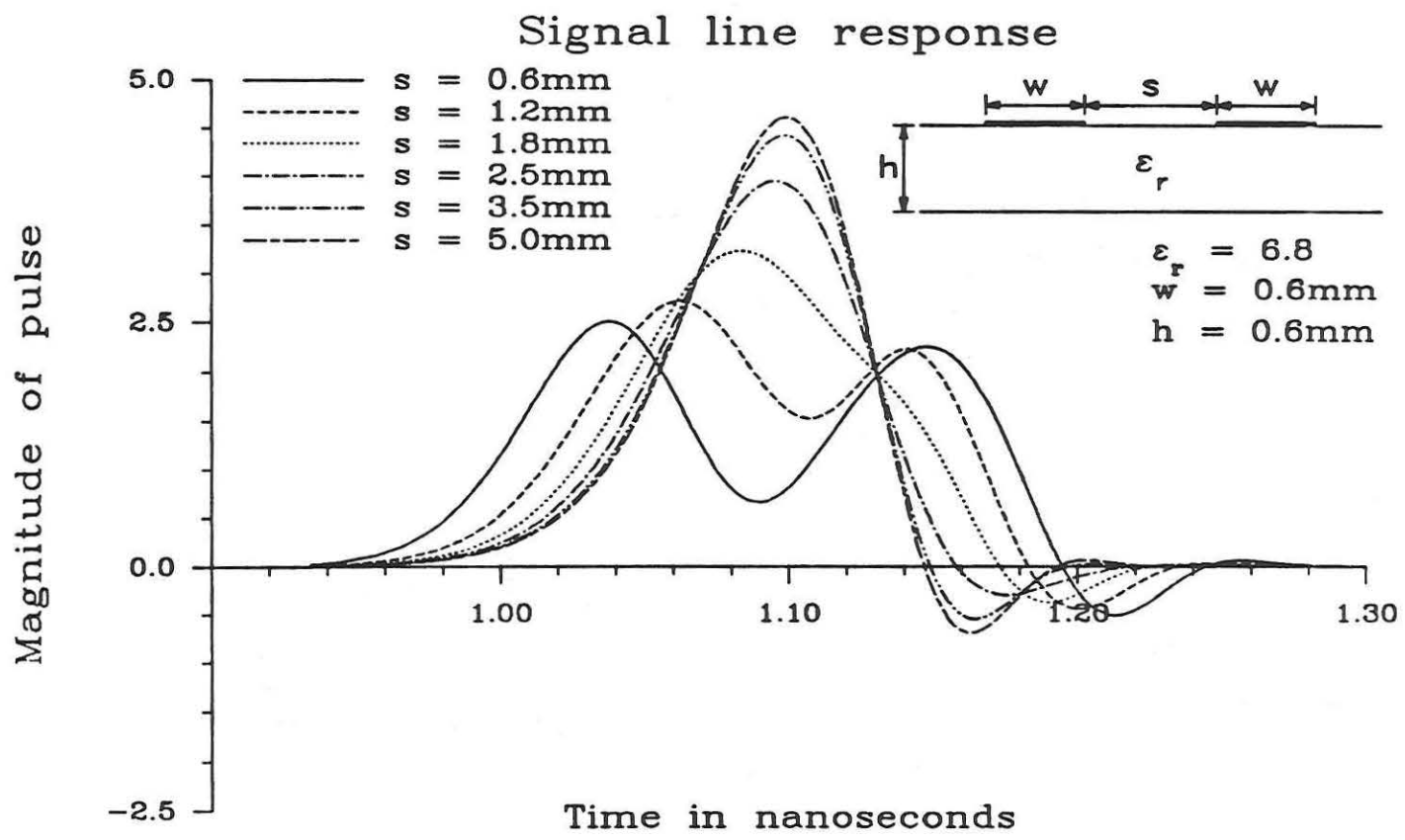
Fig. 4.21. Pulse distortion on coupled lines vs. spacing, signal line response
l = 150mm, τ = 30ps, beryllium oxide substrate.

Fig. 4.22. Pulse distortion on coupled lines vs. spacing, sense line response
$l = 150mm$, $\tau = 30ps$, beryllium oxide substrate.
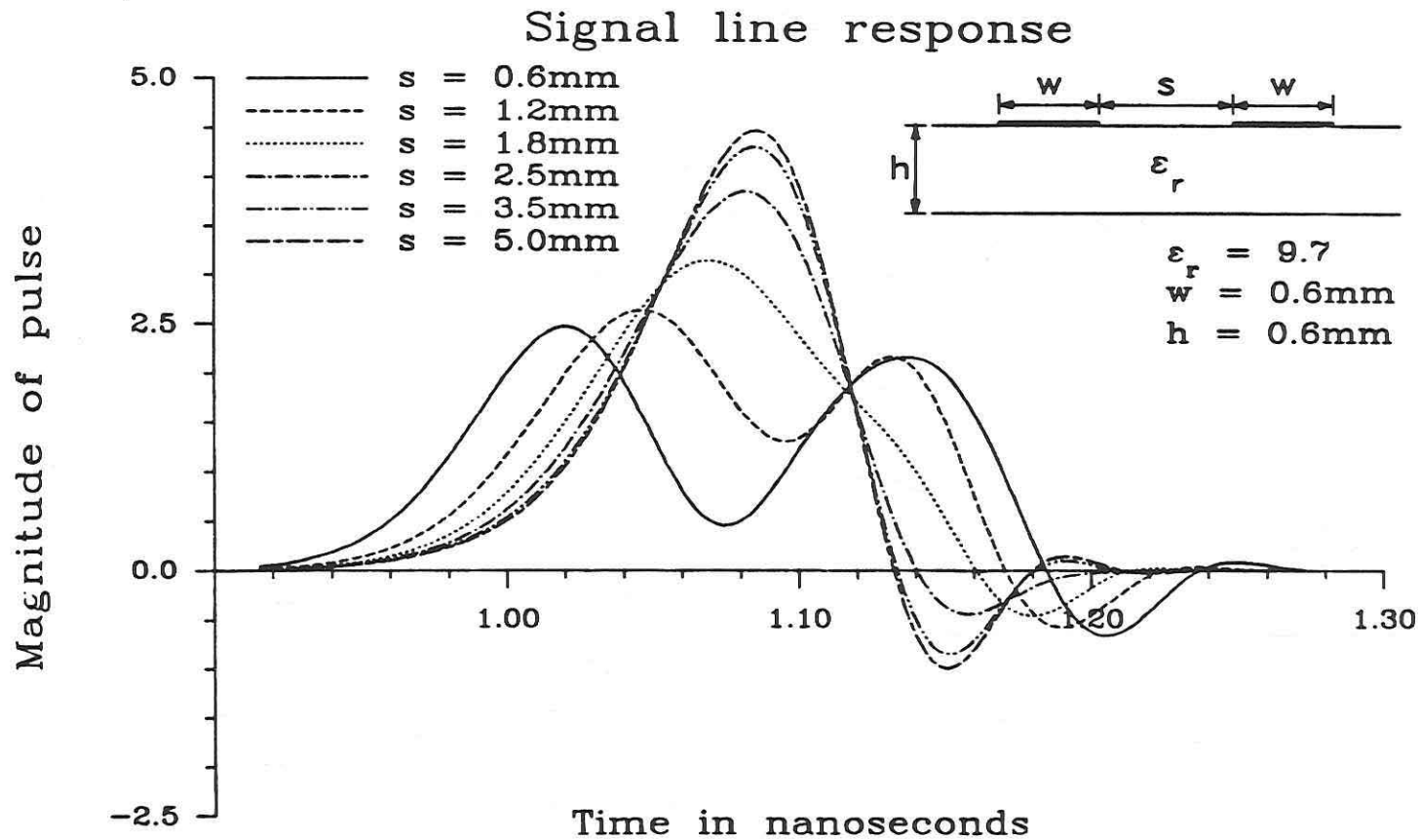
Fig. 4.23. Pulse distortion on coupled lines vs. spacing, signal line response
l = 125mm, τ = 30ps, alumina substrate.

Fig. 4.24. Pulse distortion on coupled lines vs. spacing, sense line response
$l = 125mm$, $\tau = 30ps$, alumina substrate.
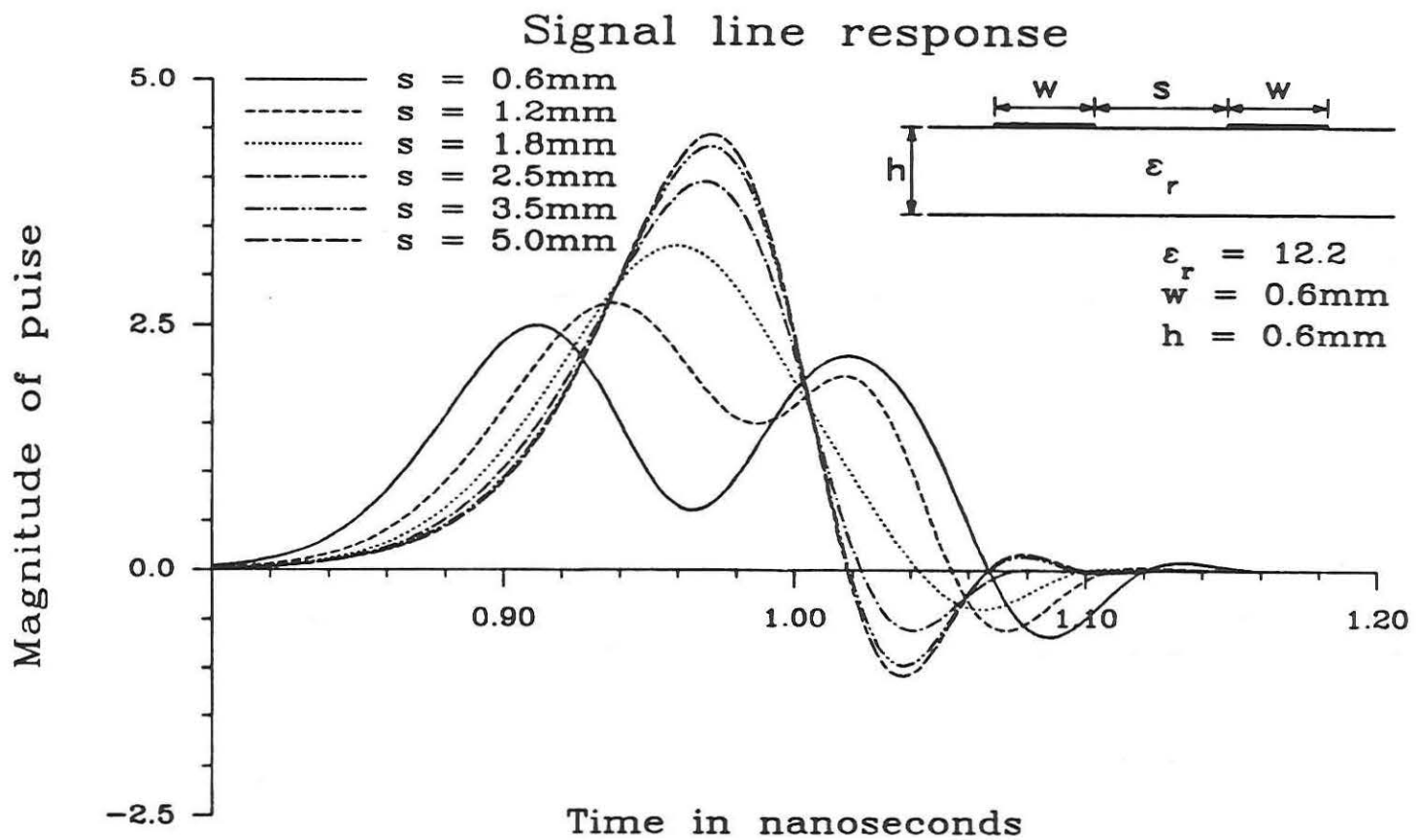
Fig. 4.25. Pulse distortion on coupled lines vs. spacing, signal line response
l = 100mm, τ = 30ps, gallium arsenide substrate.
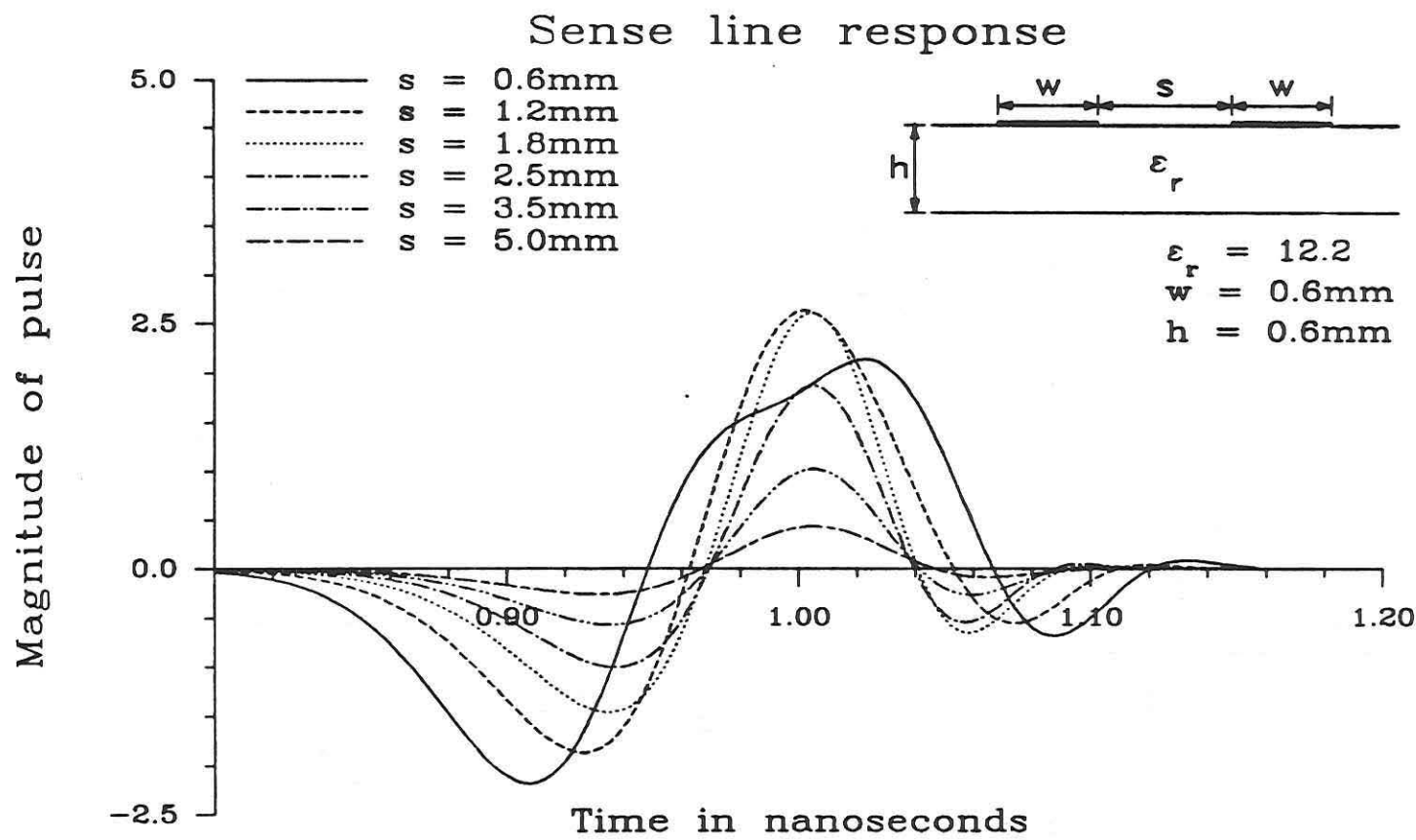
Fig. 4.26. Pulse distortion on coupled lines vs. spacing, sense line response
l = 100mm, τ = 30ps, gallium arsenide substrate.

percent, but the sense line is up to 35 percent of the initial amplitude of the input pulse. Depending on the system specification, this may be too large of a spurious signal, even though this spacing satisfies the normal design criteria.

Increasing the substrate relative dielectric constant to 6.8, Figs. 4.21 and 4.22, and 9.7, Figs. 4.23 and 4.24, increases dispersion and coupling distortion even as the distance traveled decreases. At the smaller spacings, s = 0.6 mm and s = 1.2 mm, the tighter coupling on this structure causes both the signal and sense line responses to separate into the even and odd mode pulses, i.e. two pulses in phase on the signal line, and two pulses 180 degrees out of phase on the sense line. Due to the distortion of the pulse from dispersion, the maximum positive sense line response, which is greater than one-half of the amplitude of the undistorted signal, occurs when the spacing is 1.8 mm and is slightly less for the smaller spacings. Normally, it is expected that the sense line amplitude would not exceed one-half of the input signal because, as shown in section 3.2, the magnitude of both the signal and sense line responses tend to approach one-half the original amplitude as the even and odd mode pulses separate completely.

The larger response on the sense line is a result of the increased dispersive characteristics of the line due to the higher relative dielectric constant. This can be visualized by approximating the distortion due to coupling, as in Fig. 3.2, as being a result only of the separation of the even and odd mode pulse pairs over distance due to differences in the modal phase velocity. To include the effects of dispersion, the undistorted pulse pairs in Fig. 3.2 are replaced with

one-half of the isolated line's response. This is only approximate,
because the difference in the modal phase velocity is a function of
frequency, and therefore affects each frequency component of the pulse
differently and also because the dispersive characteristics of the even
and odd modes, while being very similar, are not quite exactly the
same.

In Figs. 4.21 and 4.23, the isolated line response is
approximately the same as the s = 5.0mm graphs. In both graphs, either
ε_r = 6.8 or ε_r = 9.7, the isolated pulse has a relatively large
negative swing on the trailing edge due to the dispersion distortion.
Since the sense line response is equal to the even mode response minus
the odd mode response (eq. 3.11a), and because the odd mode leads the
even mode, the trailing negative swing of the odd mode pulse adds
constructively to the even mode pulse. This constructive interference
increases the sense line response so that it is larger than one-half of
the input signal. Therefore the maximum possible sense line response,
for a given spacing, would occur when the maximum of the negative swing
of the odd mode pulse aligns with the positive maximum of the even mode
pulse. Since the odd mode leads the even mode in this structure, there
is no possibility of constructive interference in the sense line's
negative leading response, and so it attains a maximum when the line
spacing is a minimum. Thus in order to obtain accurate predictions of
the signal and sense line responses, the dispersive characteristics of
the line, as well as the pulse spectrum must be accounted for in a
rigorous manner, such as the Fourier transform approach used in this
report.

When the relative dielectric constant of the substrate is increased to 12.2, Figs. 4.25 and 4.26, both dispersion and coupling have a significant effect on the distortion of the pulse. The signal and sense line responses on the gallium arsenide substrate are very similar to the corresponding pulse shapes for the beryllium oxide and alumina substrates, except that the pulses on the gallium arsenide structure are affected significantly more by dispersion.

The $s = 5.0$ mm graph, in which dispersion distortion is the dominant mechanism, shows a 12 percent reduction in the maximum amplitude on the signal line. In addition, the magnitude of the negative trailing swing of the signal line has risen to over 20 percent of the undistorted amplitude. Like the previous two substrate materials, the maximum positive sense line response does not occur when the spacing is the smallest but instead happens for $s = 1.2$ mm or 1.8 mm.

When $s = 1.8$ mm, the signal line response has degraded to 65 percent of the initial amplitude and the sense line response has risen to a maximum magnitude of 50 percent of the undistorted value. For most circuits, these would be unacceptable values for coupling loss and the amount of crosstalk, even though this spacing is within the three widths/heights rule of thumb. At a smaller distance, the amount of coupling will not be as great, but clearly, the allowable proximity of the transmission lines for uncoupled operation depends not only on the spacing of the center conductors, but also the substrate materials, structural dimensions, and the distance over which the lines are coupled to each other. In general, for single layer microstrips,

relatively short distances and/or small dielectric constants allow smaller spacings while longer distances and/or larger dielectric constants require larger spacings.

Using the Spectral Domain Approach to determine the line parameters and the even/odd mode formulation with the Fourier transform approach to compute the time domain results, the transient analysis of coupled lines has been analyzed, showing the effects of both dispersion and even/odd mode coupling distortion. First, the frequency dependent ε_{reff} of the coupled lines were presented for both the even and the odd modes with different line spacings and substrate materials. These results were then used to examine pulse distortion on tightly coupled lines at different distances, showing how both dispersion and even/odd mode coupling distort the input pulse and produce a spurious response on the adjacent line. Next, pulse distortion was studied as a function of the spacing between the center conductors. This analysis showed how the dispersive characteristics of the lines can cause constructive interferences on the sense line, giving a larger response than anticipated. In addition, these results showed that not only the separation of the center conductors needs to be considered in designing decoupled lines, but equally important factors are; the substrate material, structural dimensions, and the distance over which the lines are close to each other.

4.2 Multilayer Structures

The desire to improve the performance of MMIC's and the increasing interest in them has created a demand for the accurate characterization

of multi-layer structures, and therefore requires the use of rigorous analytical techniques. The desire to equalize the even and odd mode phase velocities in coupled lines, as well to limit the space requirements, have made multilayer structures attractive for many applications as well. A full wave analysis is necessary because the addition of either substrates or superstrates produces significant changes in the frequency dependent parameters that cannot be predicted accurately by quasi-static or other approximate formulations.

This section uses the generalized Green's function in conjunction with the SDA to compute the frequency dependent parameters of both single and coupled lines for multilayer structures. First the effective dielectric constant is computed as a function of frequency for different combinations of substrate materials and heights to illustrate the effect of the addition of substrates on the line's performance. Next a superstrate of varying height with the same relative dielectric constant as the substrate is added to an open coupled line structure to consider the effects of superstrates. Then as the height of the superstrate layer is fixed, an upper ground plane is introduced, and the ε_{reff} for the isolated, even, and odd mode cases is plotted as the height of the ground plane is varied. Finally, an open symmetric coupled line structure with two substrates is used to show how exchanging the two relative dielectric constants of the substrates changes both ε_{reff} and pulse propagation when all other dimensions are held constant.

Increasing the number of layers, either substrates or superstrates, can create a significant difference in the effective

dielectric constant. An open single microstrip with two substrates is used in Figs. 4.27 through 4.30 to illustrate the effects of these additional substrates. The total substrate height is held constant and six different combinations of h_{L2} and h_{L1} are used. The $h_{L2} = 0.6$ mm graph represents a single substrate structure with a relative dielectric constant of ε_{rL2}. Likewise the $h_{L2} = 0.0$ mm graph also represents a single substrate line, but with a relative dielectric constant of ε_{rL1}. The other graphs represent two substrate structures where the heights of the substrates are h_{L2} and h_{L1}, with relative dielectric constants of ε_{rL2} and ε_{rL1}, respectively.

The effective dielectric constant begins at the single layer value for ε_{rL1} when $h_{L2} = 0.0$ mm, or zero percent of the total height. Since the dielectric substrate being added has a lower relative dielectric constant than the substrate already present, as h_{L2} increases, ε_{reff} begins to decrease. The h_{L2} values of 0.1, 0.25, 0.35, and 0.5 mm represent, respectively, changes of 16.6, 41.6, 58.3 and 83.3 percent. When $h_{L2} = 0.6$ mm, or 100 percent of the total height, ε_{reff} is identical to the single layer value for ε_{rL2}. Thus the expectation is that ε_{reff} will decrease monotonically as h_{L2} increases and the total change in ε_{reff} at a given frequency will be equal to

$$\Delta\varepsilon_{reff}(f) = \varepsilon_{reff}^{L1}(f) - \varepsilon_{reff}^{L2}(f) \tag{4.4}$$

where the L1 and L2 superscripts indicate that ε_{reff} is evaluated for a single substrate microstrip with a relative dielectric constant of ε_{rL1} and ε_{rL2}, respectively.

The first structure, with its results shown in Fig. 4.27, consists of a layer of RT/duroid on top of a layer of beryllium oxide. At low
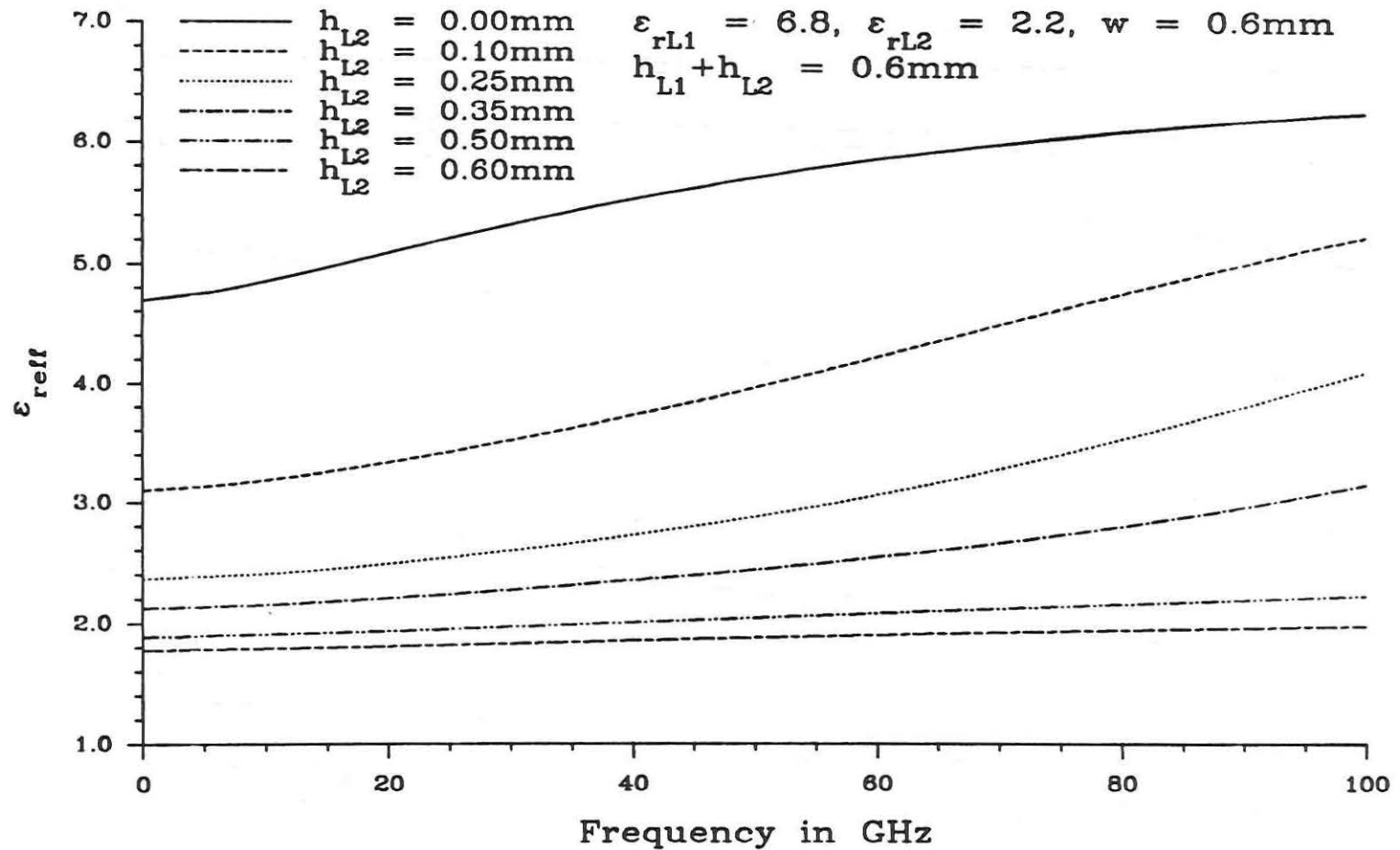
Fig. 4.27. ε_{reff} vs. frequency for open multilayer single microstrip on beryllium oxide and RT/duroid 5880 substrate.
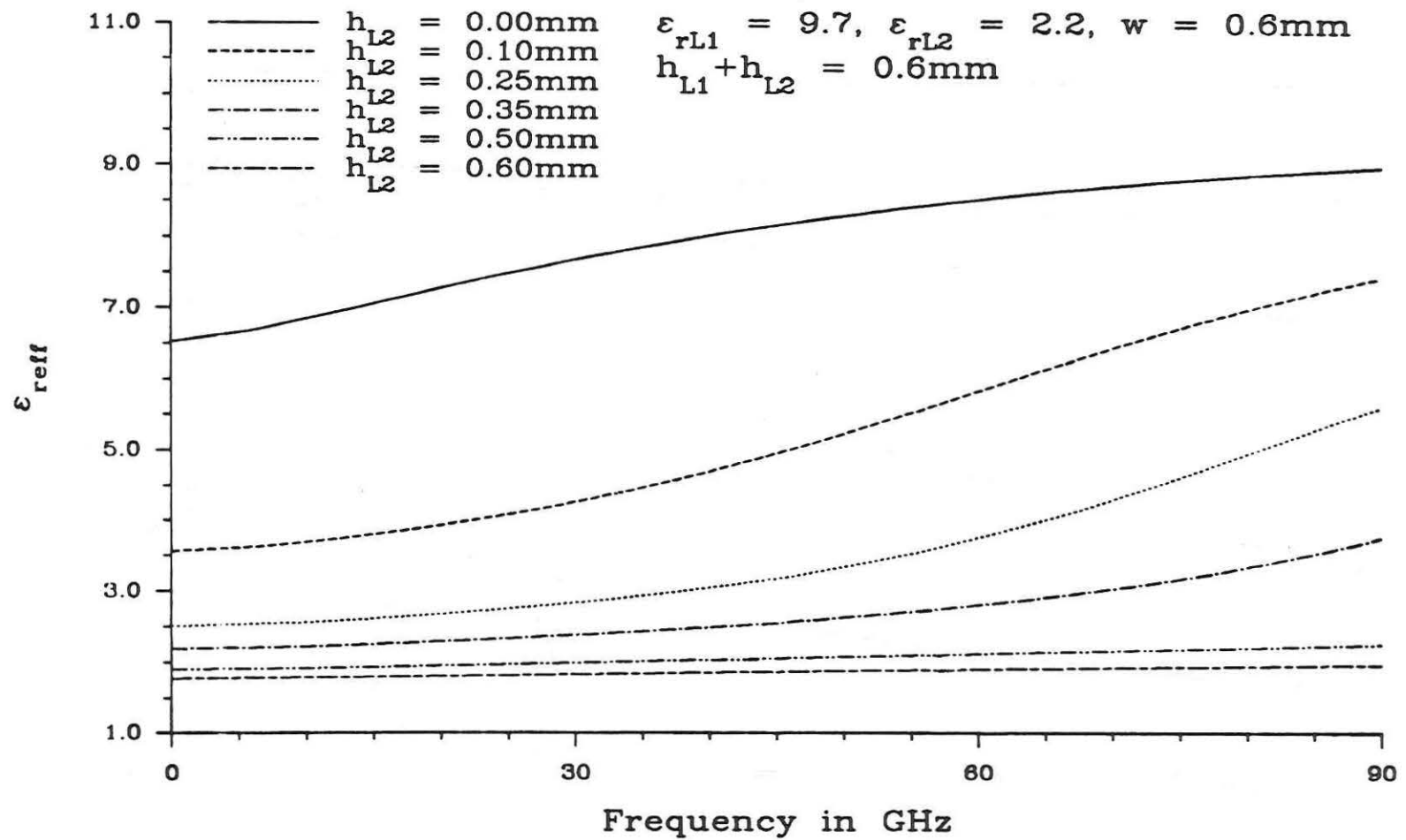
Fig. 4.28. ε_{reff} vs. frequency for open multilayer single microstrip on alumina and RT/duroid 5880 substrate.
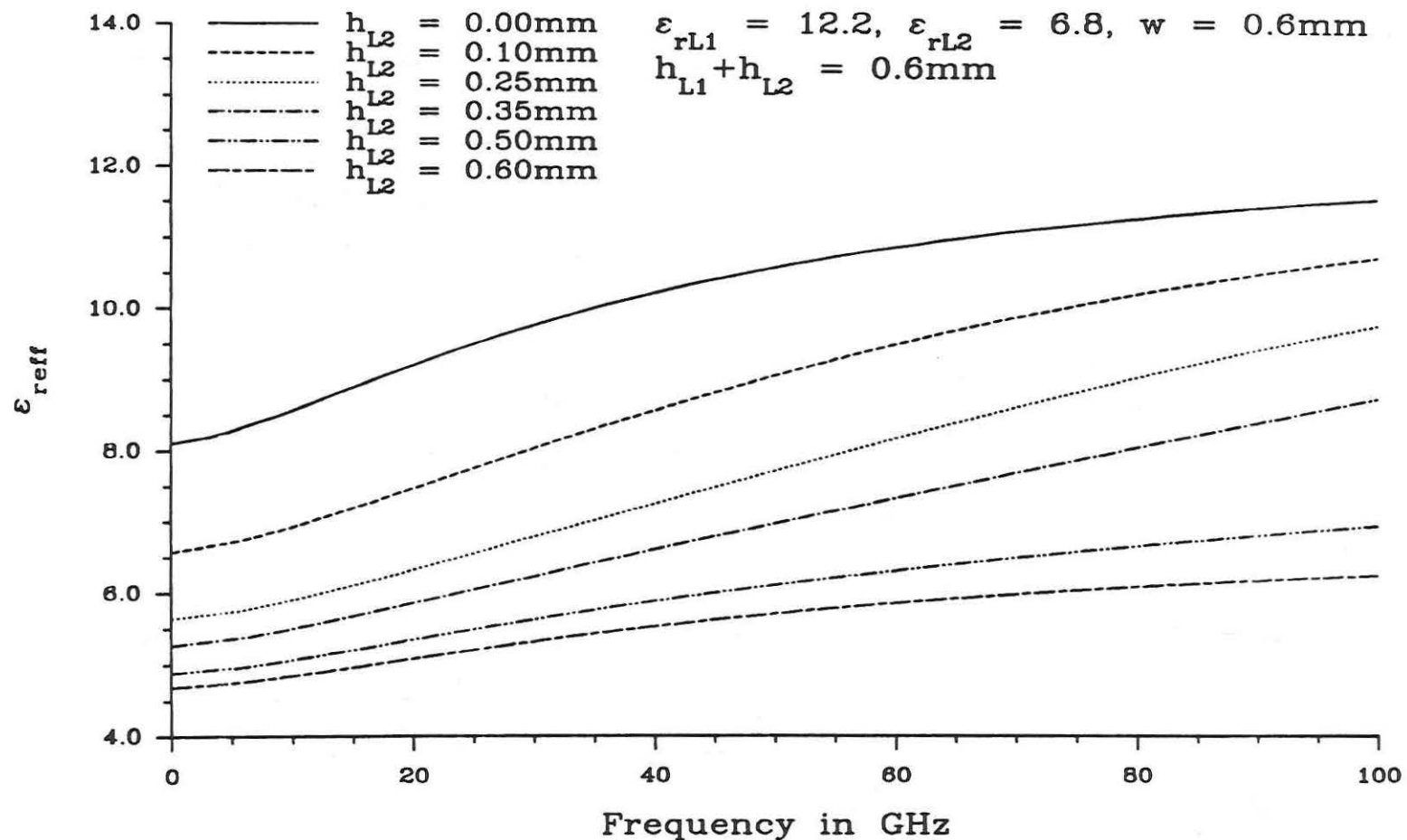
Fig. 4.29. ε_{reff} vs. frequency for open multilayer single microstrip on gallium arsenide and beryllium oxide substrate.
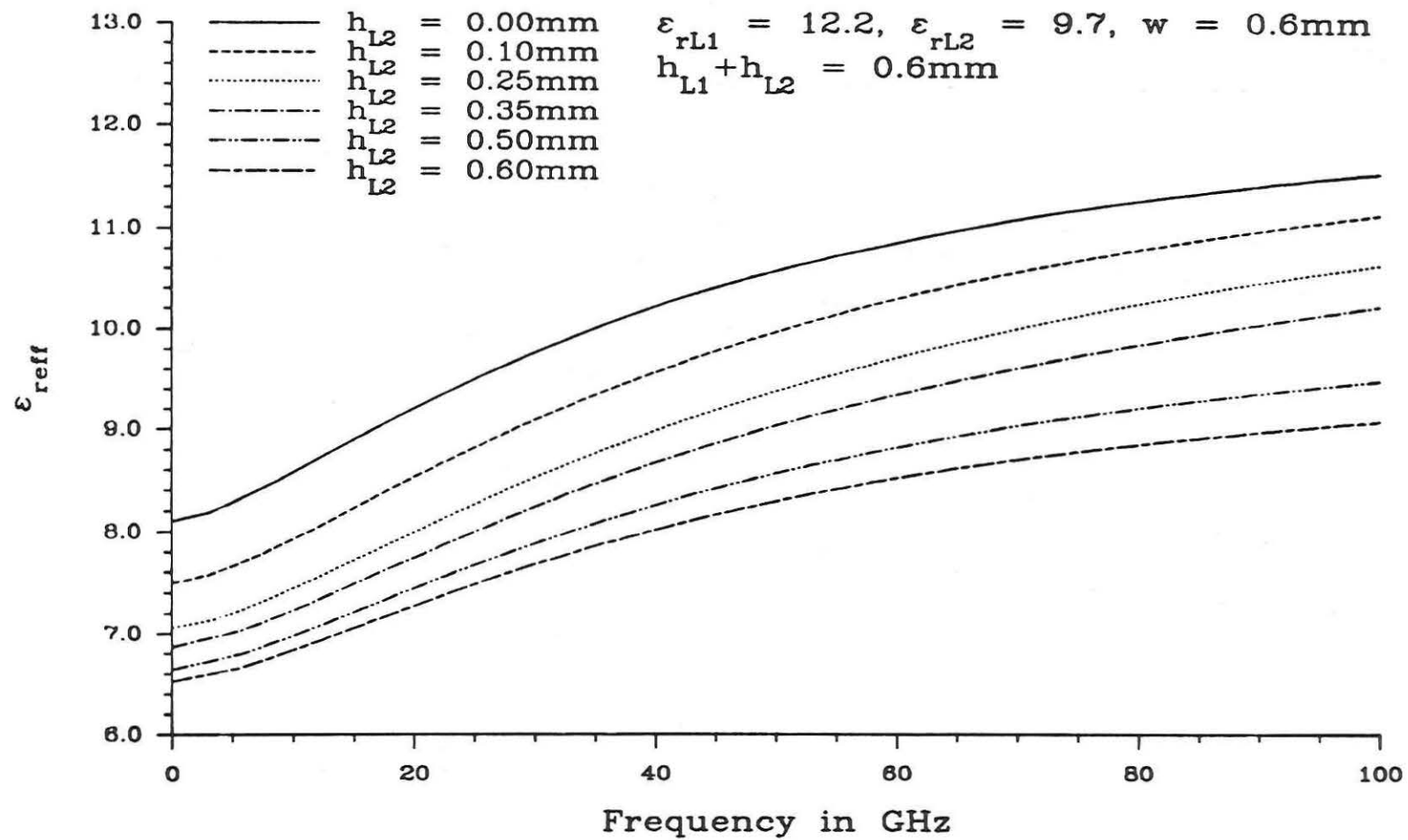
Fig. 4.30. ε_{reff} vs. frequency for open multilayer single microstrip on gallium arsenide and alumina substrate.

frequencies, the smallest duroid layer, h_{L2} = 0.1 mm, decreases ε_{reff} by 55 percent of $\Delta\varepsilon_{reff}$ even though the height added is only 16.6 percent of the total height. When h_{L2} = 0.25 mm, or 41.6 percent of the total height, the decrease in ε_{reff} is almost 80 percent. In Fig. 4.28, which represents data for a structure with duroid on alumina, the difference at low frequencies is even larger; that is the 16.6 percent height change gives a 62 percent change in ε_{reff} and the 41.6 percent height change results in a difference in ε_{reff} of 85 percent of $\Delta\varepsilon_{reff}$. Thus the addition of a relatively thin substrate can have a profound impact on the effective dielectric constant of a multilayer structure, especially for the lower frequencies.

The third structure, gallium arsenide on beryllium oxide, shown in Fig.4.29, gives results that are similar to the previous ones. The addition of the 0.1 mm layer gives a 44.7 percent decrease while the change of h_{L2} from 0.5 mm to 0.6 mm results in only a change of only 6 percent of $\Delta\varepsilon_{reff}$ at low frequencies. Therefore, while the addition of a thin upper substrate layer with a lower ε_r gives large changes in ε_{reff}, the addition of an equally thin lower substrate layer with higher ε_r results in relatively small changes in ε_{reff}. Also, as the beryllium oxide layer is increased in height, the dispersive characteristics of the structure decrease. This is expected because single layer structures are less dispersive when the relative dielectric constant of the substrate is less.

The final two substrate configuration considered has a layer of alumina on a layer of gallium arsenide. The results, plotted in Fig. 4.30, do not have as drastic of changes in ε_{reff} as those of the

previous graphs, because the relative dielectric constants of the substrates are closer to each other than those of the previous structures. At low frequencies, the 0.1 mm and 0.25 mm graphs have changes of only 38 and 64 percent of $\Delta\varepsilon_{reff}$ respectively. However, like the other structures, as frequency increases, the percent changes in ε_{reff} become closer to the percent changes in the layer height. At 100 GHz, the 0.1 and 0.25 mm structures have changes in ε_{reff} of 16.3 and 36.2 percent of $\Delta\varepsilon_{reff}$, which are much closer to the height changes of 16.7 and 41.6 percent of the total height. Additionally, the increase in h_{L1} to 0.1 mm (h_{L2} = 0.5 mm) and 0.25 mm (h_{L2} = 0.35 mm), gives changes of 16.8 and 46.7 percent respectively, which are much closer to the corresponding changes for h_{L2}. Note that while at low frequencies the addition of a thin upper substrate gives a much larger change in ε_{reff} than the addition of a thin lower substrate, as the frequency is increased, the addition of a lower substrate gives about the same change as the addition of an upper substrate.

This change in the effect of upper and lower substrates as the frequency is increased can be attributed to changes in the electric field structure as the frequency increases beyond the quasi-static region. As the frequency is increased, the electric field lines tend to bunch underneath the center conductor, connecting directly with the ground plane, rather than fringing out into the upper layers. This results in a field configuration that is similar to a parallel plate capacitor filled with two different dielectric slabs. Since the parameters of the parallel plate capacitor are independent of the relative placement of the slabs, then the microstrip parameters, in the

high frequency region, will also be independent of the substrate placement.

Since at very high frequencies the microstrip may be approximated by a parallel plate capacitor, it is instructive to consider the equivalent dielectric constant of a two-layer parallel plate capacitor. The equivalent dielectric constant, ε_{eqv}, of the dual dielectric parallel plate capacitor is the dielectric constant of a single layer of height $h_{L1} + h_{L2}$ that when used in the parallel plate capacitor gives the same capacitance as one filled with two layers that have dielectric constants ε_{L1} and ε_{L2} and heights h_{L1} and h_{L2}. Using elementary circuit theory and the capacitance formula for a parallel plate capacitor, the equivalent dielectric constant is found to be

$$\varepsilon_{eqv} = \frac{h_{L2} + h_{L1}}{h_{L2}/\varepsilon_{L2} + h_{L1}/\varepsilon_{L1}} \tag{4.5}$$

ε_{eqv} is also the high frequency limit of ε_{reff}, i.e.

$$\lim_{f \to \infty} \varepsilon_{reff}(f) = \varepsilon_{eqv} \tag{4.6}$$

Note that this equivalence applies only at frequencies that are sufficiently high so that almost all the electric field lines lie directly between the center conductor and the ground plane with almost no fringing. This concept of the equivalent dielectric constant can be extended to include more dielectric layers by characterizing each layer as another parallel plate capacitor attached in series.

Since the difference in the even and odd mode phase velocity degrades the performance of a circuit, it is advantageous to be able to equalize the modal phase velocities. One method that has been used in the past to accomplish this is to place a superstrate layer with the

same dielectric constant as the substrate on top of the center conductors. If the height of this superstrate is adjusted properly, then the even and odd mode phase velocities will be equalized. The concept behind this approach is that striplines, which have a homogeneous dielectric medium, are TEM structures where the even and odd mode phase velocities are equal. Thus the placement of such a layer of the correct thickness would make the microstrip more like the stripline, i.e. a more homogeneous medium, and hence equalize the even and odd mode phase velocities.

This method of equalizing the modal velocities is now applied to structures with four different substrates and the results are shown in Figs. 4.31 through 4.34. The configuration, which is shown in each of the figures, is an open symmetric coupled microstrip with a single substrate and two superstrates where $h_{U1} \rightarrow \infty$. All four structures are considered at $f = 100$ MHz, which is in the quasi-static region for these microstrips. This frequency was chosen because it gives very broadband characteristics, from 0 to about 1 GHz, and because many microstrip designs operate in or near the quasi-static region.

In each of the four graphs, when the superstrate layer is very thin, there is not much effect on the effective dielectric constant. However, when the thickness of the superstrate is increased to 10 percent of the substrate height, then ε_{reff} for all three cases, isolated, even mode, and odd mode, begins to increase as well. The effect of the superstrate layer is more pronounced, however, if its dielectric constant is much larger than that of the substrate. The odd mode effective dielectric constant, however, increases much faster in
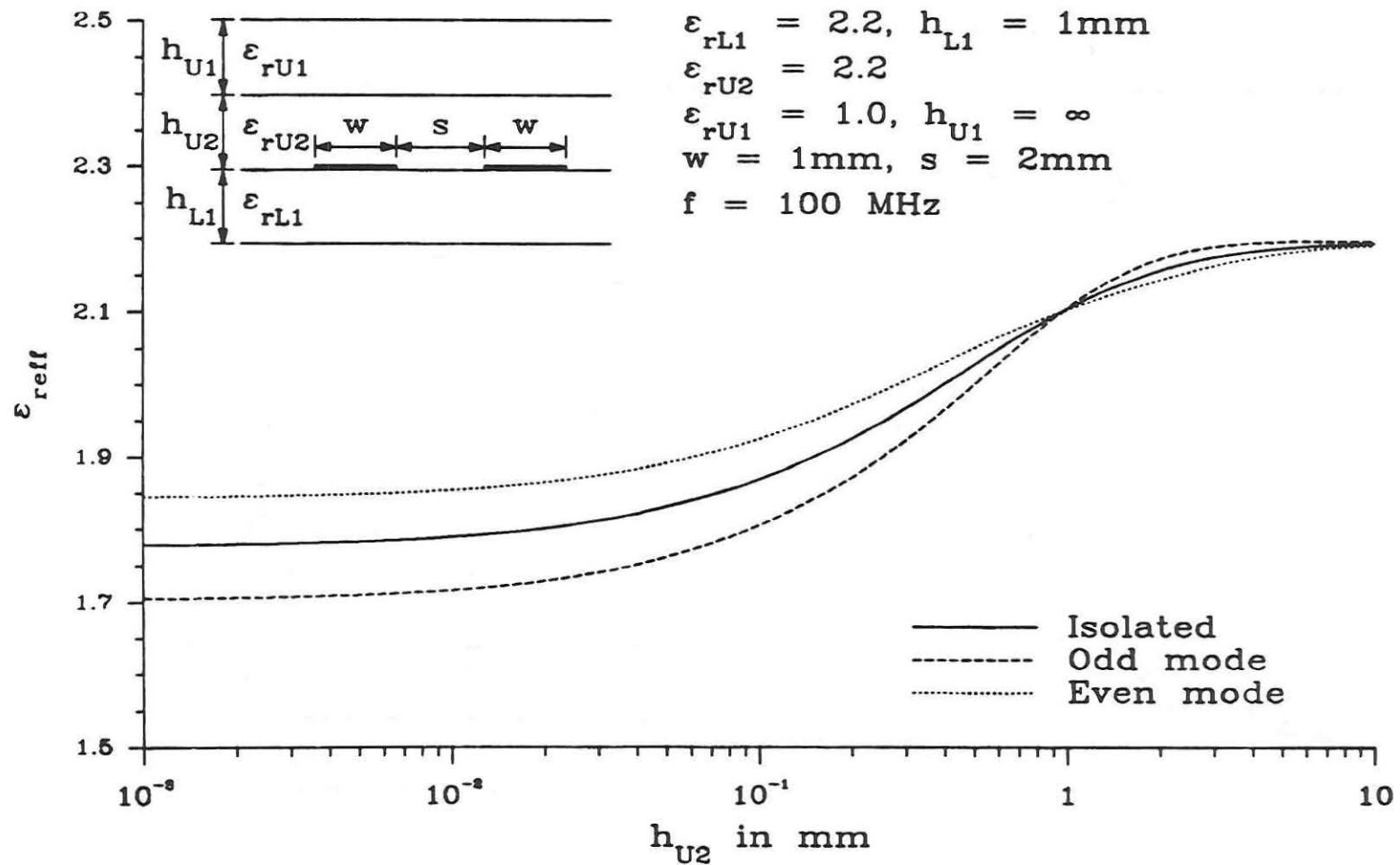
Fig. 4.31. ε_{reff} vs. cover layer height for multilayer symmetric coupled microstrips with RT/duroid 5880 superstrate and substrate.
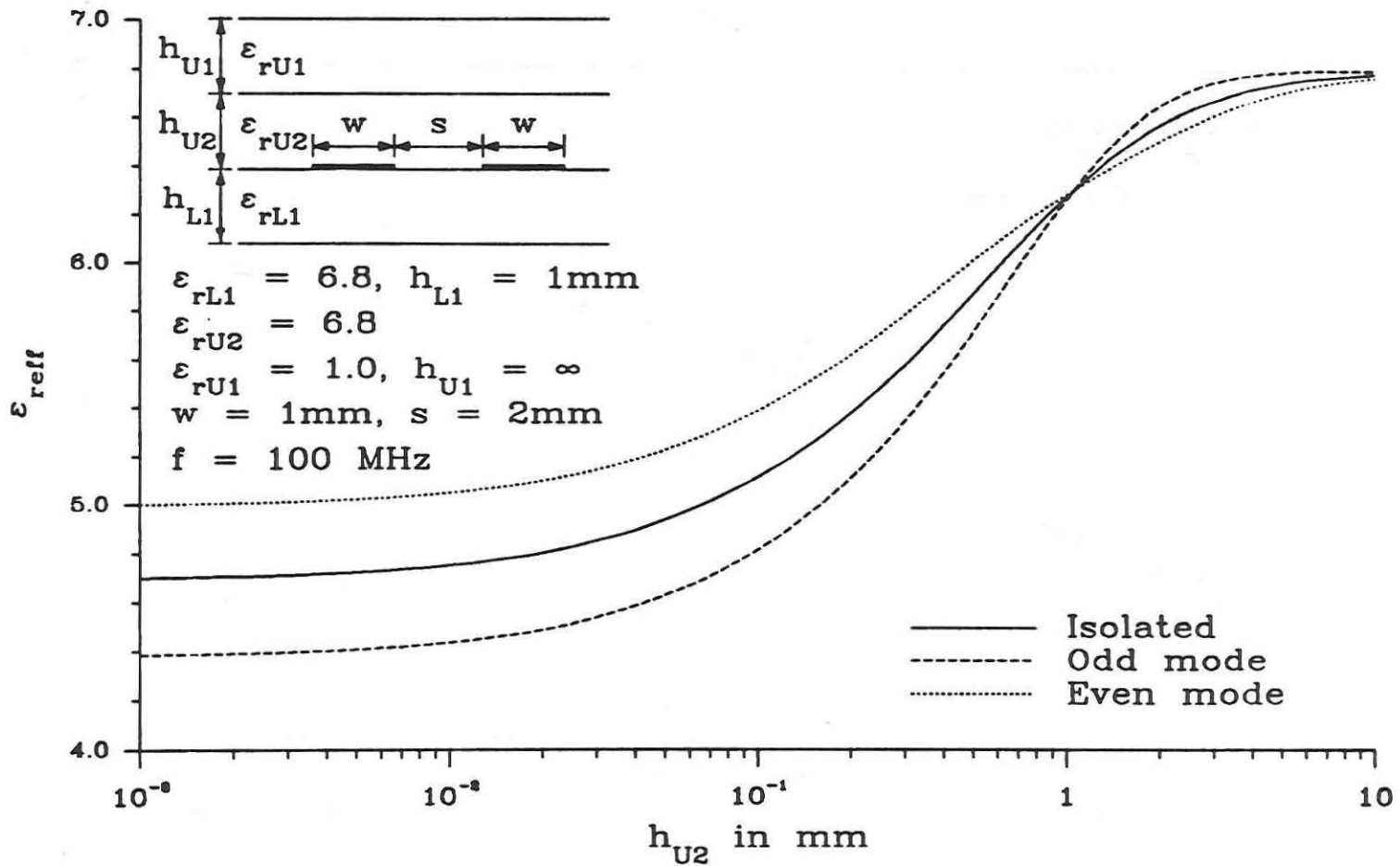
Fig. 4.32. ε_{reff} vs. cover layer height for multilayer symmetric coupled microstrips with beryllium oxide superstrate and substrate.
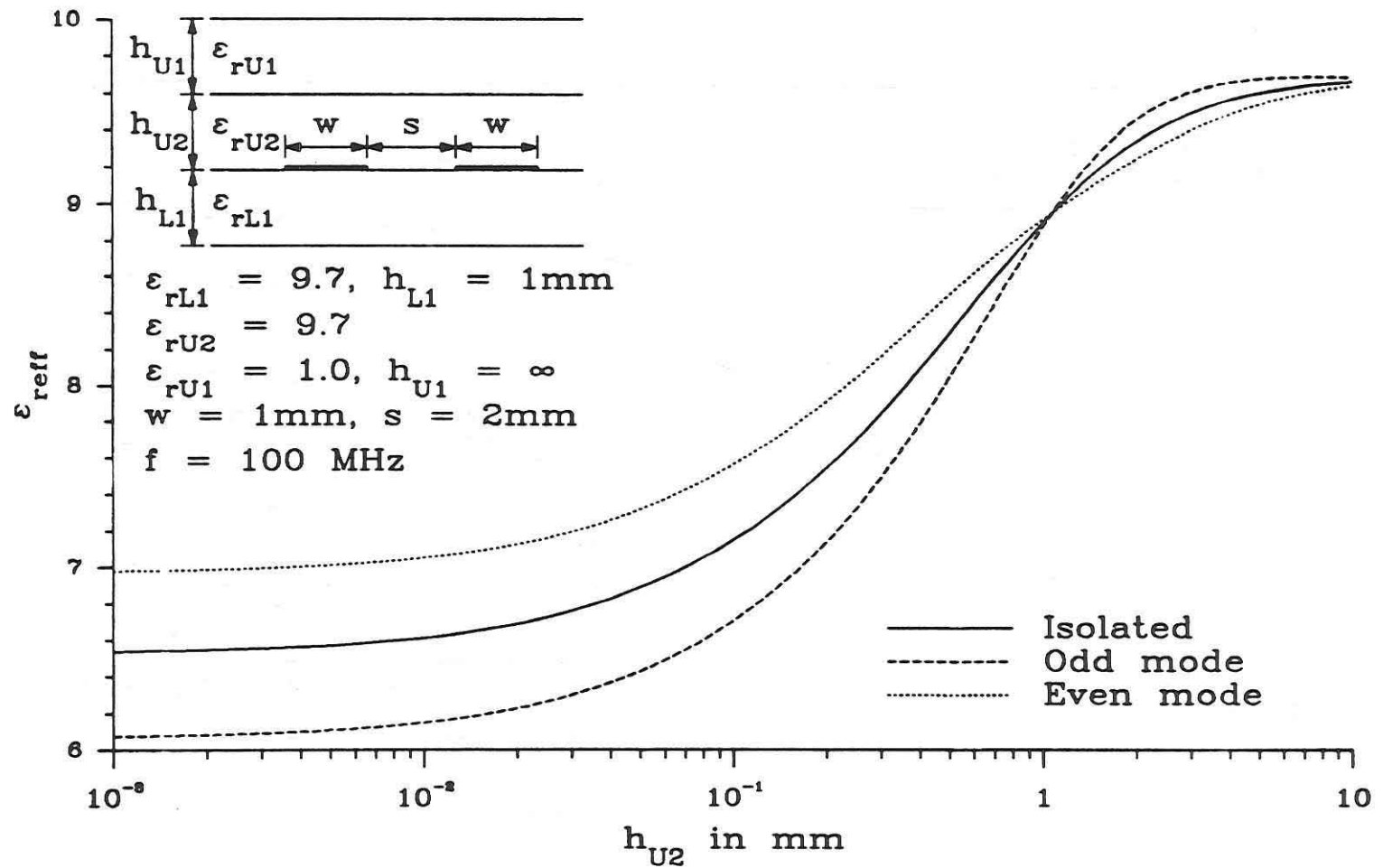
Fig. 4.33. ε_{reff} vs. cover layer height for multilayer symmetric coupled microstrips with alumina superstrate and substrate.
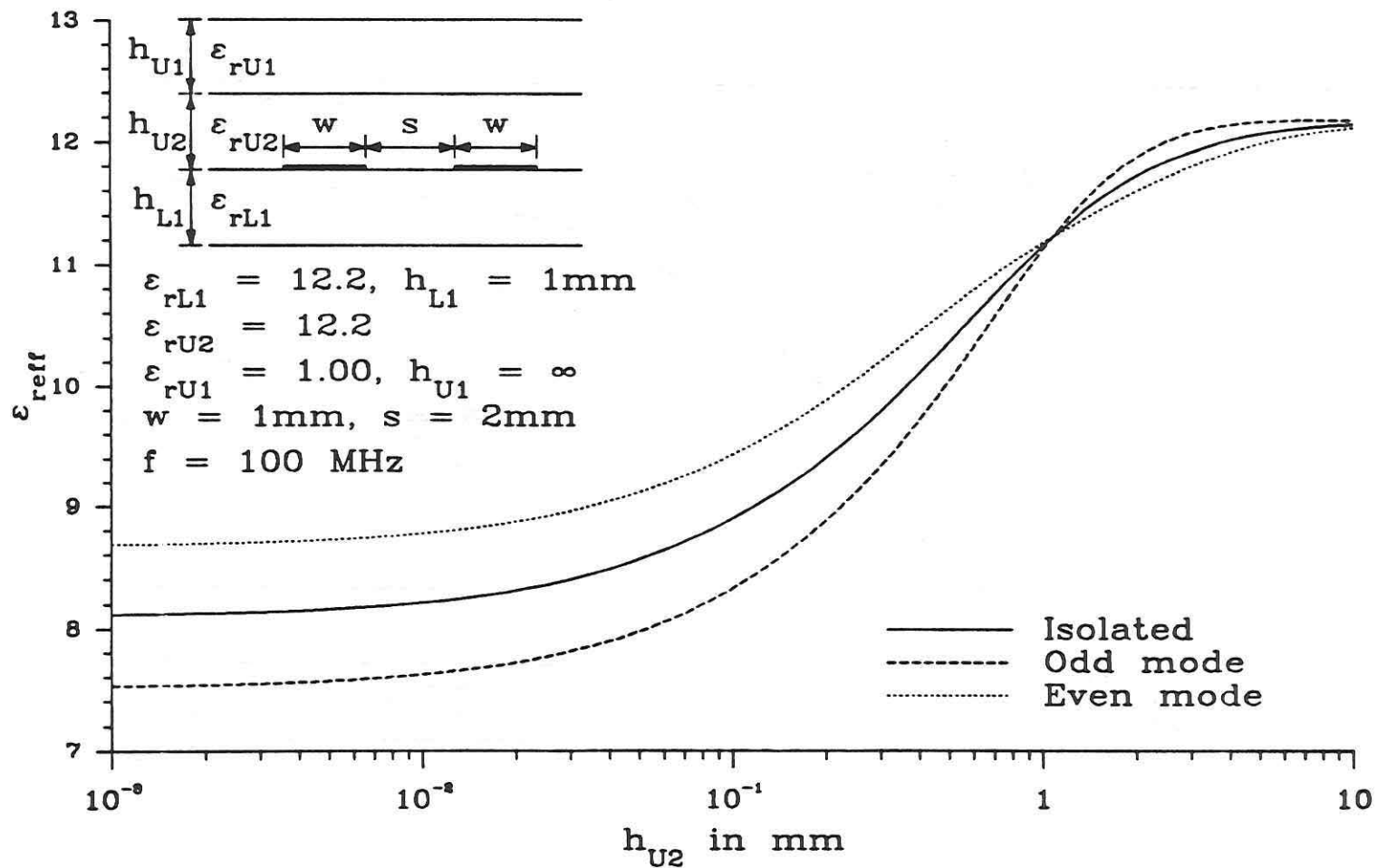
Fig. 4.34. ε_{reff} vs. cover layer height for multilayer symmetric coupled microstrips with gallium arsinide superstrate and substrate.

this region than the other two ε_{reff}'s. When h_{U2} equals infinity, then the microstrips are imbedded in a completely homogeneous medium with a relative dielectric constant of $\varepsilon_{rL1} = \varepsilon_{rU2}$. Therefore, in the limit as h_{U2} goes to infinity, the effective dielectric constants for all three cases approach the relative dielectric constant of the substrate. For the four structures used, the infinite height condition is approximately satisfied when h_{U2} is about 10 times h_{L1}, i.e. when $h_{U2} = 10$ mm.

Although the modal phase velocities are approximately equal when h_{U2} is about 10 times h_{L1}, this is not a very efficient design due to the extraordinarily large thickness of the superstrate. Aside from the expense of such a circuit, the large dielectric slab could support spurious guided wave modes at relatively low frequencies that would be excited by discontinuities in the lines. However, because the effective dielectric constant of the odd mode increases much faster than the even mode for each of the four structures, at one other h_{U2} value besides infinity, the even and odd mode phase velocities are equal. For all four materials being considered, this occurs when h_{U2} is approximately the same height as the substrate. The even/odd mode equalization occurs when $h_{U2} = 0.97$ mm for the duroid and moves slightly higher as the dielectric constant increases. For the beryllium oxide substrate and superstrate combination, the equalization occurs when h_{U2} is equal to 1.06 mm and at around 1.07 mm for both the alumina and gallium arsenide structures.

The motivation behind adding a superstrate layer to the microstrip was to make the structure more TEM, like the stripline, by making the

dielectric surrounding the center conductors seem approximately homogeneous. For the structures considered, this approximation to the stripline occurred when the superstrate layer was about ten times the substrate layer. This might have been anticipated because a shielded microstrip has approximately the same characteristics as an open microstrip. This is more evident when the distance to the upper ground plane and side walls are at least five times the substrate height or center conductor width [46]. However, the even/odd mode equalization also occurred for a much smaller h_{U2} value, a value at which the structure does not approximate the stripline and is not TEM. Also note that when h_{U2} is greater than this first equalization point, the odd mode's ε_{reff} is greater than the even mode's ε_{reff}, something that did not occur in the single layer structure. This indicates that a completely different mechanism is responsible for the equalization of the even and odd mode phase velocities.

As long as the microstrip is operated in the quasi-static region, then the location of the equalization point stays constant, because ε_{reff} is constant for the frequencies in this region. However, as the frequency increases past the quasi-static region of the structure, the location of this equalization point moves to larger values of the superstrate height. At some frequency outside the quasi-static region, the equalization point changes to a value so large that it gives no advantage in design, essentially eliminating it as a possibility. This occurs because as frequency increases, the electric field lines tend to go in a straight line from the center conductor to the ground plane with less and less lines in the superstrate regions. Thus the

superstrate has a decreasing effect on ε_{reff} as the frequency increases.

While the inability to find a realizable superstrate height that matches the even and odd mode phase velocities at high frequencies is a significant drawback to this method, many microwave circuits operate in the quasi-static region, and so there are applications that can use this concept. In addition, it will be shown in section 4.3 that this even/odd mode equalization phenomenon can also occur when multiple substrates are used in the structure instead of an additional superstrate. Since the substrates lie between the center conductor and the ground plane, as the frequency increases, they still have a significant effect on the electric field lines of the structure, increasing the potential bandwidth of the design. Also, since the even and odd mode phase velocities tend to approach each other at very high frequencies, it will be possible to achieve a very good match of the even and odd mode phase velocities over an almost infinite bandwidth.

The necessity to control electromagnetic emissions, the desire to cutoff higher order modes, as well as the need to reduce radiation losses, often necessitate shielding the microstrip circuit. To be able to accurately account for the effects of shielding on the transmission lines requires the use of a rigorous analytical approach. Fortunately, due to the general manner in which the generalized Green's function was derived, as well as the flexibility of the spectral domain approach, it is as easy, if not easier, to compute the frequency dependent parameters for shielded structures as for open ones. Figures 4.35 through 4.38 deal with the presence of an upper ground plane, or cover

sheet, in a symmetric coupled microstrip structure with one substrate and two superstrates. The same four dielectric materials are used and the effective dielectric constant for the isolated line and the even and odd modes of the coupled lines are computed as the height of the upper ground plane, h_{U1}, is varied.

As h_{U1} gets smaller, then the structure becomes more like a stripline, and so the effective dielectric constant for all three cases approaches the relative dielectric constant of the substrate. On the other hand, as h_{U1} becomes large, then the structure becomes more like an open microstrip, and the effective dielectric constants for the isolated, even and odd modes approach approach the corresponding values shown in Figs. 4.31 through 4.34 when h_{U2} = 0.3 mm. As with the previous four structures, for generality, the frequency at which the parameters are computed is 100 MHz.

The most noticeable characteristic in all four graphs is that the effective dielectric constants vary over a large range of values as the height is changed instead of monotonically decreasing from the stripline value to the open microstrip value. ε_{reff} begins at the maximum value when h_{U1} is the smallest and begins to decrease in magnitude until a minimum is reached when h_{U1} is somewhere between 0.1 and 0.4 mm, depending on the dielectric material used. As h_{U1} continues increasing past this value, ε_{reff} begins to increase as well, approaching the open microstrip value when h_{U1} is about 10 times the substrate height, i.e. when $h_{U1} \simeq 10$ mm.
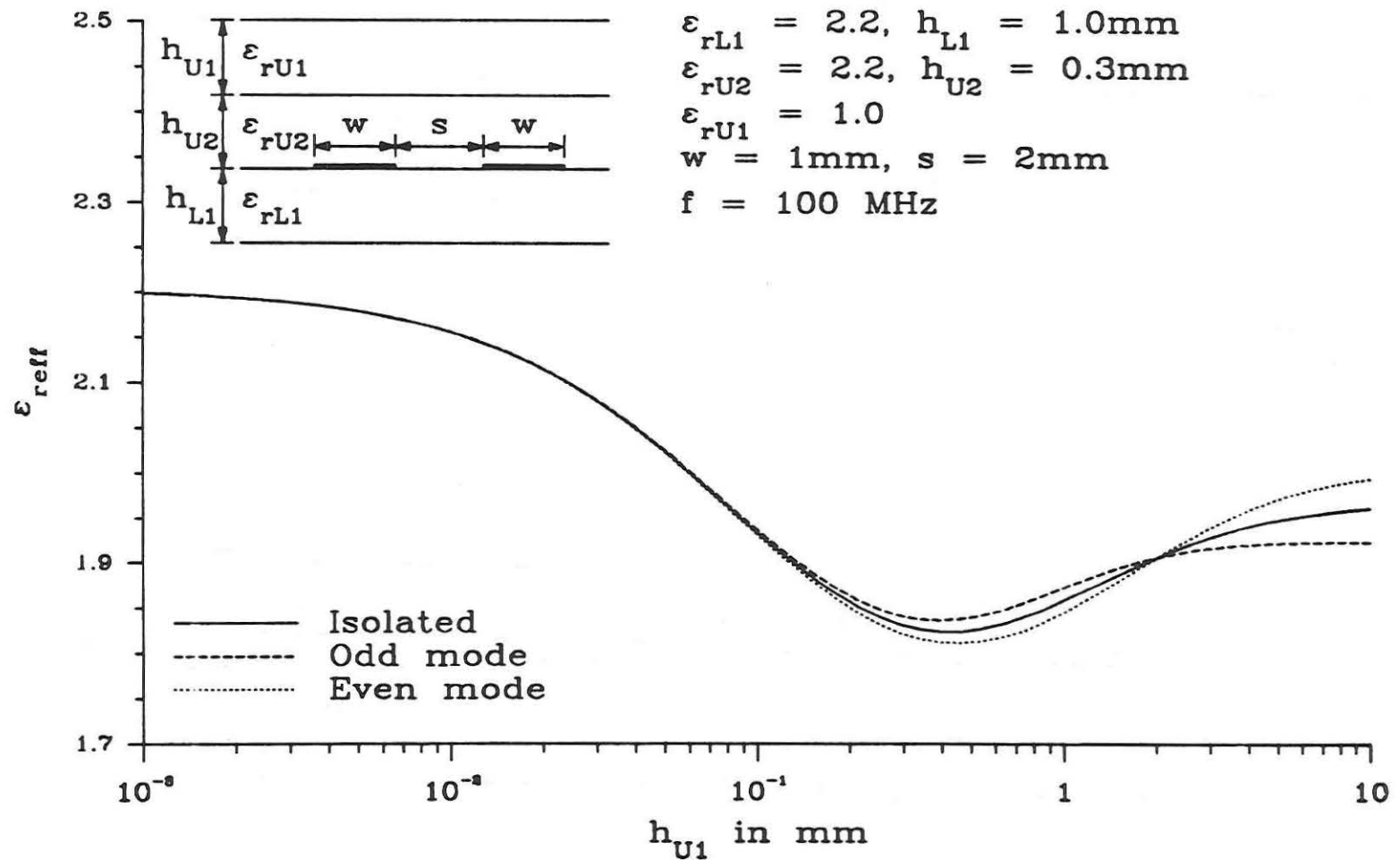
Fig. 4.35. ε_{reff} vs. cover sheet height for multilayer symmetric coupled microstrips with RT/duroid 5880 superstrate and substrate.
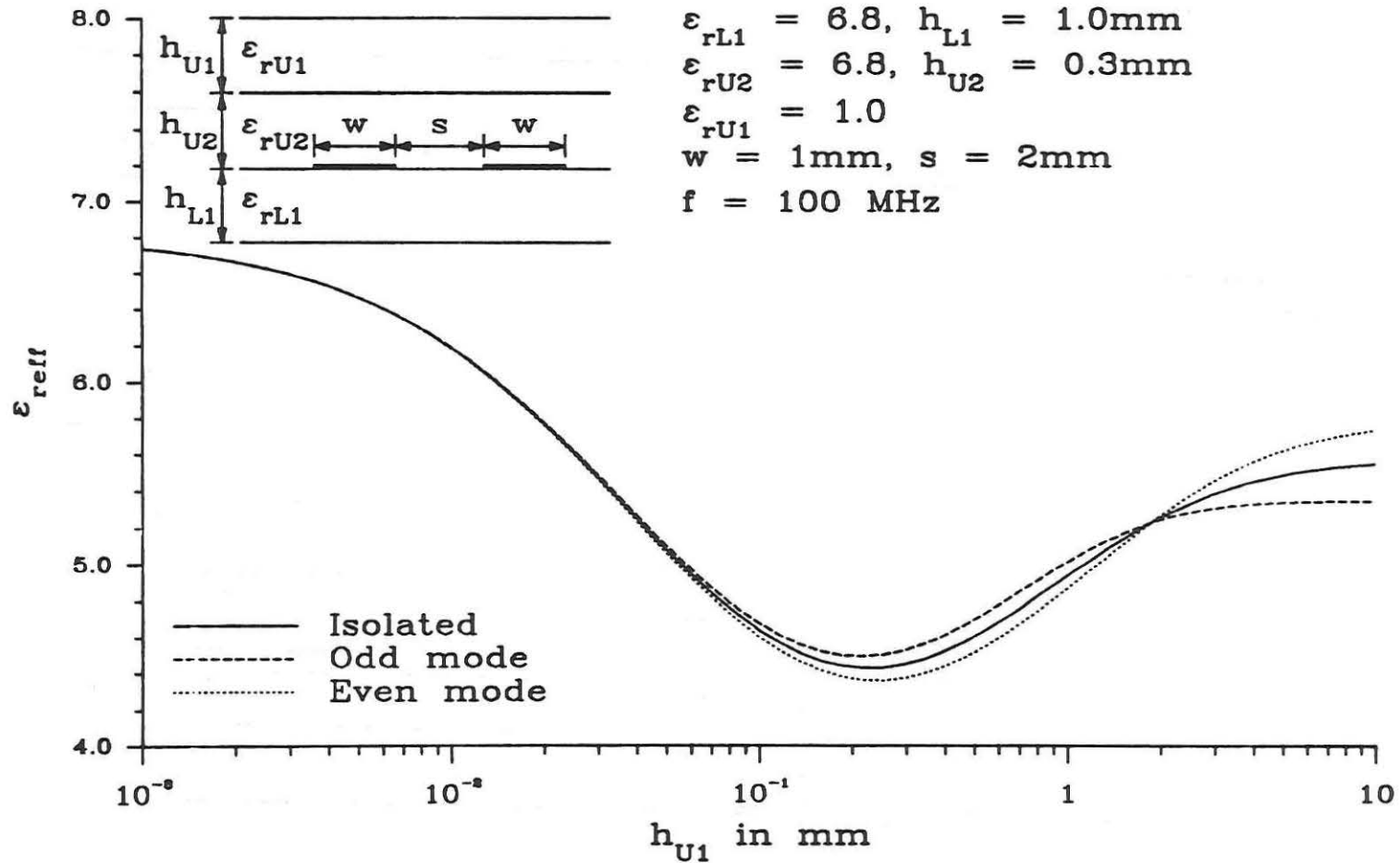
Fig. 4.36. ε_{reff} vs. cover sheet height for multilayer symmetric coupled microstrips with beryllium oxide superstrate and substrate.
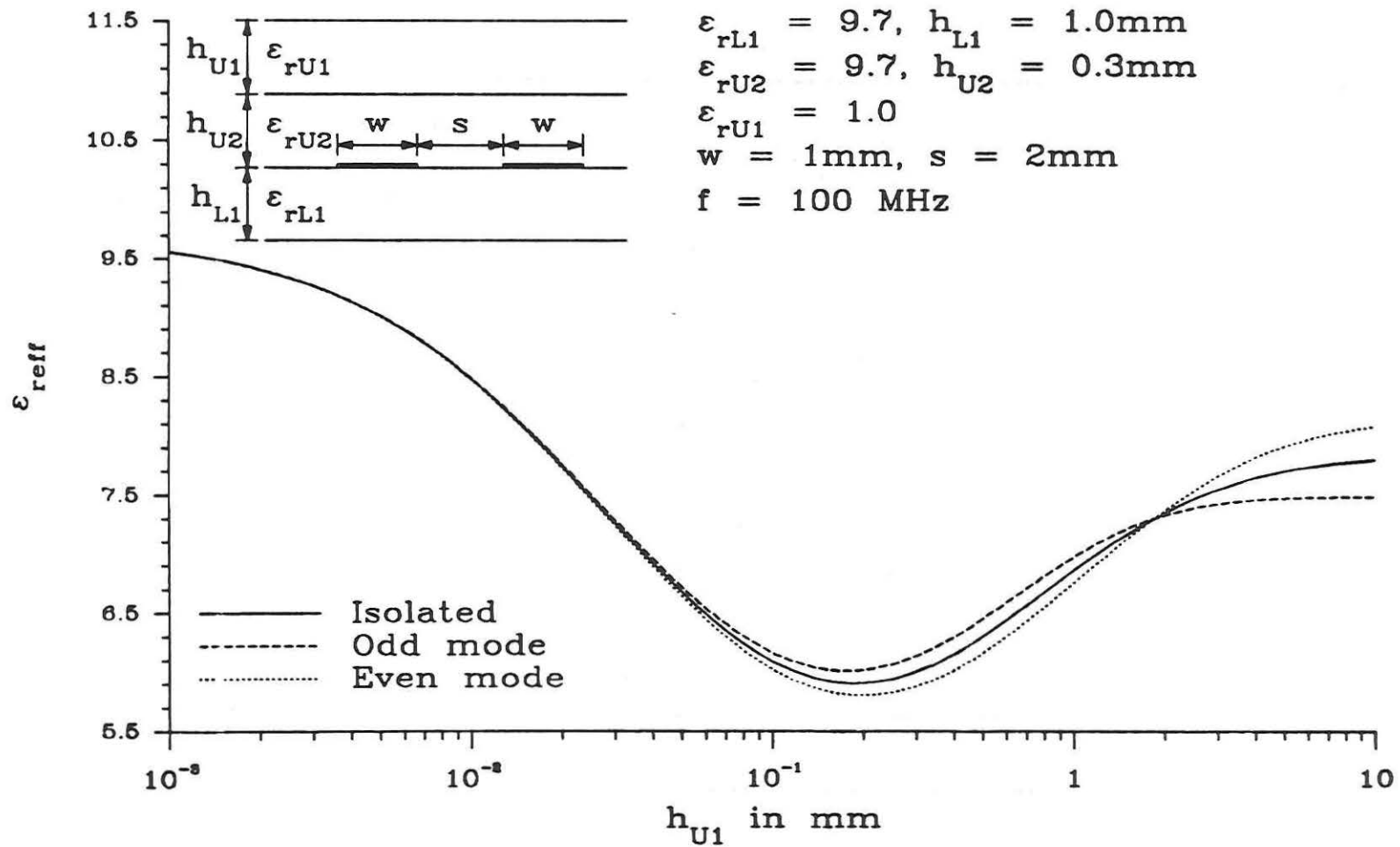
Fig. 4.37. ε_{reff} vs. cover sheet height for multilayer symmetric coupled microstrips with alumina superstrate and substrate.
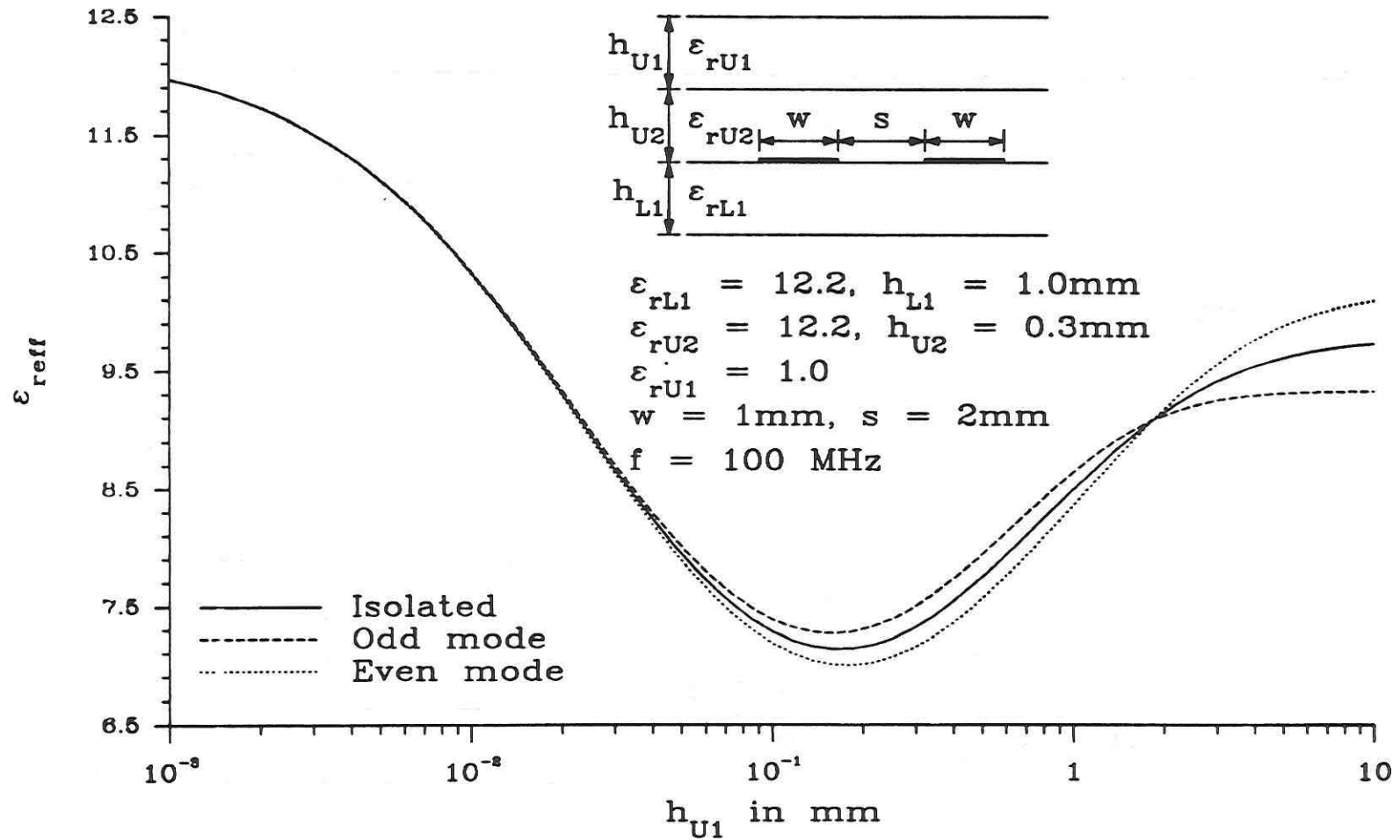
Fig. 4.38. ε_{reff} vs. cover sheet height for multilayer symmetric coupled microstrips with gallium arsenide superstrate and substrate.

The manner in which ε_{reff} changes as h_{U1} varies can be understood by considering the field structure in shielded configuration. When h_{U1} is very small, then the paths of the field lines exist almost entirely in the dielectric material with only very short distances in the air, and so ε_{reff} is approximately equal to the ε_r of the substrate. As the air gap increases in height, then the field lines that connect with the cover layer pass through an air layer whose thickness is no longer negligible and therefore has greater effect on the fields. Because the dielectric constant of the air is lower than that of the substrate or superstrate, ε_{reff} begins to decrease in value. At some point, however, the upper ground plane is sufficiently distant so that more of the electric field lines go through the substrate to ground rather than through the superstrates, bypassing the air gap and negating its effects. This occurs even though the distance from the center conductors to the upper ground plane is shorter than the distance to the lower ground plane. But, because the substrate has a higher dielectric constant than the equivalent combination of the upper two layers, it attracts more of the field lines.

As the cover sheet moves farther away from the center conductors, less field lines go from the center conductors through the air layer to the cover sheet, thereby increasing ε_{reff}. Finally, when the cover sheet is far enough away, it attracts virtually no field lines and no longer has any noticeable effect on the structure. When this happens, ε_{reff} for all three cases approach the corresponding values for the open structure.

The h_{U1} value corresponding to the minimum ε_{reff} value varies slightly as the relative dielectric constant of the substrate and superstrate changes. Additionally, while the minimum point is approximately the same for each of the three cases, it varies slightly, with the odd mode having the lowest h_{U1} value and the even mode the highest. For the RT/duroid substrate and superstrate combination, Fig. 4.35, the minima occur when h_{U1} is about 0.43 mm. If the relative dielectric constant of the material was decreased, it would be expected that the minimum point would approach 0.7 mm, so that the total superstrate height would be equal to the height of the substrate. Also, the minimum points of each of the three cases would tend to approach each other more closely with the even and odd mode ε_{reff} approaching the isolated value, which in turn would be approaching unity. In the limit as the relative dielectric constant approached unity, the graphs would flatten completely and no distinct minimum would exists.

As the dielectric constant increases, however, the minima points occur at lower values of h_{U1}, and the locations for each of the three cases increase in separation. For the beryllium oxide structure, Fig. 4.36, the minima occur for h_{U1} near 0.21 mm, while for the alumina substrate and superstrate, Fig. 4.37, they occur near 0.19 mm. When gallium arsenide is used, Fig. 4.38, the minima occur near h_{U1} = 0.16 mm, but differ noticeably for each case. The odd mode's minimum occurs at $h_{U1} \simeq 0.155$ mm while the even mode's happens around 0.175 mm. As would be expected, the minimum for the isolated case ends up between that of the even and the odd mode at $h_{U1} \simeq 0.165$ mm.

In addition to the locations of the minima moving, increasing the relative dielectric constant of the material also makes the change in ε_{reff} much greater as well. For the duroid structure, the introduction of a 0.01 mm air gap decreases ε_{reff} by about 2 percent and the 0.1 mm gap decreases it by 12 percent. The decrease at the minimum point is 17 percent lower than the stripline value and 7 percent lower than the open microstrip value. When the dielectric is changed to gallium arsenide, the changes in ε_{reff} become much more drastic. The 0.01 mm and 0.1 mm air gaps decrease ε_{reff} by 14 and 40 percent, respectively. The minimum value of ε_{reff} is now 40 percent lower than the stripline value and 23 percent lower than the open microstrip case.

Thus if a stripline circuit were designed with similar dimensions on gallium arsenide, but in production there were a 10 micron gap between the upper ground plane and the dielectric material, there would be and 8 percent increase in the wavelength and hence an equivalent decrease in the electrical dimensions of the circuit, since $\lambda \propto 1/\sqrt{\varepsilon_{reff}}$. If the air gap were 0.1 mm, however, the wavelength would be increased by 23 percent. Changes in the electrical dimensions of the circuit of this magnitude would certainly have an adverse effect on the circuit performance. If, instead, the circuit had been designed as an open structure without accounting for the shielding, then, depending on the placement of the cover sheet, there could also be significant changes in the parameters of the lines. Clearly the presence of a cover sheet, which is very common in production designs, must be taken into account using a rigorous, full wave technique like the SDA.

As with the previous dual superstrate structures, it is possible to adjust the dimensions to equalize the even and odd mode phase velocities. For the four structures under consideration, a cover layer height of slightly less than 2 mm makes the even and odd mode ε_{reff} the same. However, also like the two superstrate open structure, as the frequency increases above the quasi-static region, the h_{U1} value required to maintain the even/odd mode equalization decreases. As the frequency increases, the electric field lines tend to gather along the path with the highest capacitance. In order to maintain enough of the field lines in the superstrates, the capacitance of the upper layers must be increased, and so the cover sheet height must be reduced to maintain the even/odd mode equalization. Due to the large change in the required cover sheet height for frequencies above the quasi-static region, this method of equalizing the even/odd mode phase velocities can only be used either in the quasi-static region or for very narrowband applications at frequencies beyond the quasi-static region.

It was shown previously that the presence of multiple substrates in the microstrip structure causes significant deviations in ε_{reff} from the single layer value. However, the effect of the relative placement of the substrates has not been dealt with yet. At very high frequencies, the microstrip can be approximated by a parallel plate capacitor, and so $\varepsilon_{reff}(\infty)$ is determined by the heights and relative dielectric constants of the substrates, and not by the relative locations of the substrates. At lower frequencies, however, the position of a substrate layer relative to the other substrate layers can have an important effect on the line parameters.

To illustrate the effect of substrate placement on ε_{reff}, an open symmetric coupled microstrip structure is used with two substrates, alumina and RT/duroid 5880. The first configuration, designated structure #1, places a 0.3 mm duroid layer on top of an alumina layer of the same height. The next configuration, called structure #2, switches the substrates, placing the alumina on top of the duroid, again with both layers having the same height. The other dimensions are the same for both structures and are listed in Fig. 4.39. The effective dielectric constants for the two configurations are plotted in Fig. 4.39 as a function of frequency for the isolated case and for the even and odd modes of the coupled lines.

Structure #1 has a much lower ε_{reff} than structure #2, about 36 percent lower, indicating that structure #1 should be less dispersive than #2. On the other hand, the separation in the even and odd mode phase velocities is much greater in #1, 16 percent, compared with the 5.6 percent separation for structure #2. Thus structure #2 will have much less distortion due to coupling than #1. Also while ε_{reff} for the odd mode is lower than the even mode in #1, switching the substrate layers as in #2, results in the even mode ε_{reff} being much lower than the odd mode.

Pulse distortion on these structures is shown in Figs. 4.40 and 4.41 for a Gaussian pulse with τ = 30 ps at a distance of 250 mm. The signal line response on structure #1 has been critically distorted and has separated into the even and odd mode pulses. On the other hand, the signal line response on structure #2, while greatly reduced in magnitude, is not nearly as distorted as the response on #1 because of
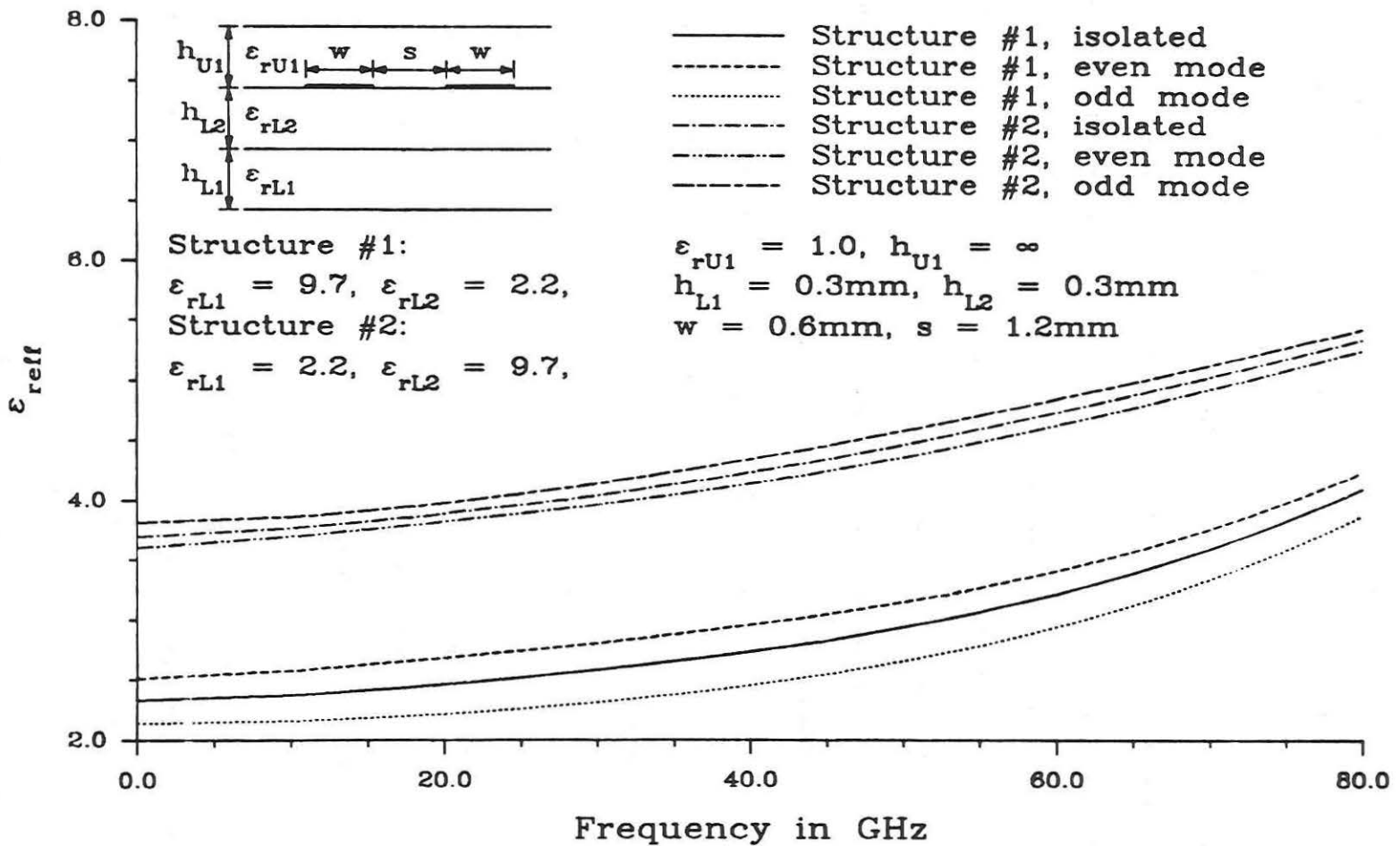
Fig. 4.39. ε_{reff} vs. frequency for open symmetric coupled multilayer microstrips on alumina and RT/duroid 5880 substrate.
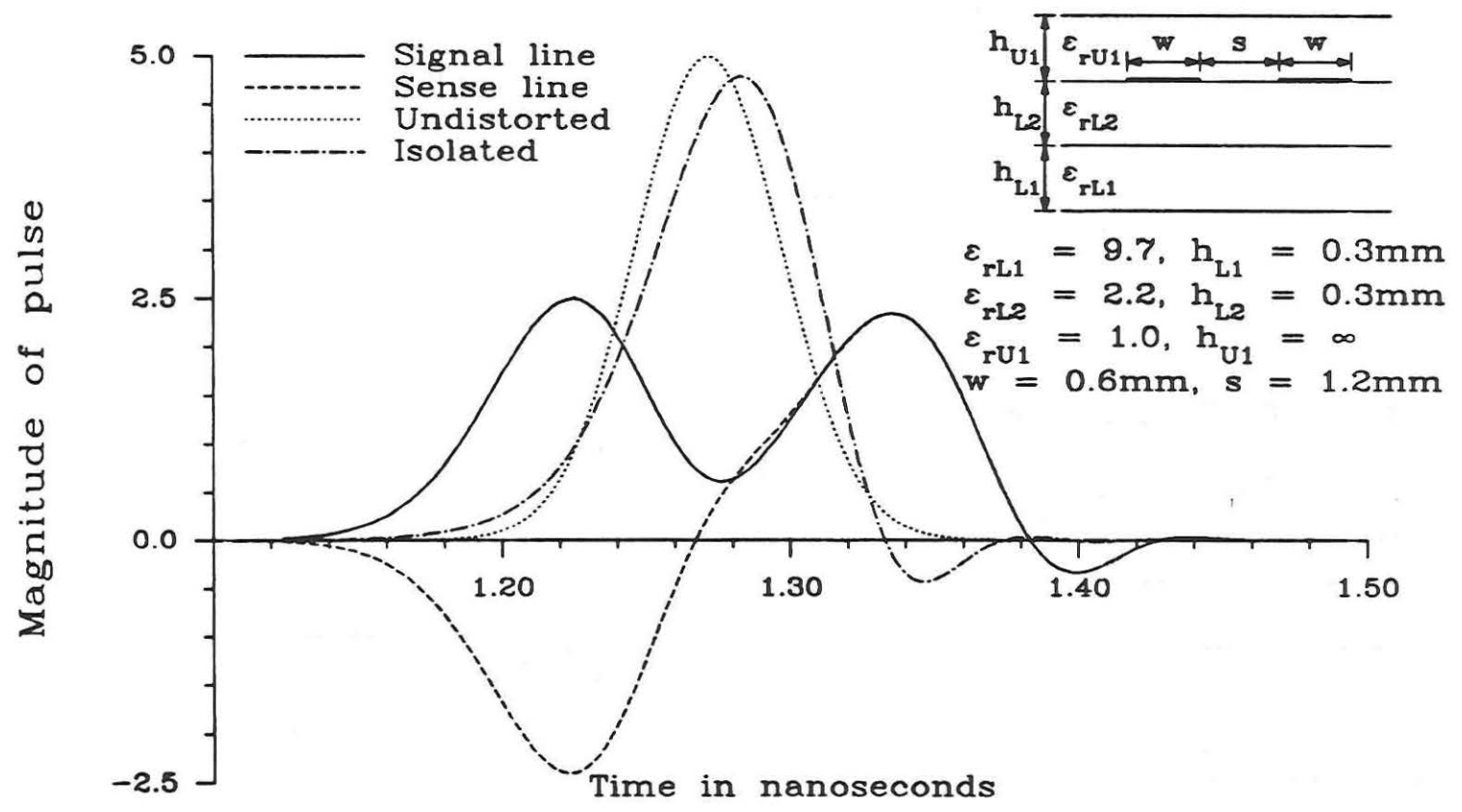
Fig. 4.40. Pulse distortion on multilayer coupled lines, $l = 250$mm,
$\tau = 30$ps, structure #1.
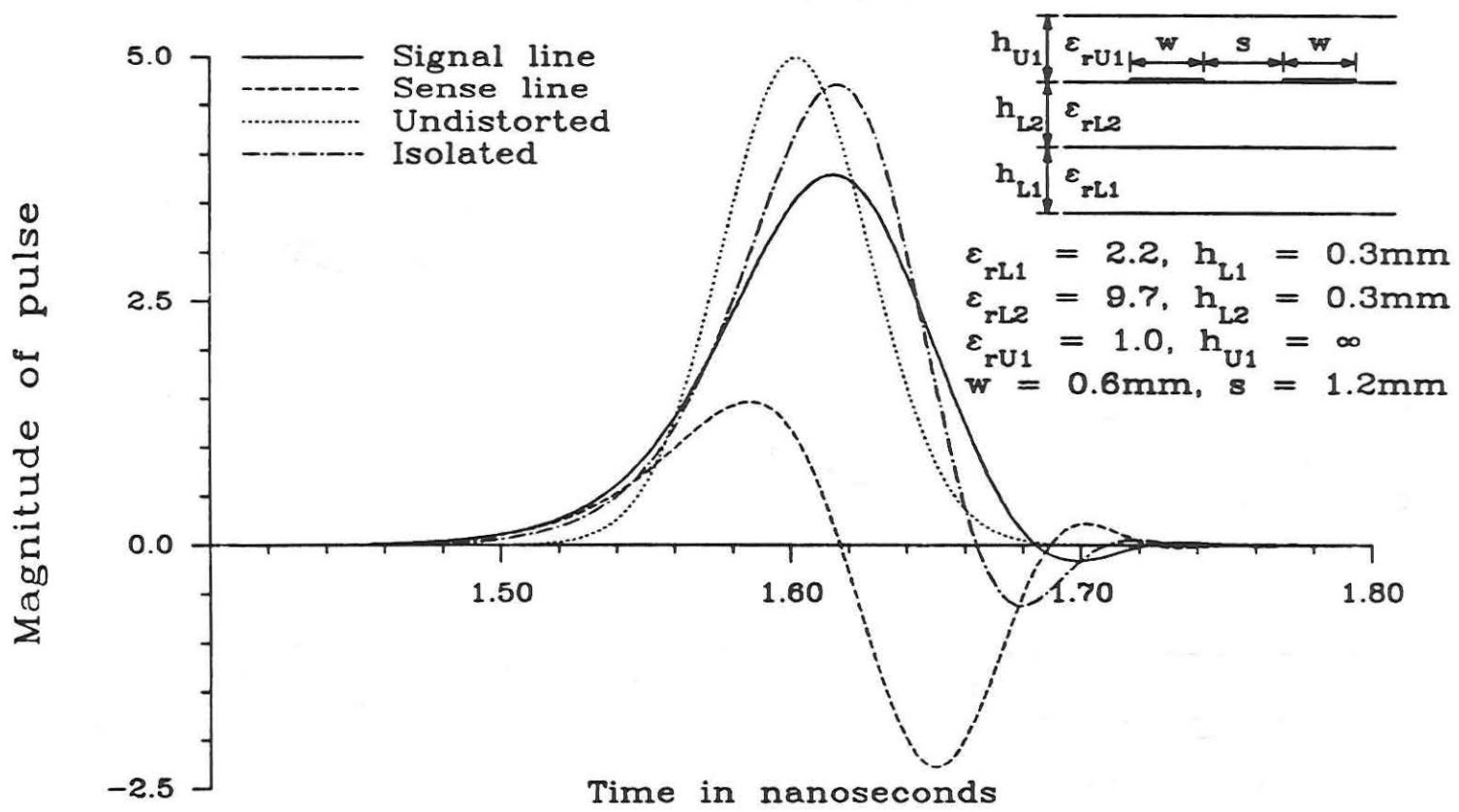
Fig. 4.41. Pulse distortion on multilayer coupled lines, l = 250mm, τ = 30ps, structure #2.

the smaller separation in the even and odd mode ε_{reff} for this configuration. The sense line responses for the two structures are also markedly different. The most important difference between the two responses is that structure #1 has a negative leading sense line response, whereas structure #2 has a positive leading response. This difference arises because the odd mode is faster than the even mode on structure #1, while the even mode is the faster of the two on structure #2. Therefore, changing the relative placement of the the substrate layers has a significant effect on the characteristics of the structure.

Using the generalized Green's function in conjunction with the spectral domain approach allowed the accurate analysis of complex multilayer microstrip structures. Initially, it was shown that the addition of even relatively thin substrate layers with different dielectric constants resulted in very large changes in ε_{reff} for the isolated line, even mode, and odd mode. Then attention was turned to the addition of superstrate layers, particularly with respect to the use of additional superstrates to equalize the even and odd mode phase velocities. While it was possible to match the even and odd modes in the quasi-static region, outside of this region the match was either very narrowband or required impractically large superstrate heights. Next a cover layer was introduced in the two superstrate structure and it was shown that the addition of this shielding layer created a wide variation in ε_{reff} for each of the three cases. Finally, the effect of changing the positions of the substrates was examined, showing that the relative position of the substrates affects not only the magnitude of

the isolated case, but also can cause the even mode ε_{reff} to be lower than the odd mode, something not possible with single substrate structures.

4.3 Zero Coupling Structures

It was shown in the previous section that the dimensions of a multiple superstrate structure could be adjusted to equalize the even and odd mode phase velocities. Unfortunately this type of design has a very narrow bandwidth and matches may not be practical at certain frequencies. The bandwidth limitation arises because the field structure that is responsible for the match lies in the superstrates and, as frequency increases, most of the fields move into the substrate layers. Thus if the even/odd mode matching conditions could be obtained using the substrate layers, then it should be possible to obtain a more broadband match.

In Fig. 4.39, the odd mode ε_{reff} was higher than the even mode ε_{reff} for structure #2. However, if the same structure were completely filled with either of the two dielectric materials instead of a combination of the two, then the odd mode ε_{reff} would be less than the even mode, as is the case with all single layer structures. Therefore there must exist a combination of h_{L1} and h_{L2} which would equalize the even and odd mode phase velocities. The existence of these even/odd mode equalization structures, or zero coupling structures, is due to a mechanism that is similar to the one that was found in the multiple superstrate structures. In order for this match to exist, the dielectric constant of the lower substrate must be less than that of

the upper substrate. In addition, it will be shown that the difference in the dielectric constants must surpass some value that depends in some way on all of the dimensional parameters of the microstrip structure. Thus even if ε_{rL1} is less than ε_{rL2} it may not be possible to equalize the even and odd mode phase velocities.

To study the characteristics of the zero coupling structures, an open symmetric coupled microstrip is used with two substrates below and air above. The total substrate height of the structure, designated h_{total}, is held constant while the heights of the two layers are varied. When h_{L1} is equal to zero, then h_{L2} is equal to h_{total} and the structure has a single substrate with a relative dielectric constant of ε_{rL2}. If h_{L1} is increased until it is equal to h_{total}, then h_{L2} is equal to zero and the structure once again has only a single substrate, this time with a relative dielectric constant of ε_{r1}.

In Fig. 4.42 the upper substrate is chosen to be beryllium oxide and the lower substrate to be either air or RT/duroid. The effective dielectric constants for the isolated, even mode, and odd mode are plotted as h_{L1} varies from zero to $h_{total} = 0.6$ mm. When ε_{rL1} is equal to unity, the places where the even and odd modes have the same ε_{reff}, referred to as the zero coupling points, occur at $h_{L1} \simeq 0.1$ mm and $h_{L1} = 0.6$ mm $= h_{total}$. The second zero coupling point occurs when $h_{L1} = h_{total}$ because this structure is a pure TEM line since the dielectric is homogeneous with a relative dielectric constant of unity. This structure is just two conductors suspended in air above a ground plane. Therefore, whenever the lower substrate is air, then one of the possible zero coupling points will be at $h_{L1} = h_{total}$.
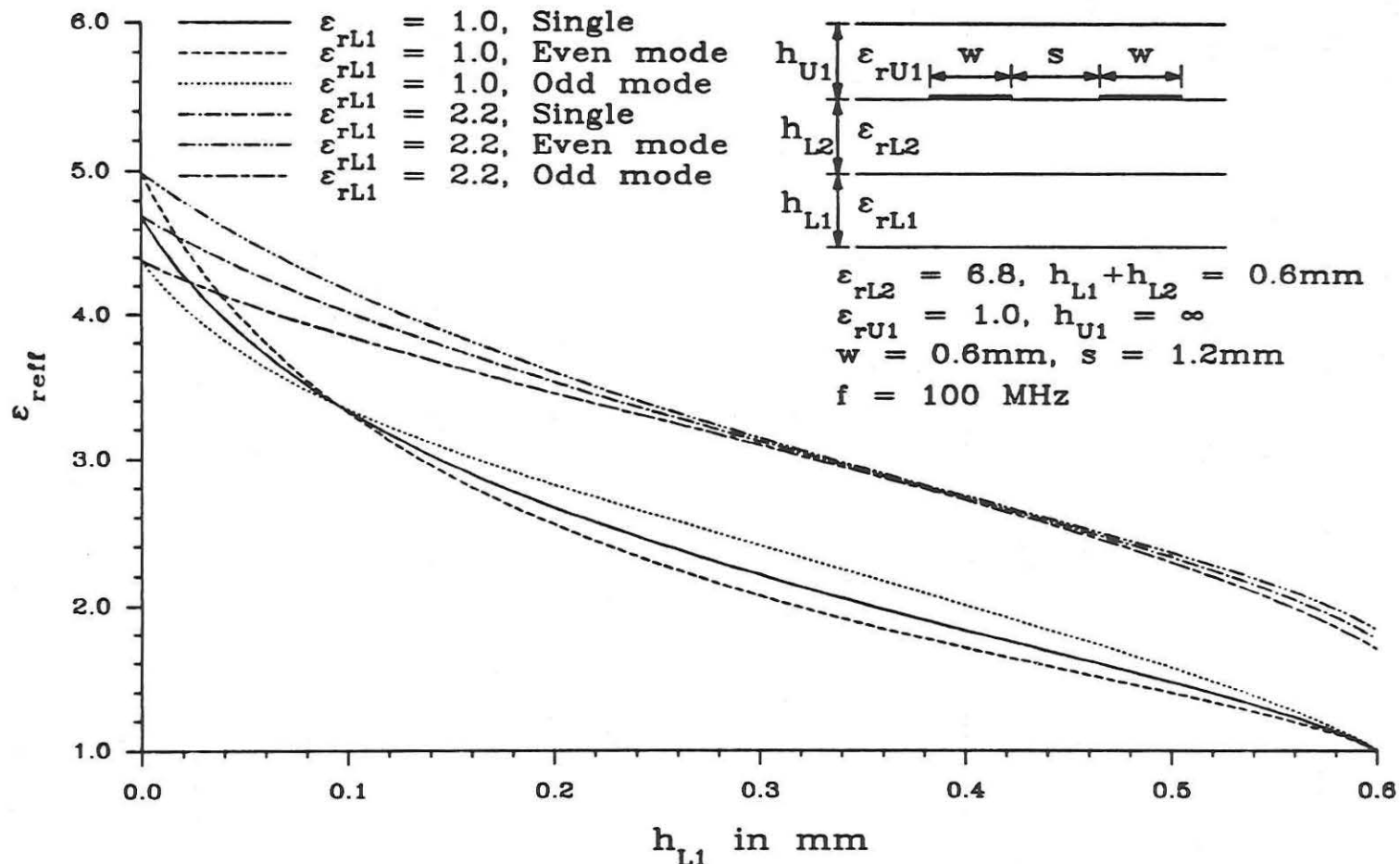
Fig. 4.42. ε_{reff} vs. h_{L1} for open symmetric coupled multilayer microstrips on beryllium oxide, with RT/duroid 5880 and air below.

When the lower substrate is changed to RT/duroid, then there is no value of h_{L1} that makes ε_{reff} the same for the even and odd modes. However, if the dielectric constant of the lower substrate is reduced slightly from 2.2 to 1.8, then zero coupling points will exist. Although there is no geometry that allows the even/odd mode equalization when $\varepsilon_{rL1} = 2.2$, it is possible to significantly minimize the difference in the modal ε_{reff} and therefore drastically reduce the effects of coupling distortion. A relatively good match in ε_{re} and ε_{ro} is obtained when h_{L1} is in between 0.32 and 0.42 mm.

The next two-substrate structure has a layer of gallium arsenide on top of either an RT/duroid or a beryllium oxide lower substrate. When the lower substrate is RT/duroid, there are two zero coupling points, one near $h_{L1} = 0.14$ mm and another near $h_{L1} = 0.54$ mm. The existence of the zero coupling points depends on having a configuration where ε_{re} is less than ε_{ro} and since at each of the dimensional boundaries, i.e. at h_{L1} equal zero and h_{L1} equal h_{total}, ε_{re} is greater than ε_{ro}, there must be at least two points where $\varepsilon_{re} = \varepsilon_{ro}$. The other possibility is that ε_{re} is greater than ε_{ro} for all h_{L1} except for one point where they are equal. This is similar to quadratic equations which always have two roots, although it is possible that the two roots will have the same value.

As the relative dielectric constant of the lower substrate is increased, the locations of the zero coupling points move closer together. At some value of ε_{rL1} the two points will have moved directly on top of each other, giving only one physical zero coupling structure. If ε_{rL1} is increased beyond this point, then the graphs for

the even and the odd modes no longer cross and there are no zero coupling points. This case is shown in Fig. 4.43 for ε_{rL1} = 6.8. Thus with the gallium arsenide and beryllium oxide combination it is not possible to make ε_{re} equal to ε_{ro} nor is there any value of h_{L1} that significantly minimizes the differences between ε_{re} and ε_{ro}.

Note that the condition on ε_{rL1} and ε_{rL2} for the existence of the zero coupling points is not dependent only on the difference between the dielectric constants. A combination of ε_{rL1} = 1.8 and ε_{rL2} = 6.8, which has zero coupling points, has a smaller change in the relative dielectric constants, $\Delta\varepsilon_r$ = 5.0, than the gallium arsenide and beryllium oxide combination, which has a $\Delta\varepsilon_r$ of 5.4. Nor is their existence dependent solely on the ratio of the relative dielectric constants. A structure with ε_{rL1} equal to unity and ε_{rL2} equal to 1.7 has zero coupling points even though the ratio of the relative dielectric constants, 1.7, is less than the gallium arsenide/beryllium oxide ratio, which is 1.79.

One reason that there is not a simple requirement on the dielectric constants of the substrates is that the existence of zero coupling points, especially at lower frequencies, will depend on the parameters of the superstrates as well as the substrates. For simplicity only open microstrips are considered, but the presence of a cover sheet or additional superstrates could also be treated in a similar manner to find the zero coupling points, if they exist, for any structure. Clearly the complexity of the microstrip boundary value problem precludes the possibility of finding a simple formula that determines if the even/odd mode equalization is possible. Indeed, none
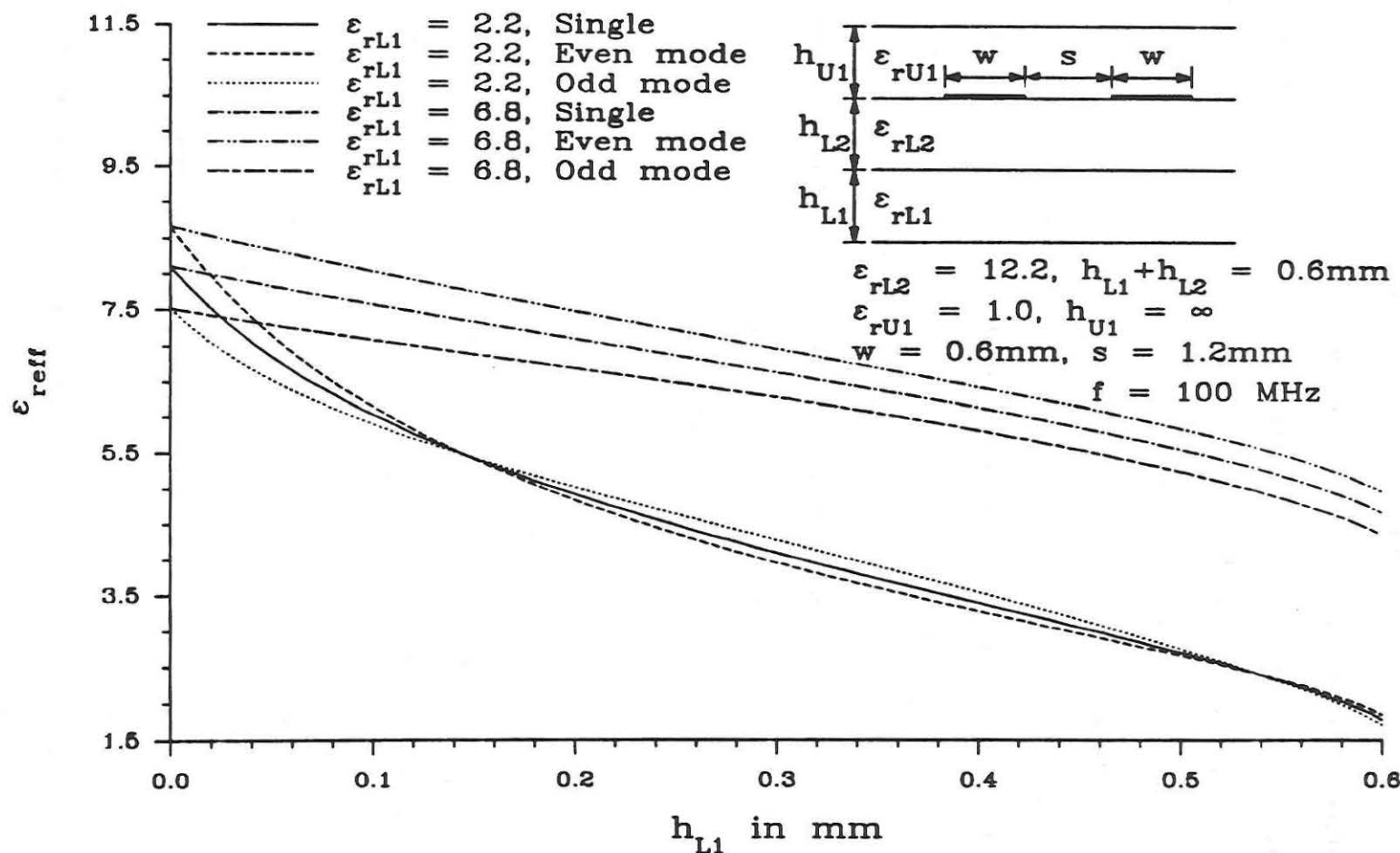
Fig. 4.43. ε_{reff} vs. h_{L1} for open symmetric coupled multilayer microstrips on gallium arsenide, with beryllium oxide and RT/duroid 5880 below.

of the approximate formulas even predict the existence of these zero coupling structures, let alone being able to determine the dimensional requirements. Therefore the analysis of these types of structures must be carried out with a rigorous solution of the boundary value problem.

Figures 4.42 and 4.43 show that zero coupling structures can exist at a single frequency. The next step is to examine the frequency dependence of the zero coupling points. In Figures 4.44 through 4.46, the locations of the zero coupling points, i.e. the value of h_{L1} that makes $\varepsilon_{re} = \varepsilon_{ro}$, are plotted versus frequency, with the frequency on a logarithmic scale. As the operating frequency is increased, ε_{re} and ε_{ro} begin to approach the isolated line value and hence the difference between them decreases. This occurs for all values of h_{L1} since the electrical separation of the conductors increases as frequency increases.

As the frequency to continues increase, a point is reached where it is not possible to uniquely determine a zero coupling point because $\varepsilon_{re} \simeq \varepsilon_{ro}$ for all h_{L1} values. Beyond this frequency, any value of h_{L1} will give a good match for ε_{re} and ε_{ro}. The frequency at which this occurs depends on how close the modal effective dielectric constants need to be for the particular design. A larger tolerance in the separation of the modal effective dielectric constants decreases this frequency and a smaller tolerance increases it. Thus the graphs in Figs. 4.44 through 4.46 are given only up to a certain frequency, after which almost any value of h_{L1} results in less than a tenth of a percent separation in ε_{re} and ε_{ro}.
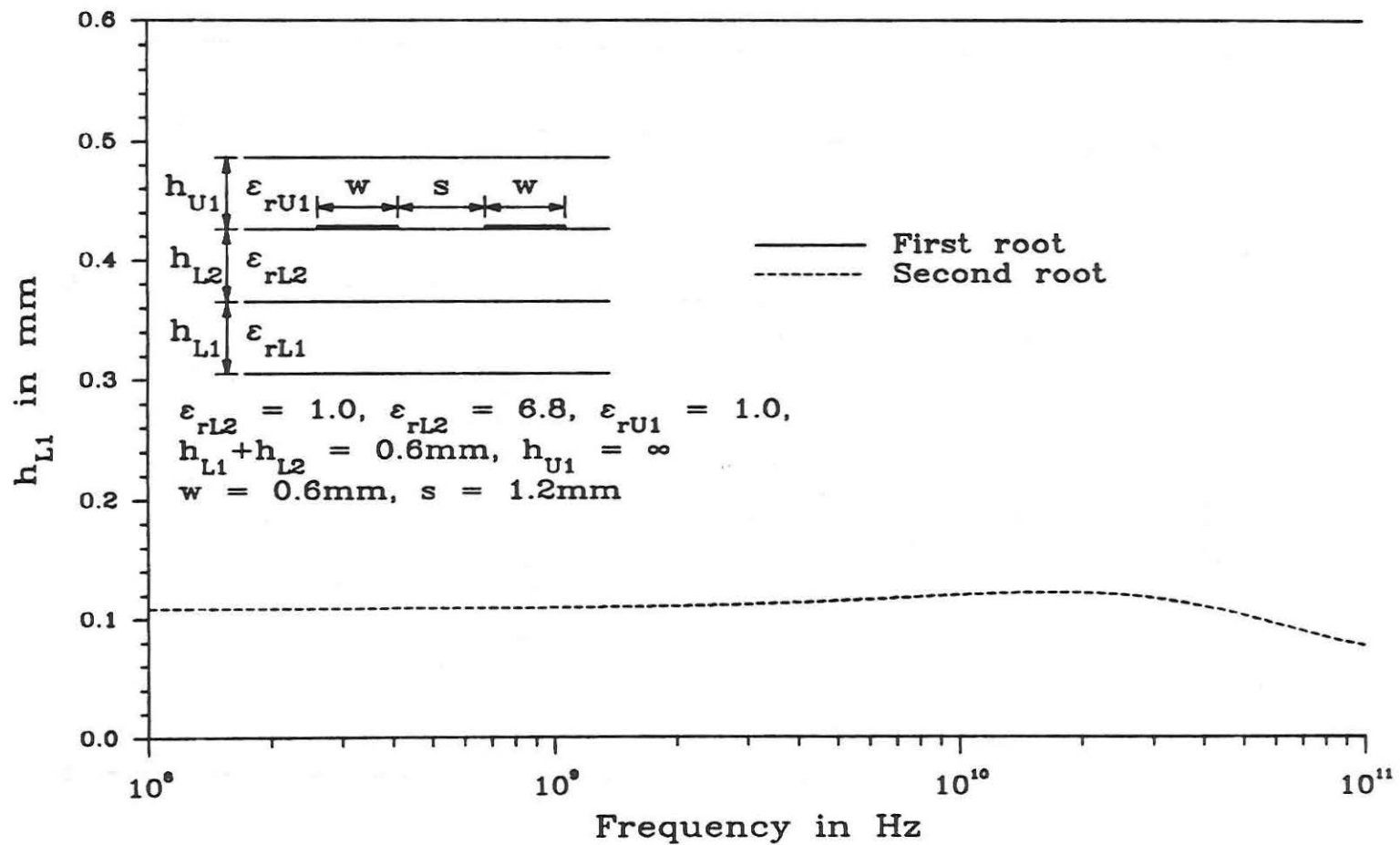
Fig. 4.44. Zero coupling points vs. frequency for coupled microstrips with beryllium oxide substrate, air below.
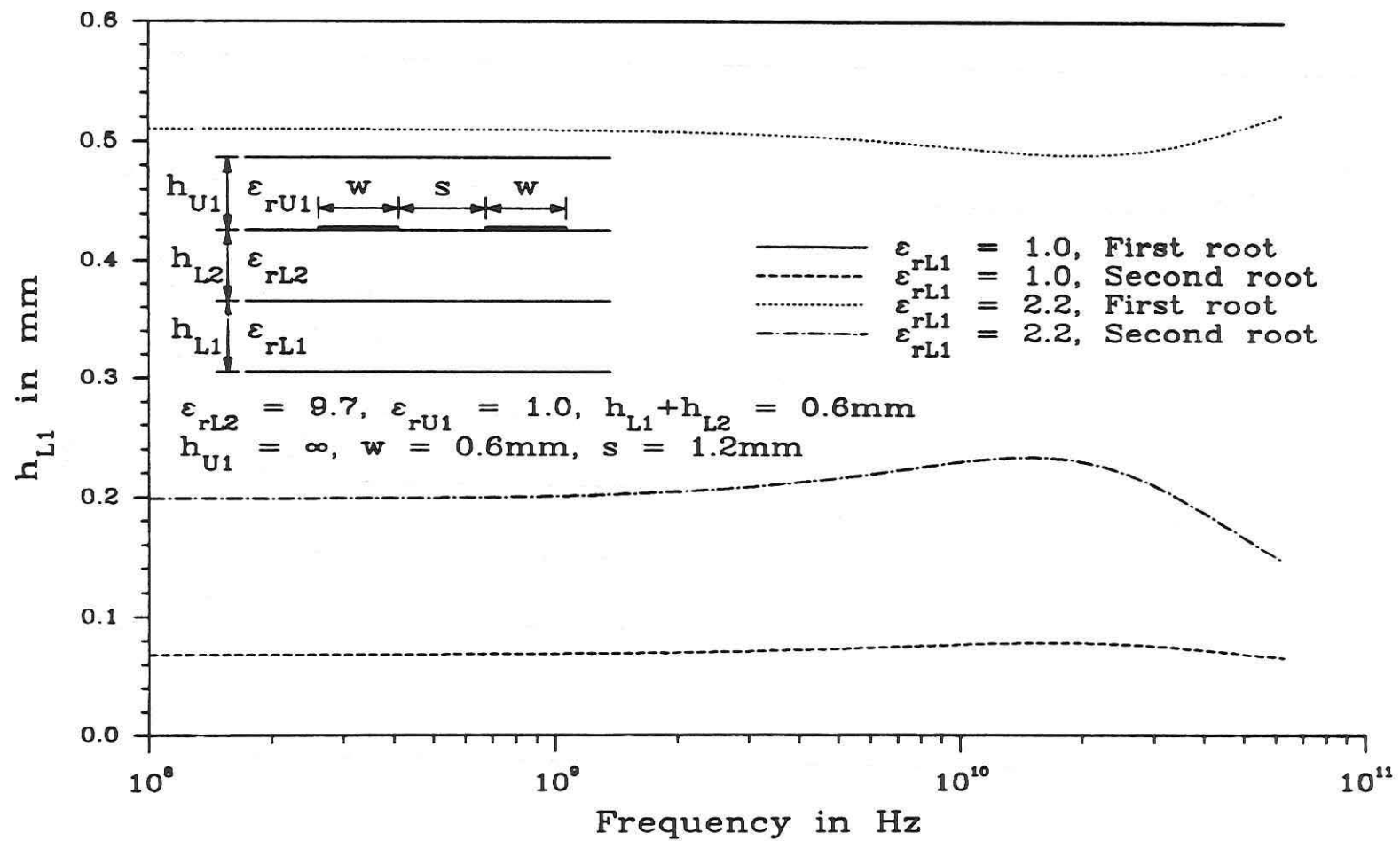
Fig. 4.45. Zero coupling points vs. frequency for coupled microstrips with alumina substrate, air and RT/duroid 5880 below.
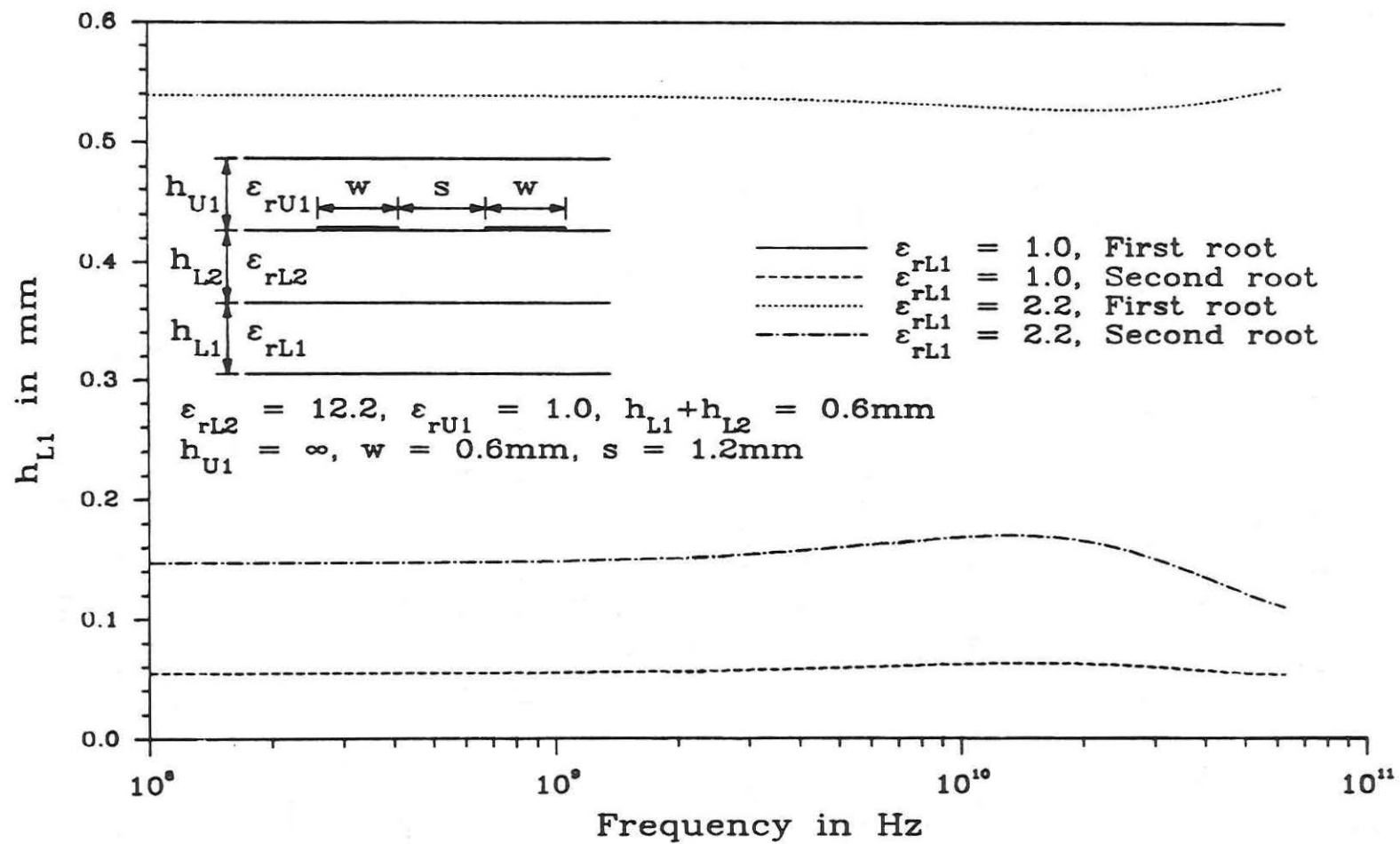
Fig. 4.46. Zero coupling points vs. frequency for coupled microstrips with gallium arsenide substrate, air and RT/duroid 5880 below.

The first zero coupling structure, whose results are shown in Fig. 4.44, uses beryllium oxide as the upper substrate and air as the lower substrate. RT/duroid could not be used for the lower substrate in this case because, as shown in Fig. 4.42, there is no value of h_{L1} which makes ε_{re} equal to ε_{ro}. Because the lower substrate is air, then one of the possible solutions is $h_{L1} = h_{total}$, and since this represents a pure TEM structure, the solution is constant for all frequencies. While this solution is not generally practical in terms of actual circuit design, the second root does represent a possible configuration, with $h_{L1} = 0.11$ mm. The zero coupling point is constant versus frequency in the quasi-static region which ends near 1 GHz. Above this frequency, the h_{L1} value rises slightly, reaching a maximum around 17 GHz, that is 10 percent higher than the low frequency value. As the frequency increases further, the second root begins decreasing slowly until the root location can no longer be determined uniquely. Although there is a fairly rapid change in the root location from 17 to 100 GHz, at these higher frequencies the separation between ε_{re} and ε_{ro} is a relatively weak function of h_{L1}. Thus in this region, increasing the frequency decreases the importance of the location of the root.

The next structure, shown in Fig. 4.45, uses alumina as the upper substrate with either air or RT/duroid below. Increasing the relative dielectric constant of the upper substrate from 6.8 to 9.7 decreases the second zero coupling point for the air substrate from 0.11 to 0.068 mm. The required h_{L1} achieves a maximum near 17 GHz, as before, but with a 14 percent deviation from the low frequency location of the

root. However, the change is only 1.6 percent of the total height of the substrate compared with a 2 percent change when beryllium oxide was the upper substrate. Thus increasing the relative dielectric constant decreases the required height of the lower substrate and stabilizes its value with respect to changes in frequency.

When the dielectric constant of the lower substrate is increased, the required values move closer together and change more rapidly with frequency outside the quasi-static region. In the low frequency region, the first root decreases from 0.6 to 0.51 mm while the second root increases from 0.068 to 0.2 mm. As ε_{rL1} is increased further, then the root locations would move closer and closer to each other until they reach the same value. If ε_{rL1} is increased past this point, then the zero coupling points would no longer exist.

As the frequency is increased above the quasi-static region, then the zero coupling points begin to change, with the first root decreasing slightly and the second root increasing in value. The minimum of the first occurs near 17 GHz and is a decrease of 3.4 percent of h_{total} while the second root reaches a maximum at 15 GHz that is 5.7 percent of h_{total}. Since the changes in the required h_{L1} are relatively small, even with the duroid substrate, using the substrates instead of the superstrates to equalize the modal phase velocities gives very wideband results.

The final structure, shown in Fig. 4.46, replaces the alumina layer with a layer of gallium arsenide and uses the same two materials for the lower substrates. With the air as the lower substrate, the quasi-static value for the roots are at 0.6 and 0.055 mm while the

duroid lower substrate give values of 0.54 and 0.15 mm. Additionally, the deviations in the zero coupling points versus frequency have been reduced from the previous configuration. With air as the lower substrate, the maximum change in h_{L1} is 1.4 percent of h_{total} and with the duroid substrate the first root varies by 1.4 percent and the second by 3.8 percent. Again these very small deviations give this configuration a very wide bandwidth.

Realistic circuit designs require many different center conductor spacings, and so it is important to consider the effects that different spacings have on the location of the zero coupling points. Figures 4.47 and 4.48 show the zero coupling points for two configurations with RT/duroid as the lower substrate and either alumina or gallium arsenide as the upper substrate. Both roots are computed for three different center conductor spacings; 0.6, 1.2, and 1.5 mm.

As the spacing increases, there are two major effects on the zero coupling points; 1) the frequency above which the roots cannot be uniquely defined decreases and 2) the zero coupling points vary more widely with frequency. As the physical spacing of the center conductors increases, the frequency at which the electrical spacing is sufficiently large to isolate the conductors decreases, causing the first effect. The second effect, which might seriously reduce the bandwidth of the design, is offset by the decreasing importance of the root location with frequency in the regions where it is changing rapidly. In addition, larger spacings have less separation between the even and odd mode ε_{reff}, and so it becomes less critical to obtain and exact match.
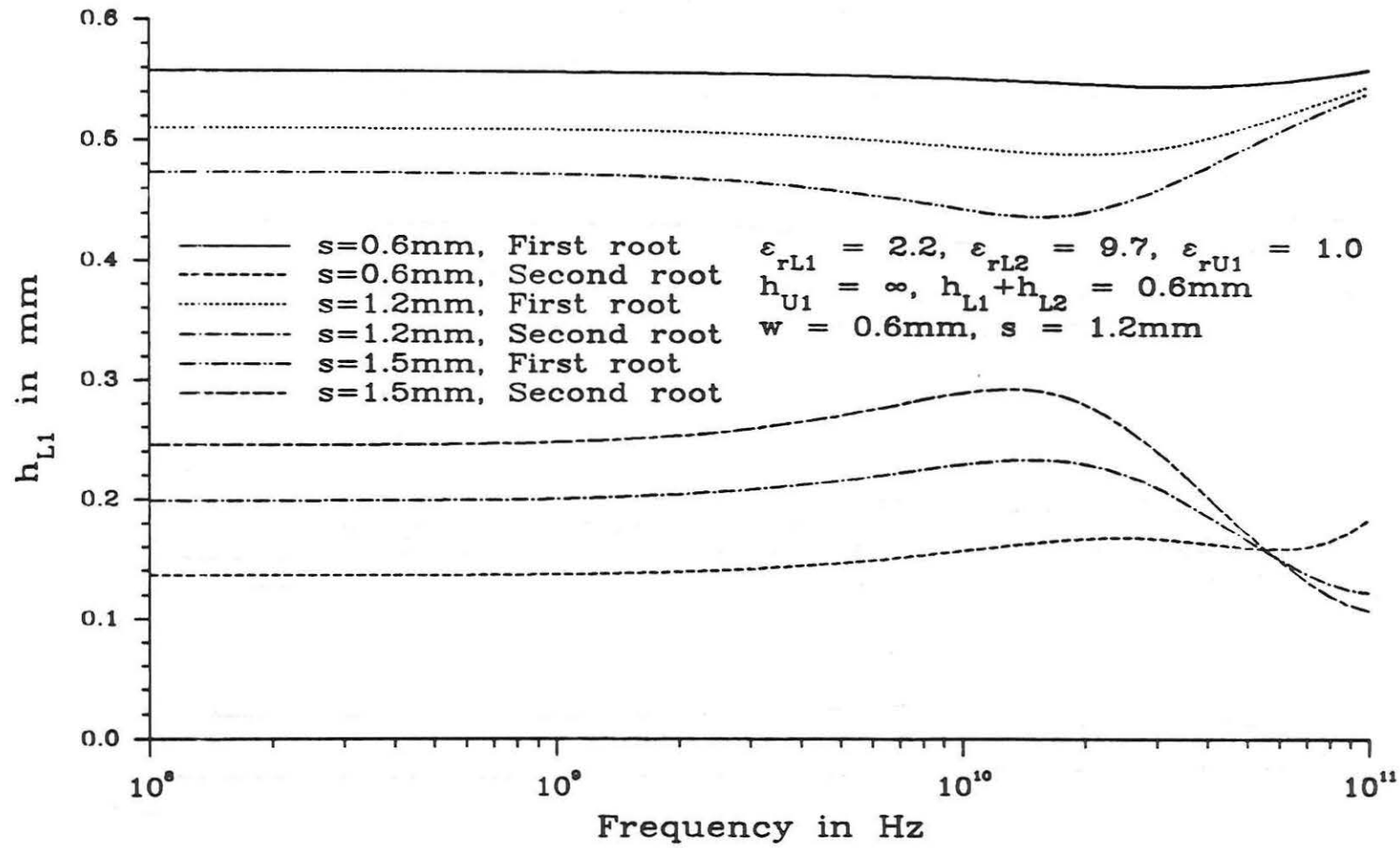
Fig. 4.47. Zero coupling points vs. frequency for coupled microstrips with alumina and RT/duroid 5880 substrate, different spacings.
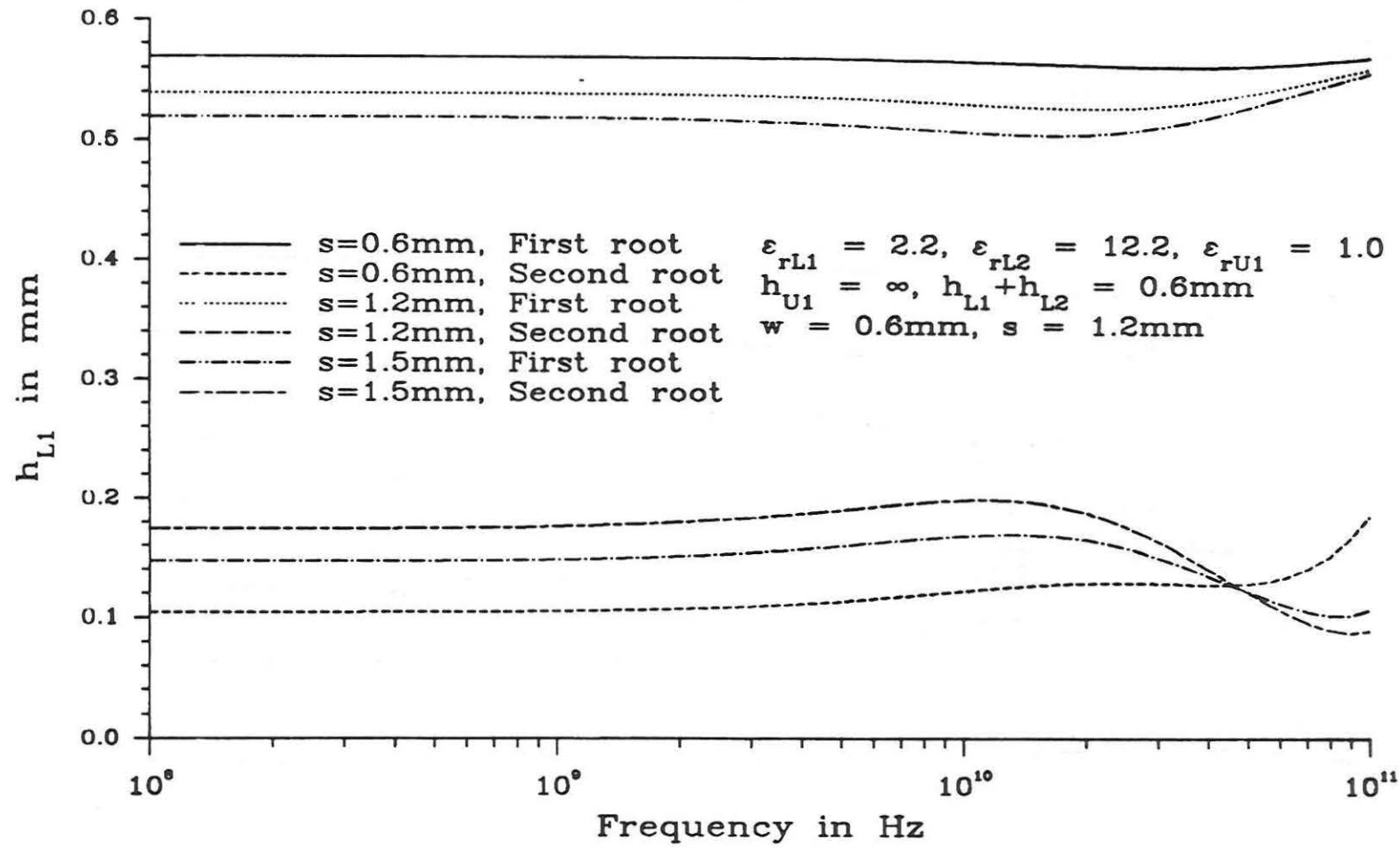
Fig. 4.48. Zero coupling points vs. frequency for coupled microstrips with gallium arsenide and RT/duroid 5880 substrate, different spacings.

Using alumina as the upper substrate, as shown in Fig. 4.47, results in a larger change in h_{L1} as both the spacing and the frequency change as compared to using gallium arsenide as in Fig. 4.48. Changing the center conductor spacing from 0.6 to 1.2 mm gives an 8 percent decrease in the first root and an 11 percent increase in the second with the alumina substrate, and a 5 percent decrease in the first root and a 7 percent increase in the second root when the upper substrate is gallium arsenide. Increasing the spacing on the alumina substrate to 1.5 mm gives 14 and 18 percent changes in the first and second roots, respectively, compared with 8 and 11 percent changes for the gallium arsenide substrate. The zero coupling points on the alumina substrate also vary much more with frequency than those for the gallium arsenide. For both upper substrates, data at the higher frequencies, i.e. around 80 to 100 GHz, are in the region where $\varepsilon_{re} \simeq \varepsilon_{ro}$ for wide ranges of h_{L1}, and so the rapid changes on the roots in this region are not as relevant.

The equalization of the even and odd mode phase velocities has many single frequency advantages; for example it increases the directivity and hence the isolation of microstrip couplers. However, the ability to achieve a good wideband match of the modal phase velocities also offers the possibility of eliminating almost completely the distortion of pulses due to coupling. Since it is impossible to get a perfect even/odd match at all frequencies, the frequency spectrum of the pulse must be considered in order to determine which band of frequencies is the most important in determining the h_{L1} value. If the pulse spectrum has no significant frequency components outside the

quasi-static region, then the low frequency value of h_{L1} could be used. However, if the pulse spectrum is very wide, as is the case with the pulses that have been considered so far, then a value of h_{L1} must be chosen that minimizes the difference between ε_{re} and ε_{ro} over the bandwidth of interest. In general, this value of h_{L1} will be somewhere between the low frequency value and the minimum value, if the first root is used, or the maximum value, if the second root is used.

To illustrate how the zero coupling points can be used to eliminate distortion due to even/odd mode coupling, the single layer open symmetric coupled microstrip on alumina substrate in Fig. 4.10 is redesigned to lower the coupling between the lines. The center conductor widths and spacing are retained and the total height of the substrate is maintained as well, but a layer of duroid is added below the alumina to equalized the even and odd mode phase velocities. This example will use the second root, as shown in Fig. 4.45, although it would be equally valid to use the first root. The low frequency value of h_{L1} is 0.1991 mm and the maximum value, which is at 15 GHz, is 0.2334 mm. The Gaussian pulse has a half width, half maximum of 30 picoseconds, and at 15 GHz, the spectrum has fallen off to 13.5 percent of the maximum value. Also, since the spectrum of the pulse falls off so rapidly, equation (4.1), the lower frequencies are the most important and frequencies higher than 15 GHz do not critically affect the pulse. Using this information, h_{L1} is chosen to be 0.22 mm.

Using the chosen dimensions, ε_{reff} is computed and is shown in Fig. 4.49 as a function of frequency both as a preliminary to the computation of pulse distortion as well as to check the validity of the
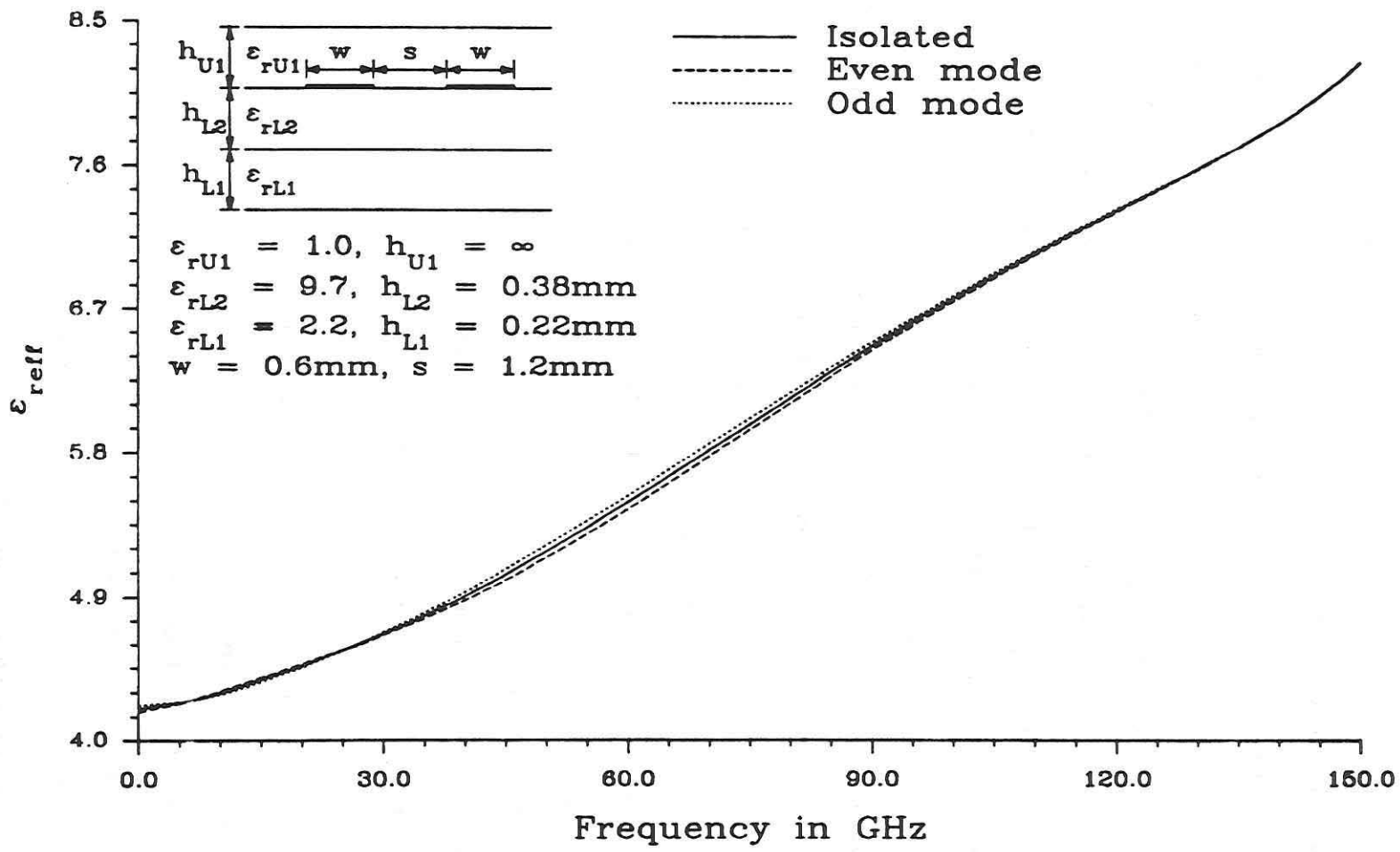
Fig. 4.49. ε_{reff} vs. frequency for low coupling structure using alumina and RT/duroid 5880 substrates.

matching process. In the quasi-static region as well as for

frequencies above 25 GHz, ε_{ro} is greater than ε_{re}, which is a reversal

of the single layer situation, while from 5 to 25 GHz, ε_{re} becomes

slightly larger than ε_{ro}. This design achieves a very good match of

the even and odd mode ε_{reff} at the lower frequencies, with less than a

one percent difference in the values up to 40 GHz. The separation

between ε_{re} and ε_{ro} is the largest in frequencies from 40 to 85 GHz and

reaches a maximum separation of less than 1.6 percent at 60 GHz. When

the frequency gets larger than 100 GHz, the separation between ε_{re} and

ε_{ro} becomes negligible due to the increasing electrical separation of

the center conductors. Since neither the even nor the odd mode ε_{reff}

is consistently larger than the other, the distortion of the pulses

will not appear the same as the previous cases, and it is not

immediately evident whether the leading sense line response will be

positive or negative. However, since the even mode is faster in the

quasi-static region, where the majority of the pulse spectrum lies, it

is probable that the leading response will be due mostly to even mode

components and therefore the sense line should have a positive leading

response.

In addition to reducing the separation of ε_{re} and ε_{ro}, the

addition of the substrate layer drastically changes the dispersive

characteristics of the lines. Comparing Fig. 4.49 with Figs. 4.9 and

4.10, shows that the new structure will be less dispersive than the

single layer alumina structure, but slightly more dispersive than the

configuration with the duroid substrate.

Having computed the effective dielectric constant for the frequency band of interest, the propagation of the pulse on the coupled lines may be computed. Three different distances are used, 62.5, 125, and 250 mm, for comparison with the previous pulse distortion results for both the duroid and alumina substrates. The 62.5 mm distance used in Fig. 4.50 corresponds to the graphs in Fig. 4.15 where the substrate is a single layer of alumina. The 125 mm length used for Fig. 4.51 is comparable to both Fig. 4.16, alumina substrate, and Fig. 4.11, the duroid substrate. Finally, Fig. 4.52 with a distance of 250 mm, corresponds to the results in Fig. 4.12 with a duroid substrate. The isolated line response is not graphed in Figs. 4.50 through 4.52 because there is no visible difference between it and the signal line response.

At 62.5 mm the signal line response is very similar to the undistorted pulse, the only difference being that it is shifted slightly with respect to it. The sense line response is negligible, having a maximum amplitude of less than one percent of the undistorted pulse. At this distance, the lines on the alumina substrate showed a significant reduction in the amplitude of the signal line, about 40 percent, and had a sense line response that approached 50 percent of the undistorted pulse.

As the pulse travels farther on the low coupling structure, reaching 125 mm, dispersion distortion begins to affect the pulse, while coupling distortion is unnoticeable. The signal line is still unaffected by coupling, and the maximum sense line response has risen to only 1.9 percent of the undistorted pulse. Contrasting this is the
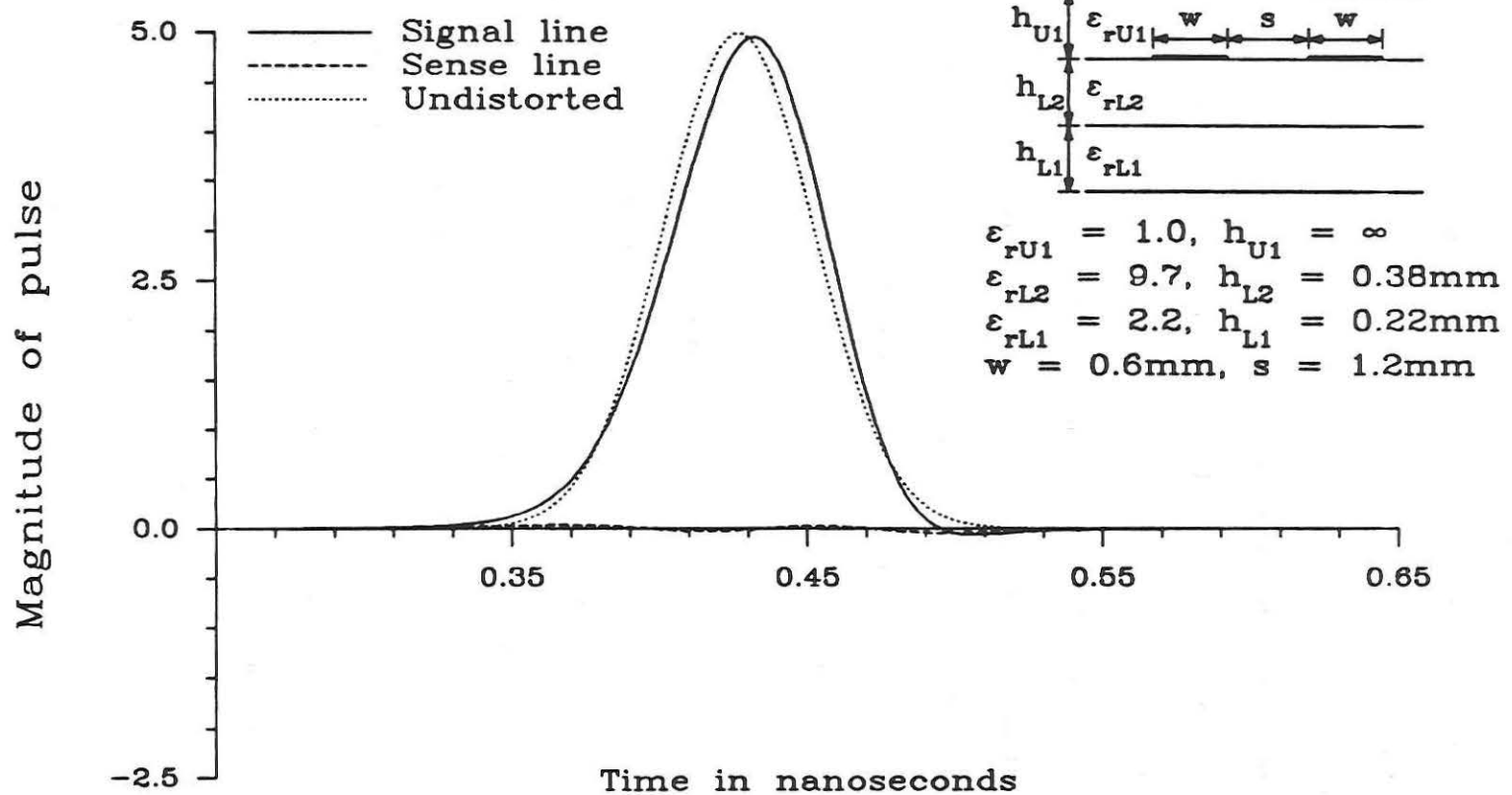
Fig. 4.50. Pulse distortion on low coupling structure, $l = 62.5$mm, $\tau = 30$ps.
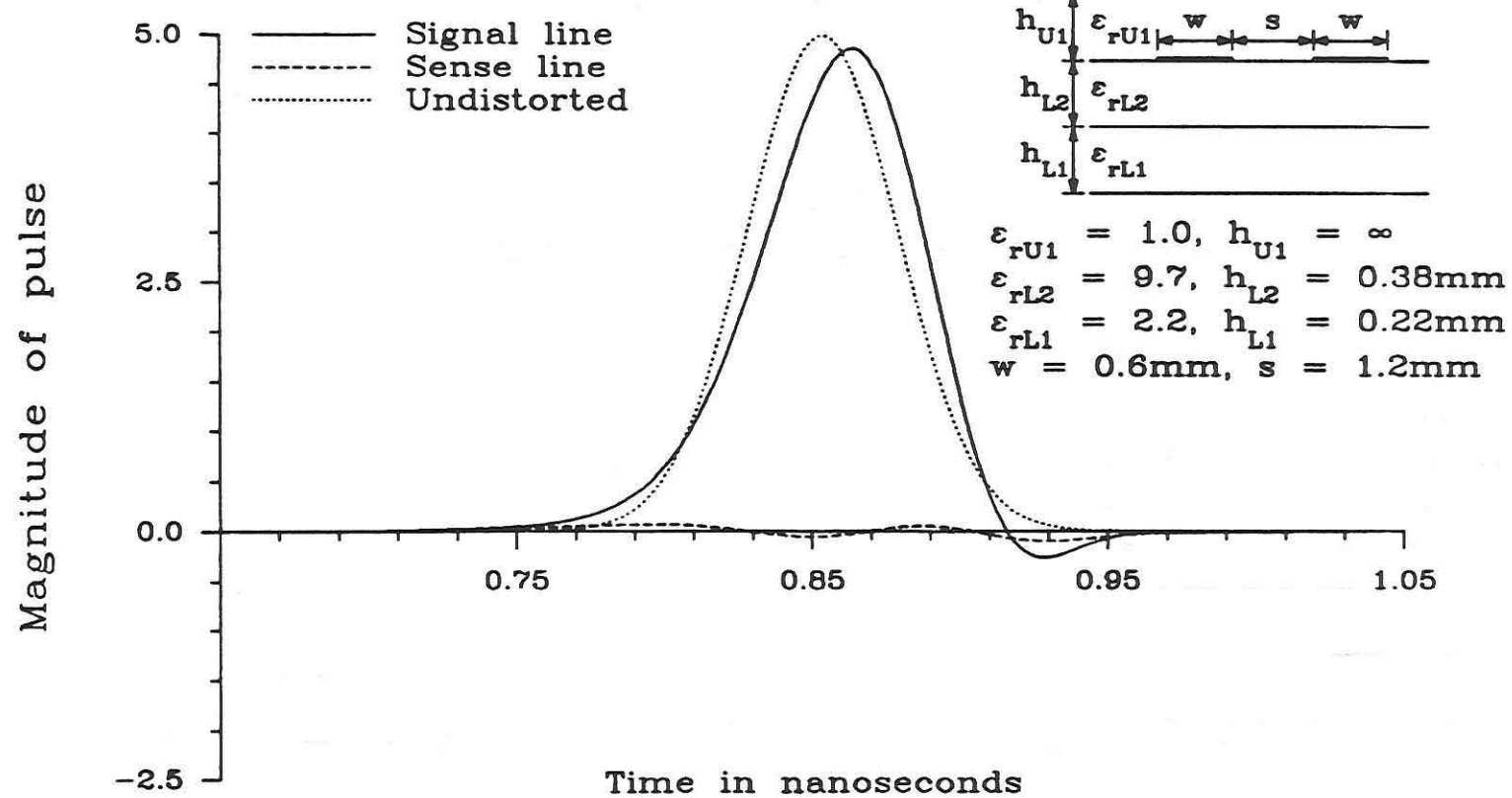
Fig. 4.51. Pulse distortion on low coupling structure, l = 125mm,
τ = 30ps.
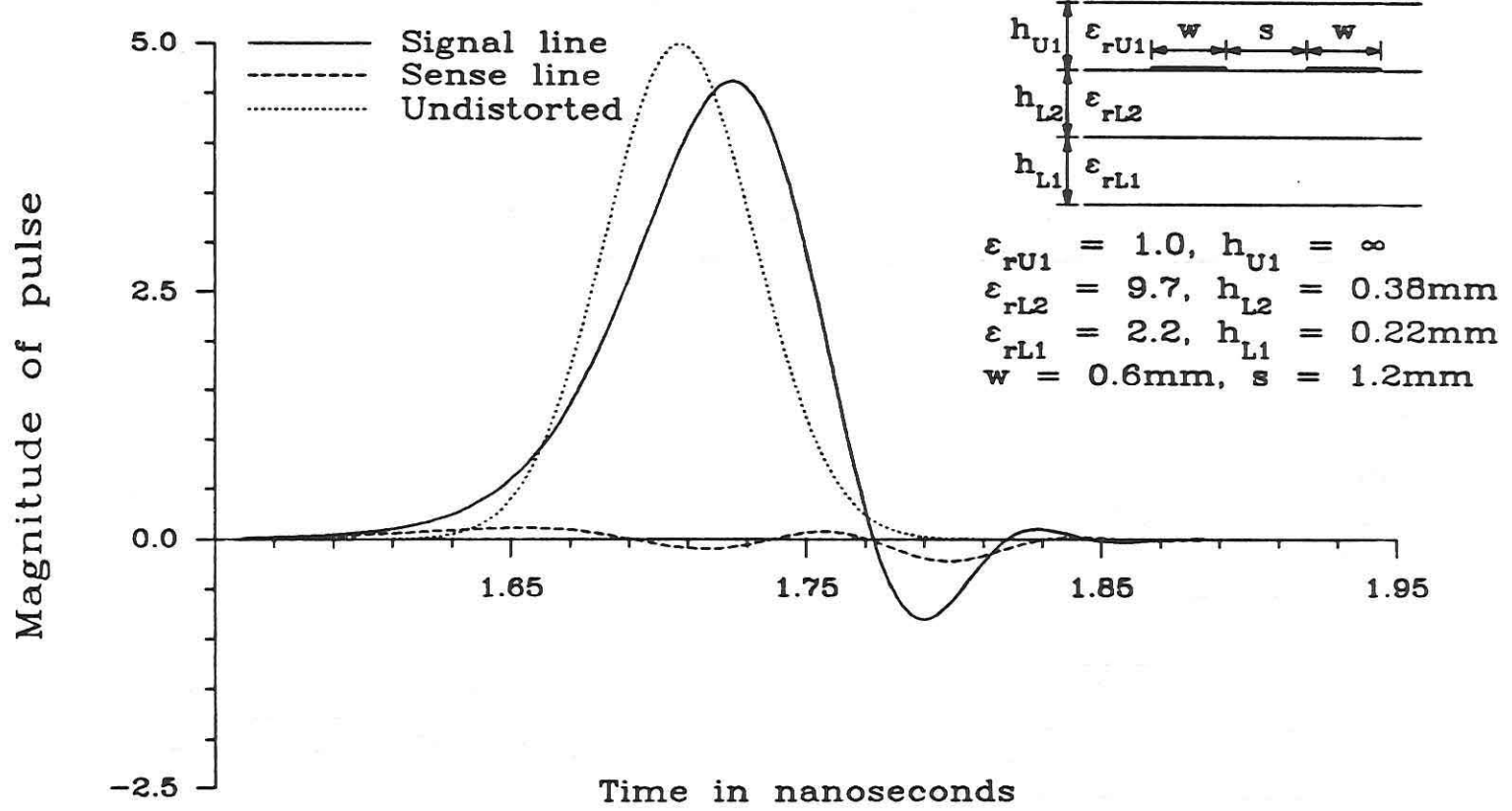
Fig. 4.52. Pulse distortion on low coupling structure, $l = 250mm$, $\tau = 30ps$.

responses shown in Figs. 4.11 and 4.16, where the signal line response on the alumina substrate had almost completely split into the even and odd mode components and on the duroid substrate it had suffered a 20 percent degradation in amplitude.

At the final distance, 250 mm, dispersion distortion has noticeably changed the signal line response, but coupling distortion has been eliminated as a limiting factor for the structure. Even at this distance, there is no visible difference between the graphs of the signal line and the isolated case, indicating that coupling has not affected the intended signal. The sense line shows a maximum response that is just a little over four percent of the undistorted pulse, which indicates that there is a negligible amount of crosstalk between the lines. The previous results for the duroid substrate, shown in Fig. 4.12, indicated that coupling was by far the dominant mechanism, producing a very large spurious response and seriously degrading the signal line pulse.

Thus through the use of the zero coupling points, even/odd mode coupling was essentially eliminated as a distortion mechanism on microstrip lines even though they were in close proximity. Using the correct combination of the two substrate materials enabled the design of a structure that exhibited better isolation between the lines than could be obtained by using either of the substrate materials alone. In spite of the extreme distances traveled, crosstalk was held to negligible levels and the intended signal suffered no noticeable distortion due to coupling.

CHAPTER 5
CONCLUSIONS

Solving the microstrip boundary value problem in a rigorous manner gave a simplified representation of multilayer coupled line structures and enabled the accurate computation of the line parameters as well as pulse propagation for these structures. First, a generalized Green's function was presented as a simple recurrence relation, that is applicable for microstrip structure with any number of superstrates or substrates. Next the Fourier transform and the even/odd mode approach were used to obtain the formulas necessary to analyze the transient response on coupled transmission line, including the effects of dispersion, losses and coupling. Numerical results were presented for both single and multilayer structures, showing that a full wave analysis in necessary for accurate results. Finally, a new method for equalizing the even and odd mode phase velocities through the control of the electrical characteristics of the substrates was presented.

The rigorous solution of the multilayer, multiconductor microstrip boundary value problem with the spectral domain approach resulted in a relatively simple formulation for the microstrip parameters. The derivation began by choosing TE^y and TM^y modes, allowing the problem to be solved separately for each mode, since the modes satisfy the boundary conditions independently in the spectral domain. Next, the SDA was used to obtain the Green's function, initially for a simple

single layer shielded structure. To illustrate the use of the SDA, a six-layer structure was considered and the derivation, resulted in a simple recurrence relation for the Green's function of multilayer configurations. The recurrence relation allows the Green's function to be easily computed with a single subroutine for any arbitrary multilayer structure, rather than requiring a different subroutine for each possible configuration. Finally, the Green's function was also expressed in a form suitable for the calculation of the parameters of slot line and coplanar waveguide type structures.

The even/odd mode analysis and the frequency domain approach were used to derive the formulas for the propagation of finite time domain signals on coupled transmission lines. Using the frequency domain approach simplified the transient analysis of the coupled line system, allowing fast, accurate computation of the output waveforms. The even/odd mode approach made it possible to split the symmetric four-port system into two simpler two-port networks. Combining the even/odd mode analysis with the frequency domain approach gave simple expressions for the time domain response of lossy and dispersive coupled transmission lines. These expressions clearly illustrated how losses, coupling, and dispersion degrade the input signal and how differences in the complex propagation constants for the even and odd modes produce a spurious response on the sense line.

Numerical results for the frequency dependent effective dielectric constant and pulse dispersion for a single layer symmetric coupled microstrip were presented, for different substrate materials, center conductor spacings, and distances. Coupling between the lines

increased when the center conductor spacing was increased, the distance increased, and/or the dielectric constant of the substrate increased. Examining the distortion of pulses at different distances showed that coupling distortion separates the input signal into even and odd mode pulses as the distance gets very large. By studying the effects of center conductor spacing, it was demonstrated that the conditions for uncoupled operation of transmission lines depended not only on the center conductor spacing or substrate height, but also on the substrate materials, the distance over which the lines are coupled, as well as the other dimensions of the structures.

The generalized Green's function was used with the SDA to consider the effects of multiple substrates and superstrates on the characteristics of coupled lines. Adding even a thin lower substrate layer with a different dielectric constant caused significant changes in the ε_{reff} of the isolated case as well as for the even and odd modes. Placing a superstrate layer with the same dielectric constant as the substrate on top of the center conductor interface also had an important effect on the microstrip parameters. By adjusting the height of this superstrate layer, it was possible to equalize the even/odd phase velocities for the structure, although the equalization was good only in the quasi-static region or over a very narrow band of frequencies. When a cover sheet was introduced to the two superstrate structure, ε_{reff} changed over a wide range of values as the height of the cover layer was varied. Finally, it was shown that the relative positions of the substrate layers changes not only the value of ε_{reff} for the isolated case, but can cause the even and odd mode ε_{reff} to

switch in relation to each other.

A new method of equalizing the even and odd mode phase velocities was presented that could obtain a match over a very wide band of frequencies. To overcome the difficulties encountered from using the superstrate equalization scheme, the modal phase velocities were equalized by choosing substrates with the appropriate dimensions and materials. Since for all frequencies most of the fields lie in the substrate layers, this matching procedure gives good results not only in the quasi-static region, but also for frequencies well above it. The appropriate substrate heights for even/odd mode equalization, called zero coupling points, were presented as functions of frequency and center conductor spacing for different substrate materials. Using these zero coupling points, a structure was designed that exhibited better isolation between the adjacent lines than could be obtained by using either of the substrate materials alone. When pulse distortion was considered for this structure, it was shown that the crosstalk was almost non-existent and the input signal had suffered no distortion due to coupling.

CHAPTER 6
RECOMMENDATIONS

Future research in this area would be concerned with increasing the speed and accuracy of the computations and considering both losses and discontinuities in a rigorous manner. To increase the accuracy of the Spectral Domain Approach, more current expansion functions should be used. It is very important to choose 'good' expansion functions since a poor choice will necessitate a very large matrix which may not even converge. Since the SDA is used in a very general manner, it is possible to include the effects of lossy dielectrics by using a complex dielectric constant. This substitution would make the Green's function complex, resulting in two equations (the real and imaginary parts) to be solved for two unknowns, α_z and β_z. The results from this research could be used to verify approximate formulas used for dielectric losses and to specify the range of validity of the approximations.

It was shown in Chapter 3 that differences in the even and odd mode attenuation constants cause coupling and distortion on coupled lines. Currently there are no approximate formulas or results from rigorous solutions available for the modal attenuation constants. The attenuation constants for the even and odd modes could be determined by using the SDA for dielectric losses and by modifying approximate formulations for the conductor losses. Once the modal attenuation constants have been determined as a function of frequency, pulse

distortion on coupled lines due to attenuation distortion and attenuation coupling could be investigated.

To accurately model complete MMIC circuits, the effects of discontinuities must be considered in a rigorous manner. The SDA can be used to consider these problems since the derivation transformed in both the z and x directions. By using the appropriate current expansion functions, which now must be functions of β_z as well as β_x, it will be possible to characterize discontinuities in the z direction of the structure. Discontinuities that might be considered include: abrupt changes in the center conductor width, gaps in the center conductor, bends, crossing lines, etc. These results could then be applied to consider the transient response of very complex circuits.

REFERENCES

[1] *IRE Transactions on Microwave Theory and Techniques,* vol. MTT-3, Mar. 1955.

[2] R. H. Jansen, R. G. Arnold, and I. G. Eddison, "A comprehensive CAD approach to the design of MMIC's up to MM-wave frequencies," *IEEE Trans. Microwave Theory Tech.,* vol. MTT-36, pp. 208-219, Feb. 1988.

[3] J. F. Whitaker, T. B. Norris, G. Mourou, and T. Y. Hsiang, "Pulse dispersion and shaping in microstrip lines," *IEEE Trans. Microwave Theory Tech.,* vol. MTT-35, pp. 41-47, Jan. 1987.

[4] H. A. Wheeler, "Transmission-line properties of parallel strips separated by a dielectric sheet," *IEEE Trans. Microwave Theory Tech.,* vol. MTT-12, pp. 172-185, Mar. 1965.

[5] W. J. Getsinger, "Microstrip dispersion model," *IEEE Trans. Microwave Theory Tech.,* vol. MTT-21, pp. 34-39, Jan. 1973.

[6] O. P. Jain, V. Makios, and W. J. Chudobiak, "Coupled-mode model of dispersion in microstrip," *Electron. Lett.,* vol. 7, pp. 405-407, 15 July 1971.

[7] M. Kobayashi, "Important role of inflection frequency in the dispersive properties of microstrip lines," *IEEE Trans. Microwave Theory Tech.,* vol. MTT-30, pp. 2057-2059, Nov. 1982.

[8] P. Bhartia and P. Pramanick, "An accurate description of dispersion in microstrip," *Microwave J.,* vol. 26, pp. 89-96, Dec. 1983.

[9] P. Bhartia and P. Pramanick, "A new microstrip dispersion model," *IEEE Trans. Microwave Theory Tech.,* vol. MTT-32, pp. 1379-1384, Oct. 1984.

[10] H. J. Carlin, "A simplified circuit model for microstrip," *IEEE Trans. Microwave Theory Tech.,* vol. MTT-21, pp. 589-591, Sept. 1973.

[11] A. S. Omar and K. Schünemann, "Formulation of the singular integral equation technique for planar transmission lines," *IEEE Trans. Microwave Theory Tech.,* vol. MTT-33, pp. 1313-1322, Dec. 1985.

[12]   R. Mittra and T. Itoh, "A new technique for the analysis of the dispersion characteristics of microstrip lines," *IEEE Trans. Microwave Theory Tech.*, vol. MTT-19, pp. 47-56, Jan. 1971.

[13]   D. G. Corr and J. B. Davies, "Computer analysis of the fundamental and higher order modes in single and coupled microstrip," *IEEE Trans. Microwave Theory Tech.*, vol. MTT-20, pp. 669-678, Oct. 1972.

[14]   X. Zhang, J. Fang, K. K. Mei, and Y. Liu, "Calculations of the dispersive characteristics of microstrips by the time-domain finite difference method," *IEEE Trans. Microwave Theory Tech.*, vol. MTT-36, pp. 263-267, Feb. 1988.

[15]   J. Dekelva and V. Roje, "Accurate numerical solution of coupled integral equations for microstrip transmission line," *Proc. Inst. Elec. Eng.*, vol. 134, pt. H, pp. 163-168, Apr. 1987.

[16]   H. Ermert, "Guided modes and radiation characteristics of covered microstrip lines," *Arch. Elek. Ubertrang.*, vol. 30, pp. 65-70, 1976.

[17]   H. Ermert, "Field Distribution of microstrip guided waves," *Arch. Elek. Ubertrang.*, vol. 31, pp. 145-149, 1977.

[18]   E. J. Delinger, "A frequency dependent solution for microstrip transmission lines," *IEEE Trans. Microwave Theory Tech.*, vol. MTT-19, pp. 30-39, Jan. 1971.

[19]   T. Itoh and R. Mittra, "Spectral-domain approach for calculating the dispersion characteristics of microstrip lines," *IEEE Trans. Microwave Theory Tech.*, vol. MTT-21, pp. 496-499, July 1973.

[20]   T. Itoh and R. Mittra, "A technique for computing dispersion characteristics of shielded microstrip lines," *IEEE Trans. Microwave Theory Tech.*, vol. MTT-22, pp. 896-898, Oct. 1974.

[21]   R. H. Jansen, "A moment method for covered microstrip dispersion," *Arch. Elek. Ubertrang.*, vol. 29, pp. 17-20, 1975.

[22]   T. Itoh, "Spectral domain immitance approach for dipsersion characteristics of generalized printed transmission lines," *IEEE Trans. Microwave Theory Tech.*, vol. MTT-28, pp. 733-736, July 1980.

[23]   N. K. Das and D. M. Pozar, "A generalized spectral-domain Green's function for multilayer dielectric substrates with application to multilayer transmission lines," *IEEE Trans. Microwave Theory Tech.*, vol. MTT-35, pp. 326-335, Mar. 1987.

[24] R. H. Jansen, "The spectral-domain approach for microwave
      integrated circuits," *IEEE Trans. Microwave Theory Tech.*, vol.
      MTT-33, pp. 1043-1056, Oct. 1985.

[25] J. Reed and G. J. Wheeler, "A method of analysis of symmetrical
      four-port networks," *IRE Trans. Microwave Theory Tech.*, vol.
      MTT-4, pp. 246-252, Oct. 1956.

[26] V. K. Tripathi, "Asymmetric coupled transmission lines in an
      inhomogeneous medium," *IEEE Trans. Microwave Theory Tech.*, vol.
      MTT-23, pp. 734-739, Sept. 1975.

[27] S. Akhtarzad, T. R. Rowbotham, and P. B. Johns, "The design of
      coupled microstrip lines," *IEEE Trans. Microwave Theory Tech.*,
      vol. MTT-23, pp. 486-492, June 1975.

[28] R. Garg and I. J. Bahl, "Characteristics of coupled microstrip-
      lines," *IEEE Trans. Microwave Theory Tech.*, vol. MTT-27, pp.
      700-705, July 1979.

[29] V. K. Tripathi, "A dispersion model for coupled microstrip," *IEEE
      Trans. Microwave Theory Tech.*, vol. MTT-34, pp. 66-71, Jan. 1986.

[30] W. J. Getsinger, "Dispersion of parallel-coupled microstrip," *IEEE
      Trans. Microwave Theory Tech.*, vol. MTT-21, pp. 144-145, Mar.
      1973.

[31] M. Kirschning and R. H. Jansen, "Accurate wide-range design
      equations for the frequency-dependent characteristics of parallel
      coupled microstrip lines," *IEEE Trans. Microwave Theory Tech.*,
      vol. MTT-32, pp. 83-90, Jan. 1984.

[32] M. K. Krage and G. I. Haddad, "Frequency dependent characteristics
      of microstrip transmission lines," *IEEE Trans. Microwave Theory
      Tech.*, vol. MTT-20, pp. 678-688, Oct. 1972.

[33] R. H. Jansen, "High-speed computation of single and coupled
      microstrip parameters including dispersion, high-order modes, loss
      and finite strip thickness," *IEEE Trans. Microwave Theory Tech.*,
      vol. MTT-26, pp. 75-82, Feb. 1978.

[34] T. M. Mu, H. Ogawa, and T. Itoh, "Characteristics of multiconduc-
      tor, asymmetric, slow-wave microstrip transmission lines," *IEEE
      Trans. Microwave Theory Tech.*, vol. MTT-34, pp. 1471-1477, Dec.
      1986.

[35] A. R. Djordjevic, T. K. Sarkar, and R. F. Harrington, "Analysis of
      lossy transmission lines with arbitrary terminal networks," *IEEE
      Trans. Microwave Theory Tech.*, vol. MTT-34, pp. 660-666, June
      1986.

[36] A. R. Djordjevic, T. K. Sarkar, and R. F. Harrington, "Time-domain response of multiconductor transmission lines," *Proc. IEEE*, vol. 75, pp. 743-764, June 1987.

[37] K. K. Li., G. Arjavalingam, A. Dienes, and J. R. Whinnery, "Propagation of picosecond pulses on microwave striplines," *IEEE Trans. Microwave Theory Tech.*, vol. MTT-30, pp. 1270-1273, Aug. 1982.

[38] G. Hasnain, G. Arjavalingam, A. Dienes, and J. R. Whinnery, "Dispersion of picoseconc pulses on microstrip transmission lines," *Picosecond Optoelectronics*, vol. 439, pp. 159-163, Aug. 1983.

[39] R. L. Veghte and C. A. Balanis, "Dispersion of transient signals in microstrip transmission lines," in *IEEE MTT-S Dig.* (Baltimore MD), 1986, pp. 691-694.

[40] R. L. Veghte and C. A. Balanis, "Dispersion of transient signals in microstrip transmission lines," *IEEE Trans. Microwave Theory Tech.*, vol. MTT-34, pp. 1427-1436, Dec. 1986.

[41] R. L. Veghte, "Dispersion of transient signals in microstrip transmission lines," M. S. Thesis, Arizona State University, 1986.

[42] B. H. Kolner, D. M. Bloom, and P. S. Cross, "Picosecond optical electronic measurements," *Picosecond Optoelectronics*, vol. 439, pp. 149-152, Aug. 1983.

[43] J. F. Whitaker, *et. al.*, "Propagation model for ultrafast signals on superconducting dispersive striplines," *IEEE Trans. Microwave Theory Tech.*, vol. MTT-36, pp. 277-285, Feb. 1988.

[44] T. Leung and C. A. Balanis, "Attenuation distortion of transient signals in microstrip," *IEEE Trans. Microwave Theory Tech.*, vol. MTT-36, pp. 765-769, Apr. 1988.

[45] T. Leung and C. A. Balanis, "Pulse dispersion distortion in open and shielded microstrips using the spectral-domain method," *IEEE Trans. Microwave Theory Tech.*, vol. MTT-36, pp. 1223-1226, July 1988.

[46] T. Leung, "Pulse signal distortions in microstrips," M. S. Thesis, Arizona State University, 1987.

[47] C. K. Tzuang and T. Itoh, "High-speed pulse transmission along a slow-wave CPW for monolithic microwave integrated circuits," *IEEE Trans. Microwave Theory Tech.*, vol. MTT-35, pp. 697-704, Aug. 1987.

[48] G. Hasnain, A. Dienes, and J. R. Whinnery, "Dispersion of picosecond pulses in coplanar transmission lines," *IEEE Trans. Microwave Theory Tech.*, vol. MTT-34, pp. 738-741, June 1986.

[49] R. W. Jackson, "Coplanar waveguide vs. microstrip for millimeter wave integrated circuits," in *IEEE MTT-S Dig.* (Baltimore MD), 1986, pp. 699-702.

[50] M. Kobayashi and F. Ando, "Dispersion characteristics of open microstrip lines," *IEEE Trans. Microwave Theory Tech.*, vol. MTT-35, pp. 101-105, Feb. 1987.

[51] W. R. LePage, *Complex Variables and the Laplace Transform for Engineers*, Dover Publications Inc., New York, 1961.

[52] R. H. Jansen, "A novel CAD tool and concept compatible with the requirements of multilayer GaAs MMIC technology," in *IEEE MTT-S Dig.* (St. Louis, MO), 1985 pp. 711-714.

APPENDIX A

GREEN'S FUNCTION FOR GENERALIZED PLANAR STRUCTURE

GREEN'S FUNCTION FOR GENERALIZED PLANAR STRUCTURE

Efficient solution of printed circuit transmission lines with the Spectral Domain Approach (SDA) requires a closed form expression for the modal input impedances, $\widetilde{Z}^{TE}$ and $\widetilde{Z}^{TM}$. The solution begins by solving the boundary value problem for a six layer structure, first for the TM^y mode and then for the TE^y mode. This derivation shows a pattern that leads to the recurrence relation presented in section 2.3.8.

Since TE^y and TM^y modes are being used, the boundary conditions can be enforced separately for each mode. In order to simplify the notation, a different geometry is used for the derivation, shown in figure A.1. The structure is surrounded perfect electric conductors on all four sides, i.e. at $x = a$, $x = -a$, $y = h_1$, $y = h_1 + h_2 + h_3 + h_4 + h_5 + h_6$. Non-shielded structures can be considered by letting $a \longrightarrow \infty$, $h_1 \longrightarrow \infty$, and/or $h_6 \longrightarrow \infty$ as is appropriate for the structure. For clarity, only one center conductor is shown, but any finite number could be considered. Beginning with the TM^y mode first, the appropriate vector potentials, $\widetilde{A}_{yi}(\beta_x, y, \beta_z)$, for each of the six regions are chosen as follows:

REGION 1: $(0 \leq y \leq h_1)$

$$\widetilde{A}_{y1} = \widetilde{B}_1(\beta_x, \beta_z) \cosh(\alpha_{y1} y) \tag{A.1a}$$

REGION 2: $(h_1 \leq y \leq d_2, \ d_2 = h_1 + h_2)$

$$\widetilde{A}_{y2} = \widetilde{B}_{2A}(\beta_x, \beta_z) \cosh[\alpha_{y2}(d_2 - y)] + \widetilde{B}_{2B}(\beta_x, \beta_z) \sinh[\alpha_{y2}(d_2 - y)] \tag{A.1b}$$
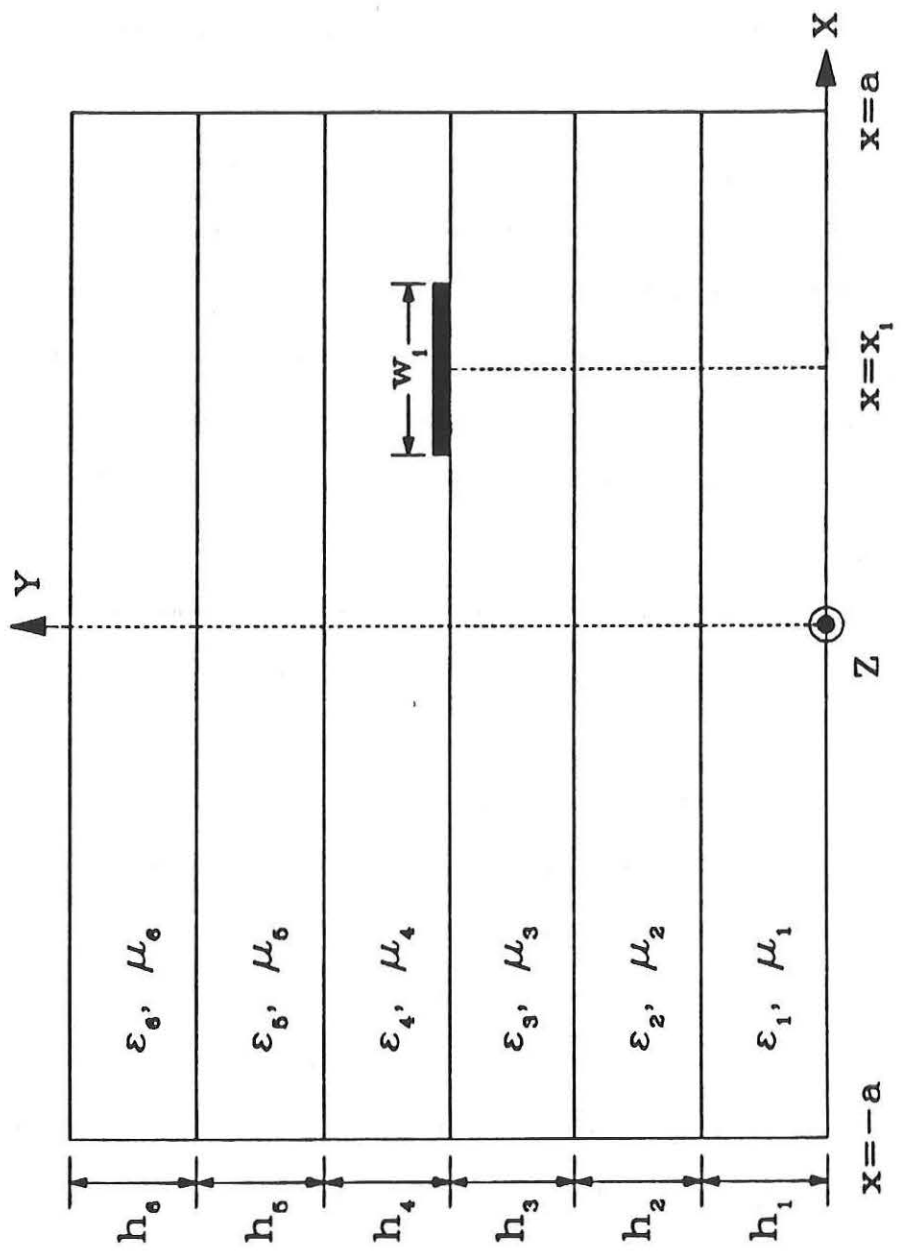
Fig. A.1. Geometry of six-layer multiconductor microstrip structure.

REGION 3: $(d_2 \leq y \leq d_3, \ d_3 = h_1 + h_2 + h_3)$

$$A_{y3} = B_{3A}(\beta_x, \beta_z) \cosh[\alpha_{y3}(d_3 - y)] + B_{3B}(\beta_x, \beta_z) \sinh[\alpha_{y3}(d_3 - y)] \qquad \text{(A.1c)}$$

REGION 4: $(d_3 \leq y \leq d_4, \ d_4 = h_1 + h_2 + h_3 + h_4)$

$$A_{y4} = B_{4A}(\beta_x, \beta_z) \cosh[\alpha_{y4}(y - d_3)] + B_{4B}(\beta_x, \beta_z) \sinh[\alpha_{y4}(y - d_3)] \qquad \text{(A.1d)}$$

REGION 5: $(d_4 \leq y \leq d_5, \ d_5 = h_1 + h_2 + h_3 + h_4 + h_5)$

$$A_{y5} = B_{5A}(\beta_x, \beta_z) \cosh[\alpha_{y5}(y - d_4)] + B_{5B}(\beta_x, \beta_z) \sinh[\alpha_{y5}(y - d_4)] \qquad \text{(A.1e)}$$

REGION 6: $(d_5 \leq y \leq d_6, \ d_6 = h_1 + h_2 + h_3 + h_4 + h_5 + h_6)$

$$A_{y6} = B_6(\beta_x, \beta_z) \cosh[\alpha_{y6}(d_6 - y)] \qquad \text{(A.1f)}$$

Where the $B_N(\beta_x, \beta_z)$'s are unknown functions of the transform variables, which are to be determined from the boundary conditions. They are abbreviated as B_N throughout. A_{y1} and A_{y6} are chosen based on; 1) the tangential $\underline{E}$ fields vanishing at $y = 0$ (at ground plane) and 2) the tangential $\underline{E}$ fields vanishing at $y = d_6$ (at the cover sheet). If the structure doesn't have a cover sheet, i.e. it is an open structure, then $d_6 \longrightarrow \infty$ because $h_6 \longrightarrow \infty$ and the fields at infinity must also vanish due to the outward radiation condition. Because the TM^y mode allows either the x or z directed fields to be used to enforce the boundary conditions, only the x directed electric and magnetic fields will be given. The six vector potentials in equations (A.1a-f) are used with equations (2.12a-f) to calculate the fields in each region.

REGION 1:

$$E_{x1}^{TM} = - B_1 \frac{\beta_x \alpha_{y1}}{\omega \mu_1 \varepsilon_1} \sinh(\alpha_{y1} y) \qquad \text{(A.2a)}$$

$$H_{x1}^{TM} = j \ B_1 \frac{\beta_z}{\mu_1} \cosh(\alpha_{y1} y) \qquad \text{(A.2b)}$$

$$\beta_1^2 = \beta_x^2 + \beta_z^2 - \alpha_{y1}^2 = \omega^2 \mu_1 \varepsilon_1 \qquad \text{(A.3)}$$

REGION 2:

$$E_{x2}^{TM} = \frac{\beta_x \alpha_{y2}}{\omega\mu_2\varepsilon_2}\left[B_{2A}\sinh[\alpha_{y2}(d_2-y)]+B_{2B}\cosh[\alpha_{y2}(d_2-y)]\right] \qquad (A.4a)$$

$$H_{x2}^{TM} = j\frac{\beta_z}{\mu_2}\left[B_{2A}\cosh[\alpha_{y2}(d_2-y)]+B_{2B}\sinh[\alpha_{y2}(d_2-y)]\right] \qquad (A.4b)$$

$$\beta_2^2 = \beta_x^2 + \beta_z^2 - \alpha_{y2}^2 = \omega^2\mu_2\varepsilon_2 \qquad (A.5)$$

REGION 3:

$$E_{x3}^{TM} = \frac{\beta_x \alpha_{y3}}{\omega\mu_3\varepsilon_3}\left[B_{3A}\sinh[\alpha_{y3}(d_3-y)]+B_{3B}\cosh[\alpha_{y3}(d_3-y)]\right] \qquad (A.6a)$$

$$H_{x3}^{TM} = j\frac{\beta_z}{\mu_3}\left[B_{3A}\cosh[\alpha_{y3}(d_3-y)]+B_{3B}\sinh[\alpha_{y3}(d_3-y)]\right] \qquad (A.6b)$$

$$\beta_3^2 = \beta_x^2 + \beta_z^2 - \alpha_{y3}^2 = \omega^2\mu_3\varepsilon_3 \qquad (A.7)$$

REGION 4:

$$E_{x4}^{TM} = -\frac{\beta_x \alpha_{y4}}{\omega\mu_4\varepsilon_4}\left[B_{4A}\sinh[\alpha_{y4}(y-d_3)]+B_{4B}\cosh[\alpha_{y4}(y-d_3)]\right] \qquad (A.8a)$$

$$E_{z4}^{TM} = -\frac{\beta_z \alpha_{y4}}{\omega\mu_4\varepsilon_4}\left[B_{4A}\sinh[\alpha_{y4}(y-d_3)]+B_{4B}\cosh[\alpha_{y4}(y-d_3)]\right] \qquad (A.8b)$$

$$H_{x4}^{TM} = j\frac{\beta_z}{\mu_4}\left[B_{4A}\cosh[\alpha_{y4}(y-d_3)]+B_{4B}\sinh[\alpha_{y4}(y-d_3)]\right] \qquad (A.8c)$$

$$\beta_4^2 = \beta_x^2 + \beta_z^2 - \alpha_{y4}^2 = \omega^2\mu_4\varepsilon_4 \qquad (A.9)$$

REGION 5:

$$E_{x5}^{TM} = -\frac{\beta_x \alpha_{y5}}{\omega\mu_5\varepsilon_5}\left[B_{5A}\sinh[\alpha_{y5}(y-d_4)]+B_{5B}\cosh[\alpha_{y5}(y-d_4)]\right] \qquad (A.10a)$$

$$H_{x5}^{TM} = j\frac{\beta_z}{\mu_5}\left[B_{5A}\cosh[\alpha_{y5}(y-d_4)]+B_{5B}\sinh[\alpha_{y5}(y-d_4)]\right] \qquad (A.10b)$$

$$\beta_5^2 = \beta_x^2 + \beta_z^2 - \alpha_{y5}^2 = \omega^2\mu_5\varepsilon_5 \qquad (A.11)$$

REGION 6:

$$E_{x6}^{TM} = B_6\frac{\beta_x \alpha_{y6}}{\omega\mu_6\varepsilon_6}\sinh[\alpha_{y6}(d_6-y)] \qquad (A.12a)$$

$$H_{x6}^{TM} = j B_6\frac{\beta_z}{\mu_6}\cosh[\alpha_{y6}(d_6-y)] \qquad (A.12b)$$

$$\beta_6^2 = \beta_x^2 + \beta_z^2 - \alpha_{y6}^2 = \omega^2 \mu_6 \varepsilon_6 \tag{A.13}$$

Since the SDA requires both the x and z directed electric fields at the center conductor interface, both E_{x4}^{TM} and E_{z4}^{TM} are included. Note that using E_{x3}^{TM} and E_{z3}^{TM} could have been used instead of the electric fields in region 4 because the center conductors are assumed to be infinitely thin.

Now that the fields have been determined, the ten independent boundary conditions (two have already been applied) can be used to eliminate the B_N's. First the tangential fields are matched at the first dielectric interface from the bottom.

1) $E_{x1}^{TM}\big|_{y=h_1} = E_{x2}^{TM}\big|_{y=h_1}$ or $E_{z1}^{TM}\big|_{y=h_1} = E_{z2}^{TM}\big|_{y=h_1}$

$$-B_1 \frac{\beta_x \alpha_{y1}}{\omega \mu_1 \varepsilon_1} \sinh(\alpha_{y1} h_1) = \frac{\beta_x \alpha_{y2}}{\omega \mu_2 \varepsilon_2}\left[B_{2A} \sinh(\alpha_{y2} h_2) + B_{2B} \cosh(\alpha_{y2} h_2)\right] \tag{A.14}$$

$$B_1 = -\text{sech}(\alpha_{y1} h_1) \frac{\mu_{r1} \varepsilon_{r1} \alpha_{y2}}{\mu_{r2} \varepsilon_{r2} \alpha_{y1}}\left[B_{2A} \sinh(\alpha_{y2} h_2) + B_{2B} \cosh(\alpha_{y2} h_2)\right] \tag{A.15}$$

2) $H_{x1}^{TM}\big|_{y=h_1} = H_{x2}^{TM}\big|_{y=h_1}$ or $H_{z1}^{TM}\big|_{y=h_1} = H_{z2}^{TM}\big|_{y=h_1}$

$$jB_1 \frac{\beta_z}{\mu_1} \cosh(\alpha_{y1} h_1) = j\frac{\beta_z}{\mu_2}\left[B_{2A} \cosh(\alpha_{y2} h_2) + B_{2B} \sinh(\alpha_{y2} h_2)\right] \tag{A.16}$$

Substituting in for B_1 using (A.15)

$$\frac{\varepsilon_{r1} \coth(\alpha_{y1} h_1)}{\alpha_{y1}} \frac{\alpha_{y2}}{\varepsilon_{r2}}\left[B_{2A} \sinh(\alpha_{y2} h_2) + B_{2B} \cosh(\alpha_{y2} h_2)\right] =$$

$$- B_{2A} \cosh(\alpha_{y2} h_2) - B_{2B} \sinh(\alpha_{y2} h_2) \tag{A.17}$$

$$\frac{\varepsilon_{r1} \coth(\alpha_{y1} h_1)}{\alpha_{y1}}\left[B_{2A} \frac{\varepsilon_{r2}}{\alpha_{y2}} + B_{2B} \frac{\varepsilon_{r2} \coth(\alpha_{y2} h_2)}{\alpha_{y2}}\right] =$$

$$- \frac{\varepsilon_{r2}}{\alpha_{y2}} B_{2A} \frac{\varepsilon_{r2} \coth(\alpha_{y2} h_2)}{\alpha_{y2}} - B_{2B}(\varepsilon_{r2}/\alpha_{y2})^2 \tag{A.18}$$

$$B_{2A} \frac{\varepsilon_{r2}}{\alpha_{y2}} \left[\frac{\varepsilon_{r1} \coth(\alpha_{y1} h_1)}{\alpha_{y1}} + \frac{\varepsilon_{r2} \coth(\alpha_{y2} h_2)}{\alpha_{y2}} \right] =$$

$$-B_{2B} \left\{ \left[\frac{\varepsilon_{r1} \coth(\alpha_{y1} h_1)}{\alpha_{y1}} \right] \left[\frac{\varepsilon_{r2} \coth(\alpha_{y2} h_2)}{\alpha_{y2}} \right] + \left[\frac{\varepsilon_{r2}}{\alpha_{y2}} \right]^2 \right\} \qquad (A.19)$$

In a similar manner, the tangential fields at the first dielectric interface from the top are now matched.

3) $E_{x5}^{TM} \Big|_{y=d_5} = E_{x6}^{TM} \Big|_{y=d_5}$ or $E_{z5}^{TM} \Big|_{y=d_5} = E_{z6}^{TM} \Big|_{y=d_5}$

$$B_6 \frac{\beta_x \alpha_{y6}}{\omega \mu_6 \varepsilon_6} \sinh(\alpha_{y6} h_6) =$$

$$- \frac{\beta_x \alpha_{y5}}{\omega \mu_5 \varepsilon_5} \left[B_{5A} \sinh(\alpha_{y5} h_5) + B_{5B} \cosh(\alpha_{y5} h_5) \right] \qquad (A.20)$$

$$B_6 = -\text{sech}(\alpha_{y6} h_6) \frac{\mu_{r6} \varepsilon_{r6} \alpha_{y5}}{\mu_{r5} \varepsilon_{r5} \alpha_{y6}} \left[B_{5A} \sinh(\alpha_{y5} h_5) + B_{5B} \cosh(\alpha_{y5} h_5) \right] \qquad (A.21)$$

4) $H_{x5}^{TM} \Big|_{y=d_5} = H_{x6}^{TM} \Big|_{y=d_5}$ or $H_{z5}^{TM} \Big|_{y=d_5} = H_{z6}^{TM} \Big|_{y=d_5}$

$$jB_6 \frac{\beta_z}{\mu_6} \cosh(\alpha_{y6} h_6) = j \frac{\beta_z}{\mu_5} \left[B_{5A} \cosh(\alpha_{y5} h_5) + B_{5B} \sinh(\alpha_{y5} h_5) \right] \qquad (A.22)$$

Substituting in for B_6 using (A.21)

$$\frac{\varepsilon_{r6} \coth(\alpha_{y6} h_6)}{\alpha_{y6}} \frac{\alpha_{y5}}{\varepsilon_{r5}} \left[B_{5A} \sinh(\alpha_{y5} h_5) + B_{5B} \cosh(\alpha_{y5} h_5) \right] =$$

$$- B_{5A} \cosh(\alpha_{y5} h_5) - B_{5B} \sinh(\alpha_{y5} h_5) \qquad (A.23)$$

$$\frac{\varepsilon_{r6} \coth(\alpha_{y6} h_6)}{\alpha_{y6}} \left[B_{5A} \frac{\varepsilon_{r5}}{\alpha_{y5}} + B_{5B} \frac{\varepsilon_{r5} \coth(\alpha_{y5} h_5)}{\alpha_{y5}} \right] =$$

$$- \frac{\varepsilon_{r5}}{\alpha_{y5}} B_{5A} \frac{\varepsilon_{r5} \coth(\alpha_{y5} h_5)}{\alpha_{y5}} - B_{5B} (\varepsilon_{r5}/\alpha_{y5})^2 \qquad (A.24)$$

$$B_{5A} \frac{\varepsilon_{r5}}{\alpha_{y5}} \left[\frac{\varepsilon_{r6} \coth(\alpha_{y6} h_6)}{\alpha_{y6}} + \frac{\varepsilon_{r5} \coth(\alpha_{y5} h_5)}{\alpha_{y5}} \right] =$$

$$-B_{5B} \left\{ \left[\frac{\varepsilon_{r6} \coth(\alpha_{y6} h_6)}{\alpha_{y6}} \right] \left[\frac{\varepsilon_{r5} \coth(\alpha_{y5} h_5)}{\alpha_{y5}} \right] + \left[\frac{\varepsilon_{r5}}{\alpha_{y5}} \right]^2 \right\} \qquad (A.25)$$

To simplify the notation, let

$$Y_{s1}^{TM} = \frac{\varepsilon_{r1}\coth(\alpha_{y1}h_1)}{\alpha_{y1}} \tag{A.26a}$$

$$Y_{s2}^{TM} = \frac{\varepsilon_{r2}\coth(\alpha_{y2}h_2)}{\alpha_{y2}} \tag{A.26b}$$

$$Y_{s3}^{TM} = \frac{\varepsilon_{r3}\coth(\alpha_{y3}h_3)}{\alpha_{y3}} \tag{A.26c}$$

$$Y_{s4}^{TM} = \frac{\varepsilon_{r4}\coth(\alpha_{y4}h_4)}{\alpha_{y4}} \tag{A.26d}$$

$$Y_{s5}^{TM} = \frac{\varepsilon_{r5}\coth(\alpha_{y5}h_5)}{\alpha_{y5}} \tag{A.26e}$$

$$Y_{s6}^{TM} = \frac{\varepsilon_{r6}\coth(\alpha_{y6}h_6)}{\alpha_{y6}} \tag{A.26f}$$

and

$$Y_2^{TM} = \frac{Y_{s1}^{TM}Y_{s2}^{TM} + (\varepsilon_{r2}/\alpha_{y2})^2}{Y_{s1}^{TM} + Y_{s2}^{TM}} \tag{A.27a}$$

$$Y_5^{TM} = \frac{Y_{s6}^{TM}Y_{s5}^{TM} + (\varepsilon_{r5}/\alpha_{y5})^2}{Y_{s6}^{TM} + Y_{s5}^{TM}} \tag{A.27b}$$

Using these expressions in equations (A.19) and (A.25) and solving them

for B_{2A} and B_{5A} respectively,

$$B_{2A} = -B_{2B}\frac{\alpha_{y2}}{\varepsilon_{r2}}\frac{Y_{s1}^{TM}Y_{s2}^{TM} + (\varepsilon_{r2}/\alpha_{y2})^2}{Y_{s1}^{TM} + Y_{s2}^{TM}} = -B_{2B}\frac{\alpha_{y2}}{\varepsilon_{r2}}Y_2^{TM} \tag{A.28a}$$

$$B_{5A} = -B_{5B}\frac{\alpha_{y5}}{\varepsilon_{r5}}\frac{Y_{s6}^{TM}Y_{s5}^{TM} + (\varepsilon_{r5}/\alpha_{y5})^2}{Y_{s6}^{TM} + Y_{s5}^{TM}} = -B_{5B}\frac{\alpha_{y5}}{\varepsilon_{r5}}Y_5^{TM} \tag{A.28b}$$

Proceeding to the next dielectric interface up from the 1-2

interface, the fields at the 2-3 interface are forced to be continuous.

5) $\left. E_{x2}^{TM}\right|_{y=d_2} = \left. E_{x3}^{TM}\right|_{y=d_2}$ or $\left. E_{z3}^{TM}\right|_{y=d_2} = \left. E_{z3}^{TM}\right|_{y=d_2}$

$$B_{2B}\frac{\beta_x\alpha_{y2}}{\omega\mu_2\varepsilon_2} = \frac{\beta_x\alpha_{y3}}{\omega\mu_3\varepsilon_3}\left[B_{3A}\sinh(\alpha_{y3}h_3) + B_{3B}\cosh(\alpha_{y3}h_3)\right] \tag{A.29}$$

$$B_{2B} \frac{\alpha_{y2}}{\varepsilon_{r2}} = \frac{\alpha_{y3}\mu_{r2}}{\varepsilon_{r3}\mu_{r3}}\left[B_{3A}\sinh(\alpha_{y3}h_3)+B_{3B}\cosh(\alpha_{y3}h_3)\right] \tag{A.30}$$

6) $\left.H^{TM}_{x2}\right|_{y=d_2} = \left.H^{TM}_{x3}\right|_{y=d_2}$ or $\left.H^{TM}_{z2}\right|_{y=d_2} = \left.H^{TM}_{z3}\right|_{y=d_2}$

$$j\, B_{2A} \frac{\beta_z}{\mu_2} = j\, \frac{\beta_z}{\mu_3}\left[B_{3A}\cosh(\alpha_{y3}h_3)+B_{3B}\sinh(\alpha_{y3}h_3)\right] \tag{A.31}$$

$$B_{2A} = \frac{\mu_{r2}}{\mu_{r3}}\left[B_{3A}\cosh(\alpha_{y3}h_3)+B_{3B}\sinh(\alpha_{y3}h_3)\right] \tag{A.32}$$

Substituting in for B_{2A} using (A.28a)

$$-B_{2B} \frac{\alpha_{y2}}{\varepsilon_{r2}} Y^{TM}_2 = \frac{\mu_{r2}}{\mu_{r3}}\left[B_{3A}\cosh(\alpha_{y3}h_3)+B_{3B}\sinh(\alpha_{y3}h_3)\right] \tag{A.33}$$

$$B_{2B} \frac{\alpha_{y2}}{\varepsilon_{r2}} = -\frac{\mu_{r2}}{\mu_{r3}}\left[B_{3A}\cosh(\alpha_{y3}h_3)+B_{3B}\sinh(\alpha_{y3}h_3)\right]\left[Y^{TM}_2\right]^{-1} \tag{A.34}$$

Equating (A.34) and (A.30)

$$\frac{\alpha_{y3}\mu_{r2}}{\varepsilon_{r3}\mu_{r3}}\left[B_{3A}\sinh(\alpha_{y3}h_3)+B_{3B}\cosh(\alpha_{y3}h_3)\right] =$$
$$-\frac{\mu_{r2}}{\mu_{r3}}\left[B_{3A}\cosh(\alpha_{y3}h_3)+B_{3B}\sinh(\alpha_{y3}h_3)\right]\left[Y^{TM}_2\right]^{-1} \tag{A.35}$$

Multiplying both sides by $[Y^{TM}_2\varepsilon_{r3}\mu_{r3}]/[\alpha_{y3}\mu_{r2}\sinh(\alpha_{y3}h_3)]$

$$\left[B_{3A}+B_{3B}\coth(\alpha_{y3}h_3)\right]\left[Y^{TM}_2\right] = -\left[B_{3A}\frac{\varepsilon_{r3}\coth(\alpha_{y3}h_3)}{\alpha_{y3}}+B_{3B}\frac{\varepsilon_{r3}}{\alpha_{y3}}\right] \tag{A.36}$$

$$B_{3A}\left[Y^{TM}_2+\frac{\varepsilon_{r3}\coth(\alpha_{y3}h_3)}{\alpha_{y3}}\right] = -B_{3B}\left[Y^{TM}_2\coth(\alpha_{y3}h_3)+\varepsilon_{r3}/\alpha_{y3}\right] \tag{A.37}$$

Using (A.26c) and factoring $\varepsilon_{r3}/\alpha_{y3}$ out of the left hand side,

$$B_{3A} = -B_{3B}\frac{\alpha_{y3}}{\varepsilon_{r3}}\frac{Y^{TM}_2 Y^{TM}_{s3}+(\varepsilon_{r3}/\alpha_{y3})^2}{Y^{TM}_2+Y^{TM}_{s3}} \tag{A.38}$$

Since this expression is very similar to (A.27a), let

$$Y^{TM}_3 = \frac{Y^{TM}_2 Y^{TM}_{s3}+(\varepsilon_{r3}/\alpha_{y3})^2}{Y^{TM}_2+Y^{TM}_{s3}} \tag{A.39}$$

Then (A.38) simplifies to;

$$B_{3A} = - B_{3B} Y_3^{TM} \frac{\alpha_{y3}}{\varepsilon_{r3}} \tag{A.40}$$

Again in a very similar manner, the tangential fields at the 4-5 dielectric interface are equated.

7) $E_{x5}^{TM}\big|_{y=d_4} = E_{x4}^{TM}\big|_{y=d_4}$ or $E_{z5}^{TM}\big|_{y=d_4} = E_{z4}^{TM}\big|_{y=d_4}$

$$- B_{5B} \frac{\beta_x \alpha_{y5}}{\omega\mu_5 \varepsilon_5} = - \frac{\beta_x \alpha_{y4}}{\omega\mu_4 \varepsilon_4} \left[B_{4A} \sinh(\alpha_{y4}h_4) + B_{4B}\cosh(\alpha_{y4}h_4) \right] \tag{A.41}$$

$$B_{5B} \frac{\alpha_{y5}}{\varepsilon_{r5}} = \frac{\alpha_{y4}\mu_{r5}}{\varepsilon_{r4}\mu_{r4}} \left[B_{4A} \sinh(\alpha_{y4}h_4) + B_{4B}\cosh(\alpha_{y4}h_4) \right] \tag{A.42}$$

8) $H_{x5}^{TM}\big|_{y=d_4} = H_{x4}^{TM}\big|_{y=d_4}$ or $H_{z5}^{TM}\big|_{y=d_4} = H_{z4}^{TM}\big|_{y=d_4}$

$$j B_{5A} \frac{\beta_z}{\mu_5} = j \frac{\beta_z}{\mu_4} \left[B_{4A} \cosh(\alpha_{y4}h_4) + B_{4B}\sinh(\alpha_{y4}h_4) \right] \tag{A.43}$$

$$B_{5A} = \frac{\mu_{r5}}{\mu_{r4}} \left[B_{4A} \cosh(\alpha_{y4}h_4) + B_{4B}\sinh(\alpha_{y4}h_4) \right] \tag{A.44}$$

Substituting in for B_{5A} using (A.28b)

$$- B_{5B} \frac{\alpha_{y5}}{\varepsilon_{r5}} Y_5^{TM} = \frac{\mu_{r5}}{\mu_{r4}} \left[B_{4A} \cosh(\alpha_{y4}h_4) + B_{4B}\sinh(\alpha_{y4}h_4) \right] \tag{A.45}$$

$$B_{5B} \frac{\alpha_{y5}}{\varepsilon_{r5}} = - \frac{\mu_{r5}}{\mu_{r4}} \left[B_{4A} \cosh(\alpha_{y4}h_4) + B_{4B}\sinh(\alpha_{y4}h_4) \right] \left[Y_5^{TM} \right]^{-1} \tag{A.46}$$

Equating (A.42) and (A.46)

$$\frac{\alpha_{y4}\mu_{r5}}{\varepsilon_{r4}\mu_{r4}} \left[B_{4A} \sinh(\alpha_{y4}h_4) + B_{4B}\cosh(\alpha_{y4}h_4) \right] =$$

$$- \frac{\mu_{r5}}{\mu_{r4}} \left[B_{4A} \cosh(\alpha_{y4}h_4) + B_{4B}\sinh(\alpha_{y4}h_4) \right] \left[Y_5^{TM} \right]^{-1} \tag{A.47}$$

Multiplying both sides by $[Y_5^{TM}\varepsilon_{r4}\mu_{r4}]/[\alpha_{y4}\mu_{r5}\sinh(\alpha_{y4}h_4)]$

$$\left[B_{4A} + B_{4B}\coth(\alpha_{y4}h_4) \right] \left[Y_5^{TM} \right] = - \left[B_{4A} \frac{\varepsilon_{r4}\coth(\alpha_{y4}h_4)}{\alpha_{y4}} + B_{4B}\frac{\varepsilon_{r4}}{\alpha_{y4}} \right] \tag{A.48}$$

$$B_{4A} \left[Y_5^{TM} + \frac{\varepsilon_{r4}\coth(\alpha_{y4}h_4)}{\alpha_{y4}} \right] = - B_{4B} \left[Y_5^{TM}\coth(\alpha_{y4}h_4) + \varepsilon_{r4}/\alpha_{y4} \right] \tag{A.49}$$

Using (A.26d) and factoring $\varepsilon_{r4}/\alpha_{y4}$ out of the left hand side,

$$B_{4A} = - B_{4B} \frac{\alpha_{y4}}{\varepsilon_{r4}} \frac{Y_5^{TM} Y_{s4}^{TM} + (\varepsilon_{r4}/\alpha_{y4})^2}{Y_5^{TM} + Y_{s4}^{TM}} \tag{A.50}$$

Again this expression is very similar to (A.27a), so let

$$Y_4^{TM} = \frac{Y_5^{TM} Y_{s4}^{TM} + (\varepsilon_{r4}/\alpha_{y4})^2}{Y_5^{TM} + Y_{s4}^{TM}} \tag{A.51}$$

Then (A.50) simplifies to;

$$B_{4A} = - B_{4B} Y_4^{TM} \frac{\alpha_{y4}}{\varepsilon_{r4}} \tag{A.52}$$

Finally, the fields at the center conductor interface are matched. Initially, the electric fields at the interface are simply set equal to each other. The condition that the fields are zero over each of the center conductors is applied implicitly through the current or electric field expansion functions when Galerkins method is used in the final step.

9) $E_{x3}^{TM}\big|_{y=d_3} = E_{x4}^{TM}\big|_{y=d_3}$ or $E_{z3}^{TM}\big|_{y=d_3} = E_{z4}^{TM}\big|_{y=d_3}$

$$B_{3B} \frac{\beta_x \alpha_{y3}}{\omega\mu_3 \varepsilon_3} \cosh(0) = - B_{4B} \frac{\beta_x \alpha_{y4}}{\omega\mu_4 \varepsilon_4} \cosh(0) \tag{A.53}$$

$$B_{3B} = - B_{4B} \frac{\alpha_{y4} \varepsilon_{r3} \mu_{r3}}{\alpha_{y3} \varepsilon_{r4} \mu_{r4}} \tag{A.54}$$

Using this relation in (A.40)

$$B_{3A} = B_{4B} Y_3^{TM} \frac{\alpha_{y4} \mu_{r3}}{\varepsilon_{r4} \mu_{r4}} \tag{A.55}$$

Finally, the discontinuity of the magnetic fields due to the current densities on the center conductor interface is used.

10) $H_{x3}^{TM}\Big|_{y=d_3} - H_{x4}^{TM}\Big|_{y=d_3} = J_z^{TM}$

$$j\frac{\beta_z}{\mu_3} B_{3A}\cosh(0) - j\frac{\beta_z}{\mu_4} B_{4A}\cosh(0) = J_z^{TM} \qquad \text{(A.56)}$$

Using (A.52) and (A.55)

$$B_{4B} Y_3^{TM}\frac{\alpha_{y4}}{\varepsilon_{r4}} + B_{4B} Y_4^{TM}\frac{\alpha_{y4}}{\varepsilon_{r4}} = -j\frac{\mu_4}{\beta_z} J_z^{TM} \qquad \text{(A.57)}$$

$$B_{4B} = -j J_z^{TM}\frac{\mu_4\varepsilon_{r4}}{\beta_z\alpha_{y4}}\frac{1}{Y_3^{TM}+Y_4^{TM}} \qquad \text{(A.58)}$$

To verify that the TM^y mode satisfies the boundary conditions in the spectral domain, it is neccesary to show that using the z directed magnetic fields at the interface gives the same result as using the x directed fields.

$H_{z3}^{TM}\Big|_{y=d_3} - H_{z4}^{TM}\Big|_{y=d_3} = -J_x^{TM}$

$$-j\frac{\beta_x}{\mu_3} B_{3A}\cosh(0) + j\frac{\beta_x}{\mu_4} B_{4A}\cosh(0) = -J_x^{TM} \qquad \text{(A.59)}$$

Using (A.52) and (A.55)

$$B_{4B} Y_3^{TM}\frac{\alpha_{y4}}{\varepsilon_{r4}} + B_{4B} Y_4^{TM}\frac{\alpha_{y4}}{\varepsilon_{r4}} = -j\frac{\mu_4}{\beta_x} J_x^{TM} \qquad \text{(A.60)}$$

$$B_{4B} = -j J_x^{TM}\frac{\mu_4\varepsilon_{r4}}{\beta_x\alpha_{y4}}\frac{1}{Y_3^{TM}+Y_4^{TM}} \qquad \text{(A.61)}$$

Equation (A.61) is equivalent to (A.58) if

$$J_x^{TM}/\beta_x = J_z^{TM}/\beta_z \qquad \text{(A.62)}$$

or

$$\beta_z J_x^{TM} = \beta_x J_z^{TM} \qquad \text{(A.63)}$$

which was shown to be true for the TM^y case in Section 2.3.2. Thus the TM^y mode does satisfy the boundary conditions in the spectral domain

and can be used independently to solve the boundary value problem. To complete the TM^y solution, substitute (A.58) into (A.52)

$$B_{4A} = j\ J_z^{TM}\ \frac{\mu_4}{\beta_z}\ \frac{Y_4^{TM}}{Y_3^{TM}+Y_4^{TM}} \tag{A.64}$$

Using (A.58) and (A.64) for B_{4B} and B_{4A}, substituting back into the equations for the electric field in region 4, equations (A.8a-b), and setting $y = d_3$, the fields at the center conductor interface are;

$$E_{x4}^{TM} = j\frac{J_z^{TM}}{\omega\varepsilon_0}\ \frac{\beta_x}{\beta_z}\ Z^{TM} \tag{A.65b}$$

$$E_{z4}^{TM} = j\frac{J_z^{TM}}{\omega\varepsilon_0}\ Z^{TM} \tag{A.65a}$$

where

$$Z^{TM} = \left[Y_4^{TM}+Y_3^{TM}\right]^{-1} \tag{A.66}$$

Y_3^{TM} and Y_4^{TM} can be thought of as the modal admittances seen by the current densities looking outward in each direction from the center conductor interface. Thus Z^{TM} is the parallel combination of these admittances.

Having completed the solution for the TM^y mode, the TE^y modal configuration is considered. The vector potentials for this mode, $F_{yi}(\beta_x,y,\beta_z)$, are chosen as follows for each of the six regions:

REGION 1: $0 \le y \le h_1$

$$F_{y1}=A_1(\beta_x,\beta_z)\sinh(\alpha_{y1}y) \tag{A.67a}$$

REGION 2: $h_1 \le y \le d_2$, $d_2 = h_1+h_2$

$$F_{y1}=A_{2A}(\beta_x,\beta_z)\cosh[\alpha_{y2}(d_2-y)]+A_{2B}(\beta_x,\beta_z)\sinh[\alpha_{y2}(d_2-y)] \tag{A.67b}$$

REGION 3: $d_2 \le y \le d_3$, $d_3 = h_1+h_2+h_3$

$$F_{y1}=A_{3A}(\beta_x,\beta_z)\cosh[\alpha_{y3}(d_3-y)]+A_{3B}(\beta_x,\beta_z)\sinh[\alpha_{y3}(d_3-y)] \tag{A.67c}$$

REGION 4: $d_3 \leq y \leq d_4$, $d_4 = h_1 + h_2 + h_3 + h_4$

$$F_{y1} = A_{4A}(\beta_x, \beta_z) \cosh[\alpha_{y4}(y - d_3)] + A_{4B}(\beta_x, \beta_z) \sinh[\alpha_{y4}(y - d_3)] \qquad (A.67d)$$

REGION 5: $d_4 \leq y \leq d_5$, $d_5 = h_1 + h_2 + h_3 + h_4 + h_5$

$$F_{y1} = A_{5A}(\beta_x, \beta_z) \cosh[\alpha_{y5}(y - d_4)] + A_{5B}(\beta_x, \beta_z) \sinh[\alpha_{y5}(y - d_4)] \qquad (A.67e)$$

REGION 6: $d_5 \leq y \leq d_6$, $d_6 = h_1 + h_2 + h_3 + h_4 + h_5 + h_6$

$$F_{y1} = A_6(\beta_x, \beta_z) \sinh[\alpha_{y6}(d_6 - y)] \qquad (A.67f)$$

Where the $A_N(\beta_x, \beta_z)$'s are unknown functions of the transform variables, which are to be determined from the boundary conditions. They are abbreviated as A_N throughout. F_{yN}'s are chosen based on 1) the tangential $\underline{E}$ fields vanishing at $y = 0$ and 2) the tangential $\underline{E}$ fields vanishing at $y = d_6$. Again, only the x directed fields are used because of the independence of the TE^y mode. The fields in each region are determined using the six vector potentials (A.67a-f) along with equations (2.38a-f).

REGION 1:

$$E_{x1}^{TE} = -j\, A_1 \frac{\beta_z}{\varepsilon_1} \sinh(\alpha_{y1} y) \qquad (A.68a)$$

$$H_{x1}^{TE} = -A_1 \frac{\beta_x \alpha_{y1}}{\omega \mu_1 \varepsilon_1} \cosh(\alpha_{y1} y) \qquad (A.68b)$$

$$\beta_1^2 = \beta_x^2 + \beta_z^2 - \alpha_{y1}^2 = \omega^2 \mu_1 \varepsilon_1 \qquad (A.69)$$

REGION 2:

$$E_{x2}^{TE} = -j\, \frac{\beta_z}{\varepsilon_2} \left[A_{2A} \cosh[\alpha_{y2}(d_2 - y)] + A_{2B} \sinh[\alpha_{y2}(d_2 - y)] \right] \qquad (A.70a)$$

$$H_{x2}^{TE} = \frac{\beta_x \alpha_{y2}}{\omega \mu_2 \varepsilon_2} \left[A_{2A} \sinh[\alpha_{y2}(d_2 - y)] + A_{2B} \cosh[\alpha_{y2}(d_2 - y)] \right] \qquad (A.70b)$$

$$\beta_2^2 = \beta_x^2 + \beta_z^2 - \alpha_{y2}^2 = \omega^2 \mu_2 \varepsilon_2 \qquad (A.71)$$

REGION 3:

$$E_{x3}^{TE} = -j \frac{\beta_z}{\varepsilon_3} \left[A_{3A} \cosh[\alpha_{y3}(d_3-y)] + A_{3B}\sinh[\alpha_{y3}(d_3-y)] \right] \tag{A.72a}$$

$$H_{x3}^{TE} = \frac{\beta_x \alpha_{y3}}{\omega\mu_3\varepsilon_3} \left[A_{3A}\sinh[\alpha_{y3}(d_3-y)] + A_{3B}\cosh[\alpha_{y3}(d_3-y)] \right] \tag{A.72b}$$

$$\beta_3^2 = \beta_x^2 + \beta_z^2 - \alpha_{y3}^2 = \omega^2\mu_3\varepsilon_3 \tag{A.73}$$

REGION 4:

$$E_{x4}^{TE} = -j \frac{\beta_z}{\varepsilon_4} \left[A_{4A}\cosh[\alpha_{y4}(y-d_3)] + A_{4B}\sinh[\alpha_{y4}(y-d_3)] \right] \tag{A.74a}$$

$$E_{z4}^{TE} = j \frac{\beta_x}{\varepsilon_4} \left[A_{4A}\cosh[\alpha_{y4}(y-d_3)] + A_{4B}\sinh[\alpha_{y4}(y-d_3)] \right] \tag{A.74b}$$

$$H_{x4}^{TE} = - \frac{\beta_x \alpha_{y4}}{\omega\mu_4\varepsilon_4} \left[A_{4A}\sinh[\alpha_{y4}(y-d_3)] + A_{4B}\cosh[\alpha_{y4}(y-d_3)] \right] \tag{A.74c}$$

$$\beta_4^2 = \beta_x^2 + \beta_z^2 - \alpha_{y4}^2 = \omega^2\mu_4\varepsilon_4 \tag{A.75}$$

REGION 5:

$$E_{x5}^{TE} = -j \frac{\beta_z}{\varepsilon_5} \left[A_{5A}\cosh[\alpha_{y5}(y-d_4)] + A_{5B}\sinh[\alpha_{y5}(y-d_4)] \right] \tag{A.76a}$$

$$H_{x5}^{TE} = - \frac{\beta_x \alpha_{y5}}{\omega\mu_5\varepsilon_5} \left[A_{5A}\sinh[\alpha_{y5}(y-d_4)] + A_{5B}\cosh[\alpha_{y5}(y-d_4)] \right] \tag{A.76b}$$

$$\beta_5^2 = \beta_x^2 + \beta_z^2 - \alpha_{y5}^2 = \omega^2\mu_5\varepsilon_5 \tag{A.77}$$

REGION 6:

$$E_{x6}^{TE} = -j A_6 \frac{\beta_z}{\varepsilon_6} \sinh[\alpha_{y6}(d_6-y)] \tag{A.78a}$$

$$H_{x6}^{TE} = A_6 \frac{\beta_x \alpha_{y6}}{\omega\mu_6\varepsilon_6} \cosh[\alpha_{y6}(d_6-y)] \tag{A.78b}$$

$$\beta_6^2 = \beta_x^2 + \beta_z^2 - \alpha_{y6}^2 = \omega^2\mu_6\varepsilon_6 \tag{A.79}$$

Now the boundary conditions are applied to eliminate the unknown constants, beginning with the continuity of the tangential fields at the first dielectric interface above the ground plane.

1) $E_{x1}^{TE}\big|_{y=h_1} = E_{x2}^{TE}\big|_{y=h_1}$ or $E_{z1}^{TE}\big|_{y=h_1} = E_{z2}^{TE}\big|_{y=h_1}$

$$-jA_1\frac{\beta_z}{\varepsilon_1}\sinh(\alpha_{y1}h_1) = -j\frac{\beta_z}{\varepsilon_2}\left[A_{2A}\cosh(\alpha_{y2}h_2)+A_{2B}\sinh(\alpha_{y2}h_2)\right] \quad (A.80)$$

$$A_1 = \operatorname{sech}(\alpha_{y1}h_1)\frac{\varepsilon_{r1}}{\varepsilon_{r2}}\left[A_{2A}\cosh(\alpha_{y2}h_2)+A_{2B}\sinh(\alpha_{y2}h_2)\right] \quad (A.81)$$

2) $H_{x1}^{TE}\big|_{y=h_1} = H_{x2}^{TE}\big|_{y=h_1}$ or $H_{z1}^{TE}\big|_{y=h_1} = H_{z2}^{TE}\big|_{y=h_1}$

$$-A_1\frac{\beta_x\alpha_{y1}}{\omega\mu_1\varepsilon_1}\cosh(\alpha_{y1}h_1) =$$

$$\frac{\beta_x\alpha_{y2}}{\omega\mu_2\varepsilon_2}\left[A_{2A}\sinh(\alpha_{y2}h_2) + A_{2B}\cosh(\alpha_{y2}h_2)\right] \quad (A.82)$$

Substituting in for A_1 using (2.3-81)

$$-\frac{\alpha_{y1}\coth(\alpha_{y1}h_1)}{\mu_{r1}}\left[A_{2A}\cosh(\alpha_{y2}h_2) + A_{2B}\sinh(\alpha_{y2}h_2)\right] =$$

$$\frac{\alpha_{y2}}{\mu_{r2}}\left[A_{2A}\sinh(\alpha_{y2}h_2) - A_{2B}\cosh(\alpha_{y2}h_2)\right] \quad (A.83)$$

$$\frac{\alpha_{y1}\coth(\alpha_{y1}h_1)}{\mu_{r1}}\left[A_{2A}\frac{\alpha_{y2}\coth(\alpha_{y2}h_2)}{\mu_{r2}} +A_{2B}\frac{\alpha_{y2}}{\mu_{r2}}\right] =$$

$$-A_{2A}(\alpha_{y2}/\mu_{r2})^2 - \frac{\alpha_{y2}}{\mu_{r2}}A_{2B}\frac{\alpha_{y2}\coth(\alpha_{y2}h_2)}{\mu_{r2}} \quad (A.84)$$

$$A_{2B}\frac{\alpha_{y2}}{\mu_{r2}}\left[\frac{\alpha_{y1}\coth(\alpha_{y1}h_1)}{\mu_{r1}} + \frac{\alpha_{y2}\coth(\alpha_{y2}h_2)}{\mu_{r2}}\right] =$$

$$-A_{2A}\left\{\left[\frac{\alpha_{y1}\coth(\alpha_{y1}h_1)}{\mu_{r1}}\right]\left[\frac{\alpha_{y2}\coth(\alpha_{y2}h_2)}{\mu_{r2}}\right]+\left[\frac{\alpha_{y2}}{\mu_{r2}}\right]^2\right\} \quad (A.85)$$

Now the continuity of the tangential fields at the first dielectric interface below the cover sheet is enforced.

3) $E_{x5}^{TE}\big|_{y=d_5} = E_{x6}^{TE}\big|_{y=d_5}$ or $E_{z5}^{TE}\big|_{y=d_5} = E_{z6}^{TE}\big|_{y=d_5}$

$$-jA_6\frac{\beta_z}{\varepsilon_6}\sinh(\alpha_{y6}h_6) =$$

$$-j\frac{\beta_z}{\varepsilon_5}\left[A_{5A}\cosh(\alpha_{y5}h_5) + A_{5B}\sinh(\alpha_{y5}h_5)\right] \quad (A.86)$$

$$A_6 = \text{sech}(\alpha_{y6} h_6) \frac{\varepsilon_{r6}}{\varepsilon_{r5}} \left[A_{5A} \cosh(\alpha_{y5} h_5) + A_{5B} \sinh(\alpha_{y5} h_5) \right] \qquad (A.87)$$

4) $\left. H_{x5}^{TE} \right|_{y=d_5} = \left. H_{x6}^{TE} \right|_{y=d_5}$ or $\left. H_{z5}^{TE} \right|_{y=d_5} = \left. H_{z6}^{TE} \right|_{y=d_5}$

$$-A_6 \frac{\beta_x \alpha_{y6}}{\omega \mu_6 \varepsilon_6} \cosh(\alpha_{y6} h_6) =$$

$$\frac{\beta_x \alpha_{y5}}{\omega \mu_5 \varepsilon_5} \left[A_{5A} \sinh(\alpha_{y5} h_5) + A_{5B} \cosh(\alpha_{y5} h_5) \right] \qquad (A.88)$$

Substituting in for A_6 using (A.87)

$$-\frac{\alpha_{y6} \coth(\alpha_{y6} h_6)}{\mu_{r6}} \left[A_{5A} \cosh(\alpha_{y5} h_5) + A_{5B} \sinh(\alpha_{y5} h_5) \right] =$$

$$\frac{\alpha_{y5}}{\mu_{r5}} \left[A_{5A} \sinh(\alpha_{y5} h_5) - A_{5B} \cosh(\alpha_{y5} h_5) \right] \qquad (A.89)$$

$$\frac{\alpha_{y6} \coth(\alpha_{y6} h_6)}{\mu_{r6}} \left[A_{5A} \frac{\alpha_{y5} \coth(\alpha_{y5} h_5)}{\mu_{r5}} + A_{5B} \frac{\alpha_{y5}}{\mu_{r5}} \right] =$$

$$- A_{5A} (\alpha_{y5}/\mu_{r5})^2 - \frac{\alpha_{y5}}{\mu_{r5}} A_{5B} \frac{\alpha_{y5} \coth(\alpha_{y5} h_5)}{\mu_{r5}} \qquad (A.90)$$

$$A_{5B} \frac{\alpha_{y5}}{\mu_{r5}} \left[\frac{\alpha_{y6} \coth(\alpha_{y6} h_6)}{\mu_{r6}} + \frac{\alpha_{y5} \coth(\alpha_{y5} h_5)}{\mu_{r5}} \right] =$$

$$- A_{5A} \left\{ \left[\frac{\alpha_{y6} \coth(\alpha_{y6} h_6)}{\mu_{r6}} \right] \left[\frac{\alpha_{y5} \coth(\alpha_{y5} h_5)}{\mu_{r5}} \right] + \left[\frac{\alpha_{y5}}{\mu_{r5}} \right]^2 \right\} \qquad (A.91)$$

Just as in the TM^y case, the notation is simplified by letting

$$Y_{s1}^{TE} = \frac{\alpha_{y1} \coth(\alpha_{y1} h_1)}{\mu_{r1}} \qquad (A.92a)$$

$$Y_{s2}^{TE} = \frac{\alpha_{y2} \coth(\alpha_{y2} h_2)}{\mu_{r2}} \qquad (A.92b)$$

$$Y_{s3}^{TE} = \frac{\alpha_{y3} \coth(\alpha_{y3} h_3)}{\mu_{r3}} \qquad (A.92c)$$

$$Y_{s4}^{TE} = \frac{\alpha_{y4} \coth(\alpha_{y4} h_4)}{\mu_{r4}} \qquad (A.92d)$$

$$Y_{s5}^{TE} = \frac{\alpha_{y5} \coth(\alpha_{y5} h_5)}{\mu_{r5}} \qquad (A.92e)$$

$$Y_{s6}^{TE} = \frac{\alpha_{y6} \coth(\alpha_{y6} h_6)}{\mu_{r6}} \qquad (A.92f)$$

and

$$Y_2^{TE} = \frac{Y_{s1}^{TE} Y_{s2}^{TE} + (\alpha_{y2}/\mu_{r2})^2}{Y_{s1}^{TE} + Y_{s2}^{TE}} \tag{A.93a}$$

$$Y_5^{TE} = \frac{Y_{s6}^{TE} Y_{s5}^{TE} + (\alpha_{y5}/\mu_{r5})^2}{Y_{s6}^{TE} + Y_{s5}^{TE}} \tag{A.93b}$$

Using these expressions in equations (A.85) and (A.91) and solving them

for A_{2A} and A_{5A} respectively;

$$A_{2B} = - A_{2A} \frac{\mu_{r2}}{\alpha_{y2}} \frac{Y_{s1}^{TE} Y_{s2}^{TE} + (\alpha_{y2}/\mu_{r2})^2}{Y_{s1}^{TE} + Y_{s2}^{TE}} = - A_{2A} \frac{\mu_{r2}}{\alpha_{y2}} Y_2^{TE} \tag{A.94a}$$

$$A_{5A} = - A_{5B} \frac{\mu_{r5}}{\alpha_{y5}} \frac{Y_{s6}^{TE} Y_{s5}^{TE} + (\alpha_{y5}/\mu_{r5})^2}{Y_{s6}^{TE} + Y_{s5}^{TE}} = - A_{5B} \frac{\mu_{r5}}{\alpha_{y5}} Y_5^{TE} \tag{A.94b}$$

The next boundary of concern is the 2-3 dielectric interface, and

so the tangential fields are forced to be continuous.

5) $\left. E_{x2}^{TE} \right|_{y=d_2} = \left. E_{x3}^{TE} \right|_{y=d_2}$ or $\left. E_{z3}^{TE} \right|_{y=d_2} = \left. E_{z3}^{TE} \right|_{y=d_2}$

$$-j A_{2A} \frac{\beta_z}{\varepsilon_2} = -j \frac{\beta_z}{\varepsilon_3}\left[A_{3A}\cosh(\alpha_{y3}h_3) + A_{3B}\sinh(\alpha_{y3}h_3)\right] \tag{A.95}$$

$$A_{2A} = \frac{\varepsilon_{r2}}{\varepsilon_{r3}}\left[A_{3A}\cosh(\alpha_{y3}h_3) + A_{3B}\sinh(\alpha_{y3}h_3)\right] \tag{A.96}$$

6) $\left. H_{x2}^{TE} \right|_{y=d_2} = \left. H_{x3}^{TE} \right|_{y=d_2}$ or $\left. H_{z2}^{TE} \right|_{y=d_2} = \left. H_{z3}^{TE} \right|_{y=d_2}$

$$A_{2B} \frac{\beta_x \alpha_{y2}}{\omega\mu_2\varepsilon_2} = \frac{\beta_x \alpha_{y3}}{\omega\mu_3\varepsilon_3}\left[A_{3A}\sinh(\alpha_{y3}h_3) + A_{3B}\cosh(\alpha_{y3}h_3)\right] \tag{A.97}$$

$$A_{2B} \frac{\alpha_{y2}}{\mu_{r2}} = \frac{\alpha_{y3}\varepsilon_{r2}}{\mu_{r3}\varepsilon_{r3}}\left[A_{3A}\sinh(\alpha_{y3}h_3) + A_{3B}\cosh(\alpha_{y3}h_3)\right] \tag{A.98}$$

Substituting in for A_{2B} using (A.94a)

$$- A_{2A}Y_2^{TE} = \frac{\alpha_{y3}\varepsilon_{r2}}{\mu_{r3}\varepsilon_{r3}}\left[A_{3A}\sinh(\alpha_{y3}h_3) + A_{3B}\cosh(\alpha_{y3}h_3)\right] \tag{A.99}$$

$$A_{2A} = - \frac{\alpha_{y3}\varepsilon_{r2}}{\mu_{r3}\varepsilon_{r3}}\left[A_{3A}\sinh(\alpha_{y3}h_3) + A_{3B}\cosh(\alpha_{y3}h_3)\right]\left[Y_2^{TE}\right]^{-1} \tag{A.100}$$

Equating (A.96) and (A.100)

$$\frac{\varepsilon_{r2}}{\varepsilon_{r3}}\left[A_{3A}\cosh(\alpha_{y3}h_3)+A_{3B}\sinh(\alpha_{y3}h_3)\right] =$$

$$-\frac{\alpha_{y3}\varepsilon_{r2}}{\mu_{r3}\varepsilon_{r3}}\left[A_{3A}\sinh(\alpha_{y3}h_3)+A_{3B}\cosh(\alpha_{y3}h_3)\right]\left[Y_2^{TE}\right]^{-1} \qquad (A.101)$$

Multiplying both sides by $[Y_2^{TE}\varepsilon_{r3}]/[\varepsilon_{r2}\sinh(\alpha_{y3}h_3)]$

$$\left[A_{3A}\coth(\alpha_{y3}h_3)+A_{3B}\right]\left[Y_2^{TE}\right] = -\frac{\alpha_{y3}}{\mu_{r3}}\left[A_{3A}+A_{3B}\coth(\alpha_{y3}h_3)\right] \qquad (A.102)$$

$$A_{3B}\left[Y_2^{TE}+\frac{\alpha_{y3}\coth(\alpha_{y3}h_3)}{\mu_{r3}}\right] = -A_{3A}\left[Y_2^{TE}\coth(\alpha_{y3}h_3)+\alpha_{y3}/\mu_{r3}\right] \qquad (A.103)$$

Using (A.92c) and factoring μ_{r3}/α_{y3} out of the left hand side,

$$A_{3B} = -A_{3A}\frac{\mu_{r3}}{\alpha_{y3}}\frac{Y_2^{TE}\,Y_{s3}^{TE}+(\alpha_{y3}/\mu_{r3})^2}{Y_2^{TE}+Y_{s3}^{TE}} \qquad (A.104)$$

Since the above equation is very similar to (A.93a). let

$$Y_3^{TE} = \frac{Y_2^{TE}\,Y_{s3}^{TE}+(\alpha_{y3}/\mu_{r3})^2}{Y_2^{TE}+Y_{s3}^{TE}} \qquad (A.105)$$

Then (A.104) simplifies to;

$$A_{3B} = -A_{3A}\,Y_3^{TE}\frac{\mu_{r3}}{\alpha_{y3}} \qquad (A.106)$$

As before, the tangential fields at the 4-5 dielectric interface are now equated.

7) $\left.E_{x5}^{TE}\right|_{y=d_4} = \left.E_{x4}^{TE}\right|_{y=d_4}$ or $\left.E_{z5}^{TE}\right|_{y=d_4} = \left.E_{z4}^{TE}\right|_{y=d_4}$

$$-j\,A_{5A}\frac{\beta_z}{\varepsilon_5} = -j\,\frac{\beta_z}{\varepsilon_4}\left[A_{4A}\cosh(\alpha_{y4}h_4)+A_{4B}\sinh(\alpha_{y4}h_4)\right] \qquad (A.107)$$

$$A_{5A} = \frac{\varepsilon_{r5}}{\varepsilon_{r4}}\left[A_{4A}\cosh(\alpha_{y4}h_4)+A_{4B}\sinh(\alpha_{y4}h_4)\right] \qquad (A.108)$$

8) $\left.H_{x5}^{TE}\right|_{y=d_4} = \left.H_{x4}^{TE}\right|_{y=d_4}$ or $\left.H_{z5}^{TE}\right|_{y=d_4} = \left.H_{z4}^{TE}\right|_{y=d_4}$

$$A_{5B}\frac{\beta_x\alpha_{y5}}{\omega\mu_5\varepsilon_5} = \frac{\beta_x\alpha_{y4}}{\omega\mu_4\varepsilon_4}\left[A_{4A}\sinh(\alpha_{y4}h_4)+A_{4B}\cosh(\alpha_{y4}h_4)\right] \qquad (A.109)$$

$$A_{5B} \frac{\alpha_{y5}}{\mu_{r5}} = \frac{\alpha_{y4}\varepsilon_{r5}}{\mu_{r4}\varepsilon_{r4}}\left[A_{4A}\sinh(\alpha_{y4}h_4)+A_{4B}\cosh(\alpha_{y4}h_4)\right] \tag{A.110}$$

Substituting in for A_{5B} using (A.94b)

$$- A_{5A}Y_5^{TE} = \frac{\alpha_{y4}\varepsilon_{r5}}{\mu_{r4}\varepsilon_{r4}}\left[A_{4A}\sinh(\alpha_{y4}h_4)+A_{4B}\cosh(\alpha_{y4}h_4)\right] \tag{A.111}$$

$$A_{5A} = - \frac{\alpha_{y4}\varepsilon_{r5}}{\mu_{r4}\varepsilon_{r4}}\left[A_{4A}\sinh(\alpha_{y4}h_4)+A_{4B}\cosh(\alpha_{y4}h_4)\right]\left[Y_4^{TE}\right]^{-1} \tag{A.112}$$

Equating (A.108) and (A.112)

$$\frac{\varepsilon_{r5}}{\varepsilon_{r4}}\left[A_{4A}\cosh(\alpha_{y4}h_4)+A_{4B}\sinh(\alpha_{y4}h_4)\right] =$$

$$- \frac{\alpha_{y4}\varepsilon_{r5}}{\mu_{r4}\varepsilon_{r4}}\left[A_{4A}\sinh(\alpha_{y4}h_4)+A_{4B}\cosh(\alpha_{y4}h_4)\right]\left[Y_5^{TE}\right]^{-1} \tag{A.113}$$

Multiplying both sides by $[Y_5^{TE}\varepsilon_{r4}]/[\varepsilon_{r5}\sinh(\alpha_{y4}h_4)]$

$$\left[A_{4A}\coth(\alpha_{y4}h_4)+A_{4B}\right]\left[Y_5^{TE}\right] = - \frac{\alpha_{y4}}{\mu_{r4}}\left[A_{4A}+A_{4B}\coth(\alpha_{y4}h_4)\right] \tag{A.114}$$

$$A_{4B}\left[Y_5^{TE}+\frac{\alpha_{y4}\coth(\alpha_{y4}h_4)}{\mu_{r4}}\right] = - A_{4A}\left[Y_5^{TE}\coth(\alpha_{y4}h_4)+\alpha_{y4}/\mu_{r4}\right] \tag{A.115}$$

Using (A.92d) and factoring μ_{r4}/α_{y4} out of the left hand side,

$$A_{4B} = - A_{4A}\frac{\mu_{r4}}{\alpha_{y4}}\frac{Y_5^{TE}Y_{s4}^{TE}+(\alpha_{y4}/\mu_{r4})^2}{Y_5^{TE}+Y_{s4}^{TE}} \tag{A.116}$$

Again this expression is very similar to (A.93a)

$$Y_4^{TE} = \frac{Y_5^{TE}Y_{s4}^{TE}+(\alpha_{y4}/\mu_{r4})^2}{Y_5^{TE}+Y_{s4}^{TE}} \tag{A.117}$$

Then (A.116) is

$$A_{4B} = - A_{4A}Y_4^{TE}\frac{\mu_{r4}}{\alpha_{y4}} \tag{A.118}$$

Having completed all the other boundary conditions, the fields at the center conductor interface are matched. As with the TM^y mode, the electric fields at the interface are intitially set equal to each other. The condition that the electic fields are zero over a finite

distance in the spatial domain is applied implicitly through the
current or electric field expansion fuctions used in Galerkin's method.

9) $E_{x3}^{TE}\Big|_{y=d_3} = E_{x4}^{TE}\Big|_{y=d_3}$ or $E_{z3}^{TE}\Big|_{y=d_3} = E_{z4}^{TE}\Big|_{y=d_3}$

$$-j \frac{\beta_z}{\varepsilon_3} A_{3A}\cosh(0) = -j \frac{\beta_z}{\varepsilon_4} A_{4A}\cosh(0) \tag{A.119}$$

$$A_{3A} = A_{4A}\frac{\varepsilon_{r3}}{\varepsilon_{r4}} \tag{A.120}$$

Using this relation in (A.106)

$$A_{3B} = -A_{4A} Y_3^{TE}\frac{\mu_{r3}\varepsilon_{r3}}{\alpha_{y3}\varepsilon_{r4}} \tag{A.121}$$

Finally, the discontinuity of the magnetic fields due to the
current densities on the center conductor interface is used.

10) $H_{x3}^{TE}\Big|_{y=d_3} - H_{x4}^{TE}\Big|_{y=d_3} = J_z^{TE}$

$$A_{3B}\frac{\beta_x\alpha_{y3}}{\omega\mu_3\varepsilon_3}\cosh(0) + A_{4B}\frac{\beta_x\alpha_{y4}}{\omega\mu_4\varepsilon_4}\cosh(0) = J_z^{TE} \tag{A.122}$$

Using (A.118) and (A.121)

$$-A_{4A} Y_3^{TE} - A_{4A} Y_4^{TE} = \frac{\omega\mu_0\varepsilon_4}{\beta_x} J_z^{TE} \tag{A.123}$$

$$A_{4A} = -\frac{1}{Y_3^{TE}+Y_4^{TE}}\frac{\omega\mu_0\varepsilon_4}{\beta_x} J_z^{TE} \tag{A.124}$$

As with the TM^y case, it is neccesary to verify that the TE^y field
configuration satisfies the boundary conditions independently in the
spectral domain. For this to be true, using the z directed magnetic
fields at the center conductor interface should yield the same answer
as using the x directed fields.

$$H^{TE}_{x3}\Big|_{y=d_3} - H^{TE}_{x4}\Big|_{y=d_3} = -J^{TE}_x$$

$$A_{3B}\frac{\beta_z\alpha_{y3}}{\omega\mu_3\epsilon_3}\cosh(0) + A_{4B}\frac{\beta_z\alpha_{y4}}{\omega\mu_4\epsilon_4}\cosh(0) = -J^{TE}_x \tag{A.125}$$

Using (A.118) and (A.121)

$$- A_{4A}Y^{TE}_3 - A_{4A}Y^{TE}_4 = - \frac{\omega\mu_0\epsilon_4}{\beta_z}J^{TE}_x \tag{A.126}$$

$$A_{4A} = \frac{1}{Y^{TE}_3+Y^{TE}_4}\frac{\omega\mu_0\epsilon_4}{\beta_z}J^{TE}_x \tag{A.127}$$

Equation (A.127) is equivalent to (A.124) if

$$- J^{TE}_x/\beta_z = J^{TE}_z/\beta_x \tag{A.128}$$

or

$$\beta_x J^{TE}_x = - \beta_z J^{TE}_z \tag{A.129}$$

which was shown to be true for the TE^y case in section 2.3.3. Thus, both the TE^y and TM^y modes satisfy the boundary conditions in the spectral domain independently. To complete the solution, substitute (A.124) into (A.118).

$$A_{4B} = \frac{Y^{TE}_4}{Y^{TE}_3+Y^{TE}_4}\frac{\mu_{r4}}{\alpha_{y4}}\frac{\omega\mu_0\epsilon_4}{\beta_x}J^{TE}_z \tag{A.130}$$

Using (A.124) and (A.130) for A_{4B} and A_{4A}, and substituting back into the equations for the electric field in region 4, equations (A.74a-b), and setting $y = d_3$, the fields at the center conductor interface are;

$$E^{TE}_{x4} = j\omega\mu_0 J^{TE}_z Z^{TE}\frac{\beta_z}{\beta_x} \tag{A.131a}$$

$$E^{TE}_{z4} = - j\omega\mu_0 J^{TE}_z Z^{TE} \tag{A.131b}$$

where

$$Z^{TE} = \left[Y_4^{TE} + Y_3^{TE} \right]^{-1} \tag{A.132}$$

Again, Y_4^{TE} and Y_3^{TE} can be thought of as the admittances seen by the current densities looking outware in each direction from the center conductor interface and Z^{TE} as the parallel combination of these admittances.

Looking over the derivation, it is evident that there is a pattern to the determination of the constants. Observing the equations defining the Y_i^{TM}; (A.27a-b), (A.39), and (A.51), and Y_i^{TE}; (A.93a-b), (A.105), and (A.117), it is evident that there is a pattern that can be used to generalize the derivation to an arbitrary number of layers. Using this pattern, with the geometry in Fig. 2.2, the modal impedances can be found using the equations in Section 2.3.8.